Thèse
de doctorat
de l'UTT

Shang LI

Development of Hybrid Light Emitters based on Photoinduced Surface Functionalization of a Diazonium Salt

Champ disciplinaire :
Sciences pour l'Ingénieur

2025TROY0022

Année 2025



utt
UNIVERSITÉ DE TECHNOLOGIE
TROYES

THESE

pour l'obtention du grade de

DOCTEUR
de l'UNIVERSITE DE TECHNOLOGIE DE TROYES

en SCIENCES POUR L'INGENIEUR

Spécialité : MATERIAUX, MECANIQUE, OPTIQUE ET NANOTECHNOLOGIE

présentée et soutenue par

Shang LI

le 10 juillet 2025

Development of Hybrid Light Emitters based on Photoinduced Surface Functionalization of a Diazonium Salt

JURY

M. Jean-Christophe LACROIX	PROFESSEUR DES UNIVERSITES	Président
M. Thierry GROSJEAN	DIRECTEUR DE RECHERCHE CNRS	Rapporteur
M. Jean-Claude WEEBER	PROFESSEUR DES UNIVERSITES	Rapporteur
Mme Shuwen ZENG	CHARGEE DE RECHERCHE CNRS	Examinatrice
M. Renaud BACHELOT	PROFESSEUR DES UNIVERSITES	Directeur de thèse
M. Xiao Wei SUN	PROFESSOR	Directeur de thèse

Table of contents

Abstract ..... **I**

Résumé ..... **II**

Chapter 1 Introduction – QD-based Hybrid nano-emitters: context, principle and state of the art – Outline of the manuscript **1**

1.1 Introduction 1

1.2 Semiconductor quantum dots 2

1.2.1 Quantum confinement effect on QDs 3

1.2.2 QDs emission properties 5

1.2.3 Spectrum measurements of QDs 6

1.2.4 Surface ligands and related surface coupling 8

1.2.5 Nano-emitters based on integrated QDs 12

1.3 Aryl diazonium salt 15

1.3.1 General properties and reactivity 15

1.3.2 Surface functionalization by grafting reactions 16

1.3.3 Molecular connection reactions 18

1.4 Outline of the manuscript 21

1.5 Summary 22

Reference 23

Chapter 2 Grafting of diazonium salt on ITO-coated glass resulting in controlled QDs adsorption on selected surfaces **29**

2.1 Introduction 29

2.2 Experimental methods 30

2.3 Surface functionalization by grafting of diazonium salt on ITO-coated glass 32

2.3.1 The morphology and thickness adjustment of grafted layer 33

2.3.2 PL emissions from the grafted layer before QD absorption 34

2.4 QDs adsorption on grafted diazonium salt layer 36

2.4.1 QDs characterization and adsorption on ITO-coated glass 36

2.4.2 The evidence of QDs adsorption by electrostatic interaction 39

2.5 Summary and Conclusions 43
Reference 44
Chapter 3 Luminescent optical fiber tip based on the QDs adsorption by diazonium salt .45
3.1 Introduction 45
3.2 Experimental methods 45
3.3 The morphology and emission of luminescent optical fiber tip 48
3.3.1 SEM and luminescent image of the optical fibered tip 49
3.3.2 Simulation of the process of fabrication of the luminescent optical fibered tip 50
3.3.3 QDs adsorption on fibered-tip by electrostatic interaction 52
3.4 Fibered sensor of concentration of ZnO nanoparticles in solution 53
3.4.1 Characterizations of the diameter of the QDs in colloid state 53
3.4.2 Sensor response with ZnO nanoparticles solution 55
3.5 Summary and conclusions 59
Reference 60
Chapter 4 Hybrid nanoemitter based on the QDs adsorption on plasmonic nanowires by diazonium salt 62
4.1 Introduction 62
4.2 Experimental methods 63
4.2.1 QDs-Au nanostrip nanoemitter fabrication 63
4.2.2 QDs-Ag NW nanoemitter fabrication 68
4.3 QDs-Au nanostrip nanoemitters: morphology and plasmonic PL emission 70
4.3.1 The morphology of the QDs-Au nanostrip nanoemitter 71
4.3.2 Plasmonic PL emission from QDs-Au nanostrip nanoemitter 71
4.3.3 ...Discussion on the influence of Au nanostrip and grafted diazonium layer on PL emission 73
4.4 The morphology and optical properties of QDs-Ag NW nanoemitter 75
4.4.1 The morphology of QDs-Ag NW nanoemitter 77
4.4.2 The PL emission from QDs-Ag NW nanoemitter 80
4.4.3 Evidence of QDs adsorption by electrostatic interaction 81
4.4.4 Plasmonic enhancement of Ag NW in nanoemitter 82
4.4.5 Remote excitation of QDs-Ag NW nanoemitter 86

4.5 Summary and conclusions 89
Reference 90
Chapter 5 Conclusion 92
Résumé en Français 94
1. Introduction 94
2 Greffage d'un sel de diazonium sur un verre recouvert d'ITO entraînant l'adsorption contrôlée de QDs sur des surfaces sélectionnées....96
2.1 Fonctionnalisation de surface par greffage de sel de diazonium sur du verre recouvert d'ITO 96
2.2 Adsorption des QDs sur la couche de sel de diazonium greffée....98
3 Pointe de fibre optique luminescente basée sur l'adsorption de QDs par un sel de diazonium ... .104
3.1 Image SEM et luminescente de l'extrémité d'une fibre optique....104
3.2 Capteur à fibres de la concentration de nanoparticules de ZnO en solution....107
4 Nanoémetteur hybride basé sur l'adsorption de QDs sur des nanofils plasmoniques par un sel de diazonium....108
4.1 Nano-émetteurs QDs-Au en bandes : morphologie et émission PL plasmonique....108
4.2 Morphologie et propriétés optiques du nano-émetteur QDs-Ag NW 110
5 Résumé et conclusions....116
Les références 116
Scientific productions 118
Acknowledgement....119

Abstract

The nanoemitter is one of the most important elements in the field of nanophotonics, which was applied to integrate into multitype of photonics device. Semiconductor quantum dots (QDs) have attracted attention as a kind of active nanosource because of the promising luminescent properties. With the enhancement of plasmonic effect, the QDs integrated nanoemitter shows benefits of scalable, high luminescence and solid-state stability.

This thesis is aimed to develop the hybrid nanoemitter with the help of surface functionalization of diazonium salt. On metal nanoparticle, this surface functionalization is induced by plasmonic generated hot electron. And the distribution of functionalized layer follows the local enhanced electromagnetic field. With the help of electrostatic adsorption, the surface modified QDs will adsorb on functionalized layer, which is at the vicinity of metal nanoparticle. The surface functionalization and QDs adsorption progress are orthogonal, which enhances versatility in nanoscale emitter design.

In this manuscript, chapter 1 is an introduction of the framework of thesis. Properties of QDs and diazonium salt were introduced. In chapter 2, the surface functionalization and electrostatic adsorption were performed on ITO. Both functionalization and QDs adsorption results were characterized. In chapter 3, the strategy was performed on optical fiber tip. With a two-step fabrication, a luminescent fiber tip was fabricated and exhibited environment-sensitivity. In chapter 4, the QDs integrated plasmonic nanoemitter was fabricated on sliver nanowire (Ag NW). The plasmonic enhancement factor could be adjusted during the fabrication steps. Moreover, the remote excitation illustrated the potential of the nanoemitter for advanced integrated photonics applications.

Keywords: Quantum dots; Photoluminescence; Surface functionalization; Diazonium salts; Nanoplasmonics

Résumé

Le nano-émetteur est l'un des éléments les plus importants dans le domaine de la nanophotonique, qui a été appliqué pour intégrer plusieurs types de dispositifs photoniques. Les points quantiques semi-conducteurs (QD) ont attiré l'attention en tant que nanosource active en raison de leurs propriétés luminescentes prometteuses. Avec l'amélioration de l'effet plasmonique, le nano-émetteur intégré aux QDs présente les avantages d'être évolutif, d'avoir une luminescence élevée et d'être stable à l'état solide.

Cette thèse vise à développer le nano-émetteur hybride à l'aide de la fonctionnalisation de surface du sel de diazonium. Sur les nanoparticules métalliques, cette fonctionnalisation de surface est induite par des électrons chauds générés par plasmonique. La distribution de la couche fonctionnalisée suit le champ électromagnétique local renforcé. Grâce à l'adsorption électrostatique, les QDs modifiés en surface s'adsorbent sur la couche fonctionnalisée, qui se trouve à proximité de la nanoparticule métallique. La fonctionnalisation de la surface et la progression de l'adsorption des QDs sont orthogonales, ce qui augmente la polyvalence dans la conception d'émetteurs à l'échelle nanométrique.

Dans ce manuscrit, le chapitre 1 est une introduction au cadre de la thèse. Les propriétés des QDs et du sel de diazonium ont été présentées. Dans le chapitre 2, la fonctionnalisation de la surface et l'adsorption électrostatique ont été réalisées sur l'ITO. Les résultats de la fonctionnalisation et de l'adsorption des QDs ont été caractérisés. Dans le chapitre 3, la stratégie a été appliquée à une pointe de fibre optique. Avec une fabrication en deux étapes, une pointe de fibre luminescente a été fabriquée et a montré une sensibilité à l'environnement. Dans le chapitre 4, le nano-émetteur plasmonique intégré aux QDs a été fabriqué sur un nanofil d'argent (Ag NW). Le facteur d'amélioration plasmonique a pu être ajusté au cours des étapes de fabrication. En outre, l'excitation à distance a illustré le potentiel du nano-émetteur pour des applications photoniques intégrées avancées.

Mots-clés: Boites quantiques; Photoluminescence; Fonctionnalisation des surfaces (chimie); Sels de diazonium; Nanoplasmonique

Chapter 1 Introduction – QD-based Hybrid nano-emitters: context, principle and state of the art – Outline of the manuscript

1.1 Introduction

Over the past two decades, nanophotonics has rapidly evolved, driving the demand for high-quality and low-cost nano-emitters integrated into photonic devices.[1,2] Quantum dots (QDs) are regarded as a promising material owing to their outstanding properties, which including high photoluminescence quantum yield, narrow full width at half maximum (FWHM), spectral tunability from visible to near-infrared ranges, and scalable fabrication compatibility.[3] To address challenges in practical applications, researchers have developed hybrid systems that integrate QDs with nanostructures, achieving unprecedented performance enhancements.[4] The fabrication of hybrid systems to integrate QDs into nano-structures and devices has been proved as one of the main approached developed on the nano-emitters research.[5,6]

In these hybrid systems, the plasmon enhanced system combining QDs and plasmonic structure has attracted attentions.[7,8] With plasmon-coupling, the PL emission of QDs would be enhanced, which is related to the enhanced electromagnetic field and the Purcell factor.[9,10] In such structure, the spatial position of QDs should be overlapped with hot spots. Controlling the nanoscale spatial distribution of QDs is one of the key points to realize the QD-based nano-emitters. Strategies involving near-field polymerization,[11] DNA strands[12] and Atomic Force Microscopy,[13] were applied.

During my thesis, we investigated a new approach, based on the connection between QDs ligands and surface chemical functional group, which is modified by diazonium salts. This strategy was applied on ITO glass, optical fiber tip, Au nanostrip and Ag nanowire. The connection method was verified and the QDs-Ag nanowire nanoemitter was fabricated in the end.

In this chapter, the research status of QDs (section 1.2) and diazonium salt (section 1.3) will be introduced. The introduction is expanded by the properties of the related materials. As a heterostructure nanoparticle, QDs will be introduced by principles of emission firstly. Then the functions of surface ligands and related reactions will be described. The development of QD-based integrated nano-emitters will be reviewed in the end. The introduction of diazonium salt will be mainly about the general properties and reactions: surface functionalization reaction and molecular connection reaction. These reactions are the main principles to implement the QDs nano-emitters in this thesis.

1.2 Semiconductor quantum dots

Researchers had put a lot of efforts to find novel luminescent material and develop varies utilization method to create photonic devices.[14,15] Physicists suggested devices like light-emitting diodes (LED) and lasers by precisely controlling the growth of different types of semiconductor material. Chemists also introduced new materials, such as organic dyes, fluorescent proteins, phosphors, as well as others.

Moreover, semiconductor QDs were developed by both physicist with the epitaxial method with grown in metal-organic chemical vapor deposition (MOCVD)[3,16] and chemists with the colloidal state with synthesized in solution.[17,18] For commonality, if the dimensions of a semiconductor nanocrystal are equal in all three directions and are within the quantum confinement regime of the material exciton, they are labeled as QDs. Theoretically, the size (diameter) of QDs must be smaller than the material's Bohr radius to follow quantum confinement.[19] Details are discussed in the next section.

The QDs discussed in this thesis are colloidal QDs, which are single-crystal semiconductor materials, normally II-VI or III-V groups elements, prepared at the nanoscale through solution-based synthesis.[20–22] Semiconductor colloidal QDs exhibit unique, exceptional optical and electrical properties, positioning them as promising luminescent materials for applications in optoelectronics and luminescence.[23] Due to the surface compatibility, this kind of QDs could be integrated into multitype of materials and structures after the synthesis completed.[24]

The colloidal QDs are in core-shell heterostructures with complex surface ligands. The core-shell heterostructure (Figure 1-1) determines the emission properties, which is the key point on multitype applications and determined by the carrier recombination process.[25] The adjustment of emission spectrum is mainly realized by controlling the core size or changing the core materials. Additionally, the surface ligands, typically, organic molecules, control the surface states, provides structural stability in solution, and can react via their functional groups to form bonds. By incorporating functional groups to form the "clickable" QDs, QDs with multiple ligand systems, such as azide,[26] maleimide,[27] biotin,[28] thiol,[29] and acrylate,[30] have been established for synthesis and proved various applications. Moreover, the surface modification and emission adjust are parallelly in synthesis progress, which provides the possibility to utilize various QDs into various integration methods.

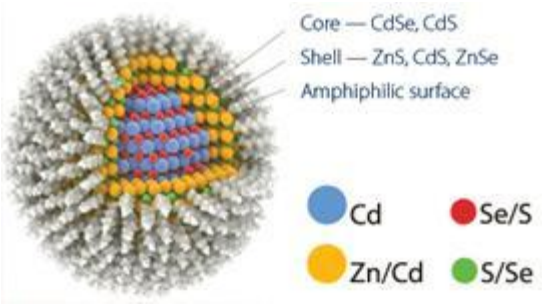

Figure 1-1. The typical core-shell structure of II-VI group colloidal quantum dots.[25]

1.2.1 Quantum confinement effect on QDs

In the early 1980s, scientists like L. Brus discovered that semiconductor crystals at the nanoscale could absorb and emit shorter wavelength light compared to their bulk materials.[31] Colloidal QDs are the nanocrystal composited by atoms of II-VI or III-V groups, such as CdSe, InP, etc. When a QD absorbs a photon, an electron in the valence band (VB) is excited to the conduction band (CB), creating a corresponding hole on VB. This a photo-generated electron-hole pair in QDs, termed as exciton, exhibits strong Coulomb interaction confined spatial proximity. A photon with shorter wavelength will emit from QD because of the exciton recombination progress.[32]

To explain this experimental phenomenon, L. Brus and others proposed the "quantum confinement effect".[31,33,34] This theory explained that when the geometric radius of a semiconductor crystal material gradually decreases shrinks below its Bohr radius, the energy levels, as well as its VB and CB, will transition from continuous to discrete distribution forms.

As illustrated in Figure 1-2, when the size of a semiconductor material is significantly larger than its Bohr radius, the exciton can freely move through the material.[35] When the semiconductor's size is comparable to Bohr radius, the exciton becomes confined in three dimensions and can no longer move freely move. When the nanocrystal size decreases continually, the exciton will not only become confined, but will also increase in energy.

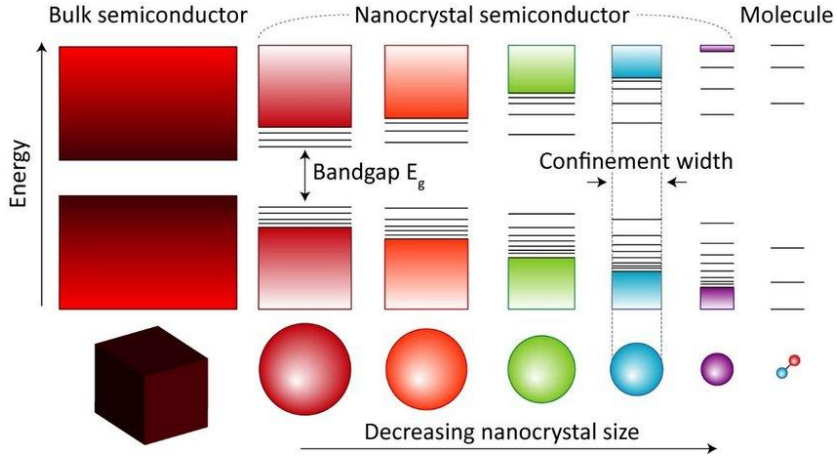

Figure 1-2. Quantum confinement effect. Comparison of bulk, NCs and molecules, indicating the size dependent bandgap of NCs and the formation of discrete states near the band edge.[35]

In 1984, L. Brus gave the relationship between the energy level of the first excited state in QDs and their sizes.[33] If we take the ground state level as the reference zero point, the specific expression for the first excited state level is as follows:

$$E = E_g + \frac{h^2\pi^2}{2R^2}\left(\frac{1}{m_e} + \frac{1}{m_h}\right) - \frac{1.8e^2}{\varepsilon R} \tag{1.1}$$

Here, the R is the radius of the QD size, m_e and m_h are the effective masses of the electron and hole, and ε is the dielectric constant of the semiconductor material.

The first part of the equation, which is E_g, represents the band gap of the semiconductor material itself, the second part is corresponding to the change of energy because of the quantum confinement effect, and the last part denotes the Coulomb interaction energy between electrons and holes.

When the QDs size decreases, both the first excited state level and the band gap increase, causing a simultaneous rise in the energy of absorbed and emitted photons. This results in a progressive blue-shift of the absorption and photoluminescence spectra, as shown in Figure 1-3. QDs exhibit a distinctive property of continuous wavelength tunability within the same material due to the quantum confinement effect, distinguishing them from other luminescent materials. Conversely, as QD size increases, the first exciton absorption peak exhibits a gradual red shift.[23]

In QD absorption spectra, several bands represent different energy levels, with the band gap width dictating the energy level of the first exciton state and resulting in a specific peak known as the first exciton absorption peak. Higher exciton levels manifest a continuous spread of absorption peaks, primarily in the shorter wavelength range, due to their denser states. QDs boast broader absorption bands and stronger absorption capabilities compared to other luminescent materials like organic dye molecules. The quantum confinement effect enables QDs to emit fluorescence light that can be continuously adjusted. For example, as CdSe QDs grow in size, their fluorescence emission peak shifts toward the red end of the spectrum, ranging from blue to red light.

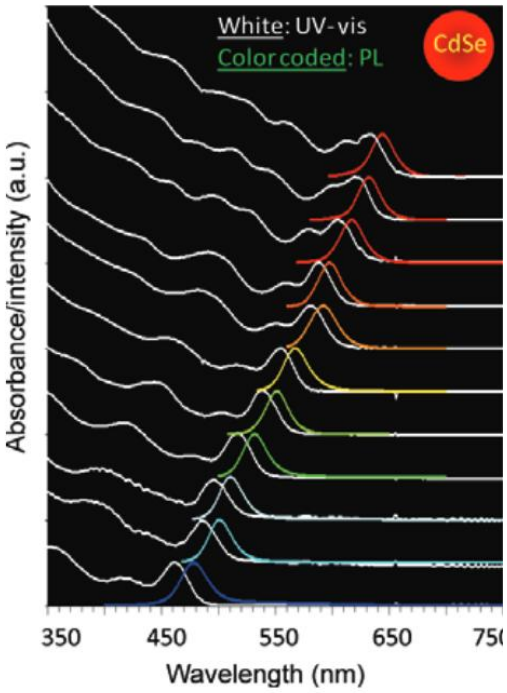

Figure 1-3. Absorption and photoluminescence (PL) spectra of different sizes of CdSe nanocrystals.[23]

The fluorescence emissions of QDs exhibit vary with the relative positioning of their valence and conduction bands, as well as the essential energy gap. Illustrated in Figure 1-4, in type I QDs, in which the core's band gap located in that of the shell, both generated electrons and holes will be confined within the core. It is resembled as the classic system. In type II or reverse type II QDs, electrons and holes are separated in the core or shell, respectively, due to energy level mismatches, leading to carrier recombination along the core-shell interface. The bandgap is determined by the highest valence band and lowest conduction band from either the core or shell. Significantly, type II QDs exhibit higher carrier mobility than type I QDs, making them well-suited for photodetectors and batteries due to their tendency toward internal carrier separation. In contrast, type I QDs predominantly undergo internal carrier

recombination, yielding higher quantum yields and enabling their widespread use in photoluminescent applications.[36]

Furthermore, in the case of type I QDs, the selection of shell material remains a crucial factor. In these core/shell configurations, the deposition of the shell layer can result in significant lattice mismatch, posing challenges in achieving a thick shell while maintaining optimal photoluminescent performance.

To illustrate, CdSe/ZnS and CdSe/CdS QDs will be compared. In CdSe/ZnS QDs, the ZnS shell has a band gap of 3.61 eV, which is larger than the CdSe core's 1.74 eV, leading to a significant lattice mismatch exceeding 11% between the shell and core. This mismatch may induce defects during synthesis.[37,38] On the other hand, CdSe/CdS QDs, with a lower lattice mismatch (~4%), are known for their superior optical characteristics.[39]

In CdSe/CdS QDs, the small energy difference between the CdSe and CdS conduction bands (about 0.1–0.2 eV) allows photoexcited electrons to delocalize across the core/shell structure, while photo-generated holes remain confined to the CdSe core due to quantum confinement. These QDs exhibit enhanced photoluminescent efficiency when synthesized with high quality. However, the asymmetric confinement of electrons and holes in their energy level structure gives rise to multiexciton and charged exciton states, leading to diverse energy gaps and a corresponding range of emitted photon energies.[40,41]

In the context of CdSe/ZnS QDs, the significant band gap difference allows for robust spatial confinement effects, primarily localizing electron and hole wave functions insides the part of CdSe core. This configuration can enhance the stability of the luminescent spectrum in CdSe/ZnS QDs, making them prevalent in commercial applications today, as well as the QDs utilized in this thesis.

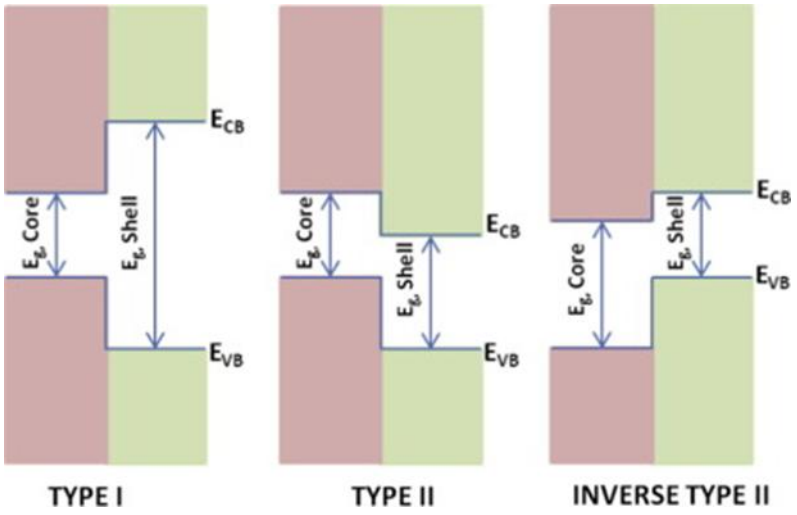

Figure 1-4. Types of core-shell QDs.[42]

1.2.2 QDs emission properties

The most crucial optical characteristic of QDs is their fluorescence emission.[43] Figure 1-5a delineates the fundamental physical and chemical mechanisms of luminescence phenomenon in the excitonic states of QDs. When QDs absorb photons from the excitation light, electrons in the valence band rapidly transition to the conduction band (Step 1). Subsequently, through vibrational relaxation processes, electrons relax to the conduction band

minimum and holes relax to the valence band maximum, forming excitons with Coulomb interaction (Step 2). If this exciton recombined with radiative, a photon whose energy corresponding to the band edge energy will be emitted (Step 3). This process is also termed the intrinsic luminescence of QDs arising from their first excited state.

Besides the intrinsic exciton emission of QDs, there is emission from defect states, as illustrated in Figure 1-5b. QDs commonly harbor surface defect states of positive and negative ions during their growth. These defects can catch light-induced charge carriers, facilitating electrons or holes into the defect energy level by processes like vibrational relaxation or electron tunneling. Trapped electrons or holes can then undergo radiative recombination within the QDs resulting in defect state emission or non-radiative recombination. Unlike exciton emission, defect state emission not only exhibits reduced efficiency but also causes a wavelength shift towards longer wavelengths.

To prevent defect state emission, effective methods must be employed to eliminate surface defects in QDs. To achieve optimal excitonic emission from QDs, it is crucial to epitaxially grow inorganic shell materials onto the core QD material. This epitaxial growth not only regulates the excitonic emission characteristics but also ensures that the wave function of the photo-induced excitons in the QDs avoids surface defects. Additionally, organic ligands on the QD surface help prevent the formation of surface ionic bonds, thereby playing a critical role in enhancing fluorescence quantum yields and overall system performance.[36]

Consequently, QDs with a core-shell structure exhibit more consistent optical properties and superior fluorescence quantum efficiency nowadays. In this thesis, the mentioned emission from QDs is assumed the intrinsic photoluminescence of QDs.

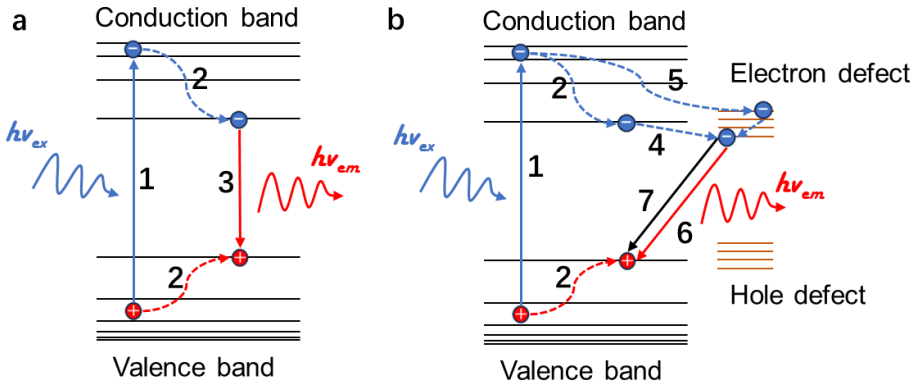

Figure 1-5. Fluorescence emission of QD. a. Schematic diagram of the photoluminescence process of QD excitons. b. Schematic diagram of the photoluminescence process of QD defects.

1.2.3 Spectrum measurements of QDs

Similar to organic dye molecule, single QD and the aggregate cluster display multiple inconsistencies in their optical characteristics.[44] These variances could serve as indicators for determining the nature of the light source.

In 1996, Louis Brus group and the Bawendi team, initially documented that individual QDs exhibit fluorescence blinking.[45] As shown in Figures 1-6a and 1-6b, continuous light excitation causes the fluorescence intensity of a single CdSe QD switches between "bright"

and "dark" states over time. The revelation of the fluorescence flickering phenomenon of single QD exposes that the luminescence of colloidal semiconductor QDs at the single-particle state differs from their respective solid-state emitter materials.

They analyzed the phenomenon by dividing fluorescence intensity by threshold and made statistics on the probability distribution frequency of bright and dark state durations (see Figure 1-6c and d). The durations of bright and dark states in QDs do not confirm to a single-exponential decay; instead, multiple exponential decay channels are observed. The decay patterns of these various fluorescence channels unveil a more complex mechanism behind this phenomenon, which goes beyond the classical physical model of quantum jump.

Furthermore, as illustrated in Figures 1-6c and 1-6d, it is evident that the average duration of the bright and dark states in a single QD (more than 1 second) which is much longer than single organic molecule by approximately 3-4 times. In Figure 1-6d, the dark state of the QD spans timescales from 40 milliseconds to over 100 seconds. Whereas single-molecule fluorescence is characterized as a photophysical process involving quantum jumps, the blinking behavior of a single QD is better described as a photochemical process.

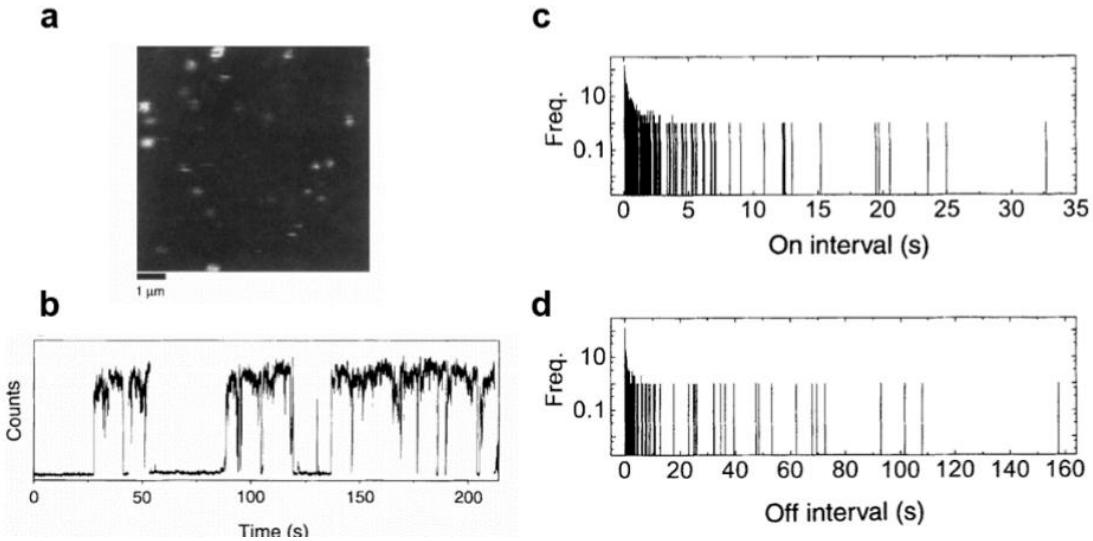

Figure 1-6. Fluorescence blinking of QD. a. The fluorescence image with single CdSe nanocrystal. (Excitation: 532 nm, 8 * 8 μm view) b. Fluorescence intensity versus time trace of single CdSe nanocrystal. c. Histogram of on time of single CdSe nanocrystal. d. Histogram of off time of single CdSe nanocrystal.[45]

In single-molecule spectroscopy, the second-order correlation curve is a commonly used tool to quantify cross-correlation in the fluorescence signal from a single molecule or particle. The second-order correlation function, denoted as $g^{(2)}(\tau)$, is shown as below,

$$g^{(2)}(\tau) = \langle I_1(t)\, I_2(t+\tau)\rangle \,/\, \langle I_1(t)\rangle\, \langle I_2(t+\tau)\rangle \tag{1.2}$$

The I_1 and I_2 are the light intensity from different two channels. τ is the time interval. For an ideal single photon emitter, when τ=0, one of $I_1(t)$ or $I_2(t+\tau)$ would be 0, and $g^{(2)}(0) = 0$.

In 2000, Michler et al. employed the Hanbury-Brown Twiss (HBT) system to analyze the second-order cross-correlation of the fluorescence signal from a single CdSe/CdS QD. It demonstrating that single QD, similar to organic molecular emitters, function effectively as single-photon signal sources (Figure 1-7).[46] In contrast, the results showed that the superposition of signals from multiple single-photon sources does not have an anti-bunching

effect. Hence, this method can be utilized to confirm if the fluorescence signal detected by the system originates from a single QD.

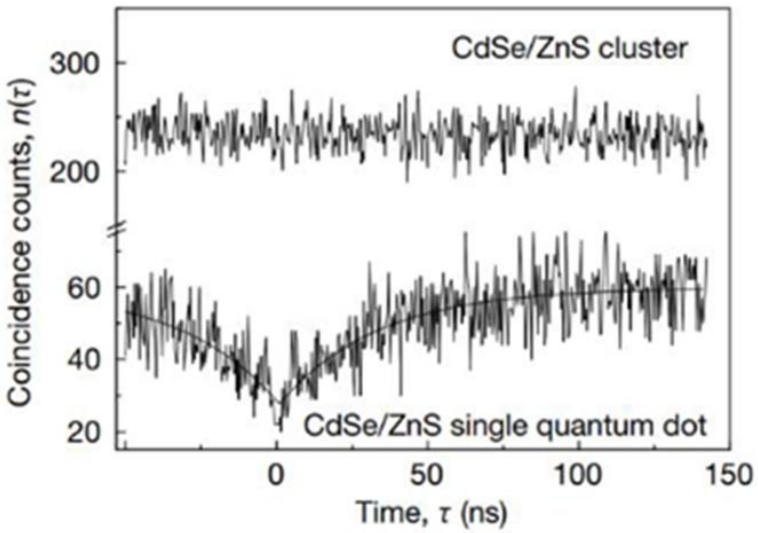

Figure 1-7. The second-order cross-correlation curve of emitting photons from CdSe/ZnS cluster and CdSe/ZnS single QD.[46]

Aggregate state optical measurements differ significantly from single-particle by concentrating on the collective optical properties of numerous organic molecules or QDs excited only once within a fixed observation time frame. In these assessments, the concentration of the aggregate QDs usually exceeds the concentration of absorbed photons, making continuous excitation challenging for individual QDs within the aggregate spectral analysis. This distinction highlights a crucial difference between QD single-molecule spectroscopy and aggregate optical measurements. Despite the potential requirement for multiple photons in certain photophysical or photochemical processes like multi-exciton Auger ionization, the low excitation light levels maintained in aggregate optical measurement limits the study of processes involving multiple photons within the QD system.[47,48] Consequently, single-molecule spectroscopy permits tailored excitation light intensities for individual QDs, allowing for the observation of their distinctive fluorescence emission properties under excitation.

To discuss the difference between single-molecule spectroscopy and aggregate optical measurements, consider the following analogy. Let's suppose that the chance of non-radiation recombination for a single QD under excitation is 1%, and the possibility of radiant luminescence emission is 99%. In single molecule spectroscopy, by analyzing the fluorescence intensity timeline, we can detect the 1% non-radiative recombination under a constant excitation light intensity by observing the duration of the bright state. However, it is difficult to capture this 1% non - radiative process when evaluating the fluorescence quantum yield of an aggregate solution. Even with exceptionally sensitive collective optical measurement tools, it is difficult to discover if the reason of fluorescence quantum efficiency decrease is the blink of the QDs.

1.2.4 Surface ligands and related surface coupling

Owing to their exceptional optical properties and solution-processable characteristics,

QDs exhibit significant potential in diverse applications such as lighting, displays, photovoltaics, and biological labeling. The quantum size effect allows for the precise tuning of QD particle sizes, enabling continuous and tunable fluorescence emission across the spectrum. By selecting suitable organic ligands for QD surface modification, it is possible to ensure their solubility and compatibility within the host environment, prevent aggregation, and preserve their optical properties.[49] The strategic adjustment of organic ligands on QDs' surfaces is critical in preventing their aggregation, ensuring their stable presence in solutions, and enhancing their processability.[50,51] Since 1993, researchers employed the "metal organic-coordination solvent-high temperature synthesis" method to produce high-quality QDs with uniform size.[52]

The key roles of QD surface ligands include regulating growth and nucleation dynamics, enhancing colloidal stability, and modifying surface physical and chemical properties. As shown in Figure 1-8, organic ligands are composed of functional groups that interact with the surface of QDs as well as the surrounding environment medium.[53]

Surface state represents a crucial aspect of QDs, alongside the quantum confinement effect. As a nanoscale-material, decreasing QDs' size significantly amplifies their specific surface area. It can be seen that the atoms in the surface state will have a significant impact on QDs.[54] When surfactants are absent, QDs are regarded as chemically "pure". However, insufficiently coordinated surface atoms can create unsaturated bonds, which in turn create localized energy levels, which is also call "defects". These defects will trap carriers, causing the increase in non-radiative exciton recombination as well as the decrease of photoluminescence efficiency. To preserve the optical properties of QDs, surface passivation with ligands is essential. This procedure helps in reducing defects, establishing a stronger potential barrier at the interface, and confining excitons within the QDs.

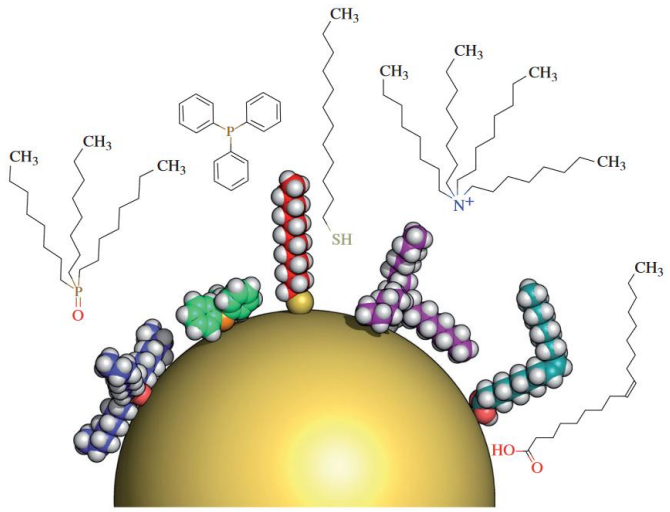

Figure 1-8. A nanoparticle with different ligand molecules. The particle is idealized as a smooth sphere, and the schematic molecule structures are shown above. Left to right: trioctylphosphine oxide (TOPO), triphenylphosphine (TPP), dodecanethiol (DDT), tetraoctylammonium bromide (TOAB) and oleic acid (OA).[53]

It is obvious that the surface ligand is bonded to QDs surface with one end. However, the orientation of another end remaining more investigation.[55,56] In 2012, Javier's team observed a change in the broadening of the ^{1}H NMR peak along the ligand chain. They noted that as one progresses from the functional group head (-COOH) to the tail of the ligand chain, the

peak broadening decreases, and the longitudinal relaxation time (T_1) increases.[57] This observation, shown in Figure 1-9, proposes that the ligand adopts a "standing" configuration on the QD surface, as this orientation facilitates a more uniform alignment of protons along the ligand chain, resulting in a smaller difference in peak broadening. Conversely, the narrowing of the peak width as the distance from the surface-bound functional group increases suggests that the ligand assumes a "standing" configuration on the nanocrystal surface, thereby forming a self-assembled monolayer. This research proved the possibility as well as the related efficiency to bond QDs by the end group of the surface ligands.

This finding provides the possibility of QDs' surface ligands connection. Due to ligands are "standing" on the surface, the functional group on another end of ligand will be in free-state in solvent. The free-state functional group could be connected with other molecule by chemical reactions. In our thesis, we connected QDs with functionalized surface by electrostatic interaction. In this progress, a bunch of free-state functional groups is necessary to maintain the progress.

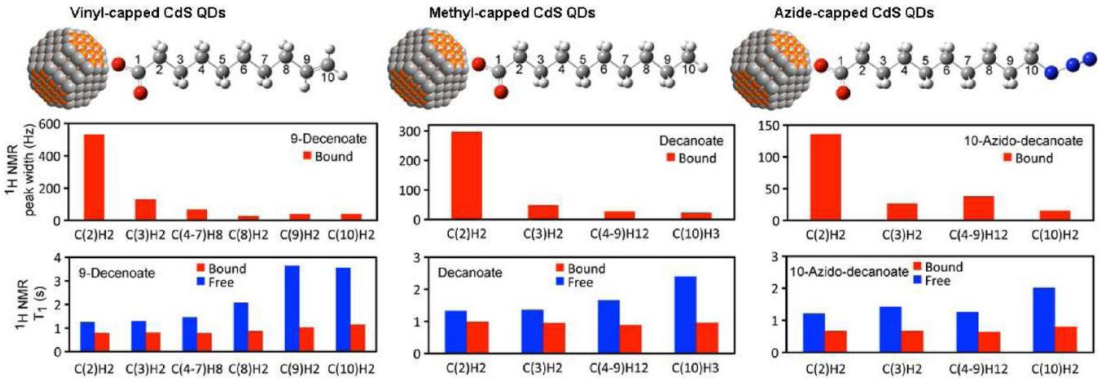

Figure 1-9. ^{1}H NMR peak widths ($v_{1/2}$) and T_1 relaxation times of CdS nanocrystal QDs capped with methyl ($-CH_3$), vinyl ($-CH=CH_2$) and azide ($-N_3$) terminated C10 carboxylate ligands.[57]

Appling the surface ligands with functional groups on QDs will introduce various functional groups, creating new functionalities in the resulting nanocomposite materials.[53] Thus, the primary purpose of surface modification is to shift highly luminescent, organic-soluble QDs into the aqueous phase and enhance their compatibility.

In 1998, Nie utilized thioglycolic acid (TGA) to effectively bind Zn^{2+} ions on CdSe/ZnS nanocrystals' surface to replace the TOP ligand and render the nanocrystals water-soluble.[58] Additionally, because the carboxyl group could be used to form covalent bonds with amino-containing biomolecules, like proteins and nucleic acids, QDs were applied to detect biomolecules. After Nie's work, various thiol molecules were applied as QDs ligands, such as mercaptopropionic acid (MPA),[59] thiopropanoic acid (MUA),[60] 4-mercaptobenzoic acid,[61] thioglycolates,[62] thiodiglycol,[63] cystamine,[64] and cysteine[65]. Binder introduced a phosphine-oxy ligand with an azide group.[66] This azide group can be linked with another compound having an azide group through heat or Cu(I)Br catalysis, facilitating the attachment of different functional groups to the QD surface.

Bawendi[67] and Mattoussi[68] developed ligands incorporating dihydrolipoic acid (DHLA) and PEG. DHLA serves as a linkage for QDs, while PEG enhances their water solubility and terminal functional group diversity. The terminal groups of PEG could be hydroxyl, carboxyl,

amino, vitamins and others. These groups enabling conjugation with various molecules such as biological substances and dyes as shown in Figure 1-10.[69] Due to almost kinds of organic group could be modified as the terminal group of PEG segment, this method provides an effective way about QD conjugation. However, it is difficult to maintain small size of QD because of the size of PEG molecule.

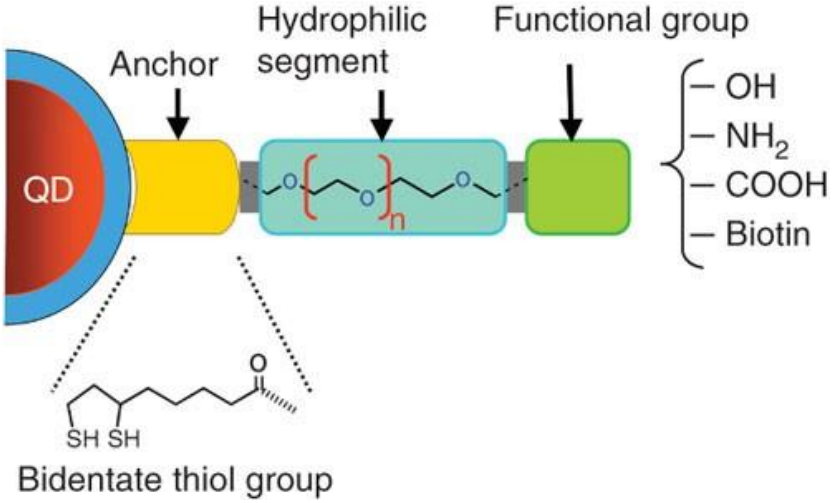

Figure 1-10. Modular design of hydrophilic ligands with terminal functional groups.[69]

The molecules with charges from functional group can be attached on the surface of QDs with opposite charges by electrostatic adsorption. This technique has been applied in fabricating nanocomposite like QD/dye, QD/polymer, and QD/protein. In 2014, Zhu connected positively charged tetrakis(1-methylpyridinium-4-yl)porphyrin (TMPyP) with CdTe QDs passivated with thioglycolic acid (negative charge), and created a QD/TMPyP nanocomposite.[70] Furthermore, micro-nano materials with amino groups can interact with QDs terminated with carboxyl groups through the electrostatic attraction between amino and carboxyl groups to form nanocomposite structures. Jinghong's group adsorbed thioglycolic modified QDs in porous amino-modified foam silicate to achieve electrocatalysis of H_2O_2.[71]

The layer-by-layer electrostatic self-assembly (LBL) is a common method on composite systems fabrication of QDs through electrostatic interactions. This technology utilizes the sequential adsorption of polyelectrolytes or molecules with opposing charges onto QDs with surface charge. Due to the cyclic progress of LBL self-assembly, it enables the formation of multilayer structures. There is an important advantage of LBL technology: the precise control over assembly thickness by regulating the number and quantity of layers assembled, whatever the size and shape of the substrate. By using LBL techniques shown in Figure 1-11, Qingbiao's group successfully developed a Fe3O4@C@CdTe core-shell structure on the surface of 300 nm magnetic nanoparticles Fe3O4.[72]

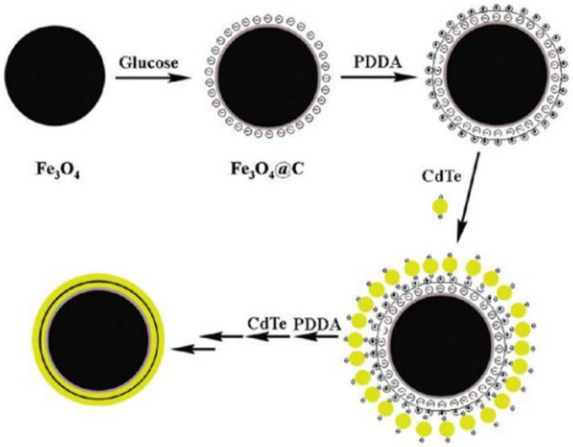

Figure 1-11. Schematic of LBL self-assembled nanocomposite structure based on electrostatic interaction.[72]

1.2.5 Nano-emitters based on integrated QDs

Integrated photonics has been developed over the last five decades to response to the growing need for higher data capacities and to complement the features of electronics.[73] This technology has developed the way for the creation of on-chip photonic components and related systems designed for processing light, especially for applications in optical communications and sensor technologies.[74,75] As presented in previous sections, QDs is one of the most promising photon sources, due to the narrow emission spectrum, long fluorescence duration, excellent material compatibility, and high quantum efficiency.[76]

Below, we describe the main fabrication methods used to integrate QDs on plasmonic metal structures. The resulted plasmonic coupling nanosystems are expected to maintain the requirements, such as scalable, tunable and easy to fabricate.[77] To keep the spatially overlap of amplified field and QDs, the spatial distribution of integrated QDs should be controlled.

In 2016, Maiken's team integrated single CdSe/ZnS QD into silver nanocube crystal. In this work, nanocube crystal served as an optical antenna and vertically directs the emission from QD. This structure improving the directivity of the radiation.[78] However, spin coating was used to integrate colloidal QDs with Ag nanocube crystals, resulting in an irregular arrangement of QDs across the substrate. While this random integration method was widely employed, it lacks efficiency.

Another method to address this issue involves incorporating a spacer layer to control the distance between emitters and metallic structures along one direction, which is important to avoid the quench of QDs.[79,80] Wang's group reported site-selective coatings based on anisotropic chemical growth on metallic nanostructures.[67] Therefore, controlling the spatial distribution of emitters near metal nanostructures in three dimensions by non-synthesis fabrication progress still remains a challenge. To realize the targeted fabrication, Riccardo's group precisely positioned the QDs and engineered a three-dimensional hybrid metal-dielectric parabolic antenna. This work involved optically induced polymerization step with confocal microscopy to realize the fabrication on the selected emitter, which improved the radiation directivity (D=106) and greatly reduced the scattering angle of the radiation (13.5°).[81]

The lithography technology, like EBL, was also used in plasmonic nanoemitter fabrication. One of the popular methods is fabricating the metal plasmonic structure after depositing QDs.[82–84] Also, the multitype of forces, like optical tweezer,[85] electro-osmosis,[86] AFM[87] and capillarity force,[24,88] were used to drive QDs on target position. These methods are powerful on single QDs integrated nanoemitter.

The DNA origami-based technique has been employed to fabricate plasmonic nanoantennas and coupling plasmonic nanostructures with nano-emitters.[89,90] As a dimer in structures with gaps, DNA origami has been used to position emitters, including single emitter.[91,92] However, the DNA-based hybrid nano-system is sensitive to environment in order to sustain DNA origami. This requirement limits the selection of metallic nanoparticles and application fields. Achieving precise spatial control during the integration of emitters in the vicinity of metallic nanostructures continues to pose a challenge.

Plasmonic photopolymerization has proven effectivity in confining QDs or molecules within polymer volumes situated at electromagnetic hotspots.[93–95] The position of emitters can be precisely controlled by selecting the specific plasmonic mode for nanophotopolymerization. In a previous study, our group introduced a method utilizing plasmon-assisted one or two-photon polymerization (TPP) to attach nanoemitters onto specific metal nanoparticles at the nanoscale. This approach of plasmonic photopolymerization is illustrated in Figure 1-12. Unlike traditional photopolymerization processes that require energy higher than the threshold for polymerization, this approach employed an exposure dose below the threshold of polymerization. This approach ensured that polymerization occurred exclusively in the vicinity of metal nanostructures, thereby increasing the local electromagnetic field energy density to exceed the threshold locally.[96]

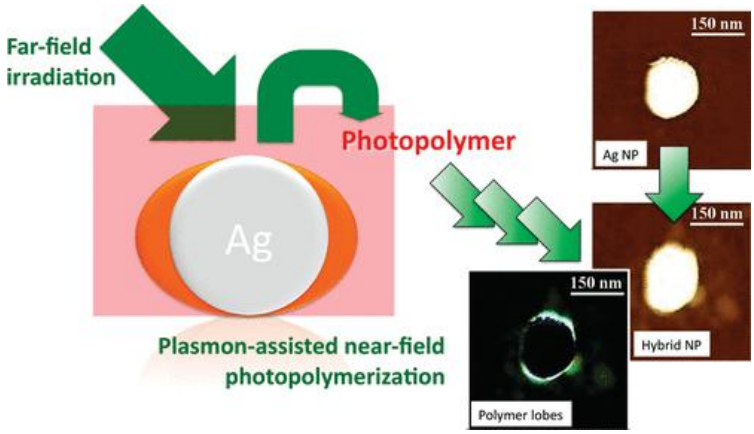

Figure 1-12. Surface plasmon dipolar resonance of individual Ag nanoparticle was used as an optical near-field source to locally trigger the reaction of a photopolymerizable formulation. Laser excitation of the nanoparticles embedded in the formulation reproducibly generates polymer features with typical dimensions ranging from 2 nm to a few tens of nanometer.[96]

Compared to one-photon excitation, two-photon excitation utilizes longer wavelengths that are less harmful and penetrate deeper into materials with minimizing damage. This method restricts two-photon absorption to the focal point, resulting in minimal reactions above and below the focal plane. In another work from our group shown in Figure 1-13, QDs are precisely positioned near plasmonic silver nanowires, based on direct laser writing using TPP of a photosensitive formulation containing QDs. This research showcased the interaction between QDs and propagative surface plasmons (SPs) by Ag nanowires, including the

scattering of surface waves at the nanowire ends.

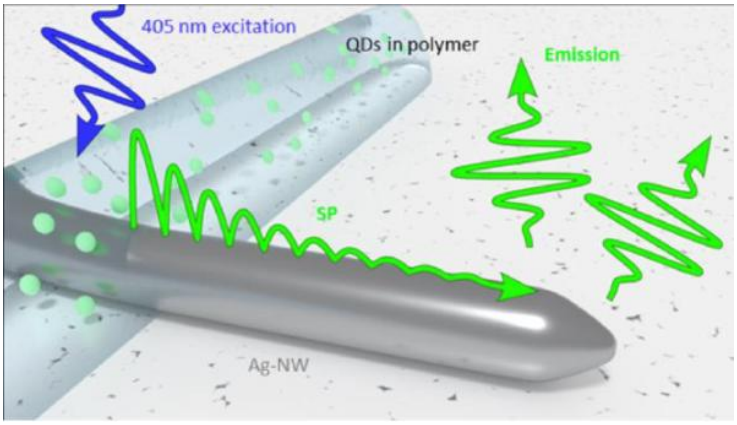

Figure 1-13. Representation of the developed hybrid nanosystem based on coupling between light emitting QDs in polymer and Surface Plasmons supported by silver nanowire.[97]

Plasmon-based TPP could be also applied for nanodisks, nanostars and nanocubes, and the resulted hybrid plasmonic structure could involve different emitters at the same time (Fig. 1-14).[98] By reducing the concentration of QDs in the polymer solution, a single QD or a few QDs can be encapsulated within the polymer lobes of the hybrid emitter, thereby enabling the hybrid nanoemitter to operate in the single-photon regime. This result paves the way for polarization-driven tunable nanoemitters and even single photon emitters (Fig. 1-15).[11] Plasmon-based TPP is a powerful method to control the scale of nanoemitter. But it still lacks of controlling the precise position of QDs inside polymer. The space gap between QDs and metal nanoparticle is uncertain.

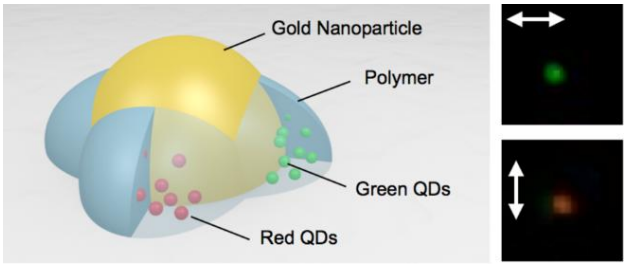

Figure 1-14. Two-color nanoemitters that enable the selection of the dominant emitting wavelength by varying the polarization of excitation light.[98]

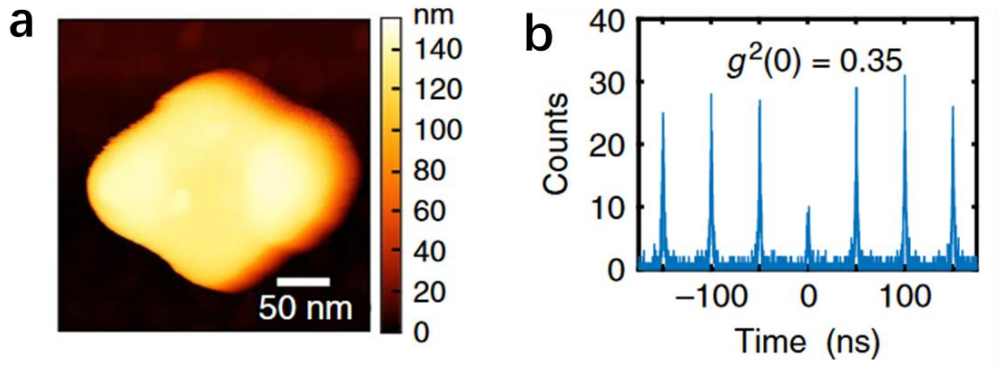

Figure 1-15. Hybrid nano-emitters in the single photon regime. a. AFM image of a nanocube-based hybrid nano-emitter. The polymer lobes contain a single or a few QDs. b. $g^{(2)}$ measurement showing $g^{(2)}(0) = 0.35$.[11]

1.3 Aryl diazonium salt

Aryl diazonium salts, a class of chemical molecules, was first discovered by Johann Peter Gries in 1858.[99] Over the past years, these salts have attracted attention due to their unique properties and reactivity. The chemical structure of diazonium salts is shown in Figure 1-16.

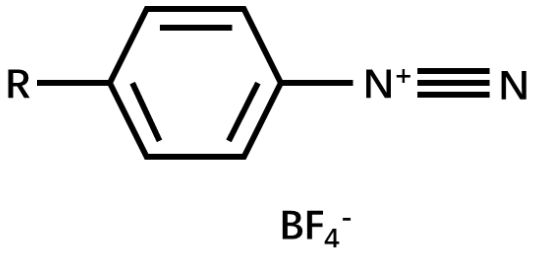

Figure 1-16. The chemical structure of diazonium salts.

Aryl diazonium salts are synthesized in acidic aqueous medium. The reaction will take place from aromatic amines with nitrous acid, which is prepared by $NaNO_2$ and acid, like HCl or HBF_4.[100] The electrophilic nature of the azo group is the primary factor governing the chemistry of diazonium salts.[101] Diazonium salts are thermally unstable and sensitive to friction. The risk of violent decomposition hazard in the solid state should be noticed.

$$ArNH_2 + HNO_2 + HX \rightarrow [ArN_2]^+X^- + 2\ H_2O \quad (1.3)$$

1.3.1 General properties and reactivity

Because of triple-bonded N≡N functional group, aromatic diazonium salts have found extensive application in synthetic chemistry,[102,103] azo dyes,[104] surface science[105] and polymer materials.[106] In some reactions of aryl diazonium salts, the N≡N functional group will be replaced to achieve substitutional reactions such as Sandmeyer reaction[107] and Meerwein arylation reaction.[108] In the view of reactant utilization rate, it is atom-efficient for only releasing two nitrogen atoms during the substitutional reactions. By coupling with diverse ligands through denitrogenation reactions, diazonium salts can react with different substitution. Currently, converting aryl diazonium salts into azo compounds by retaining the N_2 part has become an important functionalization mode in coupling chemistry.

In the surface reaction of diazonium salt, the N≡N functional group is eliminated, allowing the radical to engage with the surface. This dediazonation progress is important for the grafting mechanism, which we discuss later. The resulted Ar^+ cations or Ar. radicals could connect each other in room temperature. When the temperature to below 5 °C, it could be slowed down.[109]

Moreover, other reactions like Gomberg-Bachmann reaction[110], Merweein reactions[111] and Heck-Matsuda reaction[112] are also performed based on the dediazonation reaction. With direct reduction of the N≡N moiety or nucleophilic addition to its electrophilic nitrogen centers, it could be performed that the synthesis of aryl hydrazines and azo compounds,[113,114] and the transformation of aryl diazonium salts into nitrogen heterocycles.[115,116]

1.3.2 Surface functionalization by grafting reactions

The grafting reaction starts with the dediazonation reaction mentioned before. The resulted Ar. radicals is the key component during grafting. The grafting progress in shown in Fig. 1-17 monolayer and multilayer results.

The surface functionalization of 4-carboxybenzenediazonium tetrafluoroborate (DCOOH) diazonium salt on ITO surface is taken as example. The reduction of the diazonium salt will result to an aryl radical and dinitrogen. The radical will react and connect to the surface and form covalent bond as well as the monolayer functionalized surface. This progress involves one electron on the surface in reaction. The dinitrogen will release as a nitrogen molecule. After the monolayer fabrication, aryl radicals attach to both the substrate surface and pre-grafted phenyl groups. These progresses are shown as the "Route A" and "Route B" in Figure 1-17. As the reaction continues, the multilayer will form on ITO surface. It should be pointed that "Route A" and "Route B" could take place alternately. The resulted multilayer will contain both "phenyl- carboxyl" groups as well as azide groups. The carboxyl group will connect the layer with carbon atom, and another end will be in free space. In our work, the formation of resulted surface functionalized layer will follow these roads. When the functionalized surface is immersed in deionized water, there would be free-state -COOH groups solved in solution, which is the key component to realize the electrostatic interaction.

In specific cases, an alternative bonding type has been identified on gold surfaces, namely Au–N=N–C(aryl) structures.[117] These structures, detected by SERS and XPS,[118] are not consistently found by other surface, suggesting their formation is highly influenced by substrate conditions.[119] This bond may result from the direct interaction of an aryldiazenyl radical (Ar–N = N.) or a diazonium salt (Ar-N+≡N).

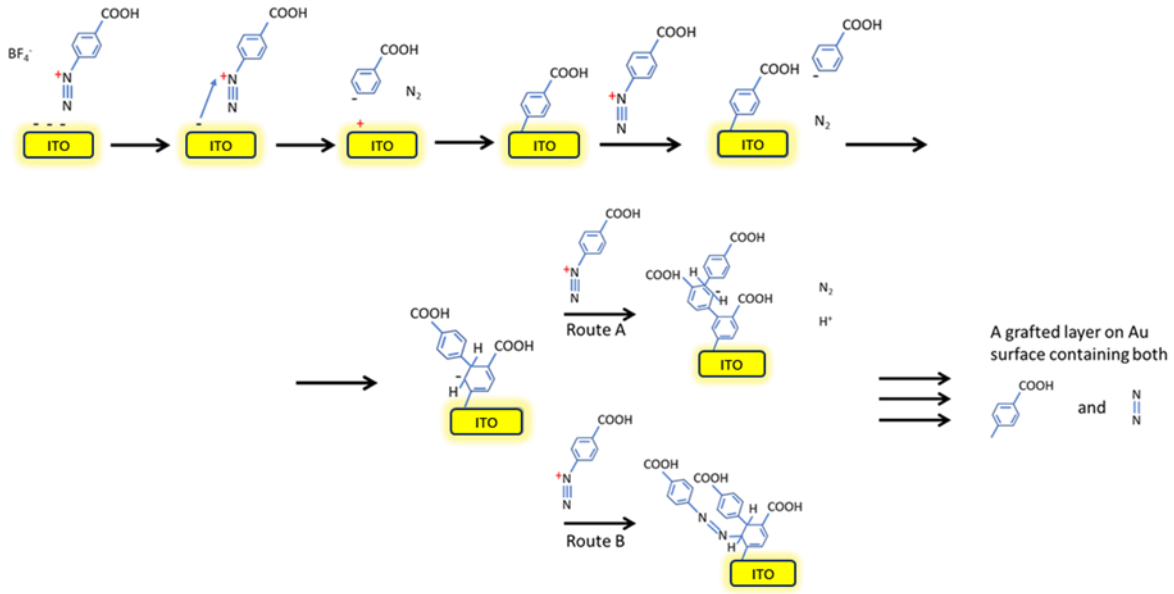

Figure 1-17. The grafting progress of monolayer and multilayer results with 4-carboxybenzenediazonium tetrafluoroborate (DCOOH) diazonium salt as example.

For certain applications like composite materials, the creation of multilayers can be advantageous. However, in cases such as biosensors where rapid electron transfer to the

detecting group is needed, multilayers can slow down this process.[120] The film formation should be restricted in monolayer or several layers in this kind of application. To control the grafting progress and achieve monolayer, there are also some methods, such as immersion time and solution concentration adjustment,[121] the electrochemical reduction control[122] and reaction rate modification.[123] Figure 1-18 shows that for polynitrophenylene groups by electrochemistry. There is a limit of layer thickness.[124] Experimentally, electrochemical detection fails to identify nitrophenyl groups within films thicker than approximately 4 nm. For such multilayered films, the reduced accessibility of the inner film regions means that only the outer layers actively participate in coupling reactions.[125]

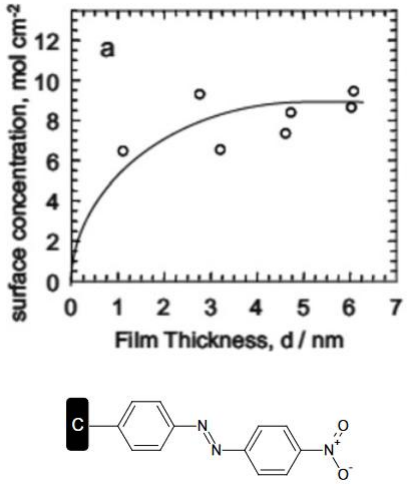

Figure 1-18. Surface concentration 4-nitroazobiphenyl groups as a function of the film thickness by electrochemistry detection.[124]

Grafting diazonium salts has proven a versatile method for achieving robust surface functionalization..[126] This functionalization relies on strong bonds, and its properties can be adjusted by varying the type of diazonium salt.[127] This grafting in the form of covalent bond could take place on different substrate, such as metal surface like Au and Ag, or carbon surface like carbon nanotube.

To carry out the graft reactions, many methods have been investigated. Electrografting is the first method in this kind of application. By repetitive scanning voltammetry with cycles, the graft reaction will be driven by electrochemical progress, and the resulting film will be thicker as the experiment continuing.[128]

Plasmonic excitation is another useful method, which is normally used on the surface of plasmonic NPs. The "hot electrons" generated by surface plasmon excitation are involved in this reaction and resulting in site-selective hot-electron mediated graft of diazonium salts. The graft film concentrates at the hot spots of plasmonic NPs. It has been applied for the regioselective functionalization of plasmonic nanostructures, including nanotriangles,[129] nanorods,[130,131] and nanodisks.[132] In our work, the plasmonic-induced diazonium salt grafting is applied on QDs-Ag NW nanoemitter. Due to the distribution of grafted diazonium salt layer following the plasmonic enhancement field, the QDs will adsorb on the hot spots, which allow the amplified PL emission of QDs integrated nanoemitter.

Photochemical dediazonation and reducing agents or surfaces are also effective methods. Whatever photochemical-immediate redox reaction or reducing agents, diazoniums will transfer to aryl radicals. Irradiating a PVC surface immersed in a photosensitizer-containing

solution with visible light exemplifies photochemical dediazonation.[133] For reducing agents or surfaces, ascorbic acid,[134] hypophosphorous acid,[135] sodium borohydride[136] and iodide[137] could also initiate the grafting reaction. Besides of methods discussed, ball milling[138] and microwaves[139] are proved to be possible to permit the grafting reaction.

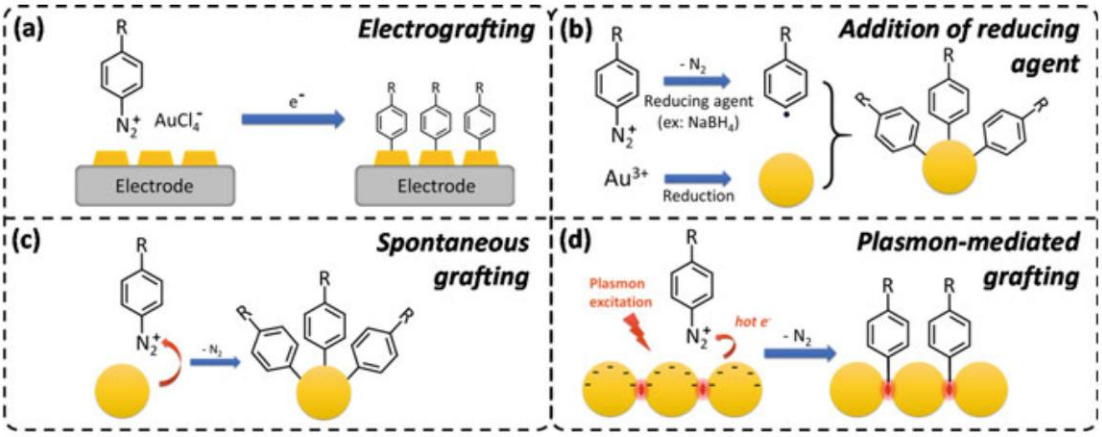

Figure 1-19. Representative scheme of the main approaches for the surface modification of plasmonic NPs by aryldiazonium salts, via a. electrografting; b. addition of a reducing agent1; c. spontaneous reaction between the diazonium salt and the NPs and d. plasmon-mediated reduction of diazonium salts.[140]

1.3.3 Molecular connection reactions

With continued development, the synthesis of aryl diazonium salts has greatly expanded, allowing for the customization of specific characteristics onto a diverse range of surfaces. Diazonium reactions facilitate the incorporation of various functional groups like nitro, amino, carboxylic acid, phosphonate, and others.[141] The flexibility of substrate materials amenable to diazonium chemistry modifications and the broad spectrum of functional groups that can be integrated onto surfaces highlight the superiority of diazonium chemistry compared to other surface modification techniques.

These diazonium cations could be transformed into radicals by the addition of a reducing agent, heating or hot-electrons.[142] These radicals possess the ability to interact with almost any surface, forming covalent bonds and enabling precise functionalization of surfaces in a controlled manner. Diazonium chemistry is employed to modify properties of surface, serving as both coating layer and adhesive layer that enables the subsequent attachment of diverse materials such as polymers, nanoparticles, or biomolecules. This approach acts as a versatile linker for connecting various types of molecules, nanoparticles, or metal surfaces, providing a robust platform for the functionalization of other materials.

One feature of diazonium chemistry connection is: for a specific surface-additives connection, there are several types of connection methods for design; for a specific connection method, there are also several types of surface-additives connection.

For the connection of QDs with graphene by diazonium chemistry, to anchor CdSe QDs, Pillai's group created hybrid heterostructures with thiolated graphene as platform. The diazonium salt of 4-aminothiophenol (4-ATP) was reacted with graphene.[143] Due to the -SH group from diazonium salt is connectable to QDs, the oleic acid ligands, which capped CdSe QDs, would been replaced with the thiolated graphene and resulted in CdSe-graphene hybrids.

The graphene was also attached on glassy carbon electrode with modification of p-nitrophenyl diazonium salt.[144] The nitro group was reduced to amine to connect graphene oxide to fabricate the electrode. This grafting-reduction method could also be applied to connect graphene nanosheets.[145]

Carbon nanotube (CNT) is another kind of wide-applied material in diazonium chemistry. Amide coupling represents a fundamental strategy. By connecting -OH group from CNT and $-NH_2$ group from p-aminobenzene diazonium salt, the vertical alignment on carbon substrate could be realized.[146] This method could also be applied to realize the micro-scale vertical alignment of CNT, which is fabricated with aminophenyl (AP) diazonium salt and shown in Figure 1-20.[147] The orthogonal bisdiazonium functionalization method have also been used to connect CNT with silicon surface.[148,149]

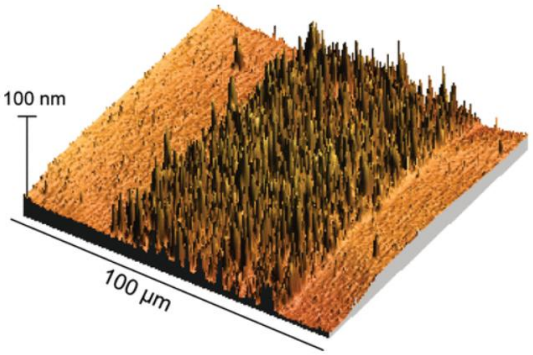

Figure 1-20. AFM image of vertically aligned carbon nanotubes (VACNTs) tethered to a patterned AP layer on PPF.[147]

By click chemistry, The azide and alkyne groups from diazonium salt are the key components. Both of them could be used as substrate and target functional groups. Henderson's group developed a reliable method for composite applications from functional carbon fibers with the copper alkyne–azide cycloaddition (CuAAC). By graft phenylacetylene diazonium salt to the carbon fiber surface, they establish a basis for surface modification through azide–alkyne click chemistry.[150] Moreover, among the connection methods with diazonium salt, it is popular that applying post-processing on the diazonium salt modified layer to carry out the connection reaction, like the reduction mentioned before. Besides these two or more steps connection reaction, click chemistry proved a one-step method in diazonium chemistry.

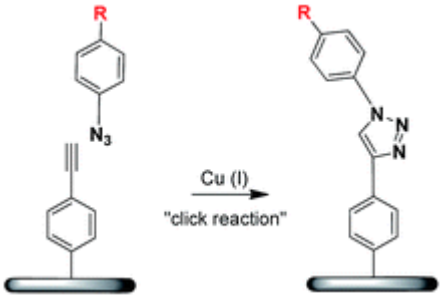

Figure 1-21. Using click chemistry to tailor the surface chemistry of carbon fibre.[150]

The electrostatic interaction is also a useful method to functionalize surfaces. This involves the surfaces with positive charges that interact with depositing material with negative charges, or surfaces with negative charges that interact with depositing material with positive

charges. The functional group with surface charge play the key roles in the reactions.

The most common examples of the immobilization are depositing negative charge material on surfaces containing ammonium groups. With a one-step process, quaternary ammoniums could be immobilized by directly connecting the grafted diazonium salt.[151] These grafted surface with positive charges could also be employed to connect inorganic anions like polyoxometalate (Figure 1-22).[152]

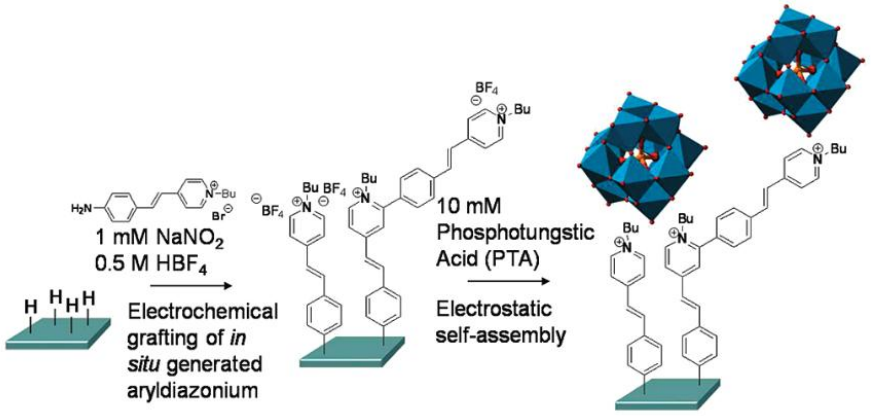

Figure 1-22. Electrochemical grafting of molecular pyridinium dye followed by electrostatic self-assembly of PTA.[152]

The in-suit reduction is another wide-applied method. This method entails grafting 4-nitrobenzene diazonium with electroreduction to generate amine group. Brozik's group[153] and Kuhn's group[154] electrostatically immobilize citrate-capped metal nanoparticles with positively charged surfaces. Moreover, there is a mixture post-reduction on carbon electrodes, which is based on the grafting of both 4-aminophenyl and 4-sulfophenyl groups,[155] which is coupled with Cu_2^+ and $PtCl_6^{2-}$ ions in solution by electrostatic interactions. The subsequent chemical reduction will transfer the captured metal ions into metal.

The in-situ reduction of deposited material could also be applied on other grafting method. To fabricate electrocatalytic, Guo and Li have deposited Pt[156] and Pd[157] nanoparticles on CNTs. Their study involved a dual electrochemical process: oxidizing single-walled carbon nanotubes (SWCNTs) to introduce COOH, OH and C=O groups from diazonium salt, followed by adsorbing Pt and Pd ions.

The choice of diazonium salt could also influence the resulted property. In a study, diazonium chemistry was employed bond a Polyetheretherketone (PEEK) coating layer onto stainless steel.[158] By evaluating the interfacial bond strength between the PEEK film and stainless steel, 4-nitrophenyl-modified stainless steel performed better than other diazonium salt. Similar results were observed when using a 4-nitrobenzenediazonium on PEEK coatings titanium surfaces.[159]

Catalyst immobilization is another example to show the influence of grafted diazonium salt layer to the resulted property. Reactive surfaces was post-functionalization. Then the electrochemical reduction of diazonium compounds was taken. The incompatible molecules could be immobilized and create mixed layers. Etienne's group developed a method featuring vinylbenzene diazonium and azidobenzene diazonium for co-grafting, facilitating the immobilization of two catalysts.[160] The modified electrode allowed the reduction of electroenzymatic, which is of D-fructose to D-sorbitol. The diazonium salts could endow

catalysts with improved dispersion, narrower size distribution, enhanced stability, and superior catalytic activity. Different catalyst concentration due to grafted layer thickness will lead to electrode passivation. Optimizing all parameters enhances the architecture of the nanocomposite, thereby improving the performance of the catalytic system.

In conclusion, surface modification by aryl diazonium salt offers advantages in terms of robustness and stability due to the formation of covalent bonds, like C−C and C−Au, and their capacity to incorporate diverse functionalities and create composites with various nanomaterials. While aryl diazonium salts have demonstrated significant advancements in various applications, challenges remain, particularly in precisely managing the thickness and diazonium salt molecule choose to enhance the aimed properties.

1.4 Outline of the manuscript

In this thesis, we propose a new method to fabricate hybrid nano-emitters based on electrostatic interaction between surface-modified QDs and locally grafted diazonium salt layers. With this method, QDs can be adsorbed on the nano-/micro-scale surface functionalization layer. This surface functionalization layer by diazonium salt has been performed on different types of surfaces, including ITO glass, glass, optical fibers, Au nanowires and Ag nanowires.

To the best of our knowledge, this is the first time electrostatic adsorption is used for fabricating QD-based nano-emitters on surfaces that are functionalized with diazonium salts. In the previous work of our group, the photopolymerization of QD-containing acrylate type photosensitive formulation has been performed by one-photon absorption, two-photon absorption with/without plasmonic excitation.[11,98,161] These methods are effective in controlling the localization of QDs at micro/nano-scale. Moreover, by two-photon absorption with localized surface plasmonic excitation, single QDs can be trapped at the vicinity of Au nanoparticle, resulting in a plasmon-driven single-photon emission which was demonstrated by second-order correlation function measurements.[5] However, as the QDs are trapped within the polymer nanovolume, the actual distance between the QDs and the plasmonic nanoparticle is not controlled. By the method of electrostatic adsorption, QDs are adsorbed at the surface of diazonium functionalized layers. The gap between QDs and plasmonic nanoparticle or adsorbed surface could be regarded as the thickness of the functionalized layers. Within the control of the functionalized layer thickness, the gap between QDs and plasmonic source or adsorbed surface could be adjusted as designed. Furthermore, as we will show throughout the section 1.3.2, unlike plasmon-induced photopolymerization, this method is not constrained by the absorption band of the photosensitive formulation, which must correspond to the plasmon resonance. Without the spectrum alignment between surface functionalization formulation and plasmon resonance, in the QDs-nanoemitter design, the surface functionalization and QDs integration could be divided as two orthogonal steps. Also, the adjustment of diazonium layer, making the nanoemitter more scalability. In summary, this approach not only resolves the spatial and spectral limitations of plasmonic photopolymerization but also enhances versatility in nanoscale emitter design.

In this work, the used QDs are CdSe/ZnS QDs that are surface-modified with cysteamine.

As discussed in section 1.2.1, quantum confinement effect on QDs, CdSe/ZnS QDs exhibit good carriers recombination property and related emission property due to the type-I core-shell structure. The surface ligands of used QDs were modified with cysteamine to replace original ligands. This replace will decrease the quantum yield from more than 90% to about 70%. But the $-NH_2$ will change to $-NH_3^+$ group when solved in deionized water, which will show positive surface charge and permit the electrostatic adsorption, which is discussed in 1.2.4 Surface ligands and related surface coupling.

4-carboxybenzenediazonium tetrafluoroborate (DCOOH) diazonium salt was used in this work to perform the surface functionalization. Due to dissociation in aqueous solution -COOH carboxy-group acquires a negative charge ($-COO^-$), which will be available for electrostatic interaction with the positively charged amino group ($-NH_3^+$) of QDs. As discussed in section 1.3.2, surface functionalization by grafting reactions, the $-COO^-$ group would be in free space without bonding and available to be coupled with $-NH_3^+$ group by electrostatic interaction.

The electrostatic adsorption effect has been proved with a reference molecule, 4-nitrobenzenediazonium tetrafluoroborate (DNO_2) diazonium salt. Rather than the $-COO^-$ group from DCOOH, there would be $-NO_2$ group in free space after DNO_2 grafting. The $-NO_2$ group is not consider having potential to engage in electrostatic interaction because there is no surface charge existing. With the reference of QDs solution depositing on DNO_2 grafted surface, the influence of other interaction, like Van der Waals force, can be discussed. By comparing the numbers of adsorbed QD, through the PL intensity, the electrostatic adsorption has been demonstrated.

In this thesis, the electrostatic adsorption between QDs and DCOOH-grafted surfaces was performed on ITO-coated glass surfaces (Chapter 2), optical fibers (Chapter 3) and Au and Ag nanowires (Chapter 4). On all of these surfaces, the process of polymerization of diazonium salt has been discussed and the subsequent electrostatic adsorption has turned out to play a role. A luminescent optical fiber tip used as a sensorwas fabricated (Chapter 3), and plasmonic effects were studied on the QDs nano-emitters based on Ag nanowires (Chapter 4).

1.5 Summary

In the first chapter, the background of the thesis was introduced. To fabricate QDs integrated nanoemitter, two key components, QDs and diazonium salt, are introduced. The quantum confinement effect as well as the emission properties of QDs were introduced. Then spectrum measurements of QDs were discussed, highlighting differences between cluster QDs and single QDs emissions. The surface ligands, surface coupling, as well as QD-based nano-emitters were overviewed, which provide possible strategies to perform the QD integration. Following the discussion on QDs, the properties of aryl diazonium salt were introduced. The grafting reactions is one of the key reactions used during this thesis, serving as the foundation for facilitating subsequent electrostatic adsorption of QDs. In addition, various molecular connection reactions were also examined, providing useful information for this thesis. Finally, the outline of the manuscript was presented.

Reference

1. Uppu, R., Midolo, L., Zhou, X., Carolan, J. & Lodahl, P. Quantum-dot-based deterministic photon–emitter interfaces for scalable photonic quantum technology. *Nat. Nanotechnol.* **16**, 1308–1317 (2021).
2. Liu, Z. *et al.* Micro-light-emitting diodes with quantum dots in display technology. *LIGHT-Sci. Appl.* **9**, 83 (2020).
3. García de Arquer, F. P. *et al.* Semiconductor quantum dots: Technological progress and future challenges. *Science* **373**, eaaz8541 (2021).
4. Heindel, T., Kim, J.-H., Gregersen, N., Rastelli, A. & Reitzenstein, S. Quantum dots for photonic quantum information technology. *Adv. Opt. Photonics* **15**, 613–738 (2023).
5. Han, Y., Chang, X., Cheng, X., Lin, Y. & Cui, B.-B. Recent Progress of Organic–Inorganic Hybrid Perovskite Quantum Dots: Preparation, Optical Regulation, and Application in Light-Emitting Diodes. *Laser Photonics Rev.* **17**, 2300383 (2023).
6. Hildebrandt, N., Lim, M., Kim, N., Yeon Choi, D. & Nam, J.-M. Plasmonic quenching and enhancement: metal–quantum dot nanohybrids for fluorescence biosensing. *Chem. Commun.* **59**, 2352–2380 (2023).
7. Pfeiffer, M. *et al.* Enhancing the optical excitation efficiency of a single self-assembled quantum dot with a plasmonic nanoantenna. *Nano Lett.* **10**, 4555–4558 (2010).
8. Yin, Z. *et al.* Local Field Modulation Induced Three-Order Upconversion Enhancement: Combining Surface Plasmon Effect and Photonic Crystal Effect. *Adv. Mater.* **28**, 2518–2525 (2016).
9. Chung, T., Lee, S.-Y., Song, E. Y., Chun, H. & Lee, B. Plasmonic Nanostructures for Nano-Scale Bio-Sensing. *Sensors* **11**, 10907–10929 (2011).
10. Seo, J. *et al.* Hybrid optical materials of plasmon-coupled CdSe/ZnS coreshells for photonic applications. *Opt. Mater. Express* **2**, 1026–1039 (2012).
11. Ge, D. *et al.* Hybrid plasmonic nano-emitters with controlled single quantum emitter positioning on the local excitation field. *Nat. Commun.* **11**, 3414 (2020).
12. Nicoli, F. *et al.* DNA-mediated self-assembly of plasmonic antennas with a single quantum dot in the hot spot. *Small* **15**, 1804418 (2019).
13. Groß, H., Hamm, J. M., Tufarelli, T., Hess, O. & Hecht, B. Near-field strong coupling of single quantum dots. *Sci. Adv.* **4**, eaar4906 (2018).
14. Mi, S., Kiss, M., Graziosi, T. & Quack, N. Integrated photonic devices in single crystal diamond. *J. Phys. Photonics* **2**, 042001 (2020).
15. Li, P., Zhou, Z., Zhao, Y. S. & Yan, Y. Recent advances in luminescent metal–organic frameworks and their photonic applications. *Chem. Commun.* **57**, 13678–13691 (2021).
16. Mittelstädt, A., Schliwa, A. & Klenovský, P. Modeling electronic and optical properties of III–V quantum dots—selected recent developments. *Light Sci. Appl.* **11**, 17 (2022).
17. Kagan, C. R., Bassett, L. C., Murray, C. B. & Thompson, S. M. Colloidal Quantum Dots as Platforms for Quantum Information Science. *Chem. Rev.* **121**, 3186–3233 (2021).
18. Zhang, J. *et al.* Colloidal Quantum Dots: Synthesis, Composition, Structure, and Emerging Optoelectronic Applications. *Laser Photonics Rev.* **17**, 2200551 (2023).
19. Klimov, V. I. *Nanocrystal Quantum Dots*. (CRC press, 2017).
20. Weller, H. Colloidal Semiconductor Q-Particles: Chemistry in the Transition Region Between Solid State and Molecules. *Angew. Chem. Int. Ed. Engl.* **32**, 41–53 (1993).
21. Alivisatos, A. P. Semiconductor clusters, nanocrystals, and quantum dots. *science* **271**, 933–937 (1996).
22. Murray, C. B., Kagan, C. R. & Bawendi, M. G. Synthesis and Characterization of Monodisperse Nanocrystals and Close-Packed Nanocrystal Assemblies. *Annu. Rev. Mater. Sci.* **30**, 545–610 (2000).
23. Peng, X. An essay on synthetic chemistry of colloidal nanocrystals. *Nano Res.* **2**, 425–447 (2009).
24. Chen, M., Lu, L., Yu, H., Li, C. & Zhao, N. Integration of Colloidal Quantum Dots with Photonic Structures for Optoelectronic and Optical Devices. *Adv. Sci.* **8**, 2101560 (2021).
25. Nasirzadeh, K., Nazarian, S. & Hayat, S. M. G. Inorganic Nanomaterials: A Brief Overview of the Applications and Developments in Sensing and Drug Delivery. **3**, (2016).
26. Schieber, C. *et al.* Conjugation of Transferrin to Azide-Modified CdSe/ZnS Core–Shell Quantum Dots using Cyclooctyne Click Chemistry*. *Angew Chem* (2012).
27. Zhou, M. *et al.* Peptide-Labeled Quantum Dots for Imaging GPCRs in Whole Cells and as Single Molecules. *Bioconjug. Chem.* **18**, 323–332 (2007).
28. Susumu, K., Uyeda, H. T., Medintz, I. L. & Mattoussi, H. Design of Biotin-Functionalized Luminescent Quantum Dots. *BioMed Res. Int.* **2007**, 090651 (2007).
29. Lystrom, L., Roberts, A., Dandu, N. & Kilina, S. Surface-Induced Deprotonation of Thiol Ligands

Impacts the Optical Response of CdS Quantum Dots. *Chem. Mater.* **33**, 892–901 (2021).
30. Chao, M.-R., Hu, C.-W. & Chen, J.-L. Comparative syntheses of tetracycline-imprinted polymeric silicate and acrylate on CdTe quantum dots as fluorescent sensors. *Biosens. Bioelectron.* **61**, 471–477 (2014).
31. Rossetti, R. & Brus, L. Electron-hole recombination emission as a probe of surface chemistry in aqueous cadmium sulfide colloids. *J. Phys. Chem.* **86**, 4470–4472 (1982).
32. Brus, L. E. Structure and electronic states of quantum semiconductor crystallites. *Nanostructured Mater.* **1**, 71–75 (1992).
33. Brus, L. E. Electron–electron and electron-hole interactions in small semiconductor crystallites: The size dependence of the lowest excited electronic state. *J. Chem. Phys.* **80**, 4403–4409 (1984).
34. Wilson, W. L., Szajowski, P. F. & Brus, L. E. Quantum Confinement in Size-Selected, Surface-Oxidized Silicon Nanocrystals. *Science* **262**, 1242–1244 (1993).
35. Akkerman, Q. Lead Halide Perovskite Nanocrystals: A New Age of Semiconductive Nanocrystals. (2019).
36. Peng, X., Schlamp, M. C., Kadavanich, A. V. & Alivisatos, A. P. Epitaxial growth of highly luminescent CdSe/CdS core/shell nanocrystals with photostability and electronic accessibility. *J. Am. Chem. Soc.* **119**, 7019–7029 (1997).
37. Hines, M. A. & Guyot-Sionnest, P. Synthesis and Characterization of Strongly Luminescing ZnS-Capped CdSe Nanocrystals. *J. Phys. Chem.* **100**, 468–471 (1996).
38. Dabbousi, B. O. *et al.* (CdSe) ZnS core- shell quantum dots: synthesis and characterization of a size series of highly luminescent nanocrystallites. *J. Phys. Chem. B* **101**, 9463–9475 (1997).
39. Talapin, D. V. *et al.* Highly Emissive Colloidal CdSe/CdS Heterostructures of Mixed Dimensionality. *Nano Lett.* **3**, 1677–1681 (2003).
40. Spinicelli, P. *et al.* Bright and Grey States in CdSe-CdS Nanocrystals Exhibiting Strongly Reduced Blinking. *Phys. Rev. Lett.* **102**, 136801 (2009).
41. Zhao, J., Chen, O., Strasfeld, D. B. & Bawendi, M. G. Biexciton Quantum Yield Heterogeneities in Single CdSe (CdS) Core (Shell) Nanocrystals and Its Correlation to Exciton Blinking. *Nano Lett.* **12**, 4477–4483 (2012).
42. Vasudevan, D., Gaddam, R. R., Trinchi, A. & Cole, I. Core–shell quantum dots: Properties and applications. *J. Alloys Compd.* **636**, 395–404 (2015).
43. Pu, C. *et al.* Synthetic Control of Exciton Behavior in Colloidal Quantum Dots. *J. Am. Chem. Soc.* **139**, 3302–3311 (2017).
44. van Sark, W. G. J. H. M., Frederix, P. L. T. M., Bol, A. A., Gerritsen, H. C. & Meijerink, A. Blueing, Bleaching, and Blinking of Single CdSe/ZnS Quantum Dots. *ChemPhysChem* **3**, 871–879 (2002).
45. Nirmal, M. *et al.* Fluorescence intermittency in single cadmium selenide nanocrystals. *Nature* **383**, 802–804 (1996).
46. Michler, P. *et al.* Quantum correlation among photons from a single quantum dot at room temperature. *Nature* **406**, 968–970 (2000).
47. Klimov, V. I. & McBranch, D. W. Auger-process-induced charge separation in semiconductor nanocrystals. *Phys. Rev. B* **55**, 13173 (1997).
48. Klimov, V. I., Mikhailovsky, A. A., McBranch, D., Leatherdale, C. A. & Bawendi, M. G. Quantization of multiparticle Auger rates in semiconductor quantum dots. *Science* **287**, 1011–1013 (2000).
49. Lin, Z. Organic–inorganic nanohybrids through the direct tailoring of semiconductor nanocrystals with conjugated polymers. *Chem. Eur. J.* **14**, 6294–6301 (2008).
50. Yin, Y. & Alivisatos, A. P. Colloidal nanocrystal synthesis and the organic–inorganic interface. *Nature* **437**, 664–670 (2005).
51. Yang, Y. *et al.* Entropic ligands for nanocrystals: from unexpected solution properties to outstanding processability. *Nano Lett.* **16**, 2133–2138 (2016).
52. Murray, C. B., Norris, D. J. & Bawendi, M. G. Synthesis and characterization of nearly monodisperse CdE (E = sulfur, selenium, tellurium) semiconductor nanocrystallites. *J. Am. Chem. Soc.* **115**, 8706–8715 (1993).
53. Sperling, R. A. & Parak, W. J. Surface modification, functionalization and bioconjugation of colloidal inorganic nanoparticles. *Philos. Trans. R. Soc. Math. Phys. Eng. Sci.* **368**, 1333–1383 (2010).
54. Peng, Z. A. & Peng, X. Nearly monodisperse and shape-controlled CdSe nanocrystals via alternative routes: nucleation and growth. *J. Am. Chem. Soc.* **124**, 3343–3353 (2002).
55. Majetich, S. A., Carter, A. C., Belot, J. & McCullough, R. D. 1H NMR characterization of the CdSe nanocrystallite surface. *J. Phys. Chem.* **98**, 13705–13710 (1994).
56. Sachleben, J. R., Colvin, V., Emsley, L., Wooten, E. W. & Alivisatos, A. P. Solution-state NMR studies of the surface structure and dynamics of semiconductor nanocrystals. *J. Phys. Chem. B* **102**, 10117–10128 (1998).
57. Tavasoli, E. *et al.* Surface Doping Quantum Dots with Chemically Active Native Ligands: Controlling

Valence without Ligand Exchange. *Chem. Mater.* **24**, 4231–4241 (2012).
58. Chan, W. C. & Nie, S. Quantum dot bioconjugates for ultrasensitive nonisotopic detection. *Science* **281**, 2016–2018 (1998).
59. Mitchell, G. P., Mirkin, C. A. & Letsinger, R. L. Programmed assembly of DNA functionalized quantum dots. *J. Am. Chem. Soc.* **121**, 8122–8123 (1999).
60. Hanaki, K. *et al.* Semiconductor quantum dot/albumin complex is a long-life and highly photostable endosome marker. *Biochem. Biophys. Res. Commun.* **302**, 496–501 (2003).
61. Chen, C.-C., Yet, C.-P., Wang, H.-N. & Chao, C.-Y. Self-assembly of monolayers of cadmium selenide nanocrystals with dual color emission. *Langmuir* **15**, 6845–6850 (1999).
62. Babu, P., Sinha, S. & Surolia, A. Sugar- quantum dot conjugates for a selective and sensitive detection of lectins. *Bioconjug. Chem.* **18**, 146–151 (2007).
63. Charvet, N. *et al.* Biotinylated CdSe/ZnSe nanocrystals for specific fluorescent labeling. *J. Mater. Chem.* **14**, 2638–2642 (2004).
64. Resch-Genger, U., Grabolle, M., Cavaliere-Jaricot, S., Nitschke, R. & Nann, T. Quantum dots versus organic dyes as fluorescent labels. *Nat. Methods* **5**, 763–775 (2008).
65. Liu, W. *et al.* Compact cysteine-coated CdSe (ZnCdS) quantum dots for in vivo applications. *J. Am. Chem. Soc.* **129**, 14530–14531 (2007).
66. Binder, W. H., Sachsenhofer, R., Straif, C. J. & Zirbs, R. Surface-modified nanoparticles via thermal and Cu (I)-mediated "click" chemistry: generation of luminescent CdSe nanoparticles with polar ligands guiding supramolecular recognition. *J. Mater. Chem.* **17**, 2125–2132 (2007).
67. Soo Choi, H. *et al.* Renal clearance of quantum dots. *Nat. Biotechnol.* **25**, 1165–1170 (2007).
68. Susumu, K., Mei, B. C. & Mattoussi, H. Multifunctional ligands based on dihydrolipoic acid and polyethylene glycol to promote biocompatibility of quantum dots. *Nat. Protoc.* **4**, 424–436 (2009).
69. Susumu, K. *et al.* Enhancing the stability and biological functionalities of quantum dots via compact multifunctional ligands. *J. Am. Chem. Soc.* **129**, 13987–13996 (2007).
70. Zhu, K., Hu, X., Ge, Q. & Sun, Q. Fluorescent recognition of deoxyribonucleic acids by a quantum dot/meso-tetrakis (N-methylpyridinium-4-yl) porphyrin complex based on a photo induced electron-transfer mechanism. *Anal. Chim. Acta* **812**, 199–205 (2014).
71. Zhang, Q., Zhang, L., Liu, B., Lu, X. & Li, J. Assembly of quantum dots-mesoporous silicate hybrid material for protein immobilization and direct electrochemistry. *Biosens. Bioelectron.* **23**, 695–700 (2007).
72. Wang, H. *et al.* Layer-by-layer assembled Fe3O4@ C@ CdTe core/shell microspheres as separable luminescent probe for sensitive sensing of Cu2+ ions. *Langmuir* **27**, 11609–11615 (2011).
73. Pelucchi, E. *et al.* The potential and global outlook of integrated photonics for quantum technologies. *Nat. Rev. Phys.* **4**, 194–208 (2022).
74. Atabaki, A. H. *et al.* Integrating photonics with silicon nanoelectronics for the next generation of systems on a chip. *Nature* **556**, 349–354 (2018).
75. Washburn, A. L. & Bailey, R. C. Photonics-on-a-chip: recent advances in integrated waveguides as enabling detection elements for real-world, lab-on-a-chip biosensing applications. *Analyst* **136**, 227–236 (2010).
76. Michler, P. *Single Quantum Dots: Fundamentals, Applications and New Concepts*. vol. 90 (Springer Science & Business Media, 2003).
77. Chen, M. *et al.* Approaches for Positioning the Active Medium in Hybrid Nanoplasmonics. Focus on Plasmon-Assisted Photopolymerization. *ACS Photonics* **11**, 3933–3953 (2024).
78. Hoang, T. B., Akselrod, G. M. & Mikkelsen, M. H. Ultrafast room-temperature single photon emission from quantum dots coupled to plasmonic nanocavities. *Nano Lett.* **16**, 270–275 (2016).
79. Russell, K. J., Liu, T.-L., Cui, S. & Hu, E. L. Large spontaneous emission enhancement in plasmonic nanocavities. *Nat. Photonics* **6**, 459–462 (2012).
80. Chikkaraddy, R. *et al.* Single-molecule strong coupling at room temperature in plasmonic nanocavities. *Nature* **535**, 127–30 (2016).
81. Morozov, S., Gaio, M., Maier, S. A. & Sapienza, R. Metal–dielectric parabolic antenna for directing single photons. *Nano Lett.* **18**, 3060–3065 (2018).
82. Song, J.-H., Atay, T., Shi, S., Urabe, H. & Nurmikko, A. V. Large enhancement of fluorescence efficiency from CdSe/ZnS quantum dots induced by resonant coupling to spatially controlled surface plasmons. *Nano Lett.* **5**, 1557–1561 (2005).
83. Belacel, C. *et al.* Controlling Spontaneous Emission with Plasmonic Optical Patch Antennas. *Nano Lett.* **13**, 1516–1521 (2013).
84. Dhawan, A. R. *et al.* Extreme multiexciton emission from deterministically assembled single-emitter subwavelength plasmonic patch antennas. *Light Sci. Appl.* **9**, 33 (2020).
85. Ghosh, S. & Ghosh, A. All optical dynamic nanomanipulation with active colloidal tweezers. *Nat. Commun.* **10**, 4191 (2019).

86. Ropp, C. *et al.* Nanoscale imaging and spontaneous emission control with a single nano-positioned quantum dot. *Nat. Commun.* **4**, 1447 (2013).
87. Ratchford, D., Shafiei, F., Kim, S., Gray, S. K. & Li, X. Manipulating Coupling between a Single Semiconductor Quantum Dot and Single Gold Nanoparticle. *Nano Lett.* **11**, 1049–1054 (2011).
88. Santhosh, K., Bitton, O., Chuntonov, L. & Haran, G. Vacuum Rabi splitting in a plasmonic cavity at the single quantum emitter limit. *Nat. Commun.* **7**, ncomms11823 (2016).
89. Lan, X. *et al.* DNA-enabled chiral gold nanoparticle–chromophore hybrid structure with resonant plasmon–exciton coupling gives unusual and strong circular dichroism. *J. Am. Chem. Soc.* **141**, 19336–19341 (2019).
90. Yeşilyurt, A. T. M. & Huang, J.-S. Emission manipulation by DNA origami-assisted plasmonic nanoantennas. *Adv. Opt. Mater.* **9**, 2100848 (2021).
91. Hübner, K. *et al.* Directing single-molecule emission with DNA origami-assembled optical antennas. *Nano Lett.* **19**, 6629–6634 (2019).
92. Acuna, G. *et al.* Fluorescence enhancement at docking sites of DNA-directed self-assembled nanoantennas. *Science* **338**, 506–510 (2012).
93. Zhou, X. *et al.* Plasmon-based photopolymerization: near-field probing, advanced photonic nanostructures and nanophotochemistry. *J. Opt.* **16**, 114002 (2014).
94. Ueno, K. *et al.* Nanoparticle plasmon-assisted two-photon polymerization induced by incoherent excitation source. *J. Am. Chem. Soc.* **130**, 6928–6929 (2008).
95. Zhan, C. *et al.* Plasmon-mediated chemical reactions. *Nat. Rev. Methods Primer* **3**, 1–21 (2023).
96. Deeb, C. *et al.* Plasmon-based free-radical photopolymerization: effect of diffusion on nanolithography processes. *J. Am. Chem. Soc.* **133**, 10535–10542 (2011).
97. Broussier, A. *et al.* Hybrid plasmonic nanosystem with controlled position of nanoemitters. *Appl. Phys. Lett.* **114**, (2019).
98. Zhou, X. *et al.* Two-Color Single Hybrid Plasmonic Nanoemitters with Real Time Switchable Dominant Emission Wavelength. *Nano Lett.* **15**, 7458–7466 (2015).
99. Griess, P. Preliminary notice of the reaction of nitrous acid with picramic acid and aminonitrophenol. *Ann Chem Pharm* **106**, 123–125 (1858).
100. Smith, M. B. *March's Advanced Organic Chemistry: Reactions, Mechanisms, and Structure*. (John Wiley & Sons, 2020).
101. Hegarty, A. F. Kinetics and mechanisms of reactions involving diazonium and diazo groups. in *Diazonium and Diazo Groups (1978)* 511–591 (1978). doi:10.1002/9780470771556.ch1.
102. Felpin, F.-X. & Sengupta, S. Biaryl synthesis with arenediazonium salts: cross-coupling, CH-arylation and annulation reactions. *Chem. Soc. Rev.* **48**, 1150–1193 (2019).
103. Sengupta, S. & Chandrasekaran, S. Modifications of amino acids using arenediazonium salts. *Org. Biomol. Chem.* **17**, 8308–8329 (2019).
104. Merino, E. Synthesis of azobenzenes: the coloured pieces of molecular materials. *Chem. Soc. Rev.* **40**, 3835–3853 (2011).
105. Mohamed, A. A. *et al.* Functionalization of nanomaterials with aryldiazonium salts. *Adv. Colloid Interface Sci.* **225**, 16–36 (2015).
106. Cao, C., Zhang, Y., Jiang, C., Qi, M. & Liu, G. Advances on aryldiazonium salt chemistry based interfacial fabrication for sensing applications. *ACS Appl. Mater. Interfaces* **9**, 5031–5049 (2017).
107. Mo, F., Qiu, D., Zhang, Y. & Wang, J. Renaissance of Sandmeyer-type reactions: conversion of aromatic C–N bonds into C–X bonds (X= B, Sn, P, or CF3). *Acc. Chem. Res.* **51**, 496–506 (2018).
108. Hari, D. P. & König, B. The photocatalyzed meerwein arylation: classic reaction of aryl diazonium salts in a new light. *Angew. Chem. Int. Ed.* **52**, 4734–4743 (2013).
109. Galli, C. Radical reactions of arenediazonium ions: An easy entry into the chemistry of the aryl radical. *Chem. Rev.* **88**, 765–792 (1988).
110. Gomberg, M. & Bachmann, W. E. The synthesis of biaryl compounds by means of the diazo reaction. *J. Am. Chem. Soc.* **46**, 2339–2343 (1924).
111. Heinrich, M. R. Intermolecular olefin functionalisation involving aryl radicals generated from arenediazonium salts. *Chem. Eur. J.* **15**, 820–833 (2009).
112. Felpin, F.-X., Nassar-Hardy, L., Le Callonnec, F. & Fouquet, E. Recent advances in the Heck–Matsuda reaction in heterocyclic chemistry. *Tetrahedron* **67**, 2815–2831 (2011).
113. Abrams, R., Lefebvre, Q. & Clayden, J. Transition metal free cycloamination of prenyl carbamates and ureas promoted by aryldiazonium salts. *Angew. Chem.* **130**, 13775–13779 (2018).
114. Taschinski, S. *et al.* Light-induced mechanistic divergence in Gold (I) catalysis: revisiting the reactivity of diazonium salts. *Angew. Chem. Int. Ed.* **58**, 16988–16993 (2019).
115. Lackner, A. D. & Fürstner, A. The Triple-Bond Metathesis of Aryldiazonium Salts: A Prospect for Dinitrogen Cleavage. *Angew. Chem.* **127**, 13005–13009 (2015).

116. Nakajima, M., Miyamoto, K., Hirano, K. & Uchiyama, M. Diaryl-λ3-chloranes: Versatile synthesis and unique reactivity as aryl cation equivalent. *J. Am. Chem. Soc.* **141**, 6499–6503 (2019).
117. Betelu, S. *et al.* Evidence of the Grafting Mechanisms of Diazonium Salts on Gold Nanostructures. *J. Phys. Chem. C* **120**, 18158–18166 (2016).
118. Mesnage, A., Lefevre, X., Jegou, P., Deniau, G. & Palacin, S. Spontaneous grafting of diazonium salts: chemical mechanism on metallic surfaces. *Langmuir* **28**, 11767–78 (2012).
119. Berisha, A. *et al.* Alkyl-Modified Gold Surfaces: Characterization of the Au–C Bond. *Langmuir* **34**, 11264–11271 (2018).
120. Hetemi, D., Noël, V. & Pinson, J. Grafting of Diazonium Salts on Surfaces: Application to Biosensors. *Biosensors* **10**, (2020).
121. Podvorica, F. I., Kanoufi, F., Pinson, J. & Combellas, C. Spontaneous grafting of diazoates on metals. *Electrochimica Acta* **54**, 2164–2170 (2009).
122. Anariba, F., Viswanathan, U., Bocian, D. F. & McCreery, R. L. Determination of the Structure and Orientation of Organic Molecules Tethered to Flat Graphitic Carbon by ATR-FT-IR and Raman Spectroscopy. *Anal. Chem.* **78**, 3104–3112 (2006).
123. Fontaine, O., Ghilane, J., Martin, P., Lacroix, J.-C. & Randriamahazaka, H. Ionic Liquid Viscosity Effects on the Functionalization of Electrode Material through the Electroreduction of Diazonium. *Langmuir* **26**, 18542–18549 (2010).
124. Brooksby, P. A. & Downard, A. J. Multilayer Nitroazobenzene Films Covalently Attached to Carbon. An AFM and Electrochemical Study. *J. Phys. Chem. B* **109**, 8791–8798 (2005).
125. Evrard, D., Lambert, F., Policar, C., Balland, V. & Limoges, B. Electrochemical Functionalization of Carbon Surfaces by Aromatic Azide or Alkyne Molecules: A Versatile Platform for Click Chemistry. *Chem. – Eur. J.* **14**, 9286–9291 (2008).
126. Mo, F., Qiu, D., Zhang, L. & Wang, J. Recent Development of Aryl Diazonium Chemistry for the Derivatization of Aromatic Compounds. *Chem. Rev.* **121**, 5741–5829 (2021).
127. Gooding, J. J. & Ciampi, S. The molecular level modification of surfaces: from self-assembled monolayers to complex molecular assemblies. *Chem. Soc. Rev.* **40**, 2704–2718 (2011).
128. Lenne, Q. *et al.* Electrochemical grafting of aryl diazonium salts in deep eutectic solvents. *Electrochimica Acta* **369**, 137672 (2021).
129. Nguyen, V.-Q., Ai, Y., Martin, P. & Lacroix, J.-C. Plasmon-induced nanolocalized reduction of diazonium salts. *ACS Omega* **2**, 1947–1955 (2017).
130. Nguyen, M. *et al.* Dynamic Plasmonic Platform To Investigate the Correlation between Far-Field Optical Response and SERS Signal of Analytes. *ACS Omega* **4**, 1144–1150 (2019).
131. Olshtrem, A. *et al.* Plasmon-assisted grafting of anisotropic nanoparticles – spatially selective surface modification and the creation of amphiphilic SERS nanoprobes. *Nanoscale* **12**, 14581–14588 (2020).
132. Tijunelyte, I. *et al.* Multi-functionalization of lithographically designed gold nanodisks by plasmon-mediated reduction of aryl diazonium salts. *Nanoscale Horiz.* **3**, 53–57 (2018).
133. Bouriga, M. *et al.* Sensitized Photografting of Diazonium Salts by Visible Light. *Chem. Mater.* **25**, 90–97 (2013).
134. González, M. C. R. *et al.* Self-limiting covalent modification of carbon surfaces: diazonium chemistry with a twist. *Nanoscale* **12**, 18782–18789 (2020).
135. Zeb, G., Viel, P., Palacin, S. & Le, X. T. On the chemical grafting of titanium nitride by diazonium chemistry. *RSC Adv.* **5**, 50298–50305 (2015).
136. Enciso, A. E. *et al.* Facile synthesis of stable, water soluble, dendron-coated gold nanoparticles. *Nanoscale* **9**, 3128–3132 (2017).
137. Xia, Y. *et al.* Iodide mediated reductive decomposition of diazonium salts: towards mild and efficient covalent functionalization of surface-supported graphene. *Nanoscale* **12**, 11916–11926 (2020).
138. Cheng, C., Jia, P., Xiao, L. & Geng, J. Tandem chemical modification/mechanical exfoliation of graphite: Scalable synthesis of high-quality, surface-functionalized graphene. *Carbon* **145**, 668–676 (2019).
139. Mamane, V. *et al.* Chemi- vs physisorption in the radical functionalization of single-walled carbon nanotubes under microwaves. *Beilstein J. Nanotechnol.* **5**, 537–545 (2014).
140. *Aryl Diazonium Salts and Related Compounds: Surface Chemistry and Applications*. (Springer International Publishing, Cham, 2022). doi:10.1007/978-3-031-04398-7.
141. Sandomierski, M. & Voelkel, A. Diazonium modification of inorganic and organic fillers for the design of robust composites: a review. *J. Inorg. Organomet. Polym. Mater.* **31**, 1–21 (2021).
142. Mahjoubi, H., Kinsella, J. M., Murshed, M. & Cerruti, M. Surface modification of poly (D, L-lactic acid) scaffolds for orthopedic applications: a biocompatible, nondestructive route via diazonium chemistry. *ACS Appl. Mater. Interfaces* **6**, 9975–9987 (2014).
143. Debgupta, J. & Pillai, V. K. Thiolated graphene – a new platform for anchoring CdSe quantum dots for hybrid heterostructures. *Nanoscale* **5**, 3615–3619 (2013).

144. Gupta, V. K., Yola, M. L., Atar, N., Ustundağ, Z. & Solak, A. O. A novel sensitive Cu(II) and Cd(II) nanosensor platform: Graphene oxide terminated p-aminophenyl modified glassy carbon surface. *Electrochimica Acta* **112**, 541–548 (2013).
145. Zhong, M. *et al.* An electrochemical immunobiosensor for ultrasensitive detection of Escherichia coli O157:H7 using CdS quantum dots-encapsulated metal-organic frameworks as signal-amplifying tags. *Biosens. Bioelectron.* **126**, 493–500 (2019).
146. Garrett, D. J., Flavel, B. S., Shapter, J. G., Baronian, K. H. R. & Downard, A. J. Robust Forests of Vertically Aligned Carbon Nanotubes Chemically Assembled on Carbon Substrates. *ACS Publications* https://pubs.acs.org/doi/full/10.1021/la902575w (2009) doi:10.1021/la902575w.
147. Lehr, J. *et al.* Patterning of Metal, Carbon, and Semiconductor Substrates with Thin Organic Films by Microcontact Printing with Aryldiazonium Salt Inks. *Anal. Chem.* **82**, 7027–7034 (2010).
148. Flatt, A. K., Chen, B. & Tour, J. M. Fabrication of Carbon Nanotube−Molecule−Silicon Junctions. *J. Am. Chem. Soc.* **127**, 8918–8919 (2005).
149. Joyeux, X., Mangiagalli, P. & Pinson, J. Localized Attachment of Carbon Nanotubes in Microelectronic Structures. *Adv. Mater.* **21**, 4404–4408 (2009).
150. Servinis, L. *et al.* Tailoring the fibre-to-matrix interface using click chemistry on carbon fibre surfaces. *J. Mater. Chem. A* **5**, 11204–11213 (2017).
151. Hadad, C. *et al.* Positive graphene by chemical design: tuning supramolecular strategies for functional surfaces. *Chem. Commun.* **50**, 885–887 (2013).
152. Zhong, Y. L., Ng, W., Yang, J.-X. & Loh, K. P. Electrostatically Self-Assembled Polyoxometalates on Molecular-Dye-Functionalized Diamond. *J. Am. Chem. Soc.* **131**, 18293–18298 (2009).
153. Harper, J. C. *et al.* A Multifunctional Thin Film Au Electrode Surface Formed by Consecutive Electrochemical Reduction of Aryl Diazonium Salts. *Langmuir* **25**, 3282–3288 (2009).
154. Kumsapaya, C. *et al.* Wireless Electrografting of Molecular Layers for Janus Particle Synthesis. *Chem. – Eur. J.* **19**, 1577–1580 (2013).
155. Vilà, N. & Bélanger, D. Mixtures of functionalized aromatic groups generated from diazonium chemistry as templates towards bimetallic species supported on carbon electrode surfaces. *Electrochimica Acta* **85**, 538–547 (2012).
156. Guo, D.-J. & Li, H.-L. High dispersion and electrocatalytic properties of Pt nanoparticles on SWNT bundles. *J. Electroanal. Chem.* **573**, 197–202 (2004).
157. Guo, D. & Li, H. Electrochemical synthesis of Pd nanoparticles on functional MWNT surfaces. *Electrochem. Commun.* **6**, 999–1003 (2004).
158. Shimizu, K. *et al.* Durability of PEEK adhesive to stainless steel modified with aryldiazonium salts. *Int. J. Adhes. Adhes.* **51**, 1–12 (2014).
159. Pan, L. *et al.* Surface characteristics and adhesive strength to polyetheretherketone of titanium electrografted with aryl diazonium salt. *Mater. Des.* **95**, 555–562 (2016).
160. Zhang, L., Vilà, N., Walcarius, A. & Etienne, M. Molecular and biological catalysts coimmobilization on electrode by combining diazonium electrografting and sequential click chemistry. *ChemElectroChem* **5**, 2208–2217 (2018).
161. Ge, D. *et al.* Advanced hybrid plasmonic nano-emitters using smart photopolymer. *Photonics Res.* **10**, 1552 (2022).

Chapter 2 Grafting of diazonium salt on ITO-coated glass resulting in controlled QDs adsorption on selected surfaces

2.1 Introduction

Chapter 1 introduced the emission properties of QDs and surface reactions of diazonium salts, which are the key materials for fabrication of the integrated hybrid light nano-sources in this thesis.

The hybrid nano-sources consisting of coupled QDs and metal nanoparticles/nanostructure are expected to have small size, stable performance and high efficiency at the same time.[1] Semiconductor QDs have been proven to be an excellent kind of nanoscale fluorescent material.[2] Simultaneously, their coupling with noble metal nanoparticles/nanostructure, can improve emission properties of QDs by enhancement of photoluminescence (PL) intensity, increase in photostability and reduced blinking due to the plasmonic effects.[3–5] However, on the heterogeneous surface, the control of the QDs spatial distribution in nanoscale, which is crucial to achieve these effects and create efficient integrated hybrid nano-sources, is still challenging task.[6] In this thesis, we propose to use laser-induced grafting of diazonium salts to create sites for a selective attachment of QDs and hence control their deposition.

The diazonium salt chemistry has proved to be an practical strategy to functionalize selected areas on metal surface.[7,8] In previous works, the functionalization on the metal nanoparticles surface was induced by plasmonic effects under the excitation of the plasmon resonance. This kind of functionalized surface can be spatially confined in micro- and nano-scale by controlling the incident energy and illumination area. The variety of functional groups available in diazonium salts can be used to maintain further reactions or interactions. In this thesis, we propose that surface-modified QDs could be selectively adsorbed on the pre-selected areas functionalized by diazonium salts, as illustrated in Figure 2-1, resulting in a controlled anisotropic distribution of QDs.[9] This selected adsorption is promising to fabricate light-emitting devices. Comparing to the previous reported hybrid plasmonic nano-sources or QDs-LED displays,[10,11] , which are succeed to control the spatial distribution, this method has a potential to precisely regulate the distance between plasmonic nanostructures and QDs.

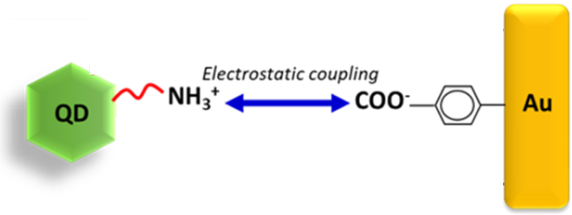

Figure 2-1. The schematic of electrostatic interaction between surface-modified QDs and diazonium salts grafted on Au nanoparticle surface.

In this chapter, we study the possibility of selectively depositing QDs on a micron-sized structures of grafted diazonium salts. 4-carboxybenzenediazonium tetrafluoroborate (DCOOH) diazonium salt was used to carry out the grafting on a ITO-coated glass substrate to form functionalized (sub)micrometer-scale areas for electrostatic interaction with QDs. Then, surface-modified QDs were deposited from the solution on functionalized ITO surface. As reference, 4-nitrobenzenediazonium tetrafluoroborate (DNO_2) diazonium salt was also used for the grafting, which is not supposed to enable electrostatic adsorption of QDs. We will show, by comparison, that the PL intensity from DCOOH-modified surface is 7.3 times higher than that from DNO_2-modified and non-grafted surfaces. The difference in the emission light intensity from two kinds of diazonium functionalized surfaces proves the selective QDs adsorption via electrostatic interaction. This work demonstrates a new method to control QD deposition on the ITO surface and has potential to perform this adsorption by fabricating photonic and optoelectronic devices.

2.2 Experimental methods

In our experiment, the surface functionalization is performed on ITO-coated glass as shown in Figure 2-2. The thickness of ITO layer on glass is 0.15 mm in this experiment. The DCOOH solution was dropped on the ITO surface. The solution concentration varied from 5 mM to 100 mM, which is one of the key parameters to determine the thickness of surface functionalization layer. A 532 nm laser light with different laser density was used to exposure the target surface. As Figure 2-2 shows, the laser light from the bottom of ITO-coated glass was focused onto the glass surface via a 100x objective lens whose N.A. is 0.85 and working distance is 0.33 mm. The expected laser spot diameter on sample surface is therefore around 760 nm. In our experiment, the exposure time varied from 20 s to 300 s. When keeping the laser light density consistent, the exposure time is proportional to the exposure energy, which is another important parameter to determine the thickness of surface functionalization layer.

Under laser light exposure, the diazonium salt will form a layer on ITO-coated glass by grafting reaction, which will functionalize the ITO surface with -COOH group. The laser-induced surface functionalization progress is the same with the schematic as Figure 1-17 of Chapter 1. In this case, due to the absorption of DCOOH diazonium salt is not nil at λ=532 nm, it is possible that the diazonium heats up, triggering the local grafting and polymerization of aryl layers derived from diazonium salt on ITO surface. The role of thermal effects on the diazonium salts reduction was described in several publication.[12,13] The resulted size along the

projection direction of grafted layer is dependent on the light spot size. And the thickness is influenced by DCOOH solution concentration and exposure time. All the parameters should be controlled in experiment and could be adjusted to get the grafted layer with different size in three dimensions.

After the laser-induced surface functionalization, plenty of micro-size grafted layer could be formed by exposure laser light at different positions of ITO-coated glass within the same DCOOH solution. After grafting completed, the DCOOH solution was rinsed by deionized water to remove the excess molecular to prevent unexpected reaction in solution. Both Scanning Electron Microscope (SEM) and Atomic Force Microscope (AFM) were used to characterize the grafted layer. Moreover, PL spectrum was used to measure the PL emission from the grafted layer. This spectrum would be used as reference relative to QDs-nanoemitter PL spectrum.

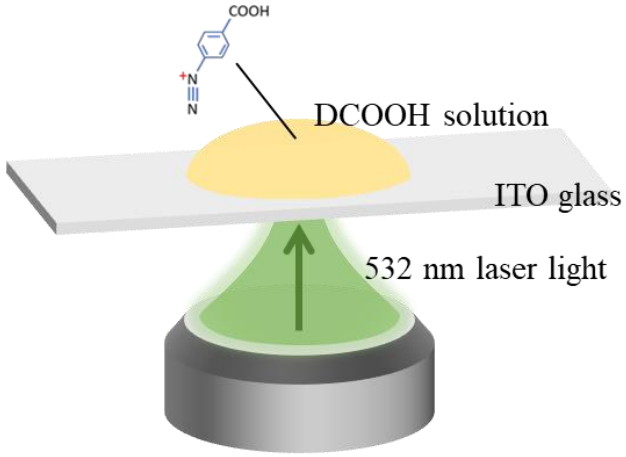

Figure 2-2. The schematic of diazonium salt surface functionalization on ITO-coated glass.

After the functionalization layer grafted, the QDs solution will be drop-casted on ITO-coated glass to cover the grafted layer as shown in Figure 2-3. The used QDs are the commercial product from Mesolight Inc. which are capped by cysteamine (CA) ligands. The structures are shown in Figure 2-4. As discussed in chapter 1 (Figure 1-4), CdSe/ZnS core/shell heterostructure QDs are chosen in our experiment due to exceptional carrier recombination property. The solvent of this kind of QDs solution is deionized water. The -NH_2 groups, which brought by CA ligands, will change to -NH_3^+ groups when solved in deionized water, and show positive surface charges. Moreover, the -COOH groups on the ITO surface will dissociate to -COO^- groups when the grafted layer is immersed into deionized water and show negative surface charges. The electrostatic adsorption is supposed to interact between -NH_3^+ groups and -COO^- groups. By this electrostatic interaction, positively-charged QDs are expected to get adsorbed on ITO surface through COOH groups. In our experiment, the concentration of QDs solution was 0.01 nmol/ml. And the deposition time is adjusted from 5 min to 60 min. The sample was rinsed by deionized water after deposition completed to remove excess of unbound QDs.

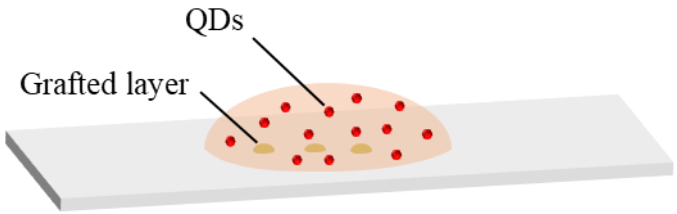

Figure 2-3. The schematic of QDs deposition progress.



Figure 2-4. Chemical structure of CA and an illustration of CdSe/ZnS (core/shell) QD capped with positively charged CA ligands.

To prove the mechanism of QDs selective adsorption due to the electrostatic interaction, the surface functionalization of ITO-coated glass was also performed with DNO_2 solution. The PL intensity from both DCOOH and DNO_2 functionalized surfaces under 473 laser light excitations was measured. The functionalized surfaced were defined by the SEM images. The PL intensity from each functionalized area could be regarded as the adsorbed QDs number for comparison the adsorption ability. Moreover, the PL intensity from the background, where any surface functionalization was performed, was also measured on similar areas.

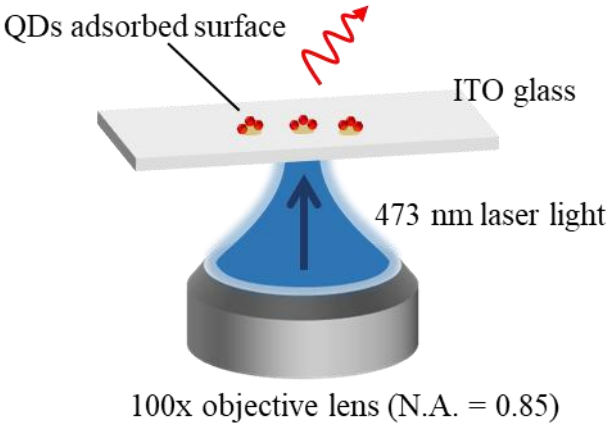

Figure 2-5. The schematic of the experiment to measure PL intensity from functionalized areas.

2.3 Surface functionalization by grafting of diazonium salt on ITO-coated glass

Following the methods introduced in the last section, the surface functionalization by

DCOOH diazonium salt grafting was performed on ITO-coated glass. The morphology of the grafted layer was characterized by SEM and AFM imaging. Moreover, in our application, since the DCOOH grafted layer is used to attach QDs, the thickness of grafted layer is the most important parameter in this case. The adjustment of the thickness will also be discussed in this section. The PL emission for DCOOH grafted layer was measured with PL and TRPL spectra. The chosen excitation laser will influence the PL emission from grafted layer.

2.3.1 The morphology and thickness adjustment of grafted layer

The morphology of a typical grafted dot is shown in Figure 2-6. The DCOOH solution, with the concentration of 100 mM, was dropped on ITO-coated glass. As a reminder, a 532 nm laser light with laser density of 0.9 mW/μm^2 was used for exposure and the diameter of laser spot was about 0.8 μm. The exposure time was 3 min for this sample. Figure 2-6a shows the SEM image of the dot, with a diameter of 1.5 ± 0.13 μm. AFM image and the cross-section profile are shown in Figure 2-6b and 2-6c. The cross-section position is shown in the AFM image. The height of the functionalized dot is 1.5 μm.

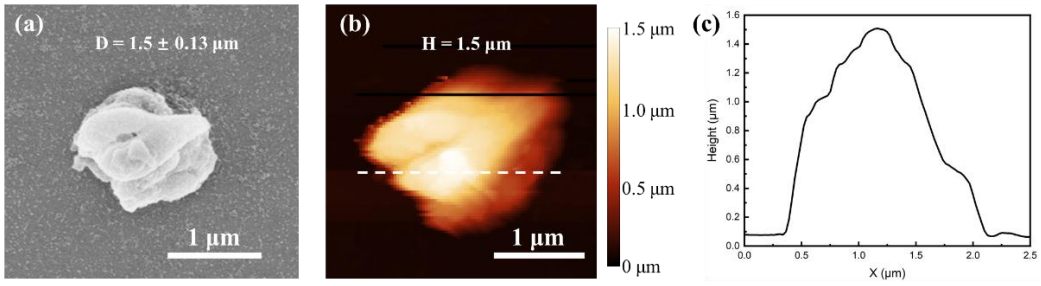

Figure 2-6. (a) The SEM image, (b) the AFM image and (c) the cross-section profile ofthe grafted layer, whose position is shown in AFM image. In the fabrication of this sample, the solution concentration of DCOOH diazonium salt is 100 mM, and the exposure time is 3 min.

The height of different functionalized dots/blocks was varied by adjusting the solution concentration and exposure time. The laser energy was kept constant at 21.23 μW/μm^2. Since the purpose of developing the functionalized layer is to adsorb QDs on the target surface, the thickness, which is measured as height, of grafting layer is an important factor.

In this case, due to the exposure laser energy is excessively high, the resulted size is two times larger than the laser spot diameter. The size change of grafted dots with exposure parameters is shown in Figure 2-7. The heights of dots were measured by AFM to evaluate the size. The DCOOH solution concentration was adjusted as 5 mM, 10 mM, 20 mM and 100 mM. The exposure time was adjusted from 20 s to 280 s. The thicknesses vary from 7 nm to 275 nm with different exposure time and solution concentration. Comparing to the result before, the thickness decreased due to the laser energy was decreased. For each solution concentration, the thickness of functionalized surface is proportional to the exposure time. Moreover, for a specific exposure time, the functionalized surface will be thicker, if the solution concentration is higher. This conclusion is the basic principle of functionalization surface fabrication in further experiments. Figure 2-8 shows the grafted dot with 7 nm thickness. For such a small dot/block, it is consists of a group of small sphere-shape dots. One thing needs to be pointed that the height of such grafted dot is measured by the highest dot.

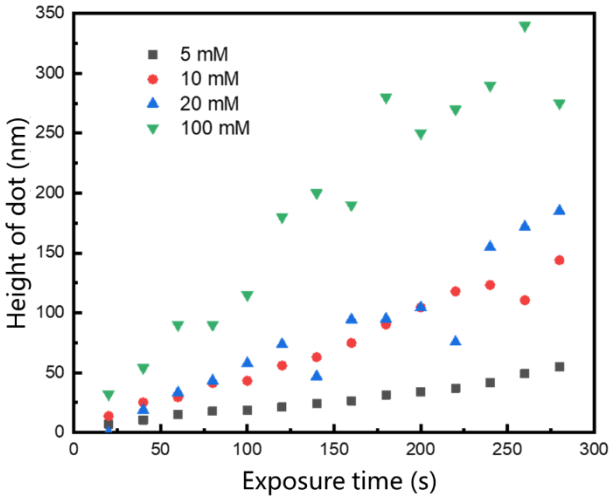

Figure 2-7. A bunch of surface functionalization results by DCOOH solution on ITO-coated glass. The height of functionalization surface varies from 7 nm to 275 nm with different exposure time and solution concentration. The exposure light intensity was kept at 21.23 $\mu W/\mu m^2$ under the excitation of 532 nm laser light.

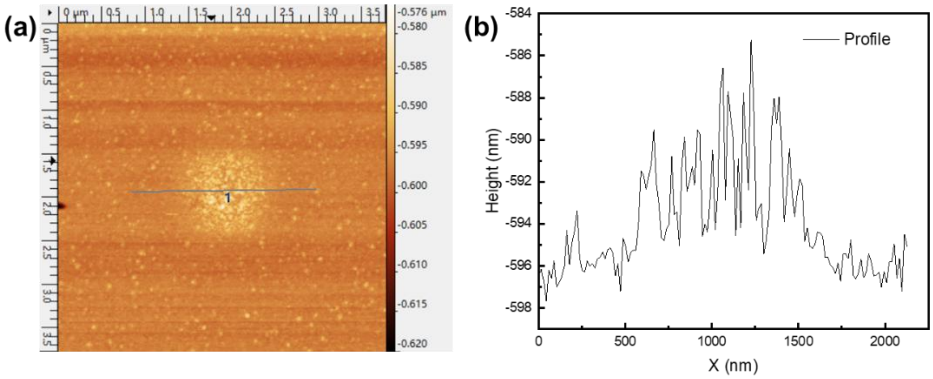

Figure 2-8. The AFM data of 7 nm grafted dot/block. (a) AFM image. (b) Profile of grafted dot/block.

2.3.2 PL emissions from the grafted layer before QD absorption

Besides the fabrication of the surface functionalization by DCOOH diazonium salt, the PL emission from the grafted structures was also investigated. Such analysis is important to assess the PL background. An example of structure is shown in Figure 2-9a. For fabrication of this structure, the exposure time was 20 s and the solution concentration was 5 mM. The used laser light density was 36.1 $\mu W/\mu m^2$. After fabrication of the dot using the protocol described in section 2.2 but without the step of QD integration shown in Fig. 2-3, PL emission was detected with the laser excitation wavelength of 532 nm. The lifetime was measured, and the time resolved photoluminescence (TRPL) curve is shown in Figure 2-9b with acquisition time of 10 min. The lifetime of grafted DCOOH layer is 0.41 ns. This lifetime is much shorter than 18.45 ns, which is the intrinsic lifetime of QDs used in colloidal state.

Moreover, the PL spectrum was measured under different light excitation. Figure 2-9c and 2-9d show the PL spectra without background under 532 nm and 405 nm laser light excitation. The laser energy is kept the same. With the intensity counts, under 405 nm light excitation, the average intensity is about 150, and the maximum is 250. Under 532 nm light

excitation, the average intensity is about 20, and the maximum is 40. The DCOOH diazonium salt grafted layer shows different PL intensity under different laser excitation.

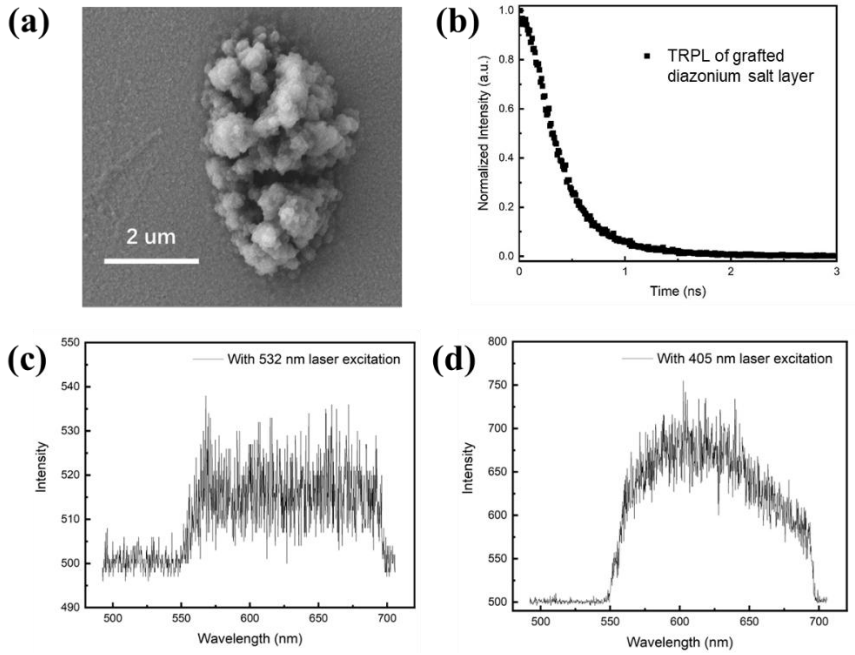

Figure 2-9. Analysis of DCOOH grafted dot. (a) SEM image. (b) PL decay curve with the excitation of 532 nm laser light revealing a PL lifetime of $\tau = 0.41$ ns. (c) PL spectrum under 532 nm laser light excitation. (d) PL spectrum under 405 nm laser light excitation.

The PL intensity difference shown in Figure 2-9c and 2-9d suggests the green light, such as 532 nm laser, is a better choice in the PL measurement of QDs-grafted diazonium salt configuration because the PL background would be lower. However, this PL background revealed for grafted DCOOH structures could have a significant impact on the PL measurement in the case of a limited amount of QD deposition. To illustrate this point, Figure 2-10a shows a sample in which surface functionalization by DCOOH was performed on a gold nanostrip (or nanowire: Au NW) and QDs were then deposited on the functionalized surface. Functionalization on metallic nanostructures will be discussed in more detail in Chapter 4. This approach allows the integration of DCOOH structures whose size is not diffraction-limited, i.e. smaller than the diameter of the incident laser spot. In Figure 2-10a, the size of the grafted spot is about 300 nm. Considering the average size of used QDs is 10 nm, the number of adsorbed QDs is limited. Figure 2-10b shows the comparison of normalize PL spectrum of QDs in colloidal state and PL emission from surface functionalization area. The excitation light for both spectra is 512 nm. It turns out that the peak of the PL spectrum from surface functionalization surface is still located around 620 nm. However, the spectral shape differs from colloidal QDs solution and contain shoulders, which is because of the PL emission from grafted diazonium salt.

It could be concluded that, when observing the PL behavior from QDs, the PL spectrum from grafted diazonium salt should be measured individually and regarded as the reference towards the total PL spectrum. Moreover, considering the lifetime difference between QDs and grafted DCOOH layer, there will be negligible impact from grafted DCOOH layer, when collecting lifetime signal from QDs-grafted DCOOH layer structure.

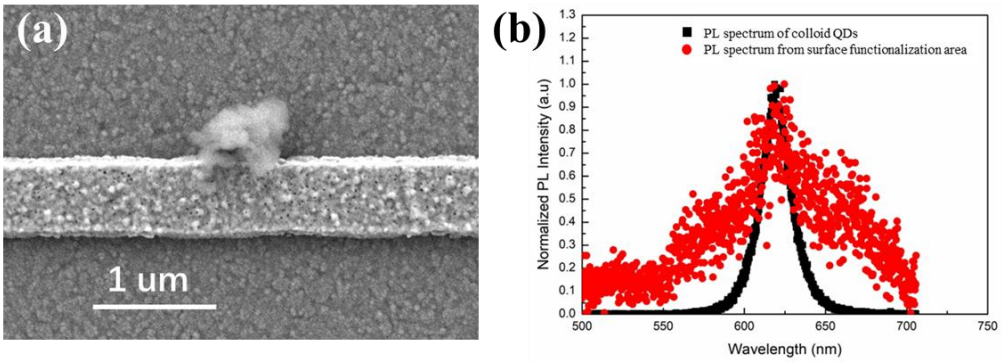

Figure 2-10. Au NW-DCOOH-QD hybrid structure (a) SEM image of a sample, in which surface functionalization by DCOOH was performed on an Au NW and QDs were deposited on the functionalization surface. (b) Comparison between PL spectrum if QDs in colloidal state and emission from surface functionalization area with QD adsorption. The excitation light for both spectra was 512 nm.

2.4 QDs adsorption on grafted diazonium salt layer

In this section, the QD adsorption is discussed. QD integration is performed on diazonium salt functionalized surface on ITO-coated glass substrate. The PL and absorption spectra as well as zeta potential of colloidal QDs were measured before adsorption. QDs' PL and TRPL spectra are compared before and after adsorption. To prove the adsorption mechanism, DNO_2 diazonium salt was used to functionalize the ITO-coated glass and performed QDs adsorption with the same processes. As the reference, grafted DNO_2 diazonium salt is not supposed to have the adsorption ability by electrostatic interaction. By comparing the PL intensity, the influence of other adsorption like Van der Waals force has been removed, and the adsorption function by electrostatic interaction was proved.

2.4.1 QDs characterization and adsorption on ITO-coated glass

As illustrated in Figure 2-4, the QDs used in this experiment are CdSe/ZnS core-shell QDs with the ligands of CA, which will bring $-NH_2$ groups on QDs' surface. For colloids in solution, the PL and absorption spectra are shown in Figure 2-11a. The optical property of surface modified QDs are kept the same. The peak position of PL spectrum is located at 626 nm.

The zeta potential distribution is shown in Figure 2-11b, which is measured in deionized water whose pH=7. The highest counts position is located at 36.9 mV. The positive zeta potential confirmed the positive surface charge of QDs. The high value (>30 mV) shows the colloidal CA-CdSe/ZnS QDs solution is stable in the deionized water.

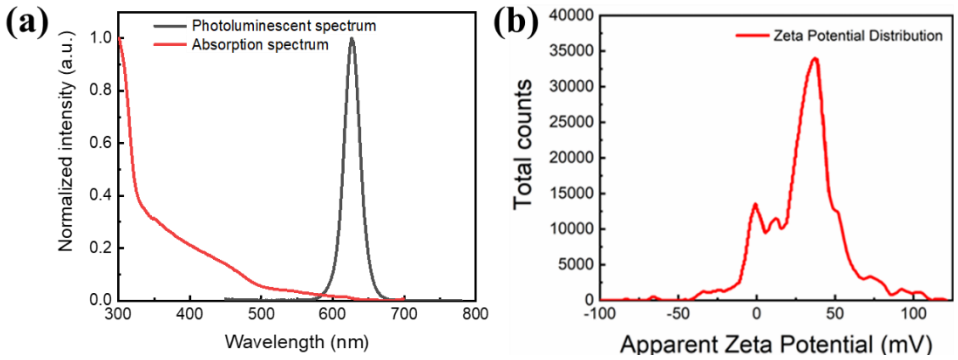

Figure 2-11. Characterization of QDs: (a) PL and absorption spectra of colloidal CA-CdSe/ZnS QDs solution. (b) Zeta potential distribution colloidal CA-CdSe/ZnS QDs solution.

Figure 2-12 shows QD adsorption results on surface functionalized by DCOOH diazonium salt. The SEM image of 17 DCOOH grafted dots is shown in Figure 2-12a, which formed a "UTT" pattern on ITO-coated glass. The CA-CdSe/ZnS QDs solution was dropped on ITO-coated glass at the designed pattern area. After 30 min deposition, the solution was removed by rinsing with deionized water. After deposition, the scanning PL image of the "UTT" pattern is shown in Figure 2-12b. In this case, due to the characterization machine configuration, 473 nm laser light was used to excite the PL emission. All the DCOOH grafted dots, constituting the pattern, emitted red light under excitation. A 633 nm/60 nm band pass filter was used at the detection side. However, there are also red lights emitting besides the grafted areas. This emission suggests that other QD adsorption took place on the sample. These undesirable interactions, such as those due to Van der Waal force, will be discussed in section 2.4.2.

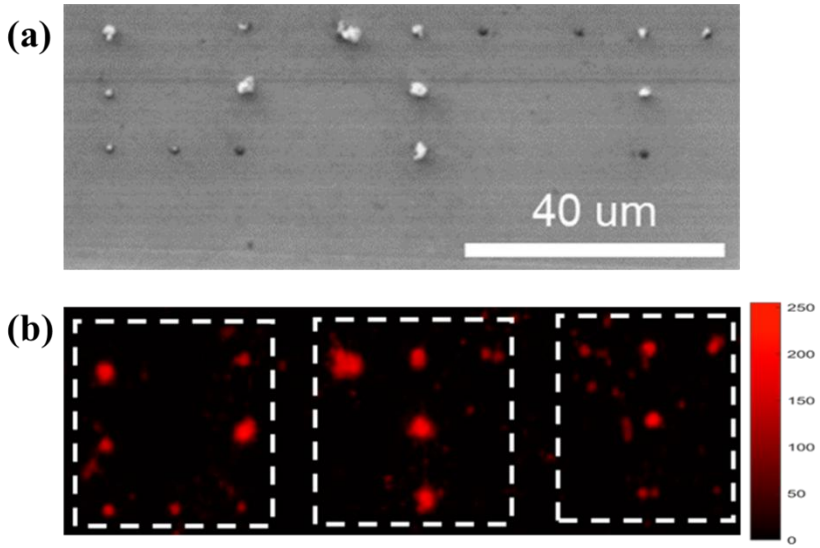

Figure 2-12. (a) The SEM image of 17 DCOOH grafted dots, which formed a "UTT" pattern on ITO-coated glass. (b) PL image of the "UTT" pattern.

Figure 2-13 and Figure 2-14 compared the PL and TRPL data before and after QDs depositions. 532 nm laser light was used for excitation in both figures. One DCOOH grafted dot was selected as shown in Figure 2-13a and Figure 2-14a. The diameters are 3.96 μm along long axis and 2.19 μm along short axis. The ellipse shape is supposed to stem from the shape of laser spot. Figure 2-13b shows the PL spectrum without normalization of the DCOOH functionalization layer before QDs' adsorption. Emission between 550 nm and 700 nm was

detected, which is consistent with the result in section 2.3.2, in which there is also weak emission in red range under 532 nm light excitation. Figure 2-13c shows the normalized PL spectrum of QDs dispersed on ITO-coated glass without any diazonium grafting. The peak position is 614.5 nm and full width at half maximum (FWHM) is 21 nm. Figure 2-13d shows the normalized PL spectrum of the grafted dot after QDs deposition. The peak position is 616.5 nm and FWHM is 20 nm. Comparing the normalized spectra in Figure 2-13c and 2-13d, the PL spectrum of QDs emissions remains consistent with or without the presence of the functionalization layer. In our work, the QDs solution was deposited on sample surface for 5 min to 60 min before rinsing. In this progress, due to fluid dynamics like coffee ring effect, the concentration of QDs remaining on sample surface is not uniform. The PL intensity is not suitable for comparison. To evaluate the Purcell effect, TRPL data is prefered in this work.

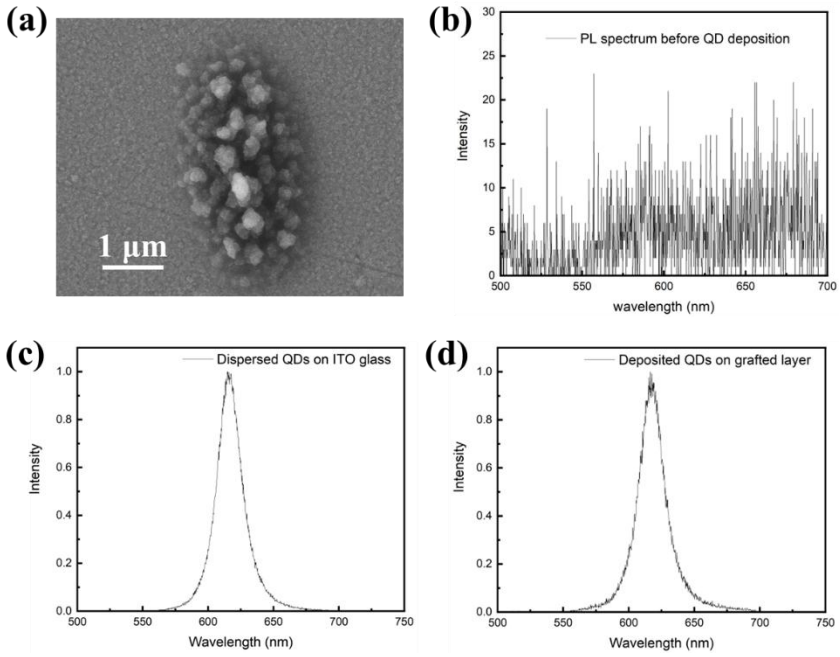

Figure 2-13. (a) SEM image of DCOOH grafted layer. (b) PL spectrum of emissions from the DCOOH grafted layer without QDs deposition. (c) PL spectrum of QDs emissions dispersed on ITO-coated glass. (d) PL spectrum of emissions from the grafted layer after QDs deposition.

As for the TRPL curve, Figure 2-14b shows this curve for DCOOH diazonium salt functionalization layer without QDs deposition. The lifetime is 0.41 ns, which is also consistent with the result in section 2.3.2. Figure 2-14c shows the TRPL spectrum of QDs dispersed on ITO-coated glass. The lifetime is 18.45 ns. However, when QDs is deposited on the DCOOH functionalization layer, the lifetime decreased to 2.42 ns (Figure 2-13d).

Regarding the QDs emission, which rise from the recombination of generated electron and hole, the lifetime varies inversely with the carrier recombination probability. Ideally, after QD absorbs one photon, there is one neutral exciton, which consists of a pair of carriers as well as one generated electron and one generated hole. If there is more than one pair of carriers existing, or trion, QDs emit light with shorter lifetime, which is also called QDs photoluminescence quench.[14,15]

In our case, the lifetime of QDs emission decreased by a factor of 7 with the presence of the DCOOH functionalization layer. The lifetime decrease indicates multi-carrier processes existing inside QDs. Considering the sample structure, there is a carrier transfer between

DCOOH functionalization layer and QDs.[16] Besides lifetime, the consistence of the PL spectrum shows the bandgap of core-shell QD's structure is not influenced by the existence of DCOOH functionalization layer.

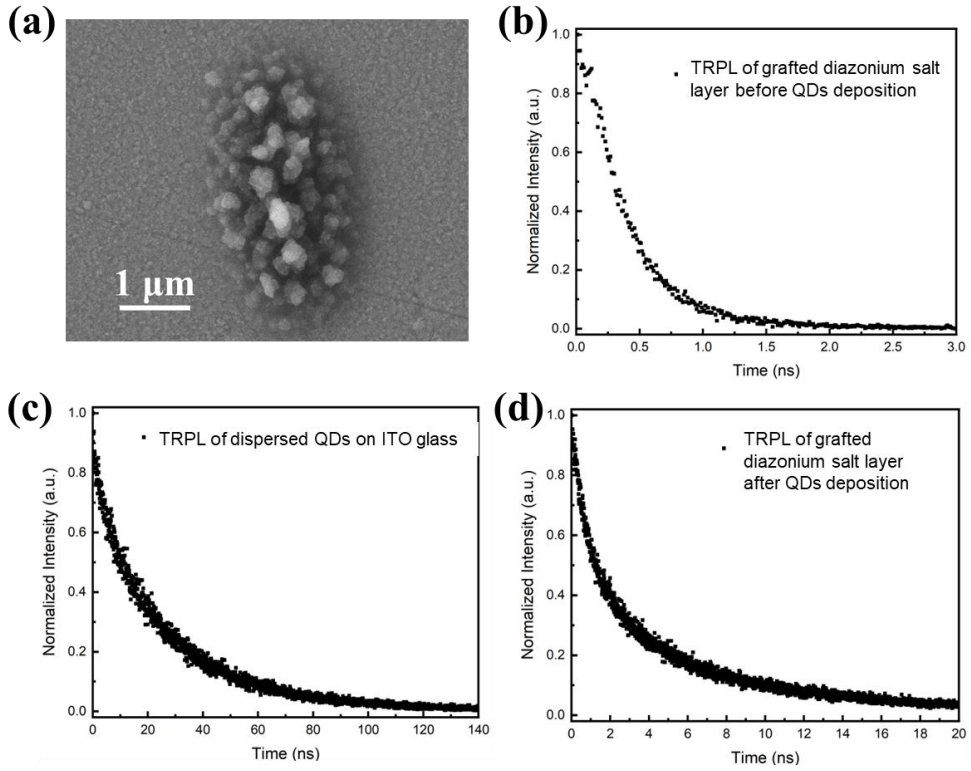

Figure 2-14. (a) SEM image of DCOOH grafted layer. (b) TRPL from the DCOOH grafted layer without QDs deposition (τ = 0.41 ns). (c) TRPL curve of QDs emissions dispersed on ITO-coated glass (τ = 18.45 ns). (d) TRPL from the grafted layer after QDs deposition (τ = 2.42 ns).

2.4.2 The evidence of QDs adsorption by electrostatic interaction

As Figure 2-12b shows, red light is emitted not only from the functionalized dots but also from the surrounding area, which illustrates there might be other QD adsorption processes taking place, such as interaction due to Van der Waal forces. To confirm that the electrostatic interaction is predominant in attachment of the QDs, DNO_2 diazonium salt was used as reference. The chemical structures of DCOOH and DNO_2 are shown in Figure 2-15. These different kinds of diazonium salt share a part of chemical group. But the change of a functional group (-R) provides a difference in chemical properties.

The -COOH group of DCOOH molecule provide the possibility to adsorb positively charges QDs by the electrostatic force between the surface charges. For DNO_2, there is the -NO_2 group at the opposite position of the azo group. The azo group guarantees the surface functionalization. However, the -NO_2 group is not supposed to have any charges when solved in deionized water. Electrostatic adsorption of QDs should therefore not occur on the DNO_2-functionalised surface. At the -NO_2 group, other interaction, such as that stemming from Van der Waal forces, could play a role on the DNO_2 functionalized surface. For comparison, the PL intensities from the DCOOH and DNO_2 functionalized surfaces, which could be regarded as proportional to the number of adsorbed QDs, were analyzed for assessing the role of

electrostatic interaction on DCOOH.

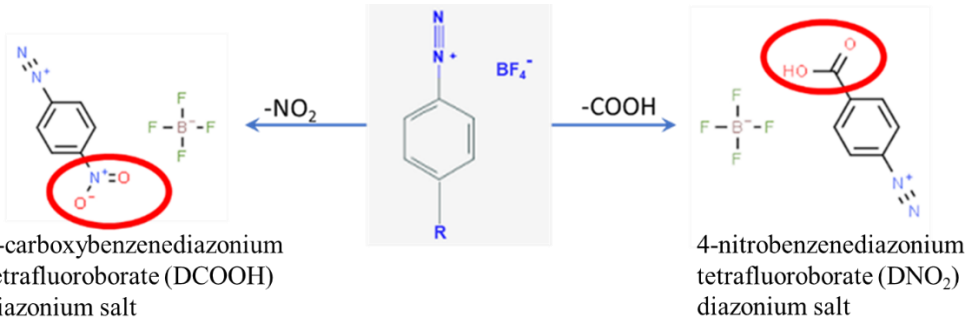

Figure 2-15. The chemical structures of the two kinds of diazoniums salt used: DCOOH and DNO_2.

For the introduced DCOOH and DNO_2 diazonium salt grafted dots, they are supposed to have different surface charge. Kelvin probe force microscopy (KPFM) was used to measure the surface potential. Figure 2-16a and 2-16c are the SEM images of DCOOH and DNO_2 diazonium salt grafted dots. The diameter of each dot is kept as 2 μm by adjusting the fabrication parameter. Figure 2-16b shows the surface potential of DNO_2 diazonium salt grafted dots. The surface potential is 0.5 V with positive value. For DCOOH diazonium salt grafted dots, whose surface potential is shown in Figure 2-16d. The surface potential is -0.3 V with negative value. The results prove the negative surface charge of DCOOH diazonium salt grafted dots and show the potential to connect surface modified QDs with positive charge. (The KPFM data is from Dr. Liudmila Trotsiuk)

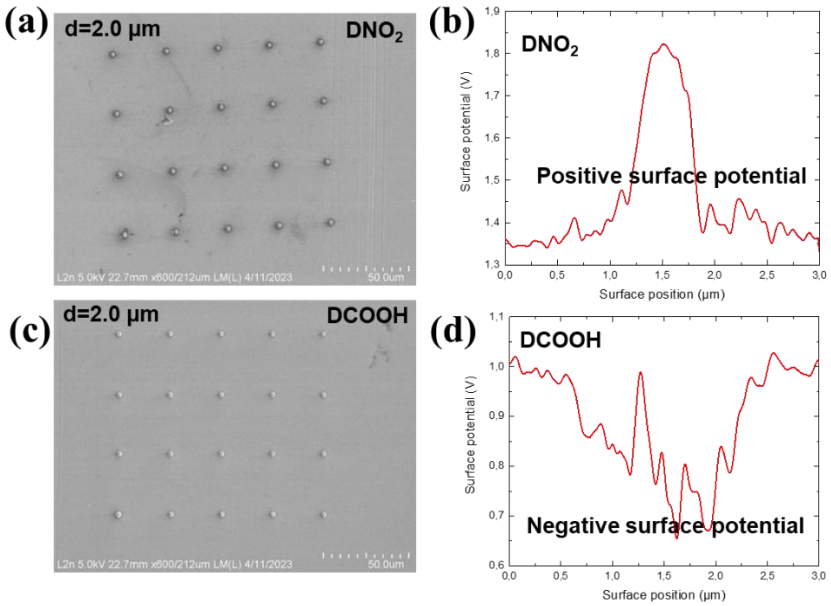

Figure 2-16. The KPFM results of DCOOH and DNO_2 grafted dots. (a) SEM images of DNO_2 diazonium salt grafted dots. (b) Surface potential of DNO_2 diazonium salt grafted dots. (c) SEM images of DCOOH diazonium salt grafted dots. (d) Surface potential of DCOOH diazonium salt grafted dots. (The data is from Dr. Liudmila Trotsiuk)

A pattern made of 12 dots was created on ITO-coated glass by combining DCOOH and DNO_2 functionalized surfaces. The SEM image of this pattern is shown in Figure 2-17a. In this pattern, four DNO_2 functionalized dots were positioned at the corners and labeled with (α), while eight DCOOH functionalized dots were arranged in a cross formation and marked

with (β). Both types of functionalized micro scale dots were fabricated with identical experimental procedures.

Following the fabrication of the surface functionalization sample, the surface-modified QDs solution were deposited on the sample, and the excess solution was eliminated by rinsing. Scanning PL image was utilized to measure the QDs emission intensity with a FLIM system. The excitation laser light was focused on a spot and moving on the sample to excite the whole surface. The statistical analyze was applied on the adsorbed QDs numbers on functionalization surfaces. The PL intensity in the image was quantified at each pixel of 0.25 μm² area. A 520 nm lowpass filter was integrated into excitation optical path, and a 625/50 bandpass filter was integrated into the detection optical path. The scanning PL images were captured before and after QDs deposition and are displayed in Figures 2-17b and 2-17c.

Both DCOOH and DNO_2 functionalization surfaces emit red light when excited by 473 nm laser light, corresponding to the PL background already discussed. However, after QDs deposition, the emission light significantly intensifies, particularly on the DCOOH dots (Figure 2-16c) where the (a) sites do not show any apparent PL. Only (b) are visible in the PL image. This result highlights the positive impact on QDs adsorption of the DCOOH functionalization surfaces.

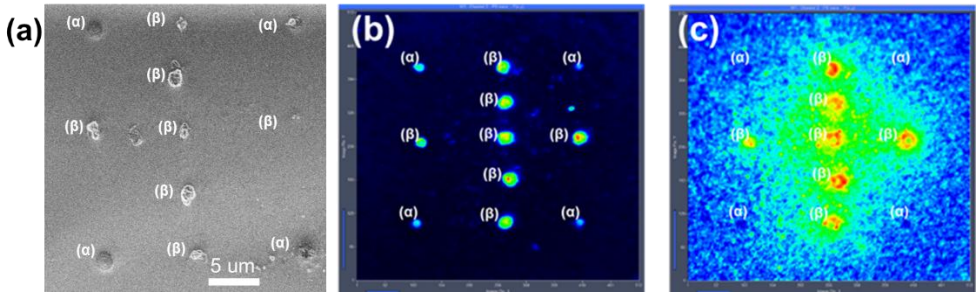

Figure 2-17. (a) SEM image of a patterns combining DCOOH and DNO_2 functionalization surfaces on ITO-coated glass. DNO_2 surface are marked with α, and DCOOH surface are marked with β. PL scanning images are shown (b) before and (c) after QDs deposition. Both the images were taken under 473 nm laser excitation. A 520 nm lowpass filter was integrated into excitation optical path. A 625/50 bandpass filter was integrated into the detection optical path.

The statistical analysis is shown in Figure 2-18. Firstly, according to the PL scanning image before QDs deposition like Figure 2-18a shows, the emitting area was selected. Actually, the PL background allows us to guess the presence of dots. The emitting light intensities per pixel were integrated and the emitting photons/pixel for each selected area was chosen as the signal to evaluate the amount of QDs adsorption. In our work, three types of surfaces are chosen for comparison: background surface (ITO-coated glass), DCOOH functionalization surface and DNO_2 functionalization surface.

PL emissions from both DCOOH and DNO_2 functionalization surfaces were measured, which would be used to prove the QDs adsorption ability on DCOOH functionalization surface by electrostatic interaction. Moreover, Van der Waals force is supposed to play roles between nanoparticles and all kinds of surface. In case of there are other interactions playing roles, background surface areas were selected as references on the bare ITO-coated glass without any surface functionalization. The analyses of background surfaces are aimed to

evaluate the effectiveness of DNO_2 functionalization surfaces as reference. In our experiments, the size of areas of selected background surfaces are similar to the size of the DCOOH and DNO_2 functionalization surfaces.

Figure 2-18b shown a statistical analysis, in terms of number of cases, photon emission from the three types of surfaces. By each experimental "case", we mean "dot/area" presenting the numerical value indicated in the abscissa axis. To intuitive express the emission intensity, the number of emitted photons per pixel was used to represent the average PL intensity with the integration time of 60s. The PL intensity was conversed into number of photons at 617 nm, which is the peak position of QDs PL emission under 473 nm laser light excitation. In Figure 2-18b, the orange bars represent the PL intensity of DCOOH functionalization surfaces. The DNO_2 functionalization surfaces and background surfaces are represented in green and blue bars respectively. It turns out that strong PL emission statistically concerns mainly DCOOH functionalization surfaces, which indicates there is more QDs adsorbed on the DCOOH functionalization surfaces. Moreover, the PL intensities are similar from DNO_2 functionalization surfaces and background surfaces.

The results confirmed the hypothesis that electrostatic adsorption plays main roles on QDs' adsorption on DCOOH functionalization surfaces. Also, on DNO_2 functionalization surfaces, the QDs adsorption ability is similar to ITO-coated glass surface. This indicated DNO_2 could be a relevant reference material to evaluate electrostatic adsorption of QDs. The comparison between DCOOH, DNO_2 functionalization areas and background helped to rule out the influence of Van der Waals forces and highlight the electrostatic adsorption effect.

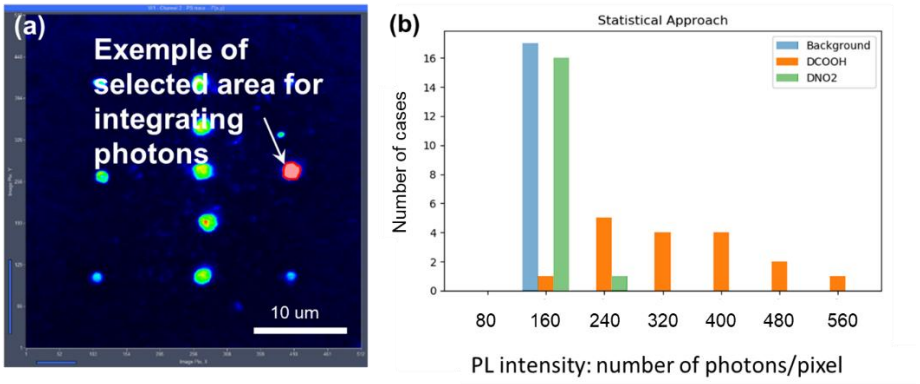

Figure 2-18. (a) The example of selected area for integrating photons on three types of surfaces: background surface, DCOOH functionalization surface and DNO_2 functionalization surface. (b) Statistical study of adsorbed QDs number. Emitting photons/pixel for each selected area was chosen to evaluate the QDs adsorption amount.

To further statistically analyze the QDs adsorption ability on the functionalization surface, the emitted photons/pixel, according to the scanning PL image shown before, was assessed with different QDs deposition times (step illustrated in Fig. 2-3). Figure 2-19 shows the statistical analysis of the same sample with different QDs deposition time: (a) 5 min, (b) 30 min, (c) 60 min and (d) 120 min. After repeating experiments, the results were classified, and the number of cases was counted.

It has been proved that, whatever the deposition time, the DCOOH functionalization surfaces emit more photons than the other two types of surfaces, which could be demonstration that the DCOOH functionalization surfaces show stronger adsorption ability to the surface-

modified QDs. The emitted photons number between DNO_2 functionalization surfaces and background surfaces are nearly the same whatever the deposition time while increasing the time seems to populate the cases corresponding to a high PL, especially in Fig. 2-19d. The PL decrease in the case of DNO_2 can be associated to a lower number of QDs adsorbed. This finding is in agreement with the presence of electrostatic adsorption in the QDs-DCOOH structure, compared to only weak possible van der Waals interaction in the QDs-DNO_2 system.

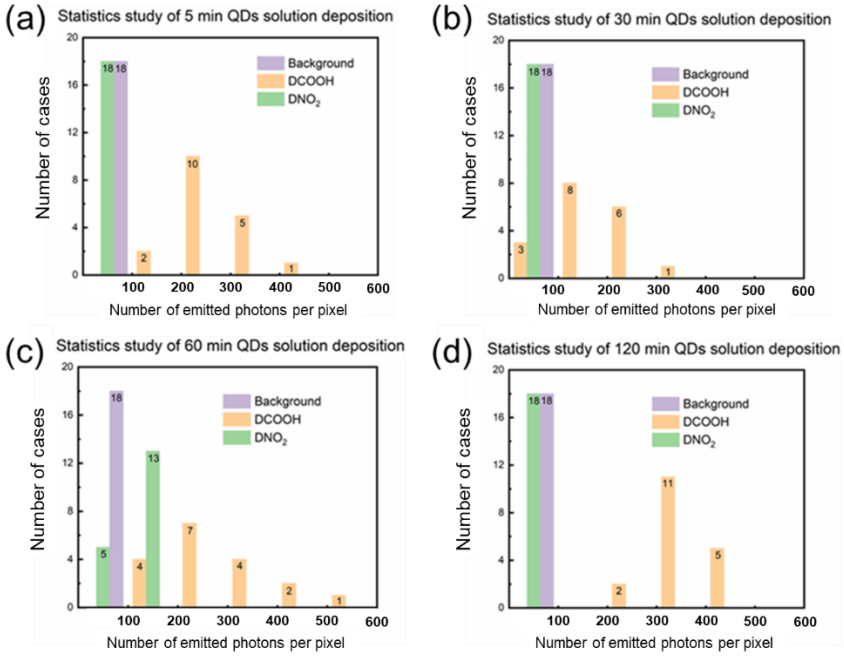

Figure 2-19. Statistical results of photons number emitted from DCOOH functionalization surfaces, DNO_2 functionalization surfaces and background surfaces with different QDs solution deposition times: (a) 5 min, (b) 30 min, (c) 60 min and (d) 120 min. The numbers of cases are marked in the histogram.

2.5 Summary and Conclusions

In this chapter, QDs adsorption was performed on ITO-coated glass with surface functionalization made beforehand with DCOOH diazonium salt. The QDs were surface modified by cysteamine ligands, which brings positively charged -NH_2 group on their surface to interact with negatively charged -COOH group of DCOOH diazonium salt. Electrostatic interaction is supposed to be the mechanism in QDs adsorption progress. The experimental methods were described in section 2.2. In section 2.3, the fabrication and morphology of DCOOH functionalized surface by grafting reaction were discussed. Moreover, the PL background emission of the DCOOH functionalized surface has been detected, which could be further managed by using green light excitation instead of a blue one.

The QDs adsorption was shown in section 2.4. The QDs properties in colloid state were measured before adsorption. A luminescent pattern was fabricated to show the adsorption results. The QDs PL emissions before and after deposition were compared. PL spectrum kept consistent, but the lifetime decreased after deposition due to possible charge transfer effect from DCOOH functionalized surface. To prove the role of electrostatic interaction in

adsorption process, another diazonium salt, based on DNO_2 molecules, was used as the reference with the same experimental procedures as for DCOOH. Characterizations using scanning PL imaging show that the number of QDs adsorbed on DCOOH functionalization surface is larger than it is for the reference areas. Moreover, as the deposition continues, the average adsorbed QDs numbers on DCOOH functionalization surfaces increases. The results reveal, for the first time to our knowledge, the selective electrostatic adsorption between surface-modified QDs and DCOOH functionalization surfaces.

The study of the adsorption of QDs on DCOOH presented in this chapter was an important step in my thesis. The methods and protocols defined will be used to fabricate other photonic devices presented in Chapters 3 and 4.

Reference

1. Ge, D. *et al.* Hybrid plasmonic nano-emitters with controlled single quantum emitter positioning on the local excitation field. *Nat. Commun.* **11**, 3414 (2020).
2. García de Arquer, F. P. *et al.* Semiconductor quantum dots: Technological progress and future challenges. *Science* **373**, eaaz8541 (2021).
3. Krivenkov, V., Samokhvalov, P., Nabiev, I. & Rakovich, Y. P. Synergy of Excitation Enhancement and the Purcell Effect for Strong Photoluminescence Enhancement in a Thin-Film Hybrid Structure Based on Quantum Dots and Plasmon Nanoparticles. *J. Phys. Chem. Lett.* **11**, 8018–8025 (2020).
4. Kulakovich, O. *et al.* Photostability enhancement of InP/ZnSe/ZnSeS/ZnS quantum dots by plasmonic nanostructures. *Nanotechnology* **32**, 035204 (2021).
5. Ji, B. *et al.* Non-blinking quantum dot with a plasmonic nanoshell resonator. *Nat. Nanotechnol.* **10**, 170–175 (2015).
6. Jia, S. *et al.* Optimizing ZnO–Quantum Dot Interface with Thiol as Ligand Modification for High-Performance Quantum Dot Light-Emitting Diodes. *Small* **20**, 2307298 (2024).
7. Li, D. *et al.* Surface functionalization of nanomaterials by aryl diazonium salts for biomedical sciences. *Adv. Colloid Interface Sci.* **294**, 102479 (2021).
8. Nguyen, M. *et al.* Regioselective surface functionalization of lithographically designed gold nanorods by plasmon-mediated reduction of aryl diazonium salts. *Chem. Commun.* **53**, 11364–11367 (2017).
9. Pereira, G. *et al.* (Bio)conjugation Strategies Applied to Fluorescent Semiconductor Quantum Dots. *J. Braz. Chem. Soc.* **30**, 2536–2560 (2019).
10. Zhao, J. *et al.* Large-area patterning of full-color quantum dot arrays beyond 1000 pixels per inch by selective electrophoretic deposition. *Nat. Commun.* **12**, 4603 (2021).
11. Ge, D. *et al.* Advanced hybrid plasmonic nano-emitters using smart photopolymer. *Photonics Res.* **10**, 1552 (2022).
12. Chehimi, M. M., Lamouri, A., Picot, M. & Pinson, J. Surface modification of polymers by reduction of diazonium salts: polymethylmethacrylate as an example. *J. Mater. Chem. C* **2**, 356–363 (2013).
13. Guselnikova, O. A. *et al.* Tuning of PEDOT:PSS Properties Through Covalent Surface Modification. *J. Polym. Sci. Part B Polym. Phys.* **55**, 378–387 (2017).
14. Park, Y.-S., Bae, W. K., Pietryga, J. M. & Klimov, V. I. Auger Recombination of Biexcitons and Negative and Positive Trions in Individual Quantum Dots. *ACS Nano* **8**, 7288–7296 (2014).
15. Jha, P. P. & Guyot-Sionnest, P. Trion Decay in Colloidal Quantum Dots. *ACS Nano* **3**, 1011–1015 (2009).
16. Liras, M., González-Béjar, M. & Scaiano, J. C. On-off QD switch that memorizes past recovery from quenching by diazonium salts. *Phys. Chem. Chem. Phys.* **12**, 9757–9762 (2010).

Chapter 3 Luminescent optical fiber tip based on the QDs adsorption by diazonium salt

3.1 Introduction

Since the introduction of optical fibers,[1] these photonic systems have shown to present many advantages, such as small size, flexible structure, strong mechanical durability, and fast signal transmission over long distances. Optical fibers have been becoming widely used devices in fields, like communications,[2] sensing,[3] lasing,[4] and imaging.[5] The development of optical fiber technology involves various methods to widen the integration of other materials, through surface modification or nanostructure integration. Methods like chemical etching, focused ion beam (FIB) etching, and physical vapor deposition (PVD)/chemical vapor deposition (CVD) have been used to develop multifunctional optical fibers.[6]

Furthermore, the atypical shape of optical fibers poses challenges in adapting standard strategies used for preparing planar micro- and nano-structures to suit fibered tips with a fast, low-cost, and easy operable method. Photo-polymerization has turned out to be an efficient technique for integrating additional tips at the extremity of optical fibers, based on a self-growing approach.[7,8] Besides, it has been possible to integrate luminescent patterns using photopolymers that are functionalized with nanoemitters,[9–11] resulting in advanced light-emitting hybrid structures that can range in size from micrometers to nanometers.[12,13]

In this chapter, the QDs adsorption was performed on optical fiber with the surface functionalization of DCOOH diazonium salt. The adsorption mechanism is the same as that described in chapter 2. A new type of luminescent optical fiber tip was fabricated, which emits red light under blue light excitation, with the same spectrum as colloidal QDs. Their morphology and features were characterized by fluorescence spectroscopy and SEM. The comparison with DNO_2 diazonium salt was also made to demonstrate that the electrostatic adsorption plays a key role in the immobilization of QDs. In particular, the PL intensity from the fibered tips modified by DNO_2 decreased by a factor of 11, compared to the ones modified by DCOOH. This new kind of QD-based luminescent fibered tip could be used for special fiber-based illuminating, such as life detection after earthquake. In this work, we used this luminescent fiber tip as a sensor to detect the concentration of ZnO NPs in solution, which is based on quenching phenomenon. This highlights its promising potential for sensing applications.

3.2 Experimental methods

In this study, we fabricated the luminescent fiber tip by developing a sequential process illustrated in Figure 3-1. The fabrication involves (a) photopolymerization of pentaerythritol triacrylate (PETA) through an optical fiber to create a polymer tip at its extremity[7], (b)

optically-induced functionalization of the polymer tip with DCOOH diazonium salt, which bears negatively charged carboxylic acid groups, and (c) electrostatic immobilization of QDs surrounded by positively charged ligands.

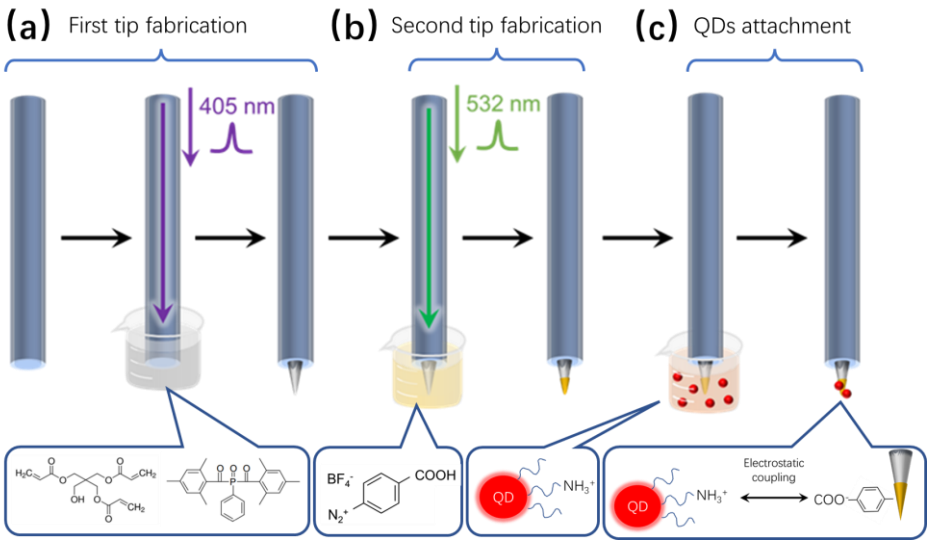

Figure 3-1. The schematic of luminescent optical fibered tip fabrication. (a) PETA and IRG 819 are used to fabricate the first tip under 405 nm laser exposure. By dipping the optical fiber into the formulation for 1 s, the first tip is formed at the end surface. The resulted tip is 10 μm for the length and 2 μm at the FWHM. (b) Diazonium salts are used to fabricate the second tip under 532 nm laser exposure. The optical fiber was dipped into 5 mM diazonium salt solution for 15 min. The resulted second tip is formed at the first tip. (c) The tip was dipped into QDs solution, which is surface modified by -NH_2 groups. QDs were supposed to adsorbed on the tip surface by the electrostatic force between -COO^- group and -NH_3^+ group and form strong bonding.

Initially, an optical fiber with core diameter of 3 μm and cladding diameter of 125 μm was coupled with a 405 nm laser on one end, and another end was dipped into a mixture solution formulation of PETA and IRG 819 as shown Figure 3-1(a). PETA (Poly-ethylene terephthalate), is a type of photo-polymer material that is widely used in lithography processes. IRG 819 (IRGACURE 819) is a photoinitiator commonly used in UV-curable systems. This approach involves using IRG 819 as a photoinitiator for polymerization under UV light exposure.[14–16]

The polymerization of PETA was initiated by the 405 nm laser light with 0.5 μW power emitted from the optical fiber emerging from another end. Following a 1s laser excitation and subsequent rinsing with methanol to wash away unreacted liquid formulation, a polymer tip was formed at the dipped end of the optical fiber.[17,18] This tip had a length of 10 μm and a width of 2 μm at its midsection.

The second step of fabrication, dedicated to tip functionalization, is shown in Figure 3-1(b). The first tip was dipped into a 5 mM diazonium salt solution with a similar configuration as the first step and illuminated through the fiber with a 532 nm excitation laser light from the other extremity. The local confined light at the extremity of the first tip initiates local polymerization of the diazonium salt, which resulting in surface functionalization of the extremity of the first tip: a second tip was formed on the first tip with 30 s of laser 532 nm

excitation with 3 μW power. The first tip acts as a micro-lens that spatially confines green light for local growth of the second tip. The second tip was constructed by the radicals from the diazonium salt produced in the functionalization process. As a result, the -$COOH^-$ groups that are distributed around the surface of the second tip, providing the possibility to subsequently adsorb surface-modified QDs on the tip surface.[19]

As far as the growth of the second tip is concerned, it should be pointed out that the nature of the polymerization trigger is not fully known, which will require further studies. We typically used a concentration of 5 mM/l and pH=7. Under these conditions, the absorption spectrum of the diazonium salt was measured (Figure 3-2a). The absorption is not nil at l=532 nm. Due to the strong electromagnetic field confinement shown in section 3.3.2, it is possible that the diazonium heats up, triggering the local grafting and polymerization of aryl layers derived from diazonium salt on its surface. The role of thermal effects on the diazonium salts reduction was described in several publication[20,21]

However, additional experimental studies showed that the absorption spectrum is strongly dependent on the pH that is not controlled for the step of fabrication of the second tip. Actually, optical absorption of diazonium salts in the visible is pretty rare and unusual. Hence, at the time being, we think that the polymerization of diazonium on the first tip is mainly due to the local heating induced by PETA first tip. The absorption spectrum of polymerized PETA was measured (Figure 3-2b).

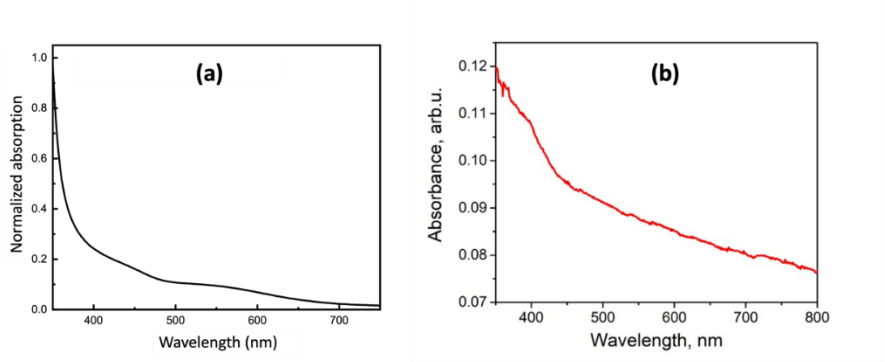

Figure 3-2. Absorption spectra. (a) DCOOH salt (3mM/l concentration). (b) polymerized PETA on glass.

In the third step shown in Figure 3-1(c), the negatively charged second tip was dipped into QDs solution without laser irradiation. The QDs were initially surface-modified with -NH_2 groups, and in the water solution, the -COO^- group from DCOOH diazonium salt and -NH_3^+ group on QDs surface were expected to connect with each other and form a strong bonding.[22] The QDs in the solution were expected to connect to the tip surface through the electrostatic force between the -COO^- group and -NH_3^+ group.[23,24] It was sufficient to dip the tip into the solution for 15 min to fabricate the QDs-based hybrid tip.

In this work, both PL and TRPL were measured with the experimental configuration shown in Figure 3-3. The optical fibered tip was put on an ITO glass with another end coupling with 405 nm laser. The 405 nm laser light with power density of 0.14 mW/μm^2 was used to excite the luminescent tip. The PL emission from adsorbed QDs was collected by a 10x objective with a N.A. of 0.25. The PL spectrum was measured by a spectrometer (Kymera 193i Spectrograph, Oxford Instruments). As shown in Figure 3-4, the TRPL curve was measured by single photon counting module (Excelitas technologies) and time-correlated single photon counting (TCSPC) unit (MultiHarp 150, PicoQuant). A 562 nm edge dichroic

beamsplitter and a FF01-632/148-25 bandpass filter were used in the measurement.

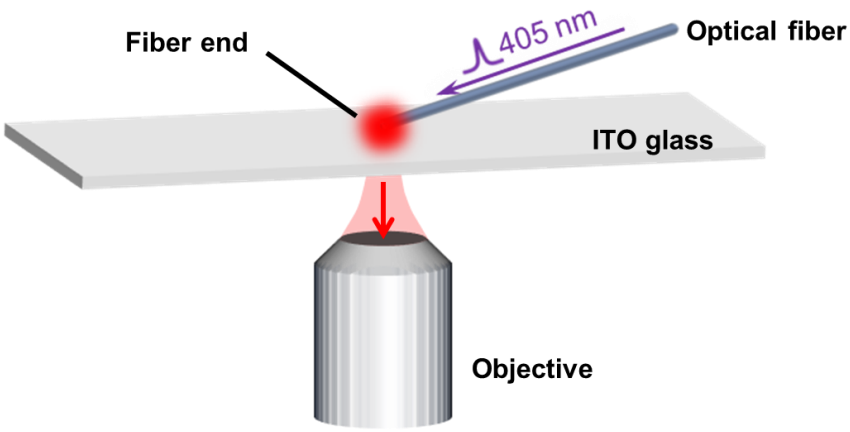

Figure 3-3. The experimental configuration to measure the PL and TRPL spectra of luminescent optical fibered tip.

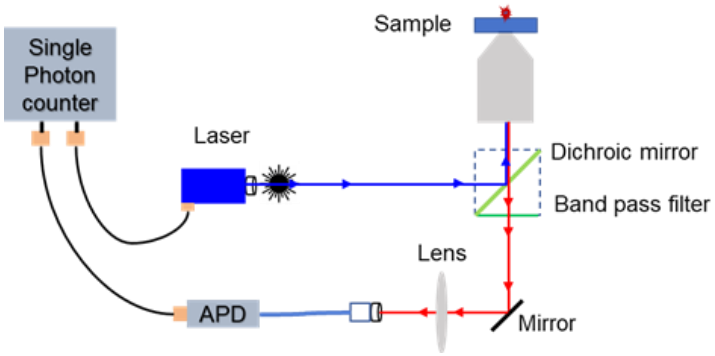

Figure 3-4. The schematic of lifetime measurement setup.

3.3 The morphology and emission of luminescent optical fiber tip

In this section, the morphology and PL emission of the fabricated luminescent optical fibered tip are described. Luminescent images were taken with 405 nm light and white light illumination. SEM are used to show the morphology. The first and second tip structures as well as the boundary are obvious in the SEM images. As it will be seen in section 3.3.2, the laser-induced fabrication progress was simulated for the first tip. The simulation result shows the first tip structure could concentrate light at the vicinity of tip forefront, which could help to fabricated the second tip in small size. As it will be shown in section 3.3.3, the QDs electrostatic adsorption process is proved by fabricating another optical fiber tip with DNO_2. Except the diazonium salt material, all experimental methods were kept the same. With the similar comparison as chapter 2, the QDs adsorption by electrostatic interaction is proved. The PL intensity of the fibered tip modified by DNO_2 decreased by a factor of 11, compared to the fiber tip modified by DCOOH.

3.3.1 SEM and luminescent image of the optical fibered tip

The SEM image before the second polymerization is shown in Figure 3-5. The first tip has a smooth surface and it is stable during the fabrication of second polymerization. After the second polymerization, a new smaller and rougher tip was fabricated at the top of the first tip.

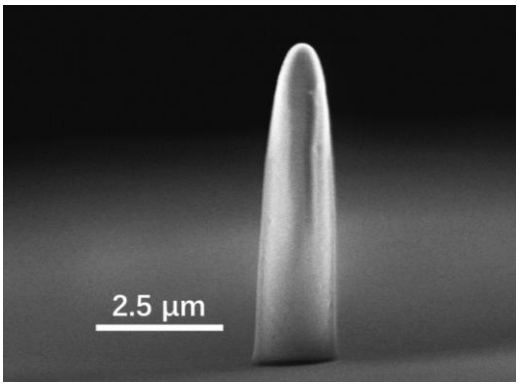

Figure 3-5. SEM image of the first PETA tip, taken before the second polymerization

Figure 3-6 presents luminescence images of the fabricated hybrid fibered tip. In Figure 3-6a, the luminescent image is captured with 405 nm laser light illuminated from the opposite end of the optical fiber. A 615/70 bandpass filter was used before the camera to capture the red-light emission from the fiber tip. A red spot indicates the position of luminescent optical fibered tip, while a white dash outlines the profile of the original optical fiber structure. Figure 3-6b displays another luminescent image under white light excitation from the exterior, using the 615/70 bandpass filter to emphasize red emission from both the optical fiber and the tip (with blue light effectively filtered out from the white light spectrum). The white dashed line also represents the original optical fiber structure, which is visible in this image because of light reflection. From these luminescence images, the light-emitting tip is observed at the center of optical fiber end and is oriented perpendicular to the end surface of optical fiber.

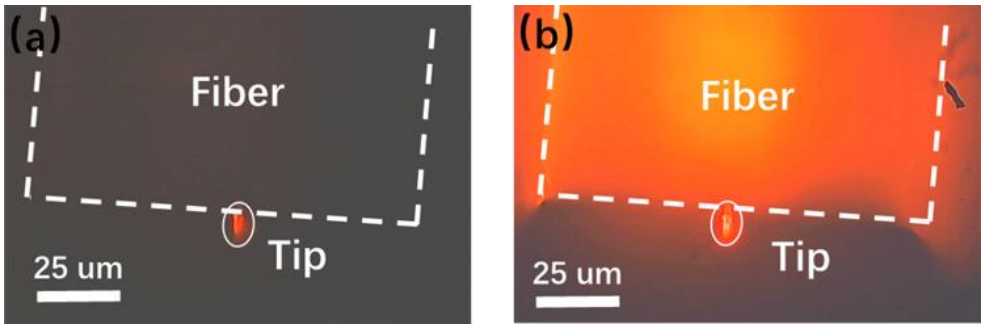

Figure 3-6. The luminescent images of the luminescent optical fibered tip. (a) The luminescent image with 405 nm laser light excited from another end of optical fiber. It is taken with a 615/70 bandpass filter before the camera. Red light emits from the tip end. (b) The luminescent image under white light excitation from environment. 615/70 bandpass filter (545-685 nm light would pass) was also used to take this image. The white dash line shows the profile of the optical fiber and the white ellipse identifies the tip position in both images.

In Figure 3-7a, SEM images depict the morphology of the functionalized optical fibered tip. The entire tip measures 11.9 µm in height, clearly displaying the boundary between the initial PETA polymer tip and the polyaryl extremity, as shown in Figure 3-7b. The polyaryl

layer exhibits a width of 2.88 μm at the junction section between the PETA tip and the polyaryl coating. The radius of curvature of the extremity of the second tipis 60.7 nm, which suggests the potential of the nanostructure as a nano-source.

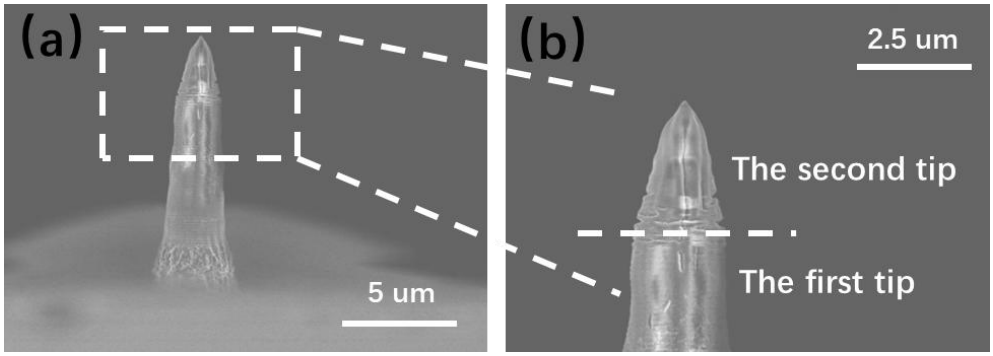

Figure 3-7. SEM images of the luminescent optical fibered tip. (a) The morphology of the whole tip, whose height is 11.9 μm. (b) The morphology of the second tip. The boundary between first and second tips is highlighted by a dashed white segment. The radius of curvature at the tip end is 60.7 nm.

3.3.2 Simulation of the process of fabrication of the luminescent optical fibered tip

To predict the fabrication progress of the first tip using PETA and the resulting optical field distribution used for making grow the second tip within diazonium salt, simulations were carried out based on the iterative numerical approach proposed before.[25] Herein, our iterative approach consists of considering the distribution of light emerging from the optical fiber in a medium with an initial refractive index of 1.48 and recalculating by FDTD the field several times while the spatial distribution of the refractive index is modified by polymerization. Figure 3-8 shows the result of the calculation. The simulation began with the laser excitation at λ=405 nm, after the optical fiber was dipped in PETA solution. The simulation results were recorded every 0.1s (the time interval), over the fabrication time. Figure 3-8a-f shows the electromagnetic field simulation results for fabrication times of t=0.1, 0.2, 0.4, 0.6, 0.8, and 1 s. Experimentally, the fabrication time was controlled by an electronic time shutter. Figure 3-8g-l show the shape of the area where field energy, accumulated over iterations, exceed the threshold (set as 84.88 nW/μm^2) of photopolymerization. These shapes of area are supposed to be the final shape of the fabricated polymer tip. This is because any liquid photopolymerizable area exposed to a dose above the threshold is assumed to withstand the rinsing procedure, while areas exposed to a dose below the threshold are dissolved. In the simulation progress, the shape for the last stage was used to simulate the electromagnetic field distribution of the next stage. It should be noted that the refractive index of the polymerizable product increases as a function of the energy accumulated during the iterations. The initial refractive index of the polymer formulation is 1.48, whereas it increases to 1.52 when polymerization is complete. The simulation continued until t=1s when the laser light was turned off, and the tip was rinsed with methanol to stop the reaction at the same time in experiment.

At Figure 3-8c, at t=0.4 s, there is a weak electromagnetic field part inside the stronger field, which is expected to lead to a liquid hole inside the solid polymer tip. This phenomenon

is likely to fragilize the tip, unless the exposure is continued. As the laser excitation continues, the liquid hole gets filled with solid polymerized PETA at t=1 s, decreasing the risk to damage the polymer tip when working. Moreover, at this time, field distribution at the extremity of the sharp first tip in PETA shows a high-density electromagnetic field that is likely to permit the efficient local growth of sharper second tip within the diazonium salt, although the wavelength used for growing the second tip is different.

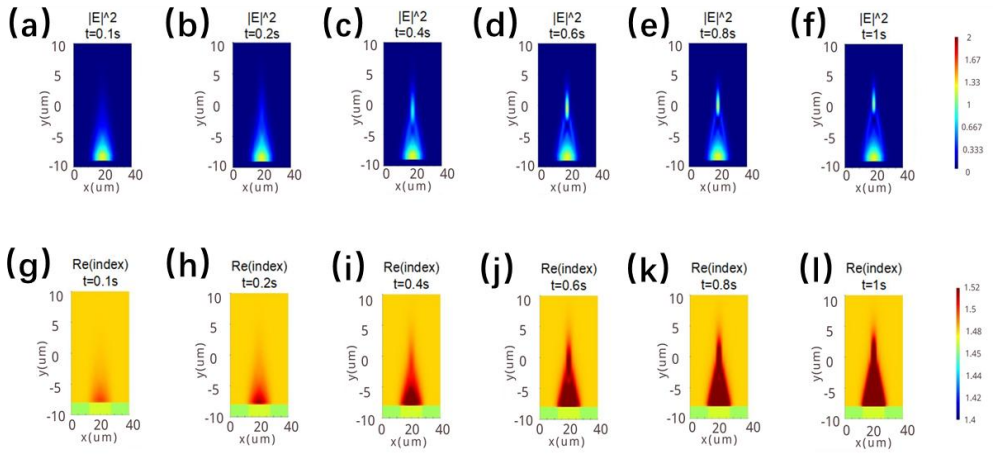

Figure 3-8. FDTD simulation of the growth of the first tip. (a)-(l) The growth progress of the first fibered tip by PETA with different fabrication times. Where the field energy over threshold of photopolymerization was supposed to be the shape of the fibered tip, which will be used in the simulation of the electromagnetic field in the next stage. The simulated shape of the final first tip with 1 s fabrication is shown in the Figure (l).

In order to access the role of the first tip in the growth of the second tip, the tip whose "numerical fabrication" was stopped at t=1 s was considered for further numerical FDTD calculation. 532 nm light was injected into the first tip (refraction index=1.52) immerged in a 1.5 index contrast (to simulate the presence of diazonium salt) and the resulting electromagnetic field distribution at the extremity of the tip is shown in Figure 3-9. Despite the low index contrast between the tip and the surrounding medium, the high-density electromagnetic area is concentrated at the vicinity of the tip forefront, which determines the growth direction of the second tip. The focusing effect is believed to result from an index gradient inside the first tip, which can be predicted by the iterative numerical simulation of the growth of the PETA tip.[25] Hence, the first PETA tip allows one to concentrate electromagnetic field, so that the second tip can be fabricated with a size that is as small as possible. In this case, the second tip was fabricated from diazonium salt, which is not a widely used material in tip fabrication, and the process is not easy to simulate.[26,27] In fact, Figure 3-7 shows the very first diazonium tip made at the end of an optical fiber using the self-growth approach.

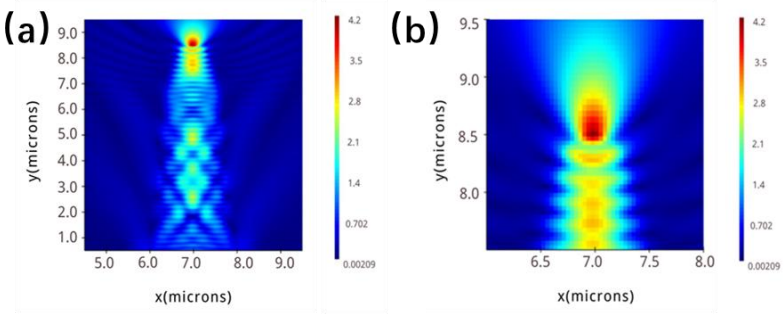

Figure 3-9. (a) and (b) The simulation results of the resulting first fibered tip with different scale bars. The high-density electromagnetic area is concentrated at the vicinal position of tip forefront, which determined the growth direction of second tip.

3.3.3 QDs adsorption on fibered-tip by electrostatic interaction

Figure 3-10a shows the PL spectrum of the extremity of the fibered tip measured using the configuration shown in Fig. 3-3. Under 405 nm laser excitation from the opposite fiber end, the peak position of resulting PL spectrum, collected though the objective lens, is 618 nm, which is the same as the colloidal QDs solution. The diazonium salt used is DCOOH, which is shown in the inset of Figure 3-10a. DCOOH is expected to have the ability to adsorb QDs by electrostatic interaction for the free $-COO^-$ group at the functionalized surface.

To highlight the role of the electrostatic adsorption rather than Van der Waals force adsorption, another optical fibered tip was fabricated based on DNO_2 as a benchmark. The chemical structure of DNO_2 is shown in the inset of Figure 3-10b, which is another kind of diazonium salt with a $-NO_2$ group, as developed in chapter 2. Since there is no potential chemical reaction or electrostatic coupling between DNO_2 and QDs ligands in water solution, QDs are not expected to be adsorbed on DNO_2 the functionalized surfaces. Only weak van der Waals forces are expected to work on the QDs adsorption on the DNO_2 functionalized fibered tip. The fabrication process of the DNO_2 functionalized optical fibered tip is the same as the DCOOH functionalized optical fibered tip, with the same parameters. With the same 405 nm laser light excitation, the resulting spectrum is shown in Figure 3-10b. The PL peak position is still 618 nm, but the intensity decreased from 2038 to 185. This 11-fold decrease suggests that electrostatic adsorption played a major role in the integration of the QDs on the DCOOH-functionalized tip.

This comparison is similar to the method performed on ITO glass in chapter 2. Combining both results, DCOOH diazonium salt turns to enable QDs adsorption by electrostatic interaction on both ITO-coated glass and optical fibered tip.

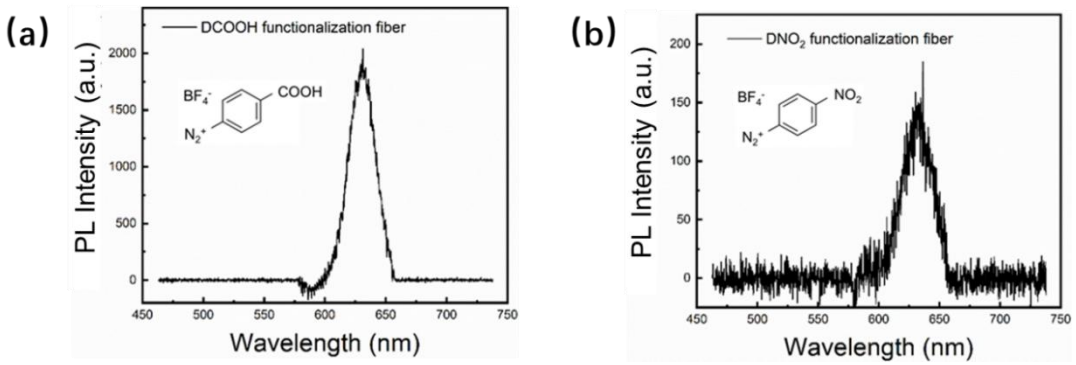

Figure 3-10. The PL spectra of two kinds of diazonium salt optical fiber tip. (a) Photoluminescence spectrum of the QDs adsorbed on the optical fibered tip with 405 nm laser excitation from the other fiber's end. DCOOH was used functionalization. (b) Photoluminescence spectrum of DNO_2-functionalized optical fiber tip. The same fabrication methods and parameters as for a) were used. The resulting PL intensity dropped by a factor of 11.

3.4 Fibered sensor of concentration of ZnO nanoparticles in solution

Rather than encapsulating QDs inside the volume,[28–30] QDs are here absorbed to the outside surface of the fabricated functionalized fibered tip, which is one of the key points leading to some potential use of the the hybrid system as QDs-based sensor. This kind of QDs-based sensors utilizes the surface charge transfer process to change the emission light from QDs. When QDs contact with another material whose bandgap is different from QDs, carriers transfer takes place between the two materials and leads to the carrier concentration change inside the QDs. The neutral exciton can be converted into trion.[31,32] The carrier recombination probability gets higher than QDs in colloid state and QDs emit light with shorter lifetime. This phenomenon is also called QDs photoluminescence quench. In this section, the sensor response of the luminescent fibered tip in ZnO nanoparticles solution will be discussed.

3.4.1 Characterizations of the diameter of the QDs in colloid state

The first use of the hybrid fiber (this section deals with) relies on carrier transfers. The QD-based fiber was considered as a sensor of nanoparticles concentration in liquid. The sensor is based on the change of PL lifetime, and the induced decrease of lifetime is chosen as the signal. The consistency of PL lifetime is the key point of the potential sensor.[33] Shell thickness is the main factor that influences the PL lifetime, which is the barrier and would determine the charge transfer process between QD core and environment. Therefore, the consistency of QDs' shell thicknesses could be equivalent to the consistency of PL lifetime.

Regarding the emission of core-shell structure QDs, it originates from the quantum confinement effect. The size of QDs core determines the emission peak position for the same material. For the QDs of the same material with the similar emission peak position would share similar core size, the QDs size is to some extent determined by the shell thickness. Thence, QDs size distribution could be used to evaluate the distribution of QDs' shell thicknesses as well as the consistency of PL lifetime.[34,35]

As a traditional method, the QDs size is easy to be measured from TEM images one by one but complex to be obtained with high-throughput quickly. To be able to evaluate the consistency of PL lifetime through QDs size information, a new method was developed to obtain the information on the particle size distribution from the TEM image. This method is developed from the traditional watershed method and can process batches of TEM images of different sizes automatically.[36,37] The working flow of analysis system shown in Figure 3-11 includes five steps: preprocessing, foreground separation, morphological labeling, image

segmentation, and data counting. The corresponding algorithm for each step is presented in the Figure 3-12. Each step with its algorithm is explained below.[38,39]

The preprocessing step improves the image contrast and balance, which facilitates the subsequent recognition of nanoparticle images through the Contrast Limited Adaptive Histogram Equalization (CLAHE) method. The input image is divided into non-overlapping sub-blocks of equal size, and each sub-block histogram and the shear threshold are calculated. For each sub-block, histogram equalization is achieved using redundant pixel reallocation, and the pixel point grayscale values are bilinearly interpolated and reconstructed. The foreground and background step including images are grabbed using the foreground extraction algorithm called Grabcuts algorithm, which defines one or more rectangles containing objects in the image. Objects in the background can be used to distinguish between the foreground and background regions inside it. Then, Gaussian Mixture Model (GMM) is performed to model the background and foreground and mark undefined pixels as possible foreground or background.

Then, the image is processed by morphologically labeling step from performing operations such as dilation and erosion on the binarized image. The combination of these two methods ensures that the size of the QDs in the final morphologically labeled images does not vary significantly. To get the results in the segmentation, the watershed method is then used to optimize the best segmentation distance in the morphological labels. The optimal segmentation distance is optimized iteratively by combining the image's local extremum results with the watershed algorithm to segment the best morphological results. Finally in the last step, the segmentation results with the best morphology are filtered and calculated. The data are output in a table. The contours array structure is obtained based on the contours retrieval function, and the coordinates (x,y) of all pixel points of each contour are used to calculate the contours area function.

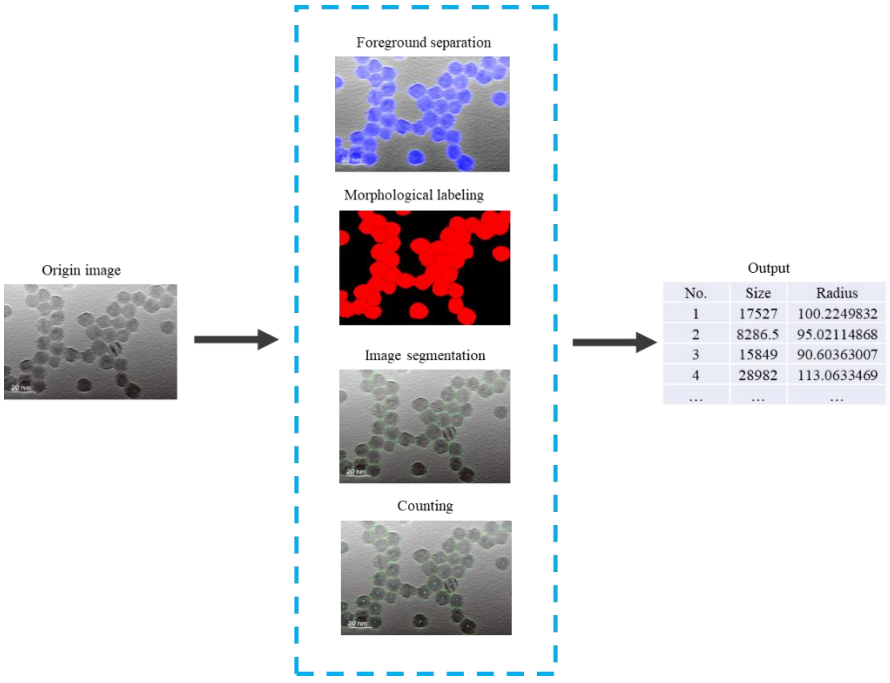

Figure 3-11. The working flow of automatic analysis system for TEM images of QDs including five steps: preprocessing, foreground separation, morphological labeling, image segmentation, and data counting. The size and radius of output data counts in pixels unit.

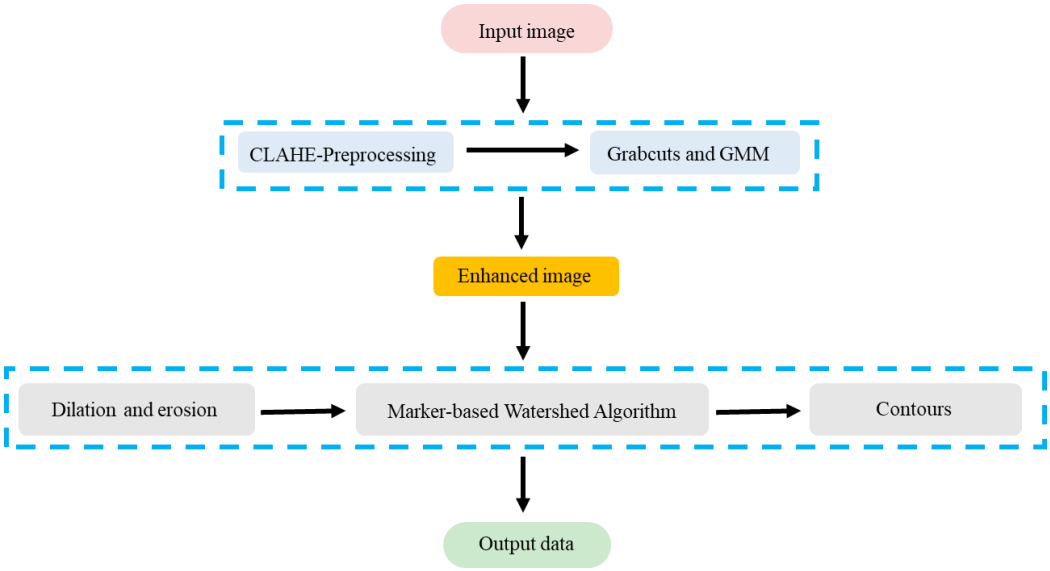

Figure 3-12. The algorithms applied in the analysis system, each algorithm corresponds with the steps above, the yellow background indicates the input, Intermediate output and final output, the blue and gray background represent algorithm.

The results of QD particle size distribution are presented in Figure 3-13 as an analysis sample. It's clear to observe the centroid center and edge of QD in TEM images, which labeled in green line. Even in the overlapping of QDs, the distinction between centroid center and edge is still clearly visible, which proves that the algorithm we used is concise and effective. The particle size distribution results are presented as counting results of each QD image is place in the right top. The x-axis represents particle diameter in nm and the y-axis represents the number of QDs. So, in Figure 3-13d summary the QDs particle size distribution in the total sample. As the results show, 52% QDs distribute in 10-15 nm and 33% QDs distribute in 15-20 nm. It shows the average size of QDs is 15.4 ± 5 nm. In fact, our analysis system can obtain hundreds of such distribution data at one time, which objectively enhances the scientific and rationality of our entire project.

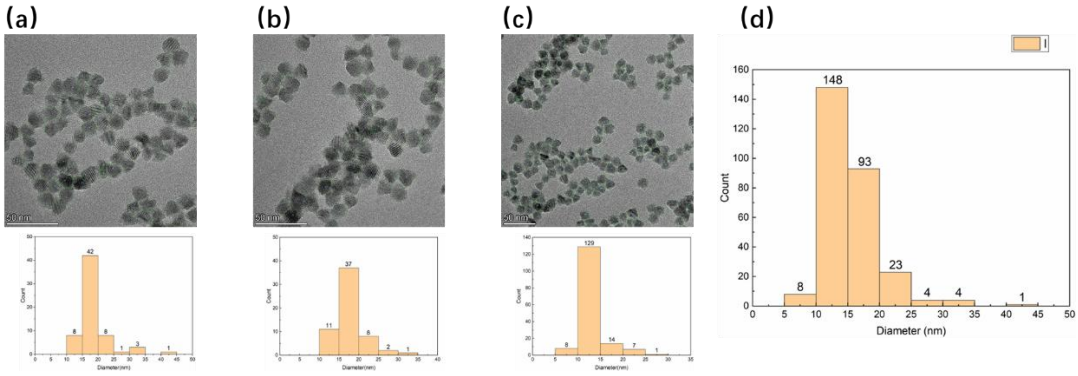

Figure 3-13. (a)-(c)TEM figure after processed by analysis system and the histogram of QDs particle size distribution. In the histograms, the X axis represents the size in diameter, and the Y axis represents the number of QDs. (d) Histogram of QDs size distribution in total sample.

3.4.2 Sensor response with ZnO nanoparticles solution

Rather than the method of encapsulating QDs inside the luminescent fibered tip,[28–30] QDs are here attached to the outside surface of the fabricated functionalized fibered tip, which is

one of the key points leading to some potential applications to be used as QDs sensor. QDs-based sensors utilize the surface charge transfer process to change the emission light from QDs. When QDs contact with another material whose bandgap is different from QDs, charge transfer takes place between the two materials and leads to the carrier concentration change inside QDs. The neutral exciton is converted into trion.[31,32] The carrier recombination probability gets higher than QDs in colloid state and QDs emit light with shorter lifetime. This phenomenon is also called QDs photoluminescence quench.

To verify the QD sensor feasibility using this principle of carrier transfer, the fabricated hybrid fibered tip was immersed in a ZnO NPs solution of different concentration. This concentration is an essential parameter when ZnO NPs are used to fabricate the electron transfer layer (ETL) of QLED.[40] Within the spin coating procedure, the ZnO NPs solution concentration influences ETL thickness and the electron injection process, which determines the brightness and luminescent efficiency of QLED. Due to the higher Fermi level of ZnO NPs compared to CdSe/ZnS QDs shown in Figure 3-14,[40] electrons transfer from ZnO NPs to QDs when contact, leading to the quenching of QDs emission due to the multiple charged excitons. The charge transfer is the main point of QDs quenching in our sensor application. The lifetime of the emitting light decreases during the quenching process. This phenomenon was thus chosen as the characterization of QDs quenching as well as the signal used for this kind of sensor.

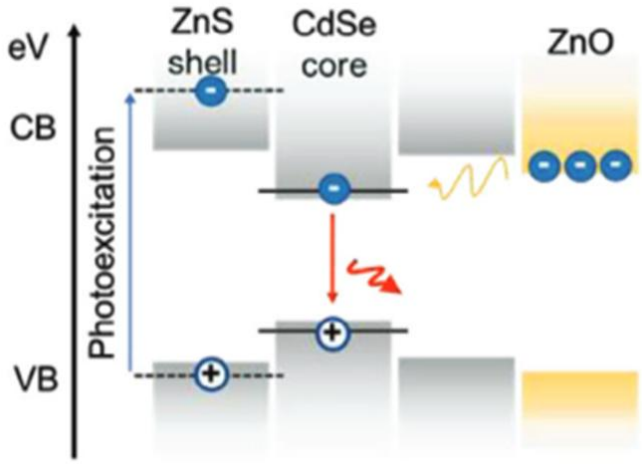

Figure 3-14. Energy diagram of a QD (Type-I) with valence (VB) and conduction (CB) bands accommodating an exciton charged by ZnO films.[40]

Figure 3-15a shows the TEM image of ZnO nanoparticles deposited on a TEM grid, which shows their uniform round shape. By the same analysis algorithm as QDs size measurement mentioned before, the diameter of ZnO NPs was determined: 3.5±0.2 nm. Figure 3-15b shows the image of fibered tip placed in ethanol solution on ITO substrate, with 0% ZnO NPs inside. Figure 3-15c shows the image of fibered tip immersed in the 35 mg/ml ZnO solution, which is also on ITO glass. Due to the exposed surface of the QDs, the intensity and lifetime of the emitted light will be influenced due to the quenching effect in ZnO NPs solution.

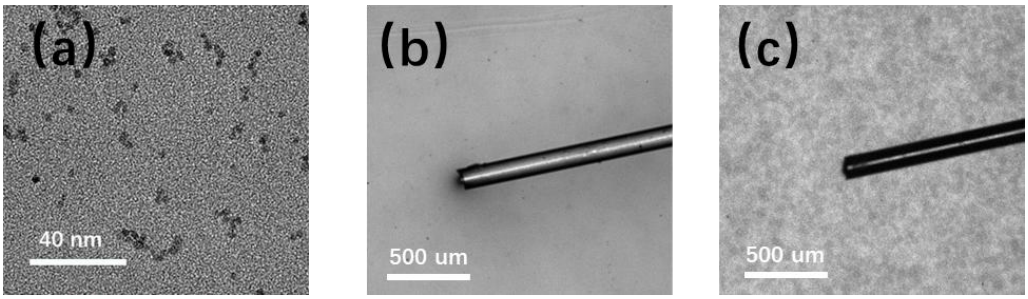

Figure 3-15. The TEM image of ZnO NPs is shown in (a), whose diameter is 3.5±0.2 nm. The optical images of the fibered tip put in ethanol solution and into ZnO NPs solution are shown in (b) and(c) respectively.

Figure 3-16 shows the absorption spectrum of ZnO NPs solutions. At the used excitation wavelength of 405 nm, the absorbance is 0.002, which is negligeable. Hence, we consider that the ZnO NPs did not get excited by the incident light, the quenching is not due to energy transfer from ZnO NPs to CdSe QDs. Only the CdSe QDs get excited by the incident blue light. In addition, Figure S7 makes it possible to exclude any Föster resonance energy transfer (FRET) from QDs to ZnO NPs, as FRET can only occur if the emission spectrum of the donor overlaps with the excitation (absorption) spectrum of the acceptor.[41]

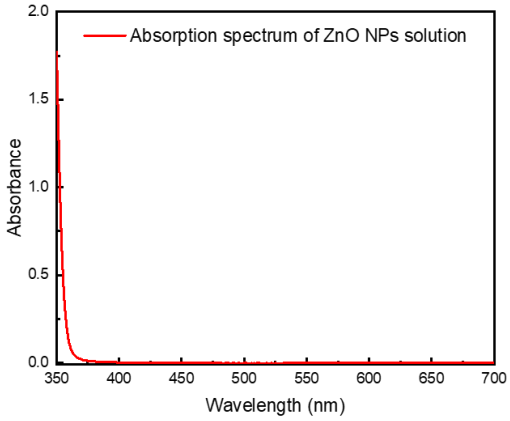

Figure 3-16. The adsorption spectrum of the ZnO NPs solution.

Figure 3-17a shows the PL spectra of the QDs-tip in ethanol solution and 35 mg/ml ZnO NPs solution. The light intensity decreased by a factor of 17.9 when the QDs-tip gets immersed in the ZnO NPs solution. Figure 3-17b shows the TRPL curves of the QDs-tip in ethanol solution and 35 mg/ml ZnO NPs solution. From the TRPL data, the lifetime decreased by a factor of 3.26 after immersion. The significant decrease of both light intensity and lifetime indicates that the QDs on the luminescent tip surface quenched when immersed in ZnO NPs solution.

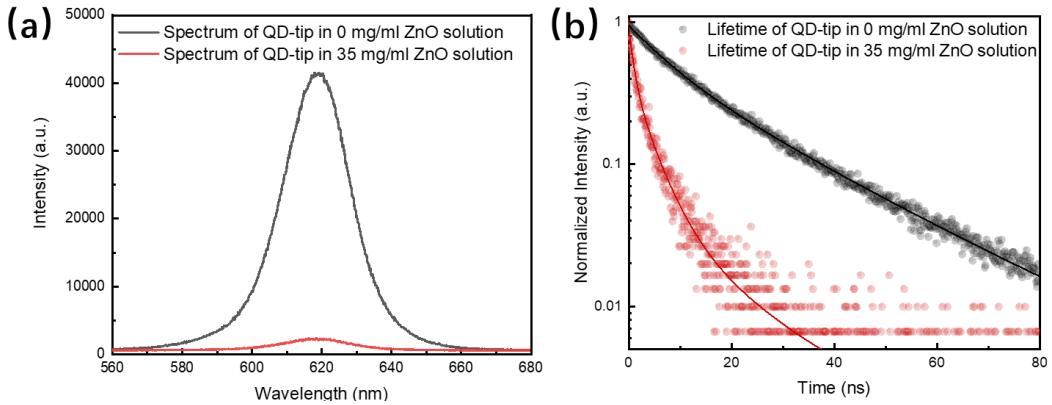

Figure 3-17. (a) The PL spectra of the QD-tip emission in ethanol solution and in 35 mg/ml ZnO NPs solution. The light intensity decreased 17.9 times after immersing the tip into the ZnO NPs solution. (b) The TRPL cuves of the QD-tip emission in ethanol solution and 35 mg/ml ZnO NPs solution. The lifetime decreased 3.26 times after immersing the tip into ZnO NPs solution.

Figure 3-18a shows the time-resolved photoluminescence (TRPL) curves of the QDs-tip in ZnO NPs solution with different concentrations ranging from 0 mg/ml to 35 mg/ml. The lifetime of emission light was 18.9 ns when the QDs tip was put into ethanol solution as well as 0 mg/ml ZnO NPs solution. With the increase of ZnO NPs concentration, the lifetimes became 12.5 ns, 10.2 ns, 7.3 ns, 5.9 ns and 5.8 ns when the concentration was 7 mg/ml, 14 mg/ml, 21 mg/ml, 28 mg/ml and 35 mg/ml, respectively. The trend of lifetime change is shown in Figure 3-17b. The lifetime decreased as the concentration of ZnO NPs increased step by step. The sensitivity of the sensor, defined as the local slope in Figure 3-18, decreases as 0.91 ns/(mg/ml), 0.33 ns/(mg/ml), 0.41 ns/(mg/ml), 0.2 ns/(mg/ml), 0.01 ns/(mg/ml) when the concentration increases as 0-7 mg/ml, 7-14 mg/ml, 14-21 mg/ml, 21-28 mg/ml and 28-35 mg/ml respectively. The sensitivity is nearly constant when concentration is in the 7-21 mg/ml range. However, when the ZnO NPs concentration is above 28 mg/ml, the lifetimes change weakly between 28 mg/ml and 35 mg/ml concentrations and the sensitivity is 0.01 ns/(mg/ml). These conclusions suggest that this approach would be more suitable for low concentration detection. There is a limitation for this QDs-tip when utilized in the detection of high density ZnO NPs solution. This limitation threshold is an important parameter in concentration detection. Since the detection is based on the charge transfer between QDs and ZnO NPs, when the ZnO concentration is increased, the interaction between two kinds of NPs gets saturated. We think this is the reason why the sensitivity decreases when ZnO concentration increasing.

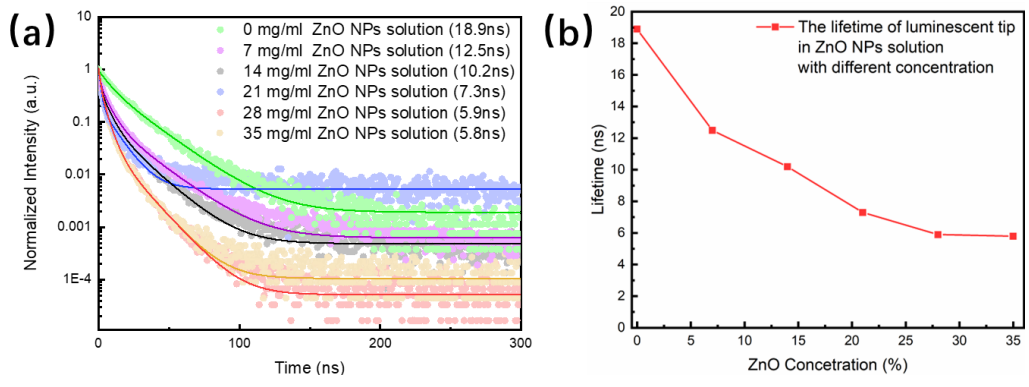

Figure 3-18. (a) PL lifetime measurement of the QD-tip in ZnO NPs solution with different concentrations. Under different conditions, the lifetime decreased from 18.9 ns to 5.8 ns. (b) The trend of the lifetime changes of the luminescent tip in ZnO NPs solution with different concentrations. The decrease of both light intensity and lifetime indicate the existence of QDs quench in ZnO NPs solution.

Considering the emission behaviors when immersing the luminescent tip into ZnO NPs solution, this kind of luminescent tip has a potential to detect in solution any kind of nanomaterial whose bandgap varies from QDs. Especially, this kind of luminescent tip has turned out to present a unique response to the ZnO NPs solution of specific concentration.

3.5 Summary and conclusions

In this chapter, a QDs-based fibered optical sensor was fabricated in the form of a luminescent polymer tip integrated at the extremity of an optical fiber. By using a two-step fabrication process with PETA and diazonium salt, QDs were adsorbed onto the grafted diazonium salt at the extremity of an optical fiber. The role of electrostatic adsorption of QDs on grafted diazonium salt was demonstrated by ruling out the influence of Van der Waals force. This electrostatic adsorption takes place between the QDs ligands and the free functional group of the diazonium salt. The resulting luminescent tip has a radius of curvature of 60.71 nm and the same photoluminescence spectrum as the colloid QDs. When the tip was immersed in 35 mg/ml ZnO solution, a 17.9-fold decrease in light intensity and a 3.26-times decrease in lifetime were observed due to QDs quenching. The lifetime clearly decreased as the ZnO NPs concentration increased from 0 mg/ml to 35 mg/ml. This phenomenon highlights the potential of using this QDs-linked luminescent tip structure as a QDs sensor. Due to the flexible structure of optical fiber, this kind of sensor could be used in the detection of marked cells or living issues in liquid without container shape limitation. Also, the analysis of QDs particle size distribution was employed to highlight the reliability of this potential QDs sensor.

This chapter presented a proof of concept for the use of the hybrid fibered tip as a sensor of concentration. The extension of the detection range and the improvement of the fibered hybrid system will be the subject of future works. In particular, while the fibered sensor cannot be reused directly, it can effectively be renewed. It is challenging to completely remove ZnO nanoparticles from the tip without affecting the QDs; however, the primary component of the sensor, the fabricated fiber tip, is robust, stable, and capable of being reused multiple times. After each use, both the QDs and ZnO nanoparticles can be removed together. Since the QDs attach electrostatically to the diazonium-functionalized fiber tip, they could be released by immersing the tip in a strongly acidic or basic solution.70 At high or low pH, the charges are neutralized, weakening the interaction between the fiber tip and QDs. Rinsing the tip with ultrapure water could then restore its negative charge due to the carboxyl groups from the diazonium salt. Finally, immersing the refreshed tip into a new QD solution could produce a freshly prepared sensor, ready for renewed use.

The effectiveness of this type of fiber-based sensor depends mainly on the existence of a charge transfer between the QDs and the environment. This charge transfer can be selective. For any particle that undergoes charge transfer with the QDs, once calibrated, this device could

potentially serve as a selective sensor. It may be also potentially possible to use this fiber-based hybrid system as a refractive index sensor, to which the lifetime of QDs may also be sensitive.

Reference

1. Kao, K. C. & Hockham, G. A. Dielectric-fibre surface waveguides for optical frequencies. in *Proceedings of the Institution of Electrical Engineers* vol. 113 1151–1158 (IET, 1966).
2. Hui, R. *Introduction to Fiber-Optic Communications*. (Academic Press, 2019).
3. Lu, P. *et al.* Distributed optical fiber sensing: Review and perspective. *Appl. Phys. Rev.* **6**, (2019).
4. Dragic, P. D., Cavillon, M. & Ballato, J. Materials for optical fiber lasers: A review. *Appl. Phys. Rev.* **5**, (2018).
5. Stellinga, D. *et al.* Time-of-flight 3D imaging through multimode optical fibers. *Science* **374**, 1395–1399 (2021).
6. Xiong, Y. & Xu, F. Multifunctional integration on optical fiber tips: challenges and opportunities. *Adv. Photonics* **2**, 064001–064001 (2020).
7. Bachelot, R., Blaize, S., Pang, C., Bruyant, A. & Royer, P. Polymer-tipped optical fibers. *Fiber Integr. Opt.* **27**, 542–558 (2008).
8. Zhang, Y. *et al.* Photopolymer self-growing technology: Towards multifunctional lab-on-fiber. *Opt. Laser Technol.* **168**, 109815 (2024).
9. Peng, Y. *et al.* 3D photoluminescent nanostructures containing quantum dots fabricated by two-photon polymerization: influence of quantum dots on the spatial resolution of laser writing. *Adv. Mater. Technol.* **4**, 1800522 (2019).
10. Issa, A. *et al.* Quantum Dot Transfer from the Organic Phase to Acrylic Monomers for the Controlled Integration of Single-Photon Sources by Photopolymerization. *ACS Appl. Mater. Interfaces* **15**, 25819–25830 (2023).
11. Lio, G. E. *et al.* Integration of nanoemitters onto photonic structures by guided evanescent-wave nano-photopolymerization. *J. Phys. Chem. C* **123**, 14669–14676 (2019).
12. Broussier, A. *et al.* Unidirectional frequency conversion of surface plasmon polaritons on metal nanowires. *Micro Nano Eng.* **19**, 100193 (2023).
13. Xu, X. *et al.* Towards the integration of nanoemitters by direct laser writing on optical glass waveguides. *Photonics Res.* **8**, 1541–1550 (2020).
14. Shao, Y. *et al.* An easy method to improve efficiency of multi-photon polymerization: Introducing solvents with nonlinear optical absorption into photoresist. *Opt. Laser Technol.* **151**, 108008 (2022).
15. Issa, A. *et al.* One Strategy for Nanoparticle Assembly onto 1D, 2D, and 3D Polymer Micro and Nanostructures. *ACS Appl. Mater. Interfaces* **13**, 41846–41856 (2021).
16. Ge, D. *et al.* Two-photon photopolymerization directly initiated by spiropyran photochromic molecules. *Light Adv. Manuf.* **4**, 14–24 (2023).
17. Jradi, S., Soppera, O., Lougnot, D. J., Bachelot, R. & Royer, P. Tailoring the geometry of polymer tips on the end of optical fibers via control of physico-chemical parameters. *Opt. Mater.* **31**, 640–646 (2009).
18. Huang, H. *et al.* Four-dimensional printing of a fiber-tip multimaterial microcantilever as a magnetic field sensor. *ACS Photonics* **10**, 1916–1924 (2023).
19. Jijana, A. N. *et al.* Quantum Dot-Sensitised Estrogen Receptor-α-Based Biosensor for 17β-Estradiol. *Biosensors* **13**, 242 (2023).
20. Chehimi, M. M., Lamouri, A., Picot, M. & Pinson, J. Surface modification of polymers by reduction of diazonium salts: polymethylmethacrylate as an example. *J. Mater. Chem. C* **2**, 356–363 (2013).
21. Guselnikova, O. A. *et al.* Tuning of PEDOT:PSS Properties Through Covalent Surface Modification. *J. Polym. Sci. Part B Polym. Phys.* **55**, 378–387 (2017).
22. Choi, M. S. *et al.* Electrostatic force analysis, optical measurements, and structural characterization of zinc oxide colloidal quantum dots synthesized by sol-gel method. *J. Appl. Phys.* **118**, (2015).
23. Roy-Gobeil, A., Miyahara, Y. & Grutter, P. Revealing energy level structure of individual quantum dots by tunneling rate measured by single-electron sensitive electrostatic force spectroscopy. *Nano Lett.* **15**, 2324–2328 (2015).
24. Tang, X. *et al.* The role of electrostatic potential polarization in the translocation of graphene quantum dots across membranes. *Nanoscale* **12**, 2732–2739 (2020).
25. Bachelot, R., Ecoffet, C., Deloeil, D., Royer, P. & Lougnot, D.-J. Integration of micrometer-sized

polymer elements at the end of optical fibers by free-radical photopolymerization. *Appl. Opt.* **40**, 5860–5871 (2001).
26. Chen, H. *et al.* Advanced active polymer probe for near-field optics. *Opt. Lett.* **48**, 4157–4160 (2023).
27. Abdelaal, A., Blaize, S., Issa, A. & Jradi, S. Strategy for Patterning Single Colloidal Gold Nanoparticles on Two Photon Polymerized and Functionalized Ultrathin Nanostructures. *Langmuir* **39**, 4583–4588 (2023).
28. Zhu, C. *et al.* High-Luminescence Electrospun Polymeric Microfibers In Situ Embedded with CdSe Quantum Dots with Excellent Environmental Stability for Heat and Humidity Wearable Sensors. *Nanomaterials* **12**, 2288 (2022).
29. Liu, Y. *et al.* Tough, stable and self-healing luminescent perovskite-polymer matrix applicable to all harsh aquatic environments. *Nat. Commun.* **13**, 1338 (2022).
30. Lin, C. C. *et al.* Water-resistant efficient stretchable perovskite-embedded fiber membranes for light-emitting diodes. *ACS Appl. Mater. Interfaces* **10**, 2210–2215 (2018).
31. Ollivier, H. *et al.* Reproducibility of high-performance quantum dot single-photon sources. *ACS Photonics* **7**, 1050–1059 (2020).
32. Wigger, D. *et al.* Controlled Coherent Coupling in a Quantum Dot Molecule Revealed by Ultrafast Four-Wave Mixing Spectroscopy. *ACS Photonics* **10**, 1504–1511 (2023).
33. Zhang, K. *et al.* Luminescence Lifetime-Based Sensing Platform Based on Cyclometalated Iridium (III) Complexes for the Detection of Perfluorooctanoic Acid in Aqueous Samples. *Anal. Chem.* **96**, 1565–1575 (2024).
34. Vishnu, E. K., Kumar Nair, A. A. & Thomas, K. G. Core-Size-Dependent Trapping and Detrapping Dynamics in CdSe/CdS/ZnS Quantum Dots. *J. Phys. Chem. C* **125**, 25706–25716 (2021).
35. de Mello Donegá, C., Bode, M. & Meijerink, A. Size-and temperature-dependence of exciton lifetimes in CdSe quantum dots. *Phys. Rev. B—Condensed Matter Mater. Phys.* **74**, 085320 (2006).
36. Cao, H. *et al.* Swin-unet: Unet-like pure transformer for medical image segmentation. in *European conference on computer vision* 205–218 (Springer, 2022).
37. Xu, G., Zhang, X., He, X. & Wu, X. Levit-unet: Make faster encoders with transformer for medical image segmentation. in *Chinese Conference on Pattern Recognition and Computer Vision (PRCV)* 42–53 (Springer, 2023).
38. Shekhar, K. *et al.* Comprehensive classification of retinal bipolar neurons by single-cell transcriptomics. *Cell* **166**, 1308–1323 (2016).
39. Zhu, Q., Shah, S., Dries, R., Cai, L. & Yuan, G.-C. Identification of spatially associated subpopulations by combining scRNAseq and sequential fluorescence in situ hybridization data. *Nat. Biotechnol.* **36**, 1183–1190 (2018).
40. Jia, S. *et al.* Optimizing ZnO–Quantum Dot Interface with Thiol as Ligand Modification for High-Performance Quantum Dot Light-Emitting Diodes. *Small* **20**, 2307298 (2024).
41. Aubret, A., Pillonnet, A., Houel, J., Dujardin, C. & Kulzer, F. CdSe/ZnS quantum dots as sensors for the local refractive index. *Nanoscale* **8**, 2317–2325 (2016).

Chapter 4 Hybrid nanoemitter based on the QDs adsorption on plasmonic nanowires by diazonium salt

4.1 Introduction

As discussed in the previous chapters, nanoemitters based on QDs integration is one of the most promising nano-scale photon sources, which utilizes the narrow emission spectrum, and high quantum efficiency and other properties. Moreover, the excellent material compatibility of QDs maintains the variety of light integration methods.[1–3] In previous works, DNA origami-based technique,[4,5] site-selective enfold,[6] and other methods[7] were employed to site-selective integrate QDs with metal nanostructure. Controlled deposition of nanosource at a specific position can be successfully achieved using two-photon polymerization (TPP) technology.[8] Dias and et al. doped photoresist with fluorophores and fabricated micrometric RGB and white light emitters by TPP method.[9] With similar method, fluorescent nanodiamonds,[10] dyes,[11] QDs[12] and rare-earth doped nanoparticles[13] were also integrated to realize 3D photoluminescent structures with multi-type emitters. Particularly, our group demonstrated the fabrication of plasmonic hybrid nanoemitters based on plasmon-assisted one or two-photon polymerization. Individual Ag[14] and Au[15] nanoparticle were used as the optical near-field source for locally triggering photopolymerization of a QD-containing photosensitive formulation, resulting in a controlled anisotropic polymerization and the trap of QDs at specific sites corresponding to the localized plasmon modes used for inducing polymerization. Moreover, the remote excitation on plasmonic nanowire[16] and single photon emission[17] were also realized with the QDs-based plasmonic hybrid emitter with the same method.

Diazonium salts are highly reactive molecules capable of forming strong covalent bonds with a wide range of surfaces, that have been widely used for nano-scale surface functionalization and molecule immobilization.[18,19] This functionalization process typically involves the reduction of the diazonium group, resulting in the formation of an aryl-surface bond. The formed molecular layers are mechanically, thermally and chemically stable.[20] The connection of nanomaterials, such as Au NPs,[21] catalysts,[22] and biomolecules, including proteins,[23,24] nucleic acids[25] and cellulase,[26] have been performed following this strategy. While conventional diazonium salt grafting strategies result in a surface coating that uniformly covers the entire functionalized surface, plasmon-mediated reduction of aryl diazonium salts enables the regioselective grafting of polyaryl layers following the distribution of plasmonic enhanced electromagnetic field.[27] Since the corresponding location can be adjusted through different plasmonic modes, multi-functionalization of gold nanodisk arrays has been achieved using different kinds of aryl diazonium salts.[28] The immobilization of nanomaterial to form hybrid structures with the help of diazonium salt was shown to be controllable over deterministic position and molecule selection.

Relying on the methods described in chapters 2 and 3, the QDs adsorption with the

functionalization of diazonium salt is likely to be an effective method for fabricating plasmonic nanoemitters. This process, driven by electrostatic interactions, has been demonstrated on both ITO-coated glass and tipped optical fiber. However, previous applications have only explored surface functionalization and electrostatic adsorption at the microscopic (or submicroscopic) scale, but not at the nanometric scale.

In this chapter, the QDs electrostatic adsorption as well as the diazonium salt surface functionalization will be performed at the nano scale. Local plasmon-induced diazonium salt functionalization was made on an Au nanostrip or a silver nanowire (Ag NW), followed by region-selective adsorption of QDs near the Ag NW through electrostatic interactions. The resulting hybrid QDs-Au nanostrip and QDs-Ag NW nanoemitters exhibited plasmonic enhanced photoluminescent (PL) emission, with controllable lifetime behavior in positive correlation to the fabrication parameters. The morphology will be analyzed using SEM and AFM, while PL spectra and TRPL curves will be measured to evaluate their emission characteristics. Plasmonic emissions were observed from both kinds of nanoemitters by TRPL analysis. Regarding the QDs-Ag NW nanoemitters. Propagating surface plasmon polaritons (SPPs) enabled remote excitation of the QDs, which could be turned off on demand by switching the excitation polarization direction used for SPP excitation. The distance, which is 2.5 μm between the excitation position and the nanoemitter locations on Ag NW, should avoid photooxidation and photobleaching of QDs from laser illumination and enhance the durability of the hybrid nanoemitter. The conditional excitation underscores the potential application for advanced integration photonic system.

4.2 Experimental methods

In this section, the experimental methods to fabricate QDs-Au nanostrip and QDs-Ag NW nanoemitters will be introduced separately. For both kind of nanoemitters, the difference in fabrication is manifested in the preparation of NWs. In our work, the Au nanostrips were fabricated by semiconductor manufacturing process, including Electron beam lithography (EBL), evaporation and lift-off etching. The Ag NWs were chemically synthesized commercial products, spread on ITO glass by spin-coating. After NWs sample preparation, the procedures of surface functionalization by diazonium salt and QDs adsorption are similar, which will also be introduced individually.

4.2.1 QDs-Au nanostrip nanoemitter fabrication

Figure 4-1 shows the design of Au nanostrip sample. The substrate is an ITO-coated glass. A Au nanostrips pattern with 1.7 mm * 1.7 mm and 9 sub-patterns with 500 nm * 500 nm were designed on the ITO layer. The pitch between each Au nanostrips is 5 μm to avoid the coupling between NWs. The thicknesses and long axis lengths of all Au nanostrips are 100 nm and 200 μm. The sizes, as well as the short axis lengths of the Au nanostrips are from 350 nm to 850 nm. In each sub-pattern, the short axis lengths were kept same as 350 nm, 400 nm, 450 nm, 500 nm, 550 nm, 700 nm, 750 nm, 800 nm and 850 nm. The short axis length number is marked for each sub-area.

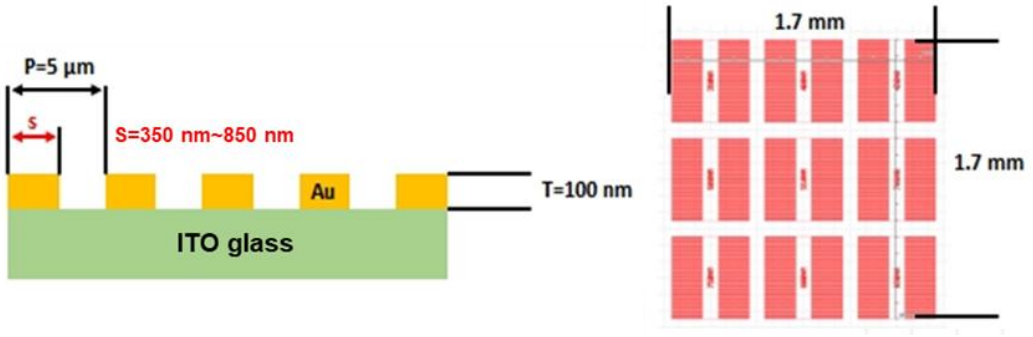

Figure 4-1. The design of Au nanostrip sample. Au nanostrips pattern as well as the sub-areas were designed on the ITO glass.

The Au nanostrip sample is fabricated on ITO glass and shown in Figure 4-2. The size of ITO glass is 22 mm * 22 mm. The thickness of ITO layer is 135 nm, and the square resistance is 15 Ω. The optical image of the whole pattern is shown in Figure 4-2a. The Au nanostrips were fabricated by EBL, evaporation and lift-off etching methods. Due to the imperfect production process, there were Au layer remaining and over lift-off existing on the sample. Some sub-patterns were covered by the unremoved Au layer. From Figure 4-2b, which shows the optical image of 550 nm sub-pattern, some broken NWs could be observed due to over lift-off.

Figure 4-2c and Figure 4-2d show the SEM image of the Au nanostrips in 500 nm sub-pattern with different scale bar. Besides the broken NWs show before, there are adequate well fabricated Au nanostrips. The structures are consistent in the middle part of Au nanostrip, where are the chosen position for the following experiments. Moreover, the width of fabricated NWs is different from designed. Table 4-1 shows the designed and fabricated widths of Au nanostrip in each sub-pattern. The corresponding width differences are also indicated. Due to the precision of the fabrication is insufficient, for most sub-pattern, the width differences are from 76 nm to 117 nm. For 800 nm and 850 nm sub-patterns, the width differences are less, as 43 nm and 31 nm.

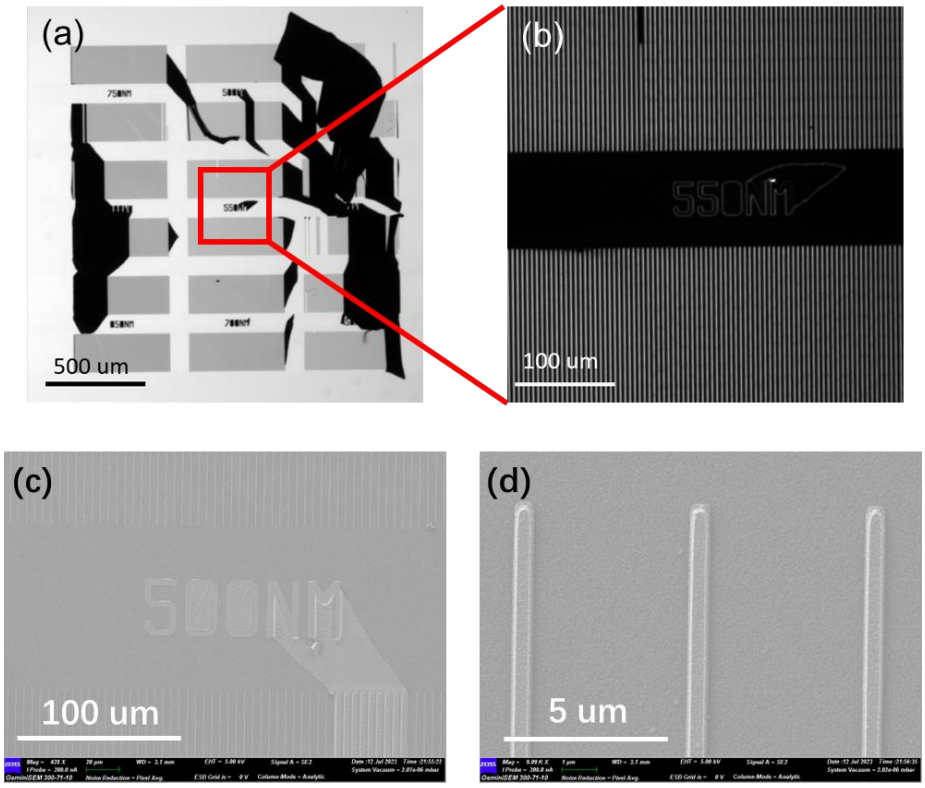

Figure 4-2. The photos of Au nanostrips. (a) The optical image of fabricated Au nanostrips pattern. (b) Optical image of fabricated 550 nm sub-pattern. (c) and (d) The SEM image of 500 nm sub-pattern with scale bar of 100 μm and 5 μm respectively.

Designed width	Fabricated width	Width difference
350 nm	431 nm	81 nm
400 nm	506 nm	106 nm
450 nm	526 nm	76 nm
500 nm	592 nm	92 nm
550 nm	667 nm	117 nm
700 nm	812 nm	112 nm
750 nm	776 nm	76 nm
800 nm	843 nm	43 nm
850 nm	881 nm	31 nm

Table 4-1. The designed and fabricated widths of Au nanostrip and the corresponding width differences

Due to the existence of width difference between design and fabrication, the scattering spectra of single Au nanostrip were compared by simulation and experiment. Figure 4-3 shows simulated the scattering spectrum of single Au nanostrip with 500 nm width. A white light is used to excite the Au nanostrip from the top, and the polarization direction is set as parallel to the short axis. There are two scattering bands located in green and red wavelength. The spectrum was taken from far field, which is main contributed by dipolar mode of the short axis.

In our experiment, 532 nm laser will be used to excite the plasmonic effect of Au nanostrip, which is associated with the plasmonic mode along the short axis. The plasmonic effect would be utilized in both diazonium salt surface functionalization and QDs adsorbed hybrid nanoemitter excitation.

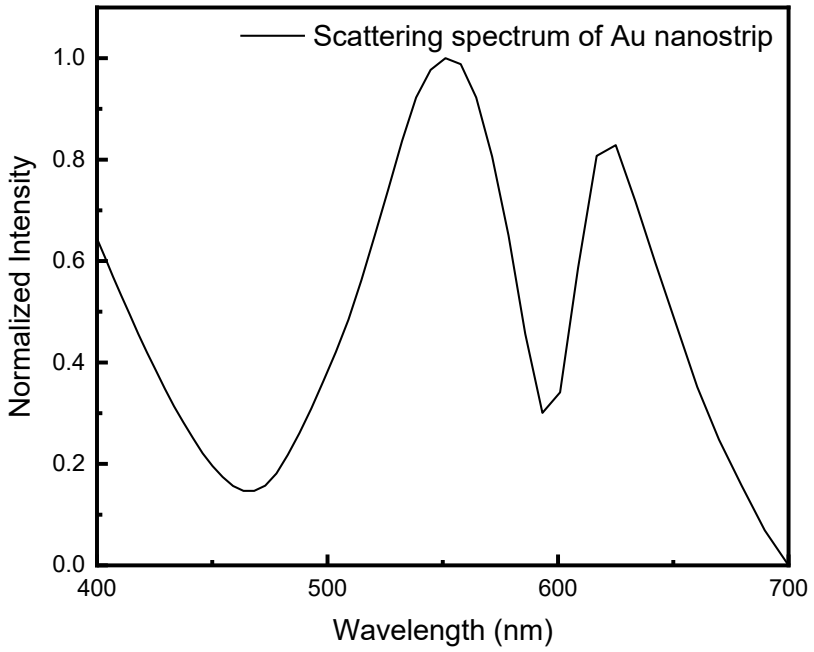

Figure 4-3. The simulated scattering spectrum of Au nanostrip with 500 nm width.

In this work, the surface functionalization by diazonium salt is performed on Au nanostrip as shown in Figure 4-4. The diazonium salt used here is the DCOOH diazonium salt, which have been presented in chapters 2 and 3. The experimental configuration is similar to the configuration of surface functionalization on ITO glass. To excite the localized surface plasmonic resonance of the short axis (dipolar mode), the polarization direction of laser light is parallel to the short axis of Au nanostrip.

After deposition of a 5 mM drop of DCOOH solution on ITO glass, a 532 nm laser light with laser density of 4.68 mW/um^2 was used to illuminate the Au nanostrip through a 20x objective. The exposure time was adjusted from 5 s to 60 s. After exposure, the sample was rinsed by deionized water to remove the excess solution and kept in water-free environment. After the surface functionalization, SEM was employed to describe the morphology before QD deposition.

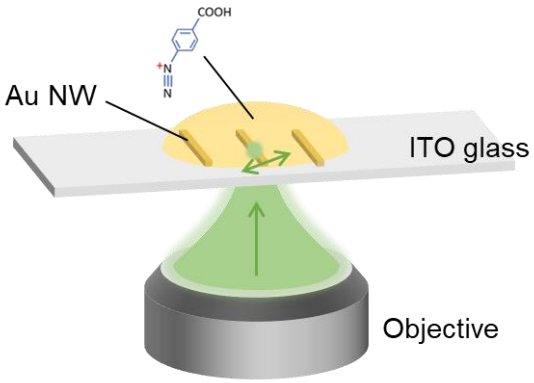

Figure 4-4. The schematic of diazonium salt surface functionalization on Au nanostrip.

After the grafting of functionalization layer, the QDs solution will be deposited on ITO glass as shown in Figure 4-5, covering the target sample area. The used QDs are the same commercial products as those used in previous chapters: from Mesolight Inc. and capped by cysteamine (CA) ligands. Again, the positive surface charges, brought by $-NH_3^+$ groups in water solution, is supposed to interact with negative charges from $-COO^-$ groups of DCOOH grafted layer. In this work, the QDs concentration was diluted to 0.01 nmol by deionized water. And the QDs solution was dropped on the sample surface and kept for 30 min. the sample was then rinsed by deionized water to remove excess solution and kept in water-free environment,

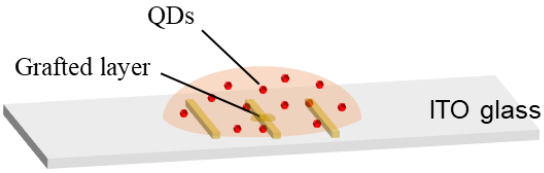

Figure 4-5. The schematic of QDs deposition process.

To evaluate the optical properties of fabricated QDs-Au nanostrip nanoemitter, the PL and TRPL were measured with the configuration shown in Figure 4-6, which is similar to the configuration used in surface functionalization shown in Figure 4-4. The excitation light is 532 nm laser light illuminated the Au nanostrip by a 20x objective. The polarization direction of laser light should also be parallel to the short axis of Au nanostrip, to excite the localized surface plasmonic resonance of the short axis as well as maintain the excitation of the QDs. The PL and TRPL signals were measured with 615/70 bandpass filter.

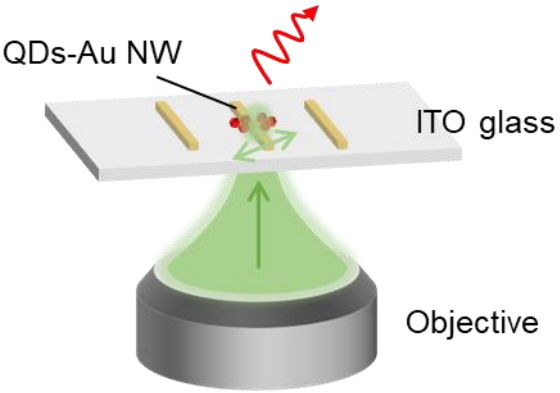

Figure 4-6. The schematic to measure PL intensity from functionalized areas.

4.2.2 QDs-Ag NW nanoemitter fabrication

In this section, the method for fabricating QDs-Ag NW nanoemitters will be introduced. Rather than the manufactured Au nanostrip, the used Ag NWs are commercial products from Nanjing XFNANO Materials Tech Co., Ltd. The original solution has a concentration 10 mg/ml and was diluted into 10 μg/ml. The diameters of Ag NWs were 70 nm, with a varying length typically bigger than 10 μm and often of several hundred micrometers These Ag NWs are solved in deionized water solution. To prepare the single NW sample, the Ag NWs solution was dropped on ITO glass with with markings that make it possible to locate and identify specific NWs. Spin-coating wa used to spread the Ag NWs.

One of the spread results of Ag NWs is shown in Figure 4-7. The substrate is ITO glass marked by laser marking machine: under strong laser light exposure, the ITO layer was destroyed and round shape marks appeared on ITO glass. The marks were aligned as shown at left and below in Figure 4-7. The NWs were separated due to spreading. In Figure 4-7, single Ag NWs are visible by optical microscopy. They can be easily selected for fabricating hybrid the plasmonic sources.

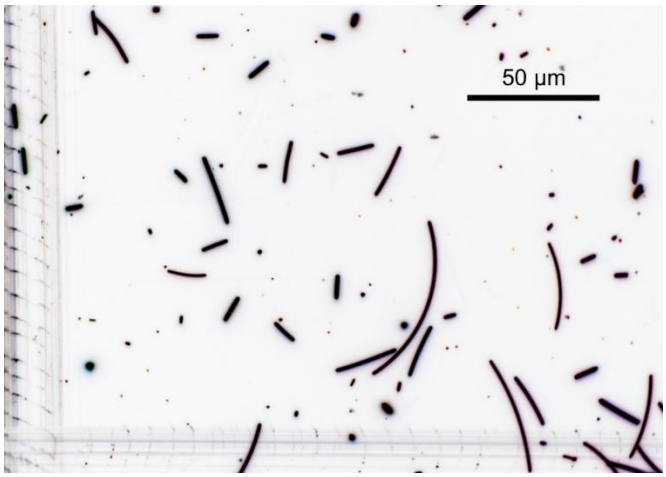

Figure 4-7. Dark-field optical image of the sample with spread Ag NWs on marked ITO.

In this work, the experimental configuration of diazonium salt surface functionalization on Ag NW is shown in Figure 4-8. The DCOOH diazonium salt is also used here. Keeping the same as the fabrication of QDs-Au nanostrip nanoemitter, the polarization direction of laser light was parallel to the short axis of Ag NW to excite the localized surface plasmonic resonance of the dipolar mode of this axis.

Firstly, DCOOH diazonium salt solution with concentration of 2 mM was dropped on the ITO glass. A 532 nm laser light was used to illuminate the Ag NW through a 10x objective. The laser energy density was adjusted from 0.0468 mW/um^2 to 0.468 mW/um^2. According to experimental results, the exposure times were adjusted from 10 s to 120 s to control the sample size. Different from Au nanostrips, whose orientations has already been aligned due to designed fabrication, the orientation of the Ag NWs is random on the ITO glass.

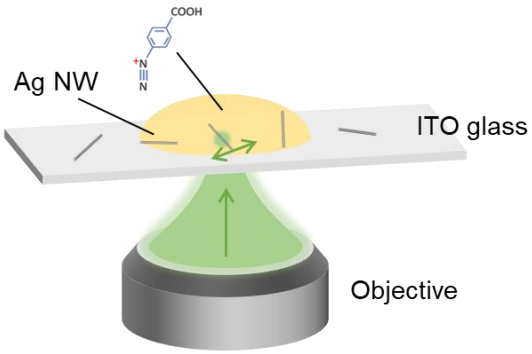

Figure 4-8. The schematic of diazonium salt surface functionalization on Ag NW.

A special sample holder was made to rotate the sample, in order to ensure the short axis of Ag NW is parallel to the polarization direction of laser light. Indeed, rotating the incident polarization direction can be limited by the polarization sensitivity of the microscope. This is why we preferred to rotate the sample. The photo of the designed sample holder is shown in Figure 4-9. After exposure, the sample was rinsed by deionized water to remove the excess solution and kept in water-free environment. After the surface functionalization, SEM was used to describe the morphology.



Figure 4-9. Photo of sample holder for QDs-Ag NW nanoemitter, which helps to the alignment of laser excitation.

As a last step, QDs solution was deposited on ITO glass as shown in Figure 4-10. The used QDs are still the QDs capped by CA ligands. In this work, the QDs concentration was diluted to 0.01 nmol/mL by deionized water. The QDs solution was dropped on sample surface and kept for 30 min. The sample was then rinsed by deionized water to remove excess solution and kept in water-free environment,

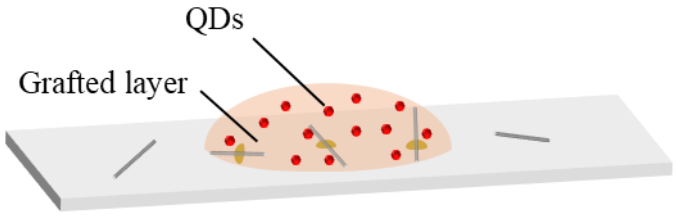

Figure 4-10. The schematic of QDs deposition

Similar to the experimental configuration of QDs-Au nanostrip nanoemitter fabrication, PL and TRPL were measured to evaluate the optical properties of fabricated QDs-Ag NW nanoemitter as shown in Figure 4-11. The excitation light is 532 nm laser light illuminated the Au nanostrip. Within the sample holder described in Figure 4-10, the polarization direction of

laser light was kept parallel to the short axis of Ag NW, to excite the localized surface plasmonic resonance. The scattering spectrum is shown in Figure 4-12. PL and TRPL were measured with 615/70 bandpass filter.

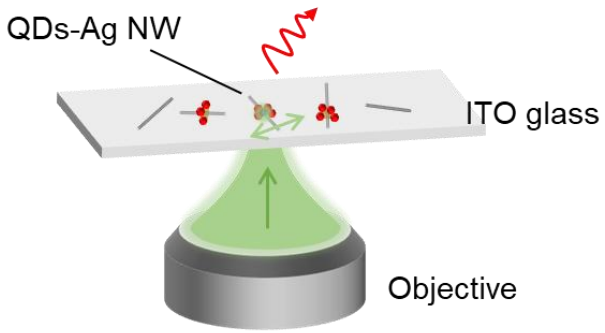

Figure 4-11. The schematic to measure PL intensity from functionalized areas.

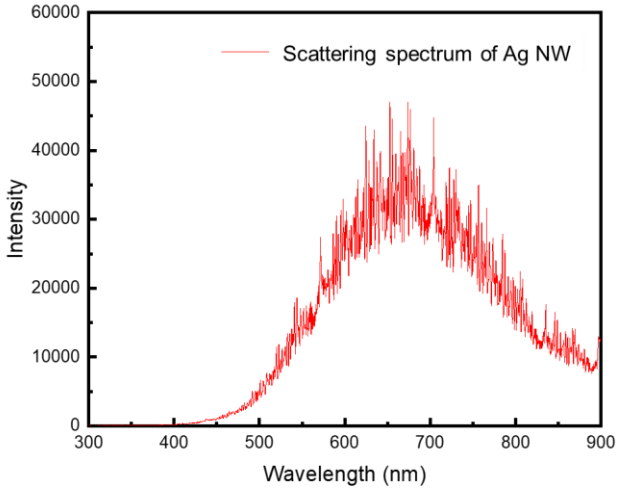

Figure 4-12. The scattering spectrum of Ag NW. The sample is single Ag NW dispersed on ITO glass. The environment is deionized water.

4.3 QDs-Au nanostrip nanoemitters: morphology and plasmonic PL emission

Following the fabrication of the QDs-Au nanostrip nanoemitter detailed section 4.2.1, this section will focus on its morphology and optical properties. The PL peak position matched that of the colloidal QDs dispersed on ITO glass. Notably, the lifetime from the TRPL spectrum increased with larger sizes, demonstrating a positive correlation with Pearson correlation factor of 0.66, consistent with the plasmonic effect. We also observed an increase in the PL emission lifetime when the Au nanostrip was removed from the hybrid structure. The same increase was also observed the emission of the grafted diazonium salt layer when Au nanostrip was removed. These findings indicate that the grafted diazonium salt layer may exhibit properties similar to semiconductor materials like QDs.

4.3.1 The morphology of the QDs-Au nanostrip nanoemitter

SEM was used to characterize the morphology of QDs-Au nanostrip nanoemitters. Figure 4-13 presents the SEM images of the fabricated nanoemitters after QDs deposition. During the surface functionalization process, the grafted layer forms along both sides of the Au nanostrip, following the distribution of the plasmonic enhanced electromagnetic field. The resulted structure is depicted in Figure 4-13a, for which the grafting exposure time is 20 seconds. While the spatial extension of the functionalization corresponds to the size of the incident laser, it is confined to the nanoscale perpendicular to the NW due to the local evanescent plasmonic field associated with the transverse dipolar plasmon mode. As the grafting reaction continues, the grafted layers near the Au nanostrip become thicker. Eventually, these two layers connect above the Au nanostrip, forming a unified layer, as shown in Figure 4-13b, where the exposure time was 50 seconds.

The growth of the grafted layer is anisotropic and aligns with the plasmonic enhanced electromagnetic field distribution. The growth is faster along the long axis of Au nanostrip. After completing the surface functionalization, QDs will adsorb onto the grafted layer by depositing QDs solution.

It is essential to specify the thickness of the grafted diazonium salt layer and the size of the fabricated devices. During the grafting process, the layers along both sides of the Au nanostrip merge into a single layer above it. In the initial step, as shown in Figure 4-14a, the thickness of the grafted diazonium salt layer can be easily measured from the SEM image. However, in the subsequent step, once the layers connect, the boundary between them becomes unclear. Thus, the midline of the Au nanostrip is used as the reference point to measure the thickness, as illustrated in Figure 4-13b. Defining the thickness concept allows for a comparison of the sizes of different QDs-Au nanostrip nanoemitters.

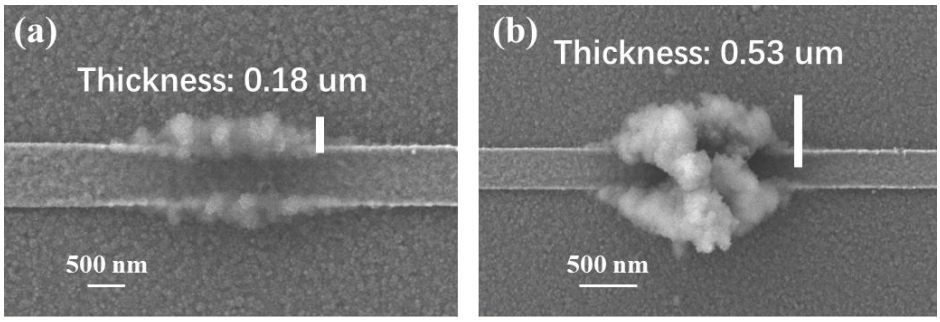

Figure 4-13. SEM image of fabricated QDs-Au nanostrip nanoemitter. (a) The exposure time of the grafting process was 20s, and the thickness is 0.18 μm. (b) The exposure time in grafting process was 50s, and the half-thickness is 0.53 μm.

4.3.2 Plasmonic PL emission from QDs-Au nanostrip nanoemitter

This section discusses the emission characteristics of QDs-Au nanostrip nanoemitter such those shown in Fig. 4-13. The PL spectrum of the QDs-Au nanostrip nanoemitter is shown in Figure 4-14a, with a peak position at 616.5 nm and a FWHM of 20 nm. In comparison, the PL spectrum of QDs spread on ITO glass is presented in Figure 4-14b, featuring a peak position at 614.5 nm and a FWHM of 21 nm. The consistency of the PL spectrum throughout the fabrication process indicates that the QDs can be effectively regarded as part of the QDs-Au

nanostrip nanoemitter.

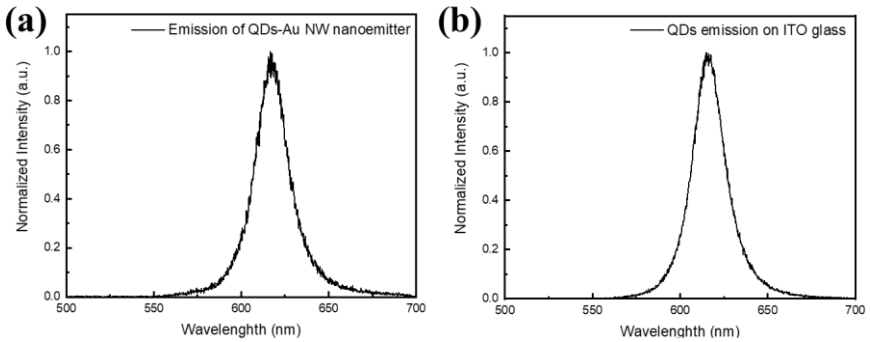

Figure 4-14. PL spectrum of (a) QDs-Au nanostrip nanoemitter (Peak position: 616.5 nm, FWHM: 20 nm) and (b) Spread QDs on ITO glass (Peak position: 614.5 nm, FWHM: 21 nm).

While the PL spectrum remained consistent, the lifetime of the PL emission varied due to coupling between QDs and Au nanostrip. In our case, the amount of deposited QDs is not in control. The lifetime is the key point to evaluate the plasmon enhance. Figure 4-15a displays the TRPL spectrum of the QDs-Au nanostrip nanoemitter, which shows a lifetime of 2.51 ns. In contrast, the TRPL spectrum of QDs spreaded on ITO glass, shown in Figure 4-15b, indicates a lifetime of 17.4 ns. The plasmonic effect and indicated carrier transfer between the QDs and the Au nanostrip is attributed to the decrease in lifetime observed after the QDs were adsorbed onto the grafted diazonium salt layer. The result proves there is a Purcell effect due to the Au nanostrip-grafted diazonium salt configuration.

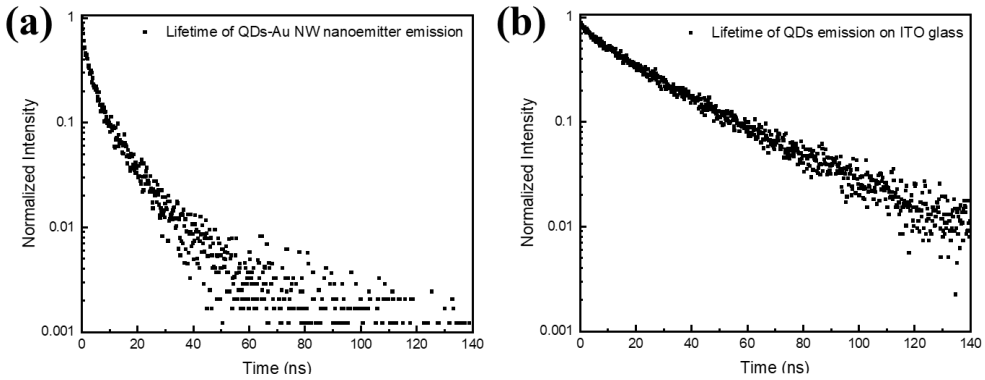

Figure 4-15. TRPL curves of (a) QDs-Au nanostrip nanoemitter (τ = 2.51 ns) and (b) Spread QDs on ITO glass (τ = 17.4 ns).

By comparing the lifetimes before and after adsorption, we explored the relationship between the lifetime and the thickness of the grafted diazonium salt layer that can also be seen as the gap between the adsorbed QDs and the Au nanostrip. This gap represents the distance between QDs and Au nanostrip. It can influence the QDs-NW coupling.

Figure 4-16 presents a scatter plot correlating thickness with the corresponding lifetime for 17 QDs-Au nanostrip nanoemitters. The data indicate a clear correlation between thicknesses and lifetimes, with a P-value of 0.0002. In statistics, the p-value is a measurement to determine the consistency between two groups of data. If $p < 0.05$, the consistency would be thought as existence. In this case, there must positive correlation between the thickness of nanoemitter and the emission lifetime.

As the grafted layer becomes thicker, the lifetime of the QDs-Au nanostrip nanoemitter

also increases, owing to the greater distance between the QDs and the Au nanostrip. This positive correlation confirms the presence of the plasmonic effect in the emission behavior of the fabricated QDs-Au nanostrip nanoemitter. Furthermore, since the thickness can be controlled during fabrication, the lifetime of this kind of nanodevice can be adjusted from approximately 2.5 ns to 3.4 ns.

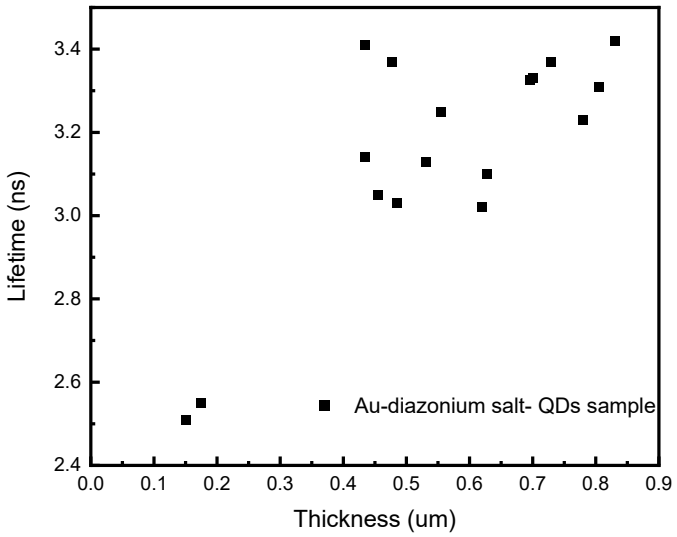

Figure 4-16. The scatter plot of thickness and lifetime for each QDs-Au nanostrip nanoemitter. Thickness and lifetime are in positive correlation with the P-value of 0.0002.

4.3.3 Discussion on the influence of Au nanostrip and grafted diazonium layer on PL emission

After measuring and comparing the PL and TRPL data with the size of the nanoemitter (i.e. its thickness), the function of each component of the QDs-Au nanostrip nanoemitter was further examined, as QDs, the grafted diazonium salt, and Au nanostrip.

As the Figure 4-16 shows, for big distance (0.9 μm), it could be expecting a lifetime close to the lifetime at the ITO glass. However, it is still very weak compared to this reference. Actually, it seems that the presence of the diazonium layer is one of the origins of lifetime decrease. Also, as we discussed in Chapter 2 (section 2.4.1), the lifetime of QDs emission decreased with the presence of the DCOOH functionalization layer on ITO surface. It indicates there are multi-carriers existing inside QDs. Considering the sample structure, there should be carriers transfer between DCOOH functionalization layer and QDs.

For assessing the role of the Au nanostrip and grafted diazonium salt, we measured the TRPL data with and without the Au nanostrip, or grafted diazonium salt, as shown in Figure 4-17. This figure indicates that the PL emission lifetime of the QDs spread on ITO glass is 18.45 ns. In contrast, the PL emission lifetime of the fabricated QDs-Au nanostrip nanoemitter, labeled “QDs-diazonium salt-Au nanostrip” in the figure, is 3.13 ns. The QDs-diazonium salt structure, using the same QDs deposition method, shows a lifetime of 3.58 ns. These results confirm the findings from Chapter 2 (section 2.4.1), indicating that the present of grafted diazonium salt layer reduces the lifetime of QDs’ PL emission. Furthermore, integrating the Au nanostrip into the nanostructure leads to an additional 14.3% decrease in lifetime.

Since the PL emission of QDs is attributed to carrier recombination, both the grafted

diazonium salt layer and the Au nanostrip can increase the carrier concentration within the QDs, resulting in a shorter lifetime. In particular, the additional 14.3% decrease in lifetime can be attributed to the Purcell effect, which makes the de-excitation rate (i.e. the inverse of lifetime) proportional to the local density of state of the Au plasmonic nanostructure.[29] For the role of grafted diazonium layer, the only conclusion got yet is it could allow carrier transfer, and contribute to the QDs lifetime decrease. More conclusions need further research.

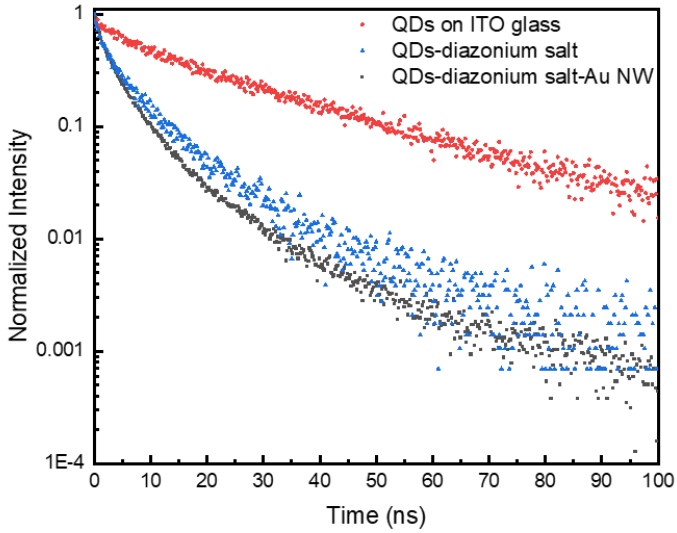

Figure 4-17. TRPL of spread QDs on ITO glass (τ_{QDs} = 18.45 ns), QDs-diazonium salt structure ($\tau_{DS\text{-}QDs}$ = 3.58 ns) and QDs-diazonium salt-Au nanostrip structure ($\tau_{Au\text{-}DS\text{-}QDs}$ = 3.13 ns).

In addition to the effects of the Au nanostrip and the grafted diazonium salt layer on the PL emission from QDs, we also examined how the Au nanostrip impacts the PL emission from the grafted diazonium salt layer itself, i.e. that PL background described in section 2.3.2 of chapter 2. To assess this influence, we selected "diazonium salt" and "diazonium salt-Au nanostrip" samples with similar dimensions, as shown in Figure 4-18. A white round frame marks the boundary. The "diazonium salt" structure, illustrated in Figure 4-18a, has an elliptical shape corresponding to the laser spot, with a long axis of 3.94 μm and a short axis of 2.08 μm, resulting in an area of 6.44 μm². The "diazonium salt-Au nanostrip" structure, shown in Figure 4-18b, is round with a diameter of 2.8 μm, yielding an area of 6.16 μm².

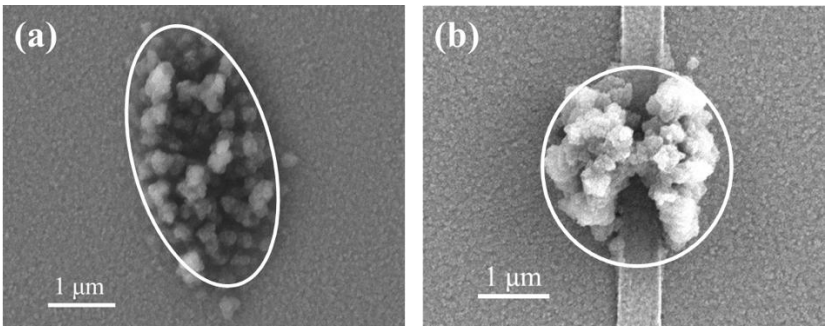

Figure 4-18. The SEM images of (a) "diazonium salt" structure and (b) diazonium salt-Au nanostrip" structure.

As Figure 4-19 shown, the lifetime of the isolated grafted diazonium salt layer is 0.42 ns. But after integrating the Au nanostrip, this lifetime decreases to 0.29 ns. This indicates that the present of Au nanostrip also reduces the PL emission lifetime of the grafted diazonium salt

layer through the Purcell effect. This observation could be also attributed to the carrier transport properties of the grafted diazonium salt layer, because the Au nanostrip could influence the PL emission. But for the conductivity of grafted diazonium lay, more research is needed to support further conclusion.

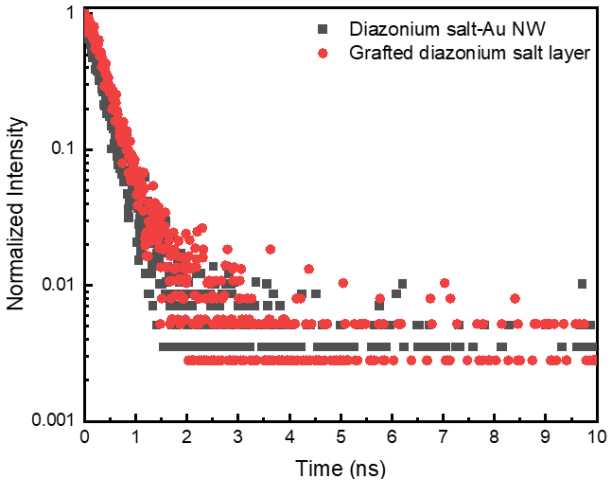

Figure 4-19. The TRPL spectra of grafted diazonium salt layer (τ_{DS} = 0.42 ns) and diazonium salt-Au nanostrip structure ($\tau_{Au\text{-}DS}$ = 0.29 ns).

4.4 The morphology and optical properties of QDs-Ag NW nanoemitter

While large thicknesses of the grafted diazonium layer are easy to observe (e.g Fig. 4-18b), the rough edges of the Au nanostrip produced by EBL, make it difficult to accurately measure the small thicknesses of the grafted diazonium salt layer. As shown in Figure 4-20, the parameters are set as 0.0468 mW/um^2 and 10 s. It is challenging to determine whether the shadow part next to the Au nanostrip is caused by the grafted diazonium salt layer or the rough edges themselves.

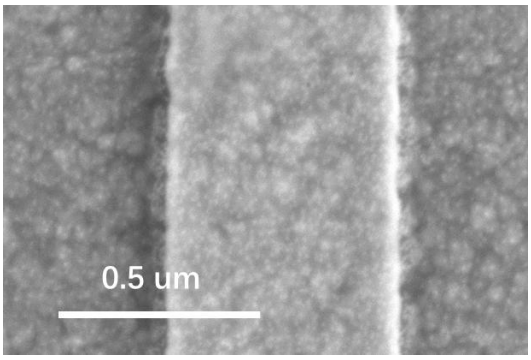

Figure 4-20. The SEM image of Au nanostrip after diazonium salt grafting process. The shadow next to the Au nanostrip is difficult to distinguish.

To achieve nanoscale surface functionalization, chemically synthesized Ag NWs were preferentially chosen as the base material because the commercial product is easier to purchase with small diameter. As shown in Figure 4-21, the Ag NW has a width of 70 nm and a length

often exceeding 50 μm, allowing it to be considered a one-dimensional plasmonic source with two kinds of plasmonic modes-: a localized mode perpendicular to the wire, a delocalized propagating SPP. When the polarization direction of the excited light is perpendicular to the long axis of the Ag NW, the enhanced electromagnetic field becomes concentrated at the NW's edges. The corresponding numerical simulation will be presented in this section. The 70 nm NW's diameter enables the integration of grafted layers at the nanoscale.

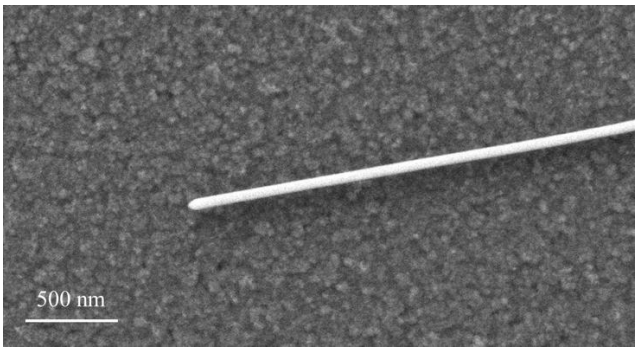

Figure 4-21. SEM image of the extremity of Ag NW deposited on ITO glass

Following surface functionalization with diazonium salt, the grafted layer forms along the Ag NW, as depicted in Figure 4-22. In contrast to the results observed with Au nanostrips, where the grafted layer mainly covers the sides, the layer on the Ag NW envelops both the top and sides, resulting in an indistinct boundary between the Ag NW and the grafted layer. The shape of QDs-Ag NW nanoemitter will be further discussed in section 4.4.1 and section 4.4.2 with simulation and AFM data.

The thickness of the grafted layer is quantified from SEMs images with the top view of the nanostructure. Comparisons between the thickness and the height of the grafted layer on Ag NW, derived from SEM and AFM data, show that the thickness is smaller than the height. After the adsorption of QDs, the thickness can be regarded as the shortest distance between the adsorbed QDs and the plasmonic NW.

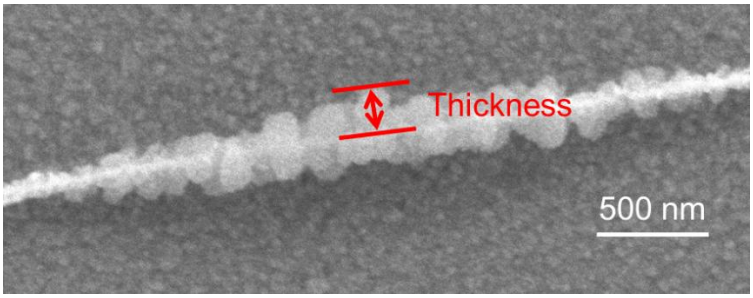

Figure 4-22. The schematic of "thickness" concept of grafted layer on surface functionalized Ag NW.

In this section, we demonstrate the possibility to selectively adsorb QDs on Ag NW through plasmon-induced polymerization of diazonium salts. The surface-grafted polyaryl layers follow the distribution of plasmonic enhanced electromagnetic field and enable the site-selective immobilization of QDs on Ag NW via electrostatic interactions. The resulting plasmonic hybrid nanoemitter enables remote excitation, making it a promising candidate for integrated photonics applications. For the QDs-Ag NW nanoemitter, the plasmonic enhancement of PL intensity and decrease in the PL lifetime were observed. PL properties can be controlled by the parameters of diazonium salt surface functionalization process, showing

a strong positive correlation. Moreover, the hybrid nanoemitter exhibits powerful SPPs-mediated remote excitation, which can be instantly switched off by altering the excitation polarization direction.

4.4.1 The morphology of QDs-Ag NW nanoemitter

To perform surface functionalization of diazonium salt on Ag NWs, procedure described in section 4.2.2 was followed. The Ag NWs were first dispersed onto a 15 mm * 15 mm ITO glass substrate with a 135 nm-thick ITO layer and the diazonium salt solution was deposited on the sample. A 532 nm laser illuminated the substrate from below, with its polarization aligned to the short axis of the Ag NW. The SEM images surface functionalization made with different illumination times T are shown in Figure 4-23. The exposure time used for plasmon-assisted surface functionalization with diazonium salts was (a) 10 s, (b) 20 s, (c) 40 s, (d) 60 s, (e) 120 s and (f) 180 s, with a fixed light power density of 0.0468 mW/μm^2. The resulting polyaryl layer thickness varied from 0.118 μm (T=10 s) to 2.504 μm (T=180 s). At the exposure time of 10 s, the functionalized layer primarily grafted along the Ag NW mainly at the NW's edges. As the exposure time increased, the grafted layer grew thicker in both horizontal and vertical dimensions. The overall shape of the layer resembled multiple spheres with diameters ranging from 20 nm to 200 nm. The origin of these sphere-shape polymerized material is not clear now. The size of these spheres increased with longer exposure times. Furthermore, when the exposure time exceeded 60 s, as illustrated in Figures 4-23e-f, surface functionalization also began to occur on the ITO surface adjacent to the Ag NW, with an interference structure expanding as the exposure time increased. Moreover, in the vicinity of Ag NW, the surface functionalization layer grew towards vertical direction over the horizontal surface as the exposure continued.

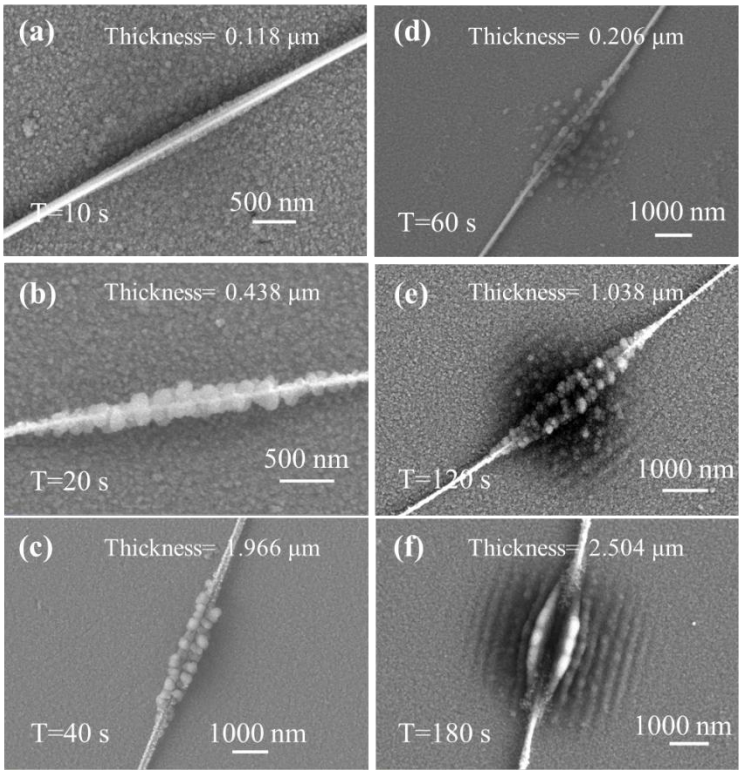

Figure 4-23. The SEM images of diazonium salt surface functionalization on Ag NWs. The exposure times were adjusted as (a) 10 s, (b) 20 s, (c) 40 s, (d) 60 s, (e) 120 s and (f) 180 s.

The thicknesses vary from 0.118 μm to 2.504 μm.

To illustrate the expected surface functionalization layer morphology formed under irradiation of the AgNW, the electromagnetic field distribution used for functionalization was simulated using FDTD method (Figure 4-24). The diameter of Ag NW was set at 70 nm, and the length was set as 3 μm, allowing us to treat it as effectively infinite relative to its diameter. To match the conditions used in the experiments, the illumination wavelength was set at 532 nm (laser spot diameter = 1 mm) and the polarization direction was parallel to the short axis. The refractive index of the surrounding environment was set at 1.33, corresponding to 2 mM DCOOH aqueous solution.

Figure 4-24a shows the electromagnetic field distribution (linear scale) in the X-Y plane (the ITO glass surface plane). The insert image indicates the field distribution at the vicinity of Ag NW within illumination center. The plasmonic enhanced field is concentrated near the Ag NW on both NW's edges. The two lobes are characteristic of a near-field dipole emission parallel to incident field, in keeping with the resulting functionalization distribution observed in Fig. 4-23a and the AFM cross section that will be shown in Figure 4-28b. The spatial extension along the long axis is linked to the size of the laser spot, while it is limited along the short axis by plasmonic near-field confinement and its evanescent nature. These spatial extensions determine the shape of the surface functionalization layer formed.

Figure 4-24b displays the distribution with an exponential scale bar. In the X direction, perpendicular to the NW, an interference pattern is observed, which is not clear with linear scale bar. It suggests that, under high laser power, the surface functionalization may occur on the ITO surface adjacent to the Ag NW with an interference structure, which corresponds to the experimental results shown in Figure 4-23. The interference may occur from the incident field and the field scattered by the NW. And the resulted composite light field induces the grafted diazonium salt layer on Ag NW.

The fact that functionalization takes place on the substrate at a distance from the NW raises the question of the process involved. A priori, charges excited by light can participate in the reduction of the diazonium salt. The involved charge density is linked to the electromagnetic field (as calculated in Fig. 4-24) through Maxwell's equations and, in particular, the Maxwell's Gauss equation. At the surface of the NW, these charges are the free charges in the conduction band (Fermi Sea) which resonates with the light. On the ITO surface, at a distance from the NW, the charges involved could be those of the ITO. However, similar functionalization has been reported on glass without ITO (i.e. without free charges),[30] where self-organized interference patterns were formed, resulting from the coupling between the incident and scattered beams on the sample surface. The scattering of the incident beam generated a ripple-like interference pattern with alternating high and low intensity regions. Extended irradiation time led to a more pronounced formation of these periodic structures, consistent with our observations in Fig. 4-23f. Since the polyaryl interference patterns extend far beyond the NW surface, a hot-electron-mediated reduction of diazonium salts from the NW is unlikely in these distant regions. Instead, the presence of these interference patterns could be attributed to the direct photoactivation of diazonium salts, as reported recently.[31] Understanding these processes remains a topical area of research,[30] and the platform proposed in this article could, in the future, eventually provide answers to chemical surface functionalization questions involving diazonium salts.

Figures 4-24c and 4-24d present the electromagnetic field distribution in the X-Z plane (perpendicular to the ITO glass surface place) with linear and exponential scale bars, respectively. The white dash line represents the surface of the substrate on the images. The X-Z cross section of the NW looks oval along Z because of the different scales used for the X and Z axes. The insert image also indicates the field distribution at the close vicinity of Ag NW. The enhancement of the electromagnetic field is significant in the Z direction, featuring two lobes on both sides. The fabricated surface functionalization layers are thus expected to align along the two sides, with lobes appearing above the horizontal plane of the Ag NW. Additionally, there is a hot spot located above the Ag NW at the X=0 position, indicating that surface functionalization layer will also form on the top of the Ag NW, as well as along the sides. The features, concentration at the vicinity, growing towards Z direction and interference structure on ITO surface, are consistent with the experimental results presented before.

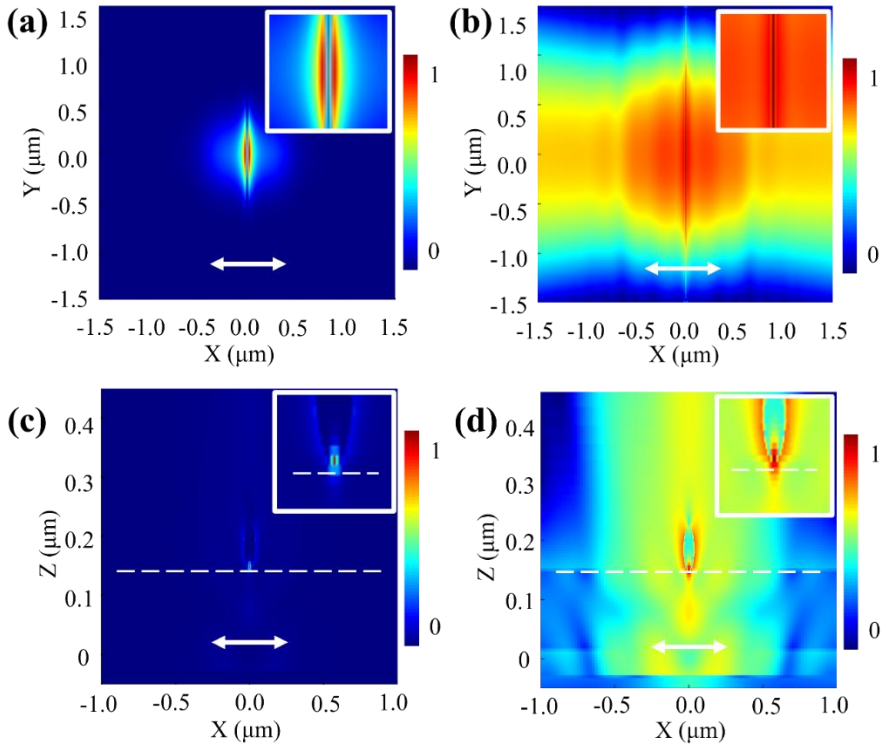

Figure 4-24. FDTD simulation. Under Gaussian light exciting Ag NW, electromagnetic field distribution at 532 nm wavelength in the X-Y plane with (a) linear scale bar and (b) exponential scale bar. The electromagnetic field distribution in X-Z plane with (c) linear scale bar and (d) exponential scale bar. The white arrow represents the direction of the incident polarization.

In addition to the previous results, we adjusted the laser energy density from 0.0468 mW/μm² to 0.468 mW/μm² and varied the exposure time from 10 s to 180 s. A total of 32 hybrid structures were fabricated using similar procedures. The grafted thicknesses as a function of the exposure light energy densities were statistically analyzed, with the results presented in Figure 4-25. The analysis revealed a positive correlation between exposure light energy density and thickness, with a correlation p-value of $1.37865*10^{-12}$ and Pearson correlation factor of 0.8866. This indicates that the resulting thickness can be controlled by adjusting the exposure light energy density.

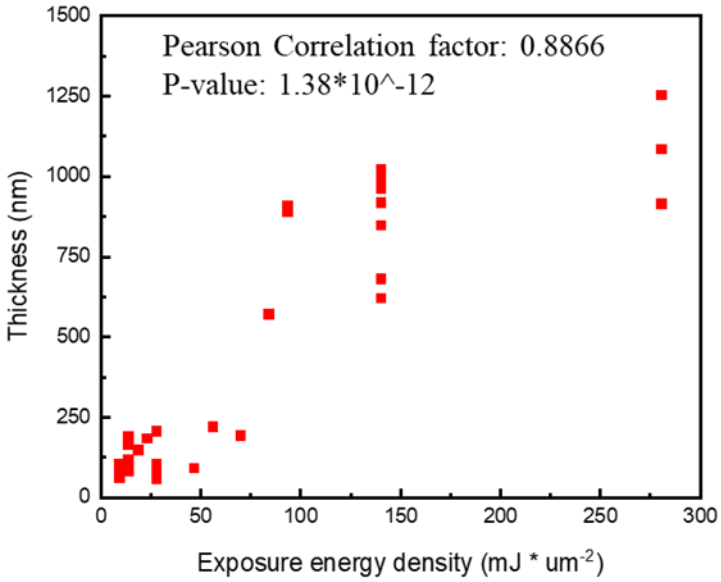

Figure 4-25. The relationship between the size of hybrid structure and laser exposure energy density. The Pearson correlation factor is 0.88658.

4.4.2 The PL emission from QDs-Ag NW nanoemitter

After surface functionalization of the Ag NW with diazonium salt, a QDs solution was deposited on the fabricated nanostructure. After a 30-minute incubation, the excess solution was removed by rinsing. The ligand-exchanged QDs were expected to adsorb onto the surface functionalization area through electrostatic interactions.

Figure 4-26a displays the PL spectrum from the hybrid nanostructures following QDs deposition, with the peak position at 617.9 nm, similar to the PL emission of the colloidal QDs solution discussed in Chapter 2. Figure 4-26b provides a statistical analysis of the emission peak positions from 130 QDs-Ag NW nanoemitter samples, revealing an average peak position of 617.58 ± 2.12 nm. This result confirms that the PL emission of the QDs remained consistent throughout the fabrication process.

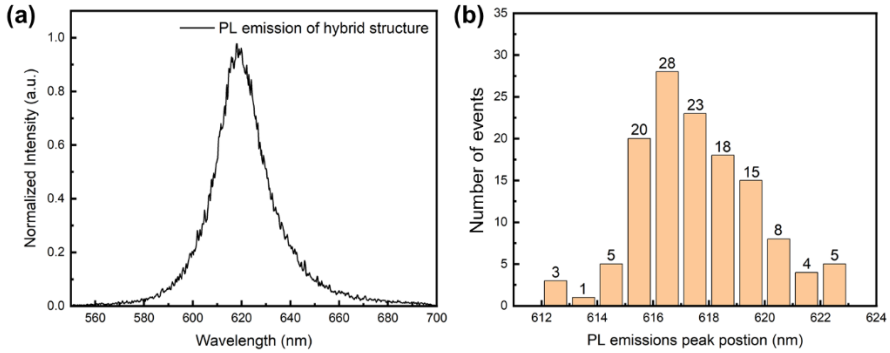

Figure 4-26. (a) PL emission of hybrid nanostructure. Peak position: 617.9 nm. (b) Statistical histogram of PL emission peak position of 130 hybrid nanoemitters.

Figure 4-27 presents the PL spectra from the nanostructure before and after the QDs deposition step. The AFM images and cross section profile are shown in Figures 4-27a and 4-27b respectively, revealing a height of 257 nm. The cross section displays two height peaks, which confirm the two lobes observed in the simulation results from Figure 4-24a. The SEM image is depicted in Figure 4-27c, indicating that the thickness of this nanostructure is 91 nm.

In Figure 4-27d, the PL intensity before QDs deposition is observed to be around 40-70, without any significant peaks, resembling the broad band grafted layer's PL background spectrum discussed in Chapter 2. However, after QDs deposition, the PL spectrum shown in Figure 4-27e reveals a prominent peak with an intensity of approximately 15,000. The substantial difference in the PL spectra confirms that the source of PL emission in this nanoemitter is the QDs, rather than other components.

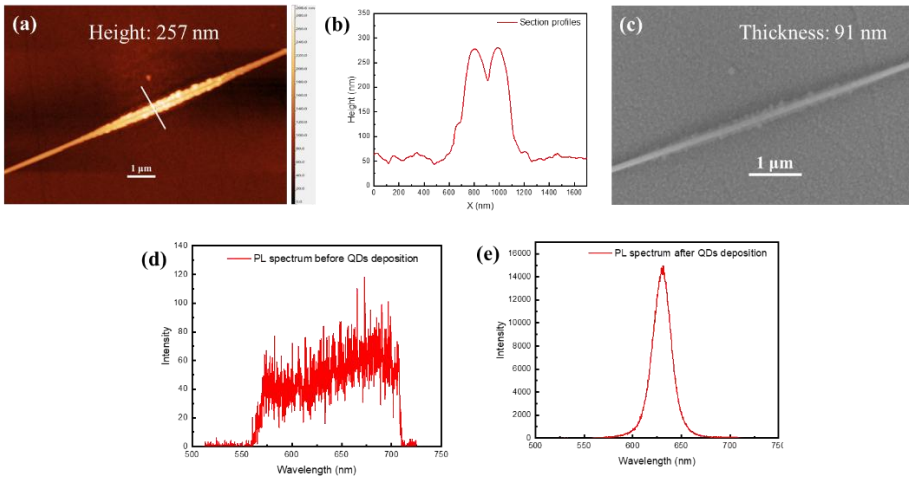

Figure 4-27. (a) and (b) the AFM and section profile, height: 231 nm. (c) the SEM image, thickness: 91 nm. (d) PL spectrum before QDs deposition: no peak position. (e) PL spectrum after QDs deposition: peak intensity ~15000.

4.4.3 Evidence of QDs adsorption by electrostatic interaction

Besides the morphology of the hybrid system and the PL properties, the electrostatic adsorption process of QDs was investigated. Similar to the studies in Chapters 2 and 3, the electrostatic adsorption of QDs was investigated using two types of diazonium salt: DCOOH and DNO_2. The chemical structures and properties of both compounds have been described previously. The DNO_2 diazonium salt was used to fabricate the nanoemitter following the same procedures as for the DCOOH diazonium salt.

The morphology of fabricated QDs-DCOOH-Ag NW and QDs-DNO_2-Ag NW nanoemitters was analyzed using SEM and AFM, as shown in Figure 4-28. The AFM image and section profile for the QDs-DCOOH-Ag NW nanoemitter are shown in Figures 4-28a, indicating a height of 231 nm. The polyaryl in-plane thickness, measured from the SEM image in Figure 4-28b, is 136 nm. In contrast, the QDs-DNO_2-Ag NW nanoemitter exhibits a height of 307 nm, as measured from the AFM image and section profile in Figures 4-28d. The polyaryl in-plane thickness for this sample, measured from the SEM image in Figure 4-28e, is 126 nm. With similar height and thickness, the two types of nanoemitters have comparable surface areas for QDs adsorption.

The PL spectrum of the QDs-DCOOH-Ag NW nanoemitter is presented in Figure 4-28c, showing a peak intensity of 13235. For the QDs-DNO_2-Ag NW nanoemitter, the maximum PL intensity is approximately 255, as shown in Figure 4-28f, which is 51.9 times lower than that of the DCOOH-based nanoemitter. The PL decrease in the case of DNO_2 can be associated to a lower number of QDs adsorbed on the Ag NW. This finding is in agreement with the presence of electrostatic adsorption in the QDs-DCOOH-Ag NW nanoemitter, compared to

only weak possible van der Waals interaction in the QDs-DNO_2-Ag NW system.

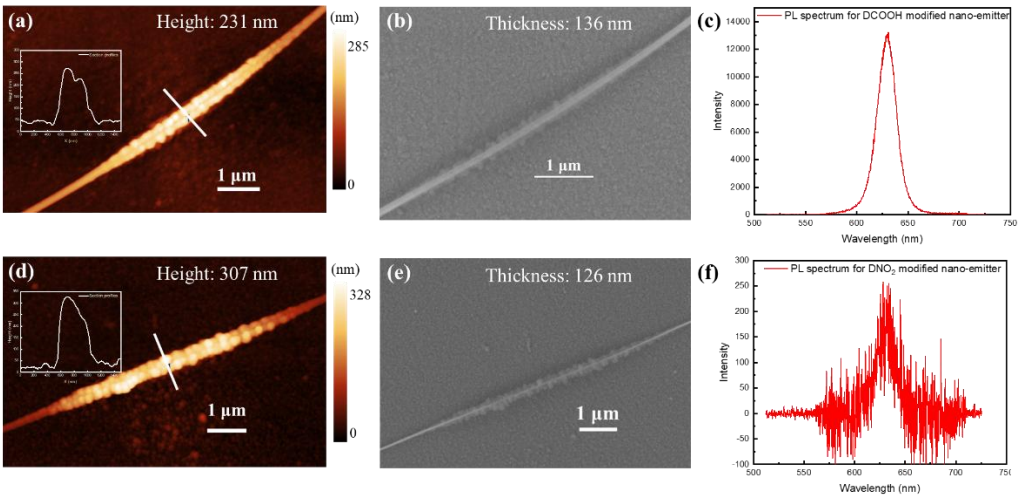

Figure 4-28. The comparison between two kinds of nanoemitter. (a-c). QDs-DCOOH -Ag NW nanoemitter. (a) AFM and cross section, height: 231 nm. (b) SEM image, thickness: 136 nm. (c) PL spectrum. PL intensity ~ 13235. (d-f) QDs-DNO_2 -Ag NW nanoemitter. (d) The AFM and section profile, height: 307 nm. (e) The SEM image, thickness: 126 nm. (f) The PL spectrum. PL intensity ~ 255 (51.9 times decrease).

4.4.4 Plasmonic enhancement of Ag NW in nanoemitter

To evaluate the plasmonic enhancement effect of Ag NW in the fabricated nanoemitter, as a reference nanostructure, a QDs-DCOOH diazonium salt nanostructure was created by removing the Ag NW from the QDs-Ag NW nanoemitter, while retaining the surface functionalization layer. To facilitate the removal of the Ag NW, we employed an oxidation and acid substitution treatment on the fabricated QDs-Ag NW nanoemitter. The Ag NWs were effectively removed by the oxidation process using a 30% H_2O_2 solution, which generates O_2, through immersion. Besides the removal of Ag NWs during the oxidation treatment, QDs' ligands are expected to detach from the core/shell structure. Nevertheless, the cysteamine ligands may still bond to the DCOOH diazonium salt functionalized surface by electrostatic interaction. To remove the remaining ligands, acid substitution treatment with 0.1 mM HCl solution was applied. Then, the QDs solution was deposited for the second time and adsorbed again to fabricate QDs-DCOOH diazonium salt nanostructures without Ag. After the treatment with 30% H_2O_2 solution and 0.1 mM HCl solution, the adsorbed QDs and ligands in the first deposition were supposed to be removed. With the same deposition procedure, the adsorbed QDs number after second deposition is supposed to be same as first time.

Figures 4-29a and 4-29b displays the SEM image of QDs-DCOOH-Ag NW nanoemitter, before and after Ag NW dissolution respectively after 10 minutes of treatment. As shown in Figure 4-29b, the Ag NW begins to be oxidized, although part of it remain protected by the grafted diazonium salt layer. Figure 4-29c displays the SEM image of QDs-DCOOH nanostructure after completed removal of the Ag NW (30 minute-treatment). The thickness is measured as 185 nm. For comparison, the thickness of QDs-DCOOH-Ag NW nanoemitter was measured as 183 nm. The consistent thickness confirms that the surface functionalization layer remained unaffected during oxidation and acid substitution.

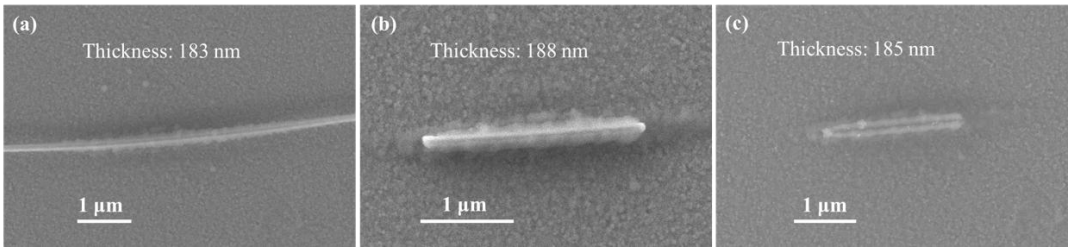

Figure 4-29. SEM images of one QDs-Ag NW in accelerate oxidation treatment, when the oxidation time is (a) 0 min, (b) 10 mins and (c) 30 mins. Ag NW disappeared in the end, while the grafted diazonium salt layer remains.

The EDS data of QDs-diazonium salt nanostructure without Ag NW is provided in Figure 4-30. The mass percentage of Ag is 0.21±0.13%, which is very low. As the elements mapping image shown in Figure 4-30c, the distribution shape is similar to the grafted diazonium salt layer. However, as the elements mapping image of Ag shown in Figure 4-30e, the distribution is uniform on the surface. For the measured elements, 1) O and Si are contributed from glass, 2) In and Sn are contributed from ITO layer, 3) C and N are contributed from diazonium salt, 4) Ag is contributed from Ag NW, 5) Cd and Se are contributed from CdSe/ZnSe QDs.

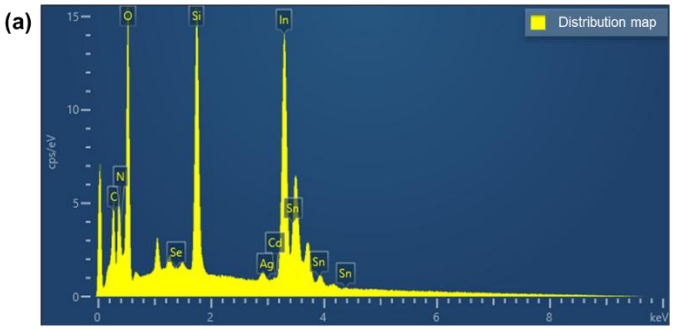

(b)

Elements	Wt%	Wt% Sigma
C	3.26	0.14
N	2.03	0.32
O	21.00	0.20
Si	11.07	0.10
Se	0.00	0.08
Ag	0.21	0.13
Cd	0.63	0.20
In	56.98	0.35
Sn	4.82	0.27
Total	100.00	

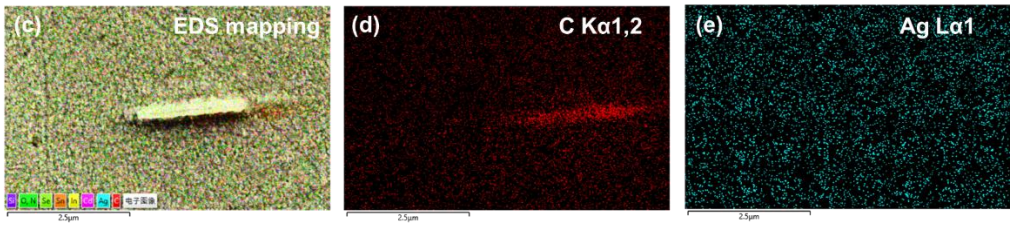

Figure 4-30. (a) The distribution map. (b) The mass percentages of C, N, O, Si, Se, Ag, Cd, In and Sn elements. (c) The elements mapping image of C, N, O, Si, Se, Ag, Cd, In and Sn. (d) The elements mapping image of C. (d) The elements mapping image of Ag.

After the second deposition of QDs solution to fabricate the QDs-DCOOH nanostructure, the PL and TRPL of the QDs-DCOOH nanostructure were measured and compared with the spectra of QDs-DCOOH-Ag NW nanoemitters. Figure 4-31a and 4-31c compares the PL spectra. Both of the maximum PL intensities are located at 631 nm, which is the same as the original colloidal QDs solution. The maximum PL intensity of QDs-DCOOH-Ag NW nanoemitters is 21277, while it is 4864 for QDs-DCOOH nanostructure. The integration times for both spectra were kept as 5s. There is a 4.37-time decrease on PL intensity after the Ag NW was removed. The TRPL spectra were compared in Figure 4-31b and 4-31d. The lifetime of QDs-DCOOH-Ag NW nanoemitters is 0.545 ns, and it is 4.32 ns for QDs-DCOOH nanostructure. The lifetime increases 7.93 times after the Ag NW was removed.

The comparison of PL intensity and lifetime confirms the presence of plasmonic effect

from the Ag NW in the fabricated nanoemitter. With the in-situ removal of the Ag NW, other components, including the QDs, grafted layer, and ITO substrate, retained their shapes and positions in both nanostructures. Based on the comparison, the Purcell factor of this nanostructure is assessed as 7.93 while the PL enhancement factor 4.37.

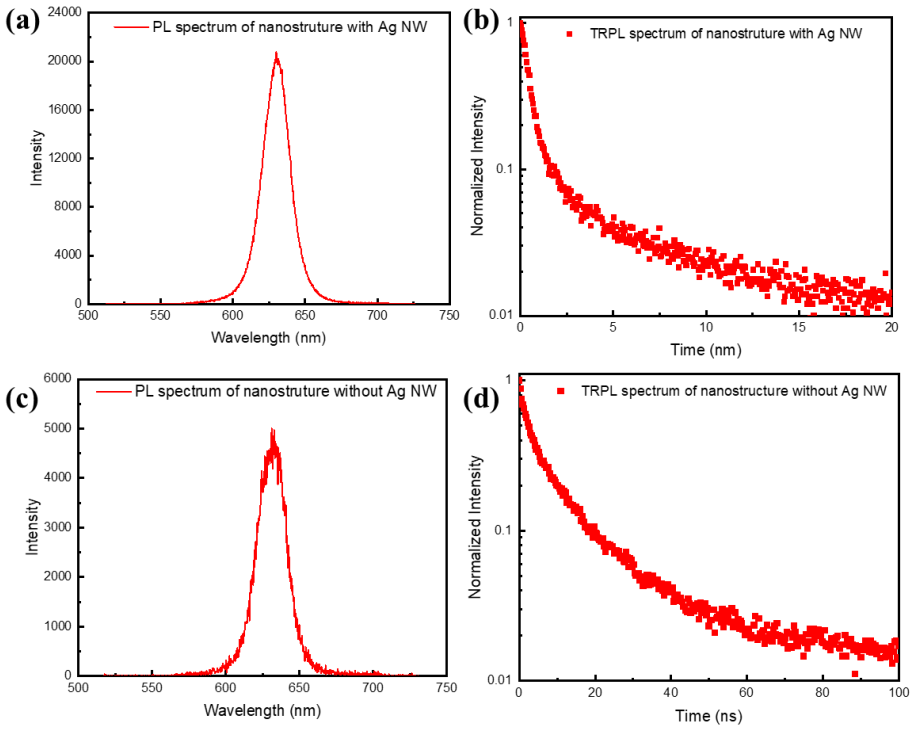

Figure 4-31. The (a) PL and (b) TRPL of QDs-DCOOH Ag NW nanoemitter. The PL intensity is 21277, and lifetime is 0.545 ns. The (c) PL and (d) TRPL of QDs-DCOOH nanoemitter. The PL intensity is 4864, and lifetime is 4.32 ns. After the remove of Ag NW from nanoemitter, the PL intensity decreased by a factor of 4.37, and the lifetime increased by a factor of 7.93.

In addition to demonstrating plasmonic enhancement in nanostructures with and without Ag NW, we also adjusted the thickness of the grafted diazonium salt layer to investigate its plasmonic effect in the QDs-DCOOH-Ag NW nanoemitter. For the fabricated QDs-DCOOH-Ag NW nanoemitter, the thickness can be considered as the distance between the Ag NW and the QDs, as well as the plasmonic source and light emitter. This distance represents the working distance of the plasmonic effect.

Figure 4-32 displays the lifetimes of the QDs-DCOOH-Ag NW nanoemitters with different polyaryl thicknesses. The measured lifetimes are also indicated. The polyaryl layer thickness was measured from SEM images. For the six selected samples, a clear correlation can be observed between the polyaryl thicknesses and the corresponding lifetimes: as the polyaryl thickness increased, the lifetime increased from 0.52 ns to 5.44 ns, as a signature of the Purcell effect which is highly sensitive to the emitters-metal surface distance.[21]

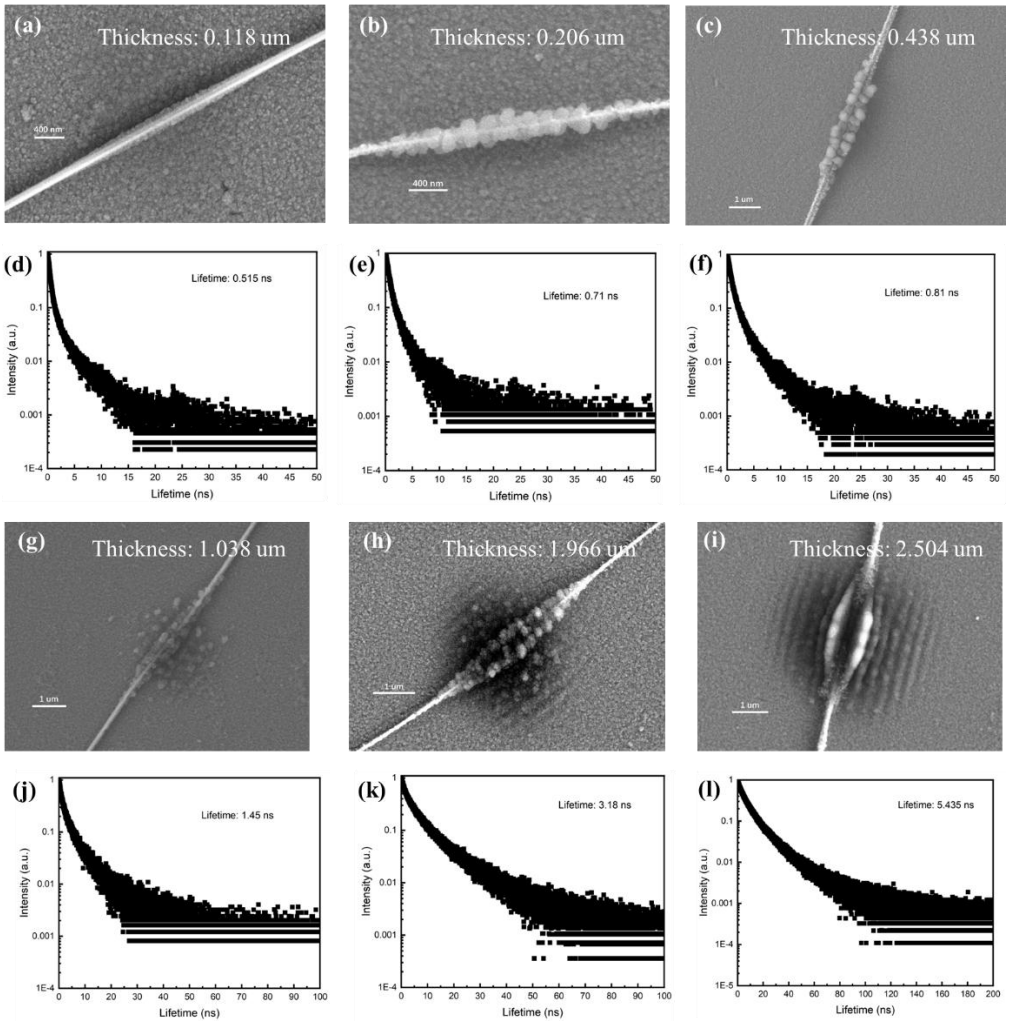

Figure 4-32. The morphologies and lifetimes of QDs-DCOOH-Ag NW nanoemitters with different DCOOH thicknesses. (a)-(c) and (g)-(i) are the SEM images to show the morphologies. (d)-(f) and (j)-(l) are the corresponding TRPL data to show the lifetimes.

To further investigate the relationship between the nanoemitter thicknesses and the corresponding lifetimes, a statistical analysis was performed, as shown in Figure 4-33. A positive correlation was observed with a p-value of $2.00595*10^{-11}$ and Pearson correlation factor of 0.9603. This result implies that, for the fabricated nanoemitters, a thicker thickness results in a longer lifetime. This finding supports the plasmonic effect, where a larger gap between the plasmonic source and the emitter leads to a smaller Purcell factor. Moreover, as shown in Figure 4-25, the thickness can be controlled through adjusting fabrication parameters. Consequently, the PL emission from QDs-DCOOH-Au nanostrip nanoemitter can be adjusted from the fabrication process.

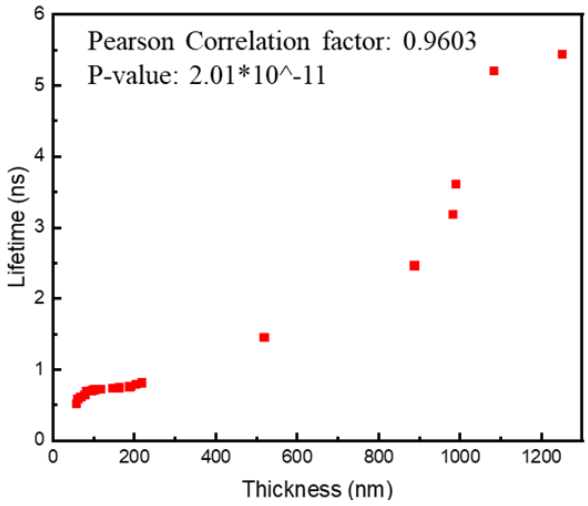

Figure 4-33. The relationship between the thickness of hybrid nanoemitters and corresponding lifetimes. The Pearson correlation factor is 0.96032.

4.4.5 Remote excitation of QDs-Ag NW nanoemitter

As an application, the potential for remote excitation of the hybrid nano-emitter based on NW was then investigated. When the Ag NW is photoexcited, surface plasmon polaritons (SPPs) can be launched and propagate along its interface.[32] As a one-dimensional plasmonic nanomaterial, the Ag NW supports plasmonic excitation with two polarization directions. If the excitation polarization is perpendicular to the NW, lateral localized surface plasmons can be excited (Fig. 4-24). We used this mode for local surface functionalization.

On the other hand, if the polarization of the excitation is aligned with the long axis of the wire, and provided that the incident wave vector in the plane is sufficiently high (possible by scattering from the nanometric end of the wire), a SPP can be launched and propagate over a distance of several micrometers. Utilizing the SPP propagation, we performed a remote excitation of emitters adsorbed to the Ag NW, similar to what had been demonstrated in references.[31]

Figure 4-34a and 4-34b illustrate the two above-evoked kinds of excitation mode on polarization, showing a 2 μm bare Ag NW (we had to find out short NWs) without any modification illuminated by a focused green laser with different polarization directions. The diameter of the used laser spot was less than 1 μm, and the wavelength of 532 nm falls within the plasmonic band. The corresponding scattering spectrum of the Ag NW is presented in Figure 4-12. When the excitation polarization is aligned with the long axis, the SPPs is launched and propagates along the entire length of the Ag NW and light emits at the opposite end by scattering, as shown in Figure 4-34a. The excitation spot is marked with green round, and excitation polarization is marked with green arrow. In contrast, when the polarization direction is perpendicular to the long axis, the propagating SPPs cannot be launched and the excited localized surface plasmons are limited at the excitation spot. As a result, no emission is observed from another end as shown in Figure 4-34b, where the Ag NW was 90° rotated while the excitation polarization was kept the same.

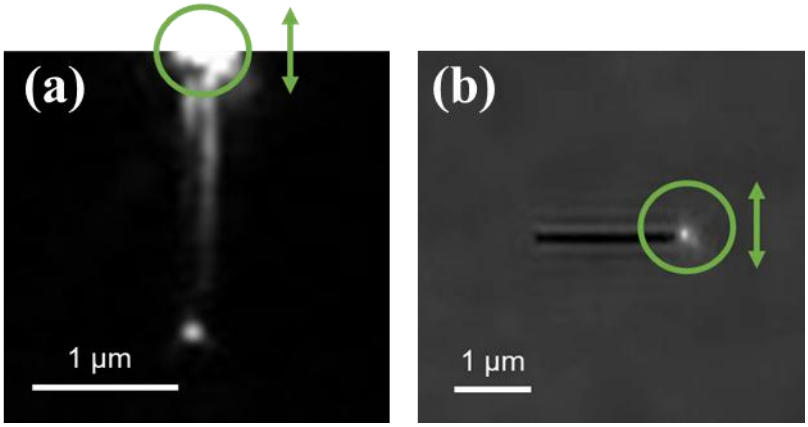

Figure 4-34. (a) The 2 μm Ag NW illuminated by focused 532 nm green laser polarized along the long axis. (b) The 2 μm Ag NW illuminated by focused 532 nm green laser polarized perpendicular to the long axis.

As previous results indicated, when the light excitation polarization aligns with the long axis of the Ag NW, the propagation distance can exceed 2 μm. By utilizing SPP propagation, it becomes possible to excite the QDs from a different position on the Ag NW. Figure 4-35 illustrates the fabricated hybrid nanoemitter used for this study. The SEM image in Figure 4-35a provides an overview of the Ag NW and the QDs-Ag NW nanoemitter, showing a distance of 2.53 μm between the end of the Ag NW and the nanoemitter. Figure 4-35b offers a detailed view of the QDs-Ag NW nanoemitter's morphology as seen in the SEM image, revealing a thickness of 122 nm. The AFM image and corresponding section profile are presented in Figures 4-35c and 4-35d, showing that the height of the QDs-Ag NW nanoemitter is 217 nm. Considering the diameter of the Ag NW is 70 nm, the effective thickness is calculated to be 87 nm, and the effective height is 147 nm. Thus, the shortest distance between the adsorbed QDs and the plasmonic source could be regarded as 87 nm. In fact, the QDs adsorbed area, as well as the grafted diazonium layer, are spread in around 1 μm along the NW. For the application of remote excitation, the spreading of QDs will lead to the different excitation energy of each adsorbed QD, as well as the PL emission. To ignore this difference, we suggest to treat the whole QDs-Ag NW nanoemitter as the sample area to measure the excited PL emission.

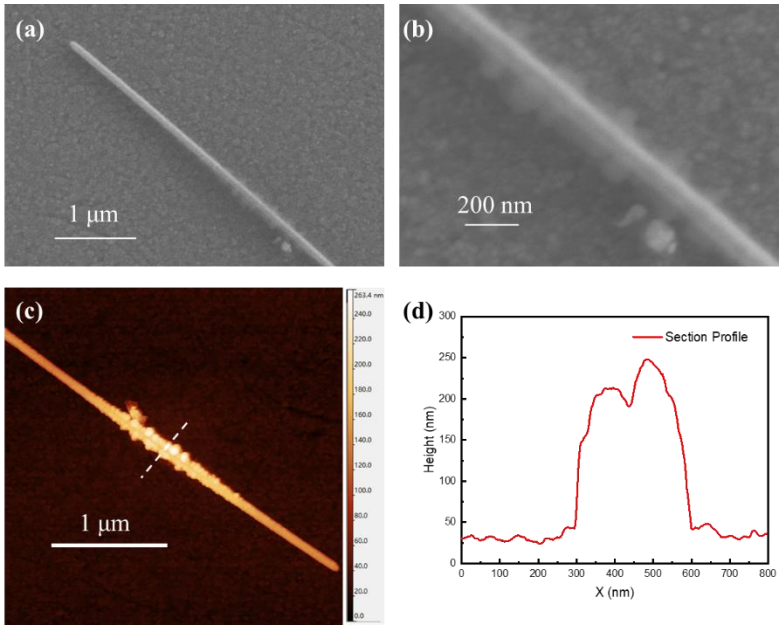

Figure 4-35. The QDs-Ag NW nanoemitter sample used to realize remote excitation. (a) and (b) are the SEM images to show the whole structure and detailed nanoemitter morphology. The thickness is 122 nm. (c) and (d) are the AFM image and cross section. The height is 217 nm. Considering the diameter of the Ag NW is 70 nm, the effective thickness is 87 nm and the effective height is 147 nm.

Figure 4-36a presents the modified SEM image illustrating the remote excitation measurement method. The excitation position A is located at the end of the Ag NW, where a 6.32 mW laser light is used for excitation with the same wavelength and spot size as in Figure 4-34a and 4-34b. Two kinds of laser polarization direction with α and β modes were utilized for the excitation at position A. The detection area with size of 1 μm*1 μm is positioned at the functionalized location where the QDs are attached, which is 2.5 μm far away from the Ag NW end. As a reference, to rule out any scattering from excitation position A, which might also excite the nanoemitter remotely, a comparison was made with excitation position B, which is controlled to maintain the same distance and excitation polarization from the nanoemitter.

Figure 4-36b displays the PL spectra obtained under different excitation conditions, as well as the background spectrum from the detection area, which is measured without any light illumination on sample. When laser excitation is focused on position A, the intensity of the PL emission strongly depends on the polarization direction. A PL emission peak is observed at 633 nm when the polarization aligned with long axis (mode α). In the case of mode β, in which polarization aligned with short axis, the PL spectrum is similar to the background spectrum. However, even though the polarization direction was set as mode α, there is no emission peak on the PL spectrum under excitation in position B. This result proves that the light from position B does not propagate through the distance by substrate or air to reach the nanoemitter area. Moreover, the spectra of position A (mode β) and position B match the obtained PL spectrum of background. Considering the four spectra, two conditions are necessary to perform the remote excitation: i) using Ag NW as the medium for surface wave propagation at 532 nm for remote excitation of the QDs, ii) and aligning the excitation polarization with its long axis to launch the surface wave.

By subtracting the background from the PL spectrum at position A (mode α), the resulting PL spectrum is shown in Figure 4-36c, with a peak at 630 nm, consistent with the local-excited PL emission of the QDs-DCOOH-Ag NW nanoemitter.

These observations confirm that, mediated by SPP propagation, the laser excites the plasmonic nanoemitter from a remote position. By switching the excitation polarization, the remote excitation could be switched "on" and "off". This result illustrates the potential application of the fabricated hybrid structures in advanced integrated photonics.

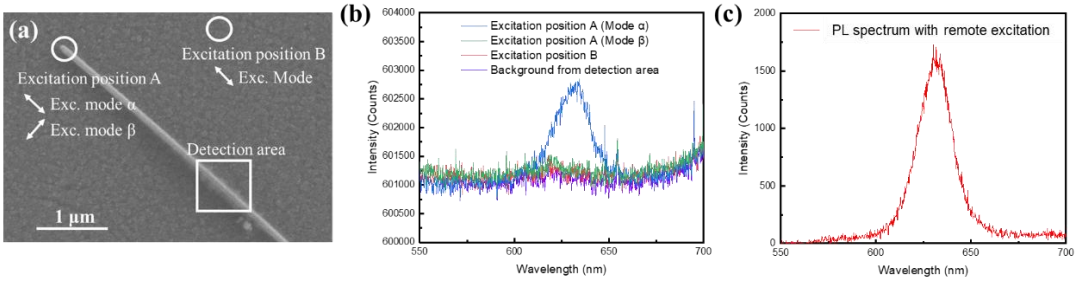

Figure 4-36. (a) The schematic of remote excitation measurement methods. (b) The PL spectra taken with different excitation conditions as well as the background from the detection area. (c) The calculated PL spectrum.

4.5 Summary and conclusions

In this chapter, we explored QDs adsorption on diazonium salt surface functionalization at the nanoscale, resulting in the fabrication of QDs-Au nanostrip and QDs-Ag NW nanoemitters. The morphology of these structures was characterized using SEM and AFM to describe the thickness and height of the grafted layer, and PL and TRPL are measured to evaluate their emission properties.

In the case of the QDs-Au nanostrip nanoemitter, the fabrication progress towards different thicknesses was investigated. The resulted PL peak positions remained consistent with those of the colloidal QDs solution. However, the lifetime of QDs-Au nanostrip decreased by a factor of 5.89 compared to the colloidal QDs solution. A positive correlation was observed between the resulting lifetimes and the structural sizes of the nanoemitters with a p-value of 0.0002. The presence of the Au nanostrip led to a lifetime decrease for the PL emissions from both the QDs and the grafted diazonium salt layer components. The grafted layer behaves like a semiconductor material with low conductivity.

Regarding the fabrication of QDs-Ag NW nanoemitter, QDs were locally adsorbed onto Ag wires, via electrostatic interaction with functional polyaryl layers derived from diazonium salt, previously integrated by plasmon-assisted nanochemistry, resulting in QDs-Ag NW nanoemitters. The electrostatic adsorption of QDs was verified through comparisons between DCOOH and DNO_2 diazonium salt-derived layers. The polyaryl layer thickness showed a positive correlation with exposure energy, evidenced by a Pearson Correlation factor of 0.89. The simulation results of electromagnetic field distribution were in consistent with the morphology of experimental results in the X, Y, and Z directions. The PL peak positions matched those of the colloidal QDs solution. The plasmonic effect from the Ag NW was measured as enhancement in PL intensity and increase in lifetime. A strong positive

correlation was found between the resulting lifetimes and sizes, with a Pearson Correlation factor of 0.96. The fabricated nanoemitter was successfully excited remotely from the end of the Ag NW, at a distance of 2.5 μm.

Our work shows a new approach to fabricate nanoemitter with controlled QDs adsorption. The electrostatic interaction maintains region selection adsorption. Additionally, the QDs adsorbed spots are in accordance with the plasmonic hot spots, which results in plasmonic enhanced PL emission. Significant lifetime decrease was observed due to the plasmonic effects of Au nanostrip and Ag NW, with positive correlations found between lifetimes and nanoemitter sizes. The enhancement factor could be adjusted in the surface functionalization process. This study provides a novel method for plasmonic nanoemitter fabrication. Moreover, the remote excitation shows another method to turn on and off the PL by switching the excitation polarization direction. Also, the excitation capacity of the nanoemitter permits the potential on advanced integrated photonics applications.

Reference

1. Singh, S. *et al.* Enhanced Photoluminescence of Gold Nanoparticle-Quantum Dot Hybrids Confined in Hairy Polymer Nanofibers. *ChemNanoMat* **7**, 831–841 (2021).
2. Huang, Q. *et al.* Enhanced Photoluminescence Property for Quantum Dot-Gold Nanoparticle Hybrid. *Nanoscale Res Lett* **10**, 400 (2015).
3. Chen, M. *et al.* Approaches for Positioning the Active Medium in Hybrid Nanoplasmonics. Focus on Plasmon-Assisted Photopolymerization. *ACS Photonics* **11**, 3933–3953 (2024).
4. Lan, X. *et al.* DNA-enabled chiral gold nanoparticle–chromophore hybrid structure with resonant plasmon–exciton coupling gives unusual and strong circular dichroism. *J. Am. Chem. Soc.* **141**, 19336–19341 (2019).
5. Yeşilyurt, A. T. M. & Huang, J.-S. Emission manipulation by DNA origami-assisted plasmonic nanoantennas. *Adv. Opt. Mater.* **9**, 2100848 (2021).
6. Pelucchi, E. *et al.* The potential and global outlook of integrated photonics for quantum technologies. *Nat. Rev. Phys.* **4**, 194–208 (2022).
7. Hoang, T. B., Akselrod, G. M. & Mikkelsen, M. H. Ultrafast room-temperature single photon emission from quantum dots coupled to plasmonic nanocavities. *Nano Lett.* **16**, 270–275 (2016).
8. Wang, H. *et al.* Two-photon polymerization lithography for optics and photonics: fundamentals, materials, technologies, and applications. *Adv. Funct. Mater.* **33**, 2214211 (2023).
9. Dias, G. O., Lecarme, O., Cordeiro, J., Picard, E. & Peyrade, D. Microscale white light emitters fabricated by two-photon polymerization lithography on functional resist. *Microelectron. Eng.* **257**, 111751 (2022).
10. Couto, F. A. *et al.* Integrating Fluorescent Nanodiamonds into Polymeric Microstructures Fabricated by Two-Photon Polymerization. *Nanomaterials* **13**, 2571 (2023).
11. Kröger, F. *et al.* Two-photon laser printing of 3D multicolor emissive polymer microstructures. *RSC Appl. Polym.* **2**, 847–856 (2024).
12. Ritacco, T. *et al.* Three-Dimensional Photoluminescent Crypto-Images Doped with (CdSe)ZnS Quantum Dots by One-Photon and Two-Photon Polymerization. *ACS Appl. Nano Mater.* **4**, 6916–6927 (2021).
13. Pathak, A. K. *et al.* Surface-Functionalization of Oleate-Capped Nano-Emitters for Stable Dispersion in 3D-Printable Polymers. *Adv. Funct. Mater.* 2412064 (2024) doi:10.1002/adfm.202412064.
14. Deeb, C. *et al.* Plasmon-based free-radical photopolymerization: effect of diffusion on nanolithography processes. *J. Am. Chem. Soc.* **133**, 10535–10542 (2011).
15. Zhou, X. *et al.* Two-Color Single Hybrid Plasmonic Nanoemitters with Real Time Switchable Dominant Emission Wavelength. *Nano Lett.* **15**, 7458–7466 (2015).
16. Broussier, A. *et al.* Hybrid plasmonic nanosystem with controlled position of nanoemitters. *Appl. Phys. Lett.* **114**, (2019).
17. Ge, D. *et al.* Hybrid plasmonic nano-emitters with controlled single quantum emitter positioning on the local excitation field. *Nat. Commun.* **11**, 3414 (2020).

18. Hetemi, D., Noël, V. & Pinson, J. Grafting of Diazonium Salts on Surfaces: Application to Biosensors. *Biosensors* **10**, (2020).
19. Gautier, C., López, I. & Breton, T. A post-functionalization toolbox for diazonium (electro)-grafted surfaces: review of the coupling methods. *Mater. Adv.* **2**, 2773–2810 (2021).
20. Smołka, S. & Krukiewicz, K. Catalyst Design through Grafting of Diazonium Salts—A Critical Review on Catalyst Stability. *Int. J. Mol. Sci.* **24**, 12575 (2023).
21. Ahmad, A. A. L. *et al.* Conceptual Developments of Aryldiazonium Salts as Modifiers for Gold Colloids and Surfaces. *Langmuir* **37**, 8897–8907 (2021).
22. Hatridge, T. A., Liu, W., Yoo, C.-J., Davies, H. M. L. & Jones, C. W. Optimized Immobilization Strategy for Dirhodium(II) Carboxylate Catalysts for C−H Functionalization and Their Implementation in a Packed Bed Flow Reactor. *Angew. Chem. Int. Ed.* **59**, 19525–19531 (2020).
23. Flavel, B. S., Gross, A. J., Garrett, D. J., Nock, V. & Downard, A. J. A Simple Approach to Patterned Protein Immobilization on Silicon via Electrografting from Diazonium Salt Solutions. *ACS Appl. Mater. Interfaces* **2**, 1184–1190 (2010).
24. Yates, N. D. *et al.* Aldehyde-Mediated Protein-to-Surface Tethering via Controlled Diazonium Electrode Functionalization Using Protected Hydroxylamines. *Langmuir* **36**, 5654–5664 (2020).
25. Meng, X., O'Hare, D. & Ladame, S. Surface immobilization strategies for the development of electrochemical nucleic acid sensors. *Biosens. Bioelectron.* **237**, 115440 (2023).
26. Wang, D., Hartz, W. F. & Moloney, M. G. Surface modified materials for active capture of enzymes. *J. Mater. Chem. B* **11**, 2377–2388 (2023).
27. Kherbouche, I. *et al.* Extending nanoscale patterning with multipolar surface plasmon resonances. *Nanoscale* **13**, 11051–11057 (2021).
28. Tijunelyte, I. *et al.* Multi-functionalization of lithographically designed gold nanodisks by plasmon-mediated reduction of aryl diazonium salts. *Nanoscale Horiz.* **3**, 53–57 (2018).
29. Castanié, E. *et al.* Distance dependence of the local density of states in the near field of a disordered plasmonic film. *Opt. Lett.* **37**, 3006–3008 (2012).
30. Therien, D. A. B., Ćulum, N. M., McRae, D. M., Mazaheri, L. & Lagugné-Labarthet, F. Single-beam inscription of plasmon-induced surface gratings. *Opt. Mater.* **112**, 110775 (2021).
31. Maillot, B., Johnson, M., Audibert, J.-F., Miomandre, F. & Brasiliense, V. Operando surface optical nanometrology reveals diazonium salts' visible photografting mechanism. *Nanoscale* **15**, 8754–8761 (2023).
32. Broussier, A. *et al.* Unidirectional frequency conversion of surface plasmon polaritons on metal nanowires. *Micro Nano Eng.* **19**, 100193 (2023).

Chapter 5 Conclusion

This thesis presents the contribution on the fabrication of hybrid nanoemitters with the help of surface functionalization of diazonium salt molecule. The work of hybrid nanoemitter is mainly focusing on integrated photonic applications and provide high quality light source at the nanoscale.

In particular, we have set-up fabrication methods combining plasmons-induced surface functionalization with diazonium salt and electrostatic adsorption with QDs. The key point of the design strategy is the electrostatic interaction between diazonium salt and QDs ligands. In this thesis, DCOOH diazonium salt was selected for the -COOH group, which forms $-COO^-$ group on surface functionalization layer when solved in deionized water, making functionalized sites negatively charged. Additionally, QDs are modified with cysteamine ligands, which form $-NH_3^+$ group when solved in deionized water. Positively charged QDs are adsorbed on the functionalized surface by electrostatic interaction between $-COO^-$ group and NH_3^+ group. Moreover, the plasmonic-induced surface functionalization starts at the plasmonic hot-spots and the spatial distribution follows the electromagnetic field as well as adsorbed QDs. Under excitation, QDs' emission is influenced by plasmonic effect. The change of PL lifetime was selected as the main signal to observe this influence.

Before achieving this goal, we have carried out different works. In the first work, the surface functionalization and electrostatic adsorption were first performed on ITO glass. The spatial distribution follows the excitation laser spot. As the distribution of adsorbed QDs follows the distribution of surface functionalization layer, the patterning of QDs on ITO was realized in the end. The electrostatic adsorption mechanism was verified by comparison with the same method using DNO_2 diazonium salts instead of DCOOH. The electrostatic adsorption could not be performed on the DNO_2 functionalized surface. However, other adsorption interaction, such as Van der Waal force, have turned out to play a role on the DNO_2 functionalized surface. By comparing the PL intensity of DCOOH and DNO2 functionalized surfaces, which can be considered proportional to the number of adsorbed QDs, the ability of DCOOH to interact electrostatically with QDs could be analyzed. The PL is 7.3 times higher in the case of DCOOH when the QD deposition time is 120 min. The results indicate the existence of an electrostatic interaction, which is one of the principles of this thesis.

After the verification of electrostatic adsorption, a similar strategy was applied on optical fibered tips. A PETA polymer tip was first fabricated at the extremity of the fiber from laser light coupled at the other end of optical fiber. The DCOOH diazonium salt was used to fabricate the second tip on the first tip. The first PETA first tip concentrate light to get a smaller DCOOH tip. The time evolution of the growth of the of first tip was numerically simulated to predict its morphology as well as the electromagnetic concentration effect. The final hybrid tip has a typical a height of 12 μm and a width of 3 μm at the junction section, where the boundary between the two tip is clearly visible. The radius of curvature of the extremity of the second tip is about 60 nm, suggesting the potential use as a nano-source. The electrostatic QDs' adsorption was also verified by comparing DCOOH and DNO_2 diazonium salts. The fabricated hybrid fiber optic tip was used as a concentration sensor for ZnO nanoparticles in liquid based on PL lifetime modification. This work illustrated a promising application of QDs adsorption by electrostatic interaction on (sub)micro-scale DCOOH functionalized surface.

Besides micro-scale functionalized surface, the QDs adsorption strategy was also applied at the nanoscale.We have successfully fabricated hybrid plasmonic nanoemitters, in which QDs are adsorbed at the close vicinity of Au NW and Ag NW. For both kinds of nanoemitter, the resulted PL peak positions remained consistent with those of the colloidal QDs solution. Again, the electrostatic adsorption process was validated in both of them. Significant lifetime decrease was observed due to the plasmonic effects of Au NW and Ag NW, with positive correlations found between lifetime and DCOOH thickness acting as a spacer. Moreover, for QDs-Ag NW nanoemitter, the FDTD simulation of the plasmonic field distribution was consistent with the experimental morphology of the functionnalization in the X, Y, and Z directions. A strong correlation was observed between QDs' lifetimes and functionalized thicknesses, as well as between thickness and exposure energy used during diazonium layer fabrication, with Pearson correlation factors of 0.96 and 0.89. The strong positive correlation shows that the PL emission enhancement factor of QDs-Ag NW nanoemitter could be adjusted during the fabrication steps. Furthermore, the QDs-Ag NW nanoemitter was activated from a remote excitation at the end of the Ag NW, positioned 2.5 μm away, based on the SPP propagation along the nanowire. It shows another method to turn on and off the hybrid nanoemitter by switching the excitation polarization direction

The work in this thesis demonstrates a new method for selectively adsorbing QDs by electrostatic interaction. The surface functionalization of diazonium salt was demonstrated on ITO glass, optical fiber and Au/Ag NW from micro-scale to nano-scale. The fabricated photonic device keeps the luminescent properties as colloid QDs. Especially, in the QDs-Ag NW nanoemitter, the QDs adsorbed spot is in accordance with the plasmonic hot spot, which results plasmonic enhanced PL emission. Moreover, the remote excitation illustrated the potential of the nanoemitter for advanced integrated photonics applications.

There are still other fields to be explored based on this thesis. When we performed the DCOOH surface functionalization on ITO glass, we found that the grafted layer emit broad band photoluminensce under laser excitation with. When the number of adsorbed QDs is low, it is difficult to distinguish QD emission from total emission. Reducing the grafted layer emission will be necessary for fabricating single-photon devices. As QDs is a semiconductor nanomaterial, the energy transfer between grafted layer and QDs would be interesting to investigate, which would help to optimize the efficiency of fabricated nanoemitter.

We hope that the works and methods presented in this thesis will provide background, prerequisites and references for future works on hybrid integrated photonics and QDs' integration techniques.

Résumé en Français

1. Introduction

Au cours des deux dernières décennies, la nanophotonique a rapidement évolué, entraînant la demande de nano-émetteurs de haute qualité et à faible coût intégrés dans des dispositifs photoniques.[1,2] Les points quantiques (QD) sont apparus comme un candidat de premier plan en raison de leurs propriétés exceptionnelles : rendement quantique élevé de la photoluminescence, largeurs de raie d'émission étroites, accordabilité spectrale entre le visible et le proche infrarouge, et compatibilité avec une fabrication modulable.[3] Pour relever les défis des applications pratiques, les chercheurs ont mis au point des systèmes hybrides qui intègrent les QD dans des nanostructures, obtenant ainsi des améliorations de performance sans précédent.[4] La fabrication de systèmes hybrides pour intégrer les QD dans des nano-structures et des dispositifs s'est avérée être l'une des principales approches développées dans la recherche sur les nano-émetteurs.[5,6]

Dans ces systèmes hybrides, le système à renforcement plasmonique combinant des QD et une structure plasmonique a attiré l'attention[7,8] Avec le couplage plasmonique, l'émission PL des QD serait renforcée, ce qui est lié au champ électromagnétique renforcé et au facteur de Purcell.[9,10] Dans une telle structure, la position spatiale des QD devrait être superposée aux points chauds. Le contrôle de distribution spatiale des QD à l'échelle nanométrique est l'un des points clés pour réaliser les nano-émetteurs à base de QD. Des stratégies impliquant la polymérisation en champ proche,[11] des brins d'ADN[12] et la microscopie à force atomique,[13] ont été appliquées.

Au cours de ma thèse, nous avons étudié une nouvelle approche, basée sur la connexion entre les ligands des QDs et le groupe fonctionnel chimique de la surface, qui est modifié par des sels de diazonium. Cette stratégie a été appliquée sur du verre ITO, des pointes de fibres optiques, des nanorubans d'Au et des nanofils d'Ag. La méthode de connexion a été vérifiée et le nano-émetteur QDs-Nanowire d'Ag a été fabriqué à la fin.

Le premier chapitre présente l'état de la recherche sur les QDs et les sels de diazonium. L'introduction est complétée par les propriétés des matériaux apparentés. En tant que nanoparticules à hétérostructure, les QDs seront tout d'abord présentés selon les principes d'émission. L'effet de confinement quantique, le schéma du niveau d'énergie et la photoluminescence (figure 1-1) ont été présentés. Les fonctions des ligands de surface et les réactions associées seront ensuite décrites. Le développement de nano-émetteurs intégrés à base de QD sera examiné à la fin.

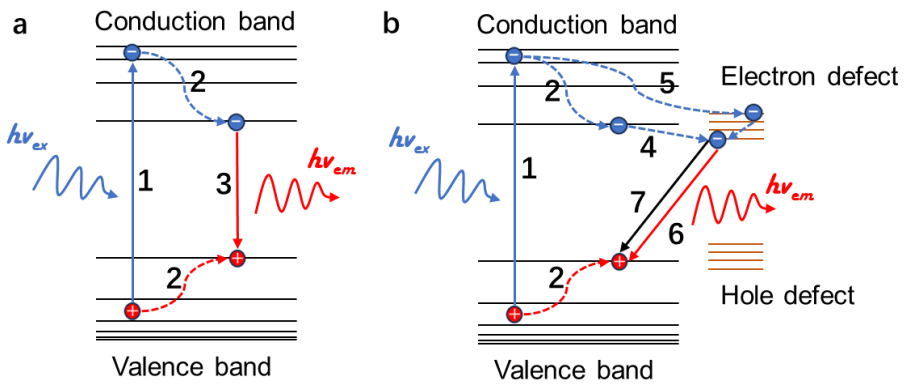

Figure 1-1. a. Schéma du processus de photoluminescence des excitons du point quantique. b. Schéma du processus de photoluminescence des défauts du point quantique.

L'introduction du sel de diazonium concerne principalement les propriétés et les réactions générales : la réaction de fonctionnalisation de la surface et la réaction de connexion moléculaire. Ces réactions sont les principes fondamentaux de la mise en œuvre des nano-émetteurs QDs dans cette thèse. La progression de la fonctionnalisation de la surface est illustrée à la figure 1-2. A la fin de la réaction, il y a des groupes -COOH à l'état libre, ce qui offre la possibilité d'une connexion moléculaire.

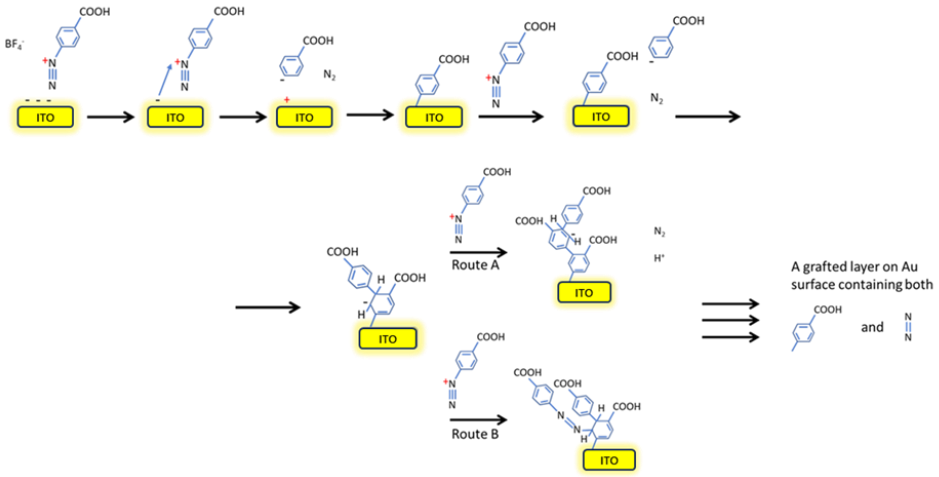

Figure 1-2. Progression du greffage des résultats monocouche et multicouche avec le sel de diazonium 4-carboxybenzenediazonium tetrafluoroborate (DCOOH) comme exemple.

Cette thèse présente une nouvelle méthode de fabrication de nano-émetteurs hybrides en tirant parti des interactions électrostatiques entre les points quantiques CdSe/ZnS modifiés en surface et les surfaces fonctionnalisées par des sels de diazonium (par exemple, le verre ITO, les fibres optiques, les nanofils Au/Ag). La distribution spatiale des QDs peut être contrôlée en fonction de la couche de sel de diazonium à proximité des nanoparticules métalliques. La fonctionnalisation de la surface et la progression de l'adsorption des QDs sont orthogonales. Cela ouvre la voie à des conceptions d'émetteurs nanométriques polyvalents dans les domaines de la détection, de l'optoélectronique et de la plasmonique.

2 Greffage d'un sel de diazonium sur un verre recouvert d'ITO entraînant l'adsorption contrôlée de QDs sur des surfaces sélectionnées

Dans ce chapitre, nous étudions la possibilité de déposer sélectivement des QDs sur des structures de taille micrométrique de sels de diazonium greffés. Le sel de diazonium 4-carboxybenzenediazonium tetrafluoroborate (DCOOH) a été utilisé pour réaliser le greffage sur un substrat de verre revêtu d'ITO afin de former des zones fonctionnalisées à l'échelle du (sous-)micromètre pour l'interaction électrostatique avec les QDs. Ensuite, des QDs modifiés en surface ont été déposés à partir de la solution sur la surface ITO fonctionnalisée. Comme référence, le sel de diazonium 4-nitrobenzenediazonium tetrafluoroborate ($DNO_{(2)}$) a également été utilisé pour le greffage, qui n'est pas censé permettre l'adsorption électrostatique des QDs. Nous montrerons, par comparaison, que l'intensité PL de la surface modifiée par DCOOH est 7,3 fois plus élevée que celle des surfaces modifiées par DNO_2et non greffées. La différence d'intensité de la lumière émise par les deux types de surfaces fonctionnalisées au diazonium prouve l'adsorption sélective des QDs par interaction électrostatique. Ce travail démontre une nouvelle méthode pour contrôler le dépôt de QDs sur la surface ITO et a le potentiel de réaliser cette adsorption en fabriquant des dispositifs photoniques et optoélectroniques.

2.1 Fonctionnalisation de surface par greffage de sel de diazonium sur du verre recouvert d'ITO

La morphologie d'un point greffé typique est illustrée à la figure 2-1. La solution de DCOOH, dont la concentration est de 100 mM, a été déposée sur du verre recouvert d'ITO. Pour rappel, une lumière laser de 532 nm avec une densité laser de 0,9 mW/µm^{2}a été utilisée pour l'exposition et le diamètre du spot laser était d'environ 0,8 µm. Le temps d'exposition était de 3 min pour cet échantillon. La figure 2-6a montre l'image SEM du point, avec un diamètre de 1,5 ± 0,13 µm. L'image AFM et le profil de la section transversale sont présentés dans les figures 2-6b et 2-6c. La position de la section transversale est indiquée dans l'image AFM. La hauteur du point fonctionnalisé est de 1,5 µm

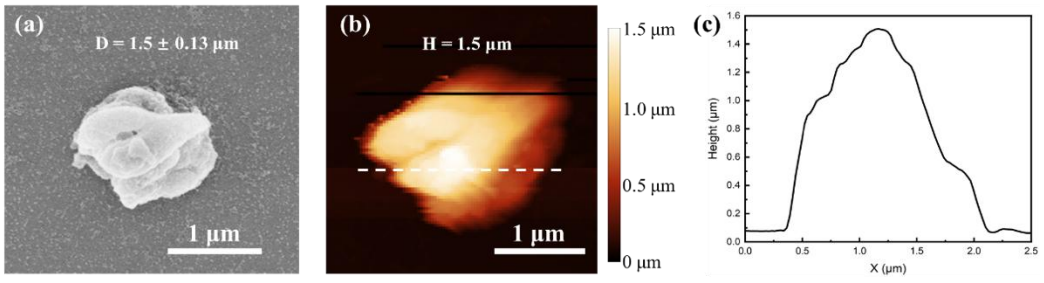

Figure 2-1. (a) L'image SEM, (b) l'image AFM et (c) le profil de la section transversale de la couche greffée, dont la position est indiquée sur l'image AFM. Pour la fabrication de cet échantillon, la concentration de la solution de sel de diazonium DCOOH est de 100 mM et le temps d'exposition est de 3 minutes.

La hauteur des différents points/blocs fonctionnalisés a été modifiée en ajustant la concentration de la solution et le temps d'exposition. L'énergie du laser a été maintenue constante à 21,23 μW/μm^2. Étant donné que le but du développement de la couche fonctionnalisée est d'adsorber les QDs sur la surface de la cible, l'épaisseur, qui est mesurée en hauteur, de la couche de greffage est un facteur important

Dans ce cas, l'énergie du laser d'exposition étant excessivement élevée, la taille obtenue est deux fois plus grande que le diamètre du spot laser. L'évolution de la taille des points greffés en fonction des paramètres d'exposition est illustrée à la figure 2-2. Les hauteurs des points ont été mesurées par AFM pour évaluer la taille. La concentration de la solution de DCOOH a été ajustée à 5 mM, 10 mM, 20 mM et 100 mM. Le temps d'exposition a été ajusté de 20 s à 280 s. Les épaisseurs varient de 7 nm à 275 nm en fonction du temps d'exposition et de la concentration de la solution. Par rapport au résultat précédent, l'épaisseur a diminué en raison de la baisse de l'énergie du laser. Pour chaque concentration de solution, l'épaisseur de la surface fonctionnalisée est proportionnelle au temps d'exposition. De plus, pour un temps d'exposition spécifique, la surface fonctionnalisée sera plus épaisse si la concentration de la solution est plus élevée. Cette conclusion constitue le principe de base de la fabrication de la surface fonctionnalisée dans les expériences ultérieures

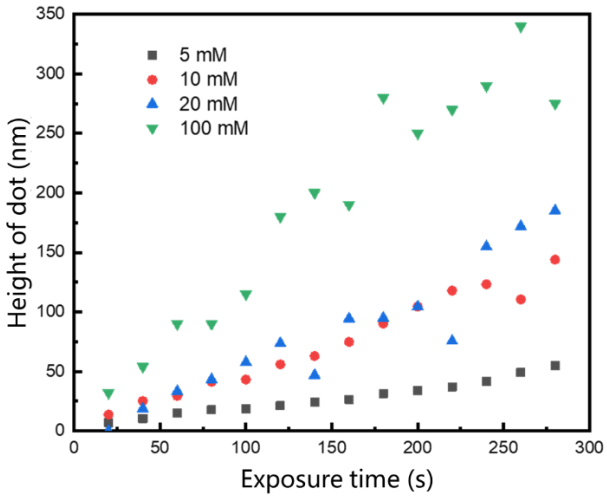

Figure 2-2. Un ensemble de résultats de fonctionnalisation de surface par la solution de DCOOH sur du verre recouvert d'ITO. La hauteur de la surface de fonctionnalisation varie de 7 nm à 275 nm avec différents temps d'exposition et concentration de solution. L'intensité de la lumière d'exposition a été maintenue à 21,23 μW/μm^{2}sous l'excitation de la lumière laser de 532 nm

Outre la fabrication de la fonctionnalisation de surface par le sel de diazonium DCOOH, l'émission PL des structures greffées a également été étudiée. Cette analyse est importante pour évaluer l'arrière-plan PL. Un exemple de structure est illustré à la figure 2-3a. Pour la fabrication de cette structure, le temps d'exposition était de 20 s et la concentration de la solution était de 5 mM. La densité de lumière laser utilisée était de 36,1 μW/μm^2. Après la fabrication du point à l'aide du protocole décrit dans la section 2.2, mais sans l'étape d'intégration du QD illustrée à la figure 2-3, l'émission PL a été détectée avec la longueur d'onde d'excitation du laser de 532 nm. La durée de vie a été mesurée et la courbe de photoluminescence résolue dans le temps (TRPL) est illustrée à la figure 2-3b avec un temps d'acquisition de 10 minutes. La durée de vie de la couche de DCOOH greffée est de 0,41 ns.

Cette durée de vie est beaucoup plus courte que 18,45 ns, qui est la durée de vie intrinsèque des QDs utilisés à l'état colloïdal.

En outre, le spectre PL a été mesuré sous différentes excitations lumineuses. Les figures 2-3c et 2-3d montrent les spectres PL sans arrière-plan sous une excitation lumineuse laser de 532 nm et 405 nm. L'énergie du laser est la même. Avec les comptes d'intensité, sous une excitation lumineuse de 405 nm, l'intensité moyenne est d'environ 150, et le maximum est de 250. Sous une excitation lumineuse de 532 nm, l'intensité moyenne est d'environ 20, et le maximum de 40. La couche greffée de sel de diazonium DCOOH présente une intensité PL différente sous différentes excitations laser.

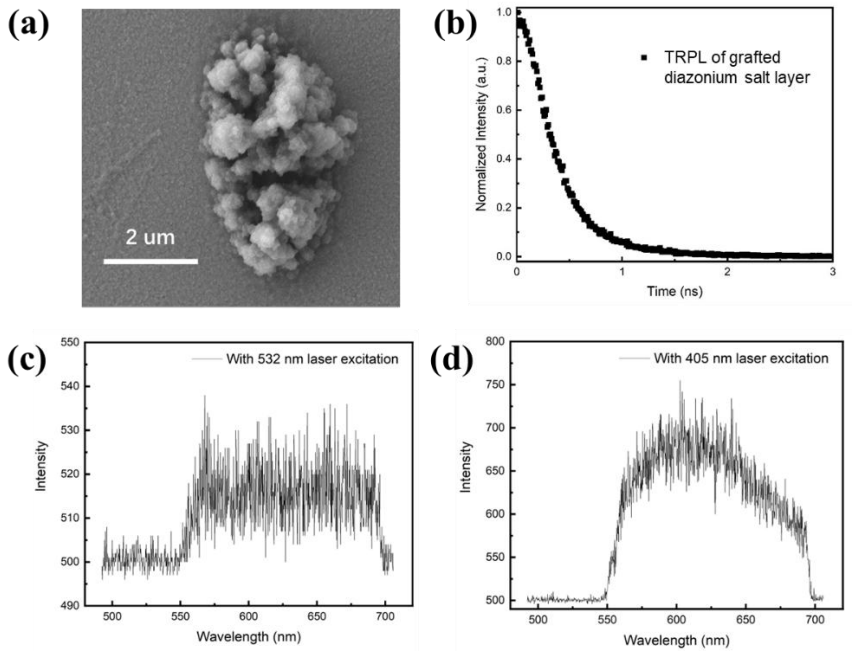

Figure 2-3. Analyse du point greffé DCOOH (a) Image SEM. (b) Courbe de décroissance PL avec l'excitation d'une lumière laser de 532 nm révélant une durée de vie PL de τ = 0,41 ns. (c) Spectre PL sous l'excitation d'une lumière laser de 532 nm. (d) Spectre PL sous excitation de lumière laser 405 nm.

2.2 Adsorption des QDs sur la couche de sel de diazonium greffée

Les QDs utilisés dans cette expérience sont des QDs CdSe/ZnS core-shell avec les ligands de CA, ce qui apportera des groupes -NH_2à la surface des QDs. Pour les colloïdes en solution, les spectres PL et d'absorption sont présentés à la figure 2-4a. Les propriétés optiques des QDs à surface modifiée restent les mêmes. La position du pic du spectre PL est située à 626 nm.

La distribution du potentiel zêta est illustrée à la figure 2-4b, qui est mesurée dans de l'eau déionisée dont le pH est de 7. La position de comptage la plus élevée est située à 36,9 mV. Le potentiel zêta positif confirme la charge de surface positive des QDs. La valeur élevée (>30 mV) montre que la solution colloïdale de QDs CA-CdSe/ZnS est stable dans l'eau désionisée.

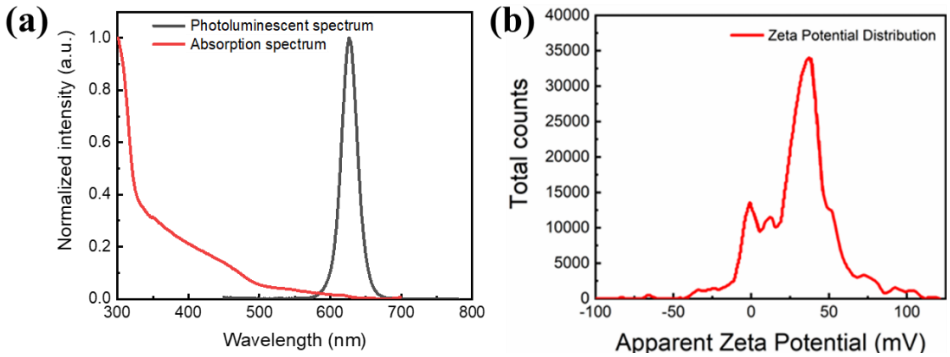

Figure 2-4. Caractérisation des QDs : (a) Spectres PL et d'absorption de la solution colloïdale de CA-CdSe/ZnS QDs. (b) Distribution du potentiel zêta de la solution colloïdale de QDs CA-CdSe/ZnS.

Les figures 2-5 et 2-6 comparent les données PL et TRPL avant et après les dépôts de QDs. La lumière laser de 532 nm a été utilisée pour l'excitation dans les deux figures. Un point greffé DCOOH a été sélectionné comme indiqué dans la figure 2-5a et la figure 2-6a. Les diamètres sont de 3,96 µm le long de l'axe long et de 2,19 µm le long de l'axe court. La forme d'ellipse est supposée provenir de la forme du spot laser. La figure 2-5b montre le spectre PL sans normalisation de la couche de fonctionnalisation DCOOH avant l'adsorption des QDs. Une émission entre 550 nm et 700 nm a été détectée, ce qui est cohérent avec le résultat de la section 2.3.2, dans lequel il y a également une faible émission dans la gamme rouge sous une excitation lumineuse de 532 nm. La figure 2-5c montre le spectre PL normalisé de QDs dispersés sur du verre recouvert d'ITO sans aucun greffage de diazonium. La position du pic est de 614,5 nm et la largeur totale à mi-maximum (FWHM) est de 21 nm. La figure 2-5d montre le spectre PL normalisé du point greffé après le dépôt de QDs. La position du pic est de 616,5 nm et la largeur à mi-hauteur (FWHM) est de 20 nm. En comparant les spectres normalisés des figures 2-5c et 2-5d, le spectre PL des émissions de QDs reste cohérent ou sans la présence de la couche de fonctionnalisation. Dans notre travail, la solution de QDs a été déposée sur la surface de l'échantillon pendant 5 à 60 minutes avant d'être rincée. Au cours de ce processus, en raison de la dynamique des fluides comme l'effet de cercle de café, la concentration de QDs restant sur la surface de l'échantillon n'est pas uniforme. L'intensité PL n'est pas adaptée à la comparaison. Pour évaluer l'effet Purcell, les données TRPL sont préférées dans ce travail.

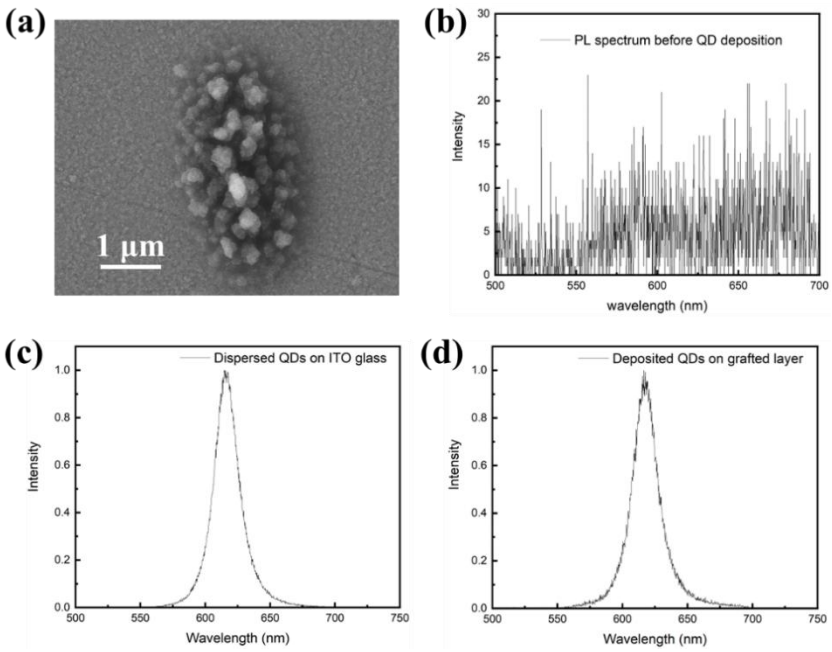

Figure 2-5. (a) Image SEM de la couche greffée de DCOOH. (b) Spectre PL des émissions de la couche greffée de DCOOH sans dépôt de QDs. (c) Spectre PL des émissions de QDs dispersés sur du verre recouvert d'ITO. (d) Spectre PL des émissions de la couche greffée après dépôt de QDs.

Quant à la courbe TRPL, la figure 2-6b montre cette courbe pour la couche de fonctionnalisation de sel de diazonium DCOOH sans dépôt de QDs. La durée de vie est de 0,41 ns, qui est également cohérent avec les résultats de la section 2.3.2. La figure 2-6c montre le spectre TRPL de QDs dispersés sur du verre recouvert d'ITO. La durée de vie est de 18,45 ns. Cependant, lorsque les QDs sont déposés sur la couche de fonctionnalisation DCOOH, la durée de vie diminue à 2,42 ns (Figure 2-6d).

En ce qui concerne l'émission des QDs, qui provient de la recombinaison des électrons et des trous générés, la durée de vie varie inversement à la probabilité de recombinaison des porteurs. Idéalement, après que le QD a absorbé un photon, il y a un exciton neutre, qui se compose d'une paire de porteurs ainsi que d'un électron et d'un trou générés. S'il existe plus d'une paire de porteurs, ou trion, les QD émettent de la lumière avec une durée de vie plus courte, ce qui est également appelé l'extinction de la photoluminescence des QD.[14,15]

Dans notre cas, la durée de vie de l'émission des QDs a diminué d'un facteur 7 avec la présence de la couche de fonctionnalisation DCOOH. La diminution de la durée de vie indique l'existence de processus multi-porteurs à l'intérieur des QDs. Compte tenu de la structure de l'échantillon, il y a un transfert de porteurs entre la couche de fonctionnalisation DCOOH et les QDs.[16] Outre la durée de vie, la cohérence du spectre PL montre que la bande interdite de la structure des QDs core-shell n'est pas influencée par l'existence de la couche de fonctionnalisation DCOOH.

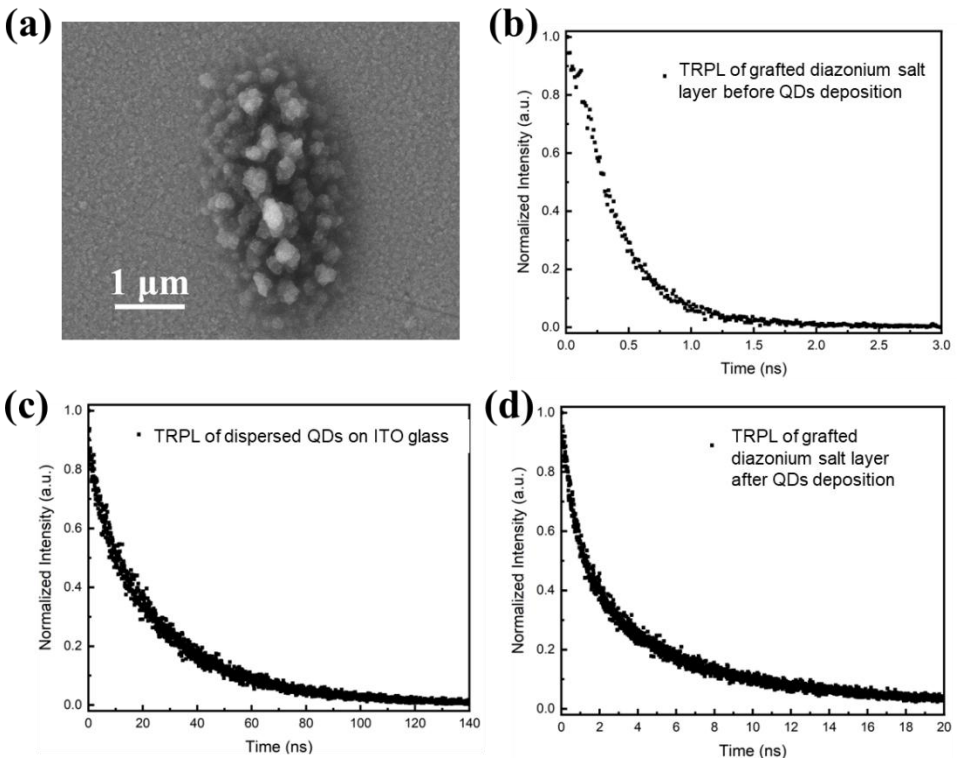

Figure 2-6. (a) Image SEM de la couche greffée de DCOOH. (b) TRPL de la couche greffée de DCOOH sans dépôt de QDs (τ= 0.41 ns). (c) Courbe TRPL des émissions de QDs dispersés sur le verre recouvert d'ITO (τ= 18.45 ns). (d) TRPL de la couche greffée après le dépôt de QDs (τ= 2.42 ns).

Pour confirmer que l'interaction électrostatique est prédominante dans la fixation des QDs, le sel de diazonium DNO_2a été utilisé comme référence. Les structures chimiques du DCOOH et du DNO_2sont présentées à la figure 2-7. Ces différents types de sel de diazonium partagent une partie du groupe chimique. Mais le changement d'un groupe fonctionnel (-R) entraîne une différence dans les propriétés chimiques.

Le groupe -COOH de la molécule DCOOH permet d'adsorber des QDs chargés positivement par la force électrostatique entre les charges de surface. Pour le DNO_2, le groupe $-NO_2$se trouve à l'opposé du groupe azoïque. Le groupe azoïque garantit la fonctionnalisation de la surface. Cependant, le groupe $-NO_2$n'est pas censé avoir de charges lorsqu'il est dissous dans de l'eau désionisée. L'adsorption électrostatique des QDs ne devrait donc pas se produire sur la surface fonctionnalisée au DNO_2. Au niveau du groupe $-NO_2$, d'autres interactions, telles que celles découlant des forces de Van der Waal, pourraient jouer un rôle sur la surface fonctionnalisée au $DNO_{(2)}$.Pour comparaison, les intensités PL des surfaces fonctionnalisées DCOOH et DNO_2, qui peuvent être considérées comme proportionnelles au nombre de QD adsorbés, ont été analysées pour évaluer le rôle de l'interaction électrostatique sur DCOOH.

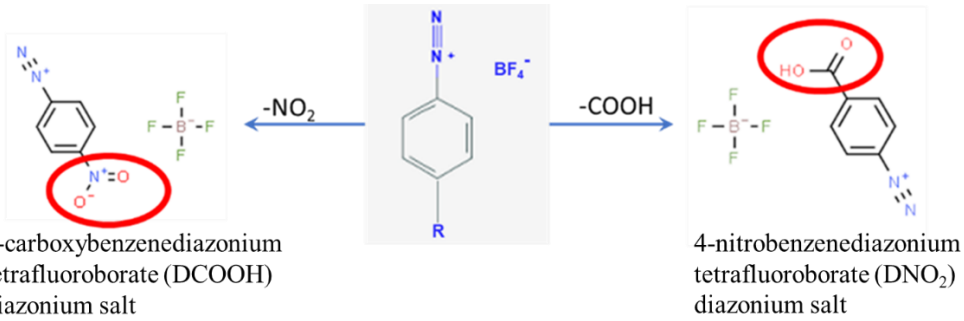

Figure 2-7. Structures chimiques des deux types de sels de diazoniums utilisés : DCOOH et DNO_2.

L'analyse statistique est présentée dans la figure 2-8. Tout d'abord, la zone d'émission a été sélectionnée en fonction de l'image de balayage PL avant le dépôt des QDs, comme le montre la figure 2-8a. En fait, l'arrière-plan PL nous permet de deviner la présence des points. Les intensités de lumière émise par pixel ont été intégrées et le nombre de photons émis/pixel pour chaque zone sélectionnée a été choisi comme signal pour évaluer le degré d'adsorption des QDs. Dans notre travail, trois types de surfaces ont été choisis pour la comparaison : la surface de fond (verre recouvert d'ITO), la surface de fonctionnalisation DCOOH et la surface de fonctionnalisation DNO_2

Les émissions PL des surfaces de fonctionnalisation DCOOH et DNO_2ont été mesurées, ce qui prouverait la capacité d'adsorption des QDs sur la surface de fonctionnalisation DCOOH par interaction électrostatique. En outre, la force de Van der Waals est supposée jouer un rôle entre les nanoparticules et tous les types de surface. Dans le cas où d'autres interactions joueraient un rôle, des surfaces de fond ont été sélectionnées comme références sur le verre nu revêtu d'ITO sans aucune fonctionnalisation de surface. Les analyses des surfaces de fond visent à évaluer l'efficacité des surfaces de fonctionnalisation du DNO_2en tant que référence. Dans nos expériences, la taille des surfaces d'arrière-plan sélectionnées est similaire à la taille des surfaces de fonctionnalisation DCOOH et $DNO_{(2)}$.

La figure 2-8b présente une analyse statistique, en termes de nombre de cas, de l'émission de photons par les trois types de surfaces. Par chaque "cas" expérimental, nous entendons un "point/zone" présentant la valeur numérique indiquée dans l'axe des abscisses. Pour exprimer intuitivement l'intensité de l'émission, le nombre de photons émis par pixel a été utilisé pour représenter l'intensité PL moyenne avec un temps d'intégration de 60s. L'intensité PL a été convertie en nombre de photons à 617 nm, qui est la position de crête de l'émission PL des QDs sous une excitation de lumière laser de 473 nm. Dans la figure 2-8b, les barres orange représentent l'intensité PL des surfaces de fonctionnalisation DCOOH. Les surfaces de fonctionnalisation DNO_2et les surfaces de fond sont représentées par des barres vertes et bleues respectivement. Il s'avère que la forte émission PL concerne statistiquement principalement les surfaces de fonctionnalisation DCOOH, ce qui indique qu'il y a plus de QDs adsorbés sur les surfaces de fonctionnalisation DCOOH. En outre, les intensités PL sont similaires pour les surfaces de fonctionnalisation DNO_2et les surfaces de fond.

Les résultats ont confirmé l'hypothèse selon laquelle l'adsorption électrostatique joue un rôle important dans l'adsorption des QDs sur les surfaces de fonctionnalisation DCOOH. En outre, sur les surfaces de fonctionnalisation DNO_2, la capacité d'adsorption des QDs est similaire à celle de la surface de verre recouverte d'ITO. Cela indique que le DNO_2pourrait

être un matériau de référence pertinent pour évaluer l'adsorption électrostatique des QDs. La comparaison entre les zones de fonctionnalisation DCOOH, DNO_2 et l'arrière-plan a permis d'exclure l'influence des forces de Van der Waals et de mettre en évidence l'effet d'adsorption électrostatique.

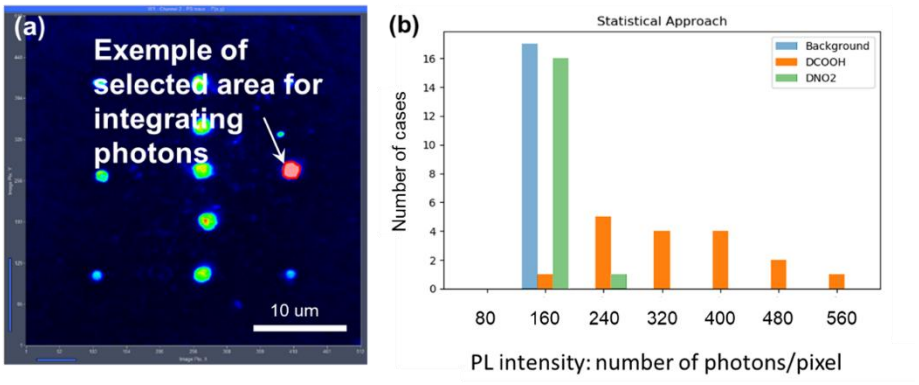

Figure 2-8. (a) Exemple de zone sélectionnée pour l'intégration des photons sur trois types de surfaces : surface de fond, surface de fonctionnalisation DCOOH et surface de fonctionnalisation DNO_2. (b) Étude statistique du nombre de QDs adsorbés. Les photons émis/pixel pour chaque zone sélectionnée ont été choisis pour évaluer la quantité d'adsorption des QDs.

Pour approfondir l'analyse statistique de la capacité d'adsorption des QDs sur la surface de fonctionnalisation, les photons/pixels émis, selon l'image PL à balayage montrée précédemment, ont été évalués avec différents temps de dépôt des QDs. La figure 2-9 montre l'analyse statistique du même échantillon avec différents temps de dépôt de QDs : (a) 5 min, (b) 30 min, (c) 60 min et (d) 120 min. Après avoir répété les expériences, les résultats ont été classés et le nombre de cas a été compté.

Il a été prouvé que, quel que soit le temps de dépôt, les surfaces de fonctionnalisation DCOOH émettent plus de photons que les deux autres types de surfaces, ce qui pourrait démontrer que les surfaces de fonctionnalisation DCOOH présentent une plus forte capacité d'adsorption des QDs modifiés en surface. Le nombre de photons émis entre les surfaces de fonctionnalisation DNO_2et les surfaces de fond est presque le même quel que soit le temps de dépôt, tandis que l'augmentation du temps semble peupler les cas correspondant à un PL élevé, en particulier dans la Fig. 2-9d. La diminution du PL dans le cas du DNO_2peut être associée à un nombre plus faible de QDs adsorbés. Ce résultat est en accord avec la présence d'une adsorption électrostatique dans la structure QDs-DCOOH, comparée à une faible interaction de van der Waals possible dans le système QDs-DNO_2.

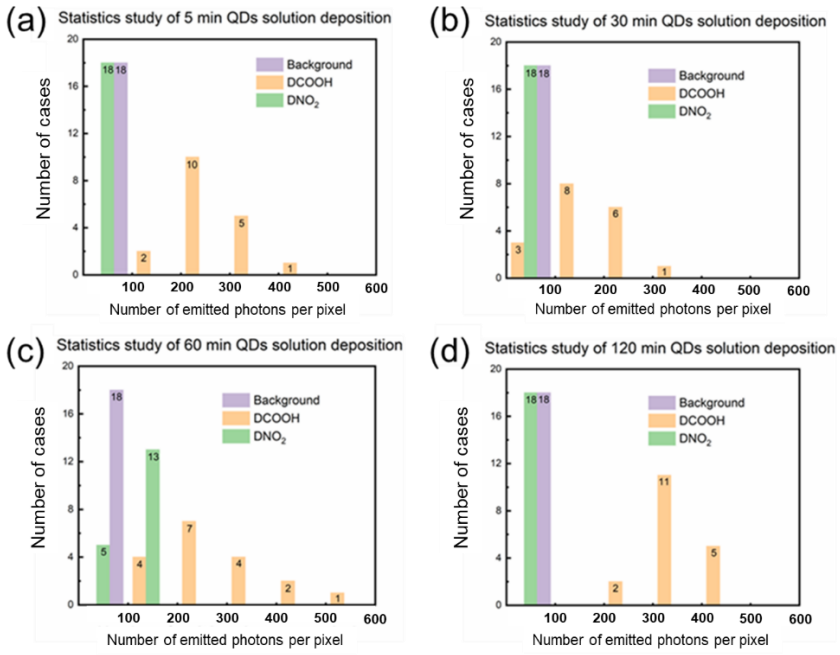

Figure 2-9. Résultats statistiques du nombre de photons émis par les surfaces de fonctionnalisation DCOOH, les surfaces de fonctionnalisation DNO_2et les surfaces de fond avec différents temps de dépôt de la solution de QDs : (a) 5 min, (b) 30 min, (c) 60 min et (d) 120 min. Le nombre de cas est indiqué dans l'histogramme

3 Pointe de fibre optique luminescente basée sur l'adsorption de QDs par un sel de diazonium

Dans ce chapitre, l'adsorption des QDs a été réalisée sur une fibre optique avec la fonctionnalisation de surface du sel de diazonium DCOOH. Le mécanisme d'adsorption est le même que celui décrit au chapitre 2. Un nouveau type de pointe de fibre optique luminescente a été fabriqué, qui émet de la lumière rouge sous excitation de lumière bleue, avec le même spectre que les QDs colloïdaux. Leur morphologie et leurs caractéristiques ont été caractérisées par spectroscopie de fluorescence et MEB. La comparaison avec le sel de diazonium DNO_2a également été effectuée pour démontrer que l'adsorption électrostatique joue un rôle clé dans l'immobilisation des QDs. En particulier, l'intensité PL des pointes fibrées modifiées par le DNO_2a diminué d'un facteur 11 par rapport à celles modifiées par le DCOOH. Ce nouveau type de pointe luminescente à base de QD pourrait être utilisé pour des éclairages spéciaux à base de fibres, tels que la détection de la vie après d'autres catastrophes. Dans ce travail, nous avons utilisé cette pointe de fibre luminescente comme capteur pour détecter la concentration de NP de ZnO en solution, ce qui est basé sur le phénomène d'extinction. Cela met en évidence son potentiel prometteur pour les applications de détection

3.1 Image SEM et luminescente de l'extrémité d'une fibre optique

La figure 3-1 présente des images de luminescence de la pointe en fibre hybride fabriquée. Dans la figure 3-1a, l'image luminescente est capturée avec une lumière laser de 405 nm

éclairée depuis l'extrémité opposée de la fibre optique. Un filtre passe-bande 615/70 a été utilisé devant la caméra pour capturer l'émission de lumière rouge de la pointe de la fibre. Un point rouge indique la position de l'extrémité luminescente de la fibre optique, tandis qu'un tiret blanc souligne le profil de la structure originale de la fibre optique. La figure 3-1b présente une autre image luminescente sous excitation de lumière blanche provenant de l'extérieur, en utilisant le filtre passe-bande 615/70 pour accentuer l'émission rouge de la fibre optique et de la pointe (la lumière bleue étant effectivement filtrée du spectre de la lumière blanche). La ligne blanche en pointillés représente également la structure originale de la fibre optique, qui est visible sur cette image en raison de la réflexion de la lumière. D'après ces images de luminescence, la pointe émettrice de lumière est observée au centre de l'extrémité de la fibre optique et est orientée perpendiculairement à la surface de l'extrémité de la fibre optique.

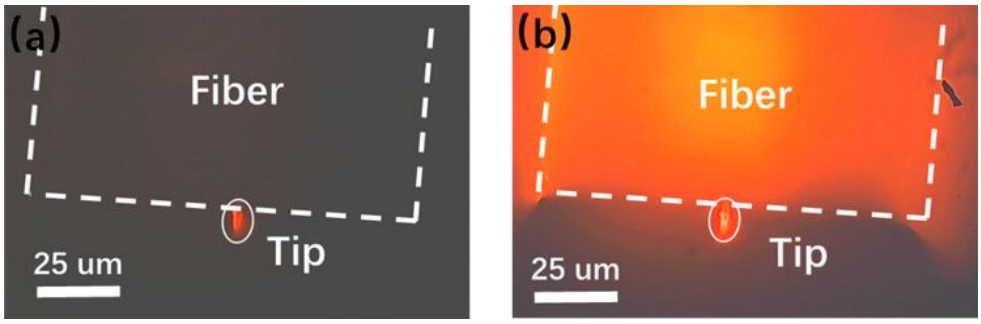

Figure 3-1. Images luminescentes de l'extrémité luminescente de la fibre optique. (a) L'image luminescente avec une lumière laser de 405 nm excitée à partir d'une autre extrémité de la fibre optique. Elle est prise avec un filtre passe-bande 615/70 avant l'appareil photo. La lumière rouge est émise par l'extrémité de la pointe. (b) L'image luminescente sous excitation de lumière blanche provenant de l'environnement. Un filtre passe-bande 615/70 (la lumière 545-685 nm passe) a également été utilisé pour prendre cette image. La ligne blanche en tirets montre le profil de la fibre optique et l'ellipse blanche identifie la position de la pointe dans les deux images.

Dans la figure 3-2a, les images SEM décrivent la morphologie de la pointe en fibre optique fonctionnalisée. La pointe entière mesure 11,9 µm de hauteur, affichant clairement la limite entre la pointe initiale en polymère PETA et l'extrémité polyaryle, comme le montre la figure 3-2b. La couche de polyaryle présente une largeur de 2,88 µm à la section de jonction entre la pointe PETA et le revêtement de polyaryle. Le rayon de courbure de 'extrémité de la deuxième pointe est de 60,7 nm, ce qui suggère le potentiel de la nanostructure en tant que nano-source.

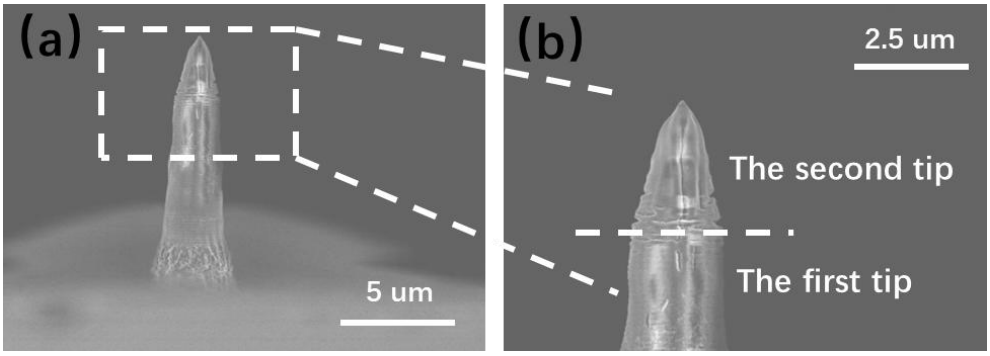

Figure 3-2. Images SEM de la pointe en fibre optique luminescente. (a) La morphologie de la

pointe entière, dont la hauteur est de 11,9 μm. (b) La morphologie de la deuxième pointe. La limite entre la première et la deuxième pointe est mise en évidence par un segment blanc en pointillé. Le rayon de courbure à l'extrémité de la pointe est de 60,7 nm.

La figure 3-3a montre le spectre PL de l'extrémité de la pointe fibrée mesuré à l'aide de la configuration illustrée à la figure 3-3. Sous une excitation laser de 405 nm provenant de l'extrémité opposée de la fibre, la position du pic du spectre PL obtenu, collecté à travers la lentille de l'objectif, est de 618 nm, ce qui est identique à la solution colloïdale de QDs. Le sel de diazonium utilisé est le DCOOH, illustré dans l'encadré de la figure 3-3a. Le DCOOH devrait avoir la capacité d'adsorber les QDs par interaction électrostatique pour le groupe -COO^-libre à la surface fonctionnalisée.

Pour mettre en évidence le rôle de l'adsorption électrostatique plutôt que celui de l'adsorption par la force de Van der Waals, une autre pointe en fibre optique a été fabriquée en utilisant le DNO_2comme référence. La structure chimique du DNO_2est présentée dans l'encadré de la figure 3-3b. Il s'agit d'un autre type de sel de diazonium avec un groupe -NO_2, comme indiqué au chapitre 2. Comme il n'y a pas de réaction chimique potentielle ou de couplage électrostatique entre le DNO_2et les ligands des QDs en solution aqueuse, les QDs ne devraient pas être adsorbés sur les surfaces fonctionnalisées par le DNO_2. Seules de faibles forces de van der Waals devraient agir sur l'adsorption des QDs sur la pointe fibrée fonctionnalisée au DNO_2. Le processus de fabrication de la pointe en fibre optique fonctionnalisée au DNO_2est le même que celui de la pointe en fibre optique fonctionnalisée au DCOOH, avec les mêmes paramètres. Avec la même excitation de lumière laser de 405 nm, le spectre résultant est montré dans la figure 3-3b. La position du pic PL est toujours de 618 nm, mais l'intensité a diminué de 2038 à 185. Cette diminution de 11 fois suggère que l'adsorption électrostatique a joué un rôle majeur dans l'intégration des QDs sur la pointe fonctionnalisée au DCOOH.

Cette comparaison est similaire à la méthode réalisée sur le verre ITO au chapitre 2. En combinant les deux résultats, le sel de diazonium DCOOH s'avère permettre l'adsorption des QDs par interaction électrostatique à la fois sur le verre recouvert d'ITO et sur la pointe en fibre optique.

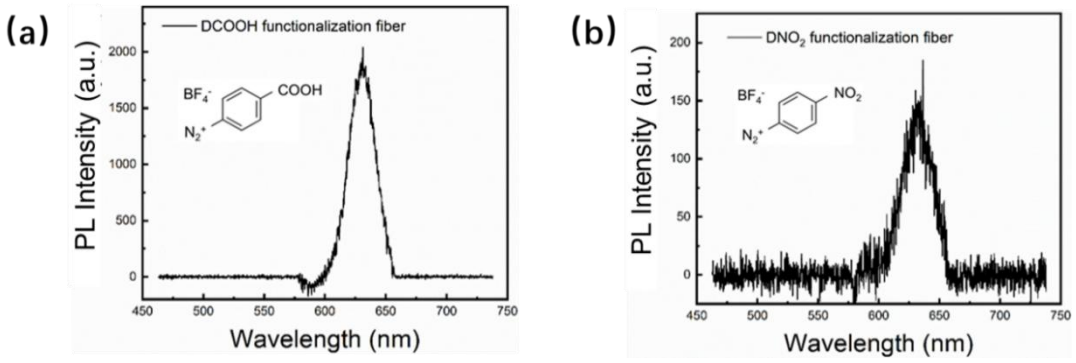

Figure 3-3. Spectres PL de deux types de pointes de fibres optiques en sel de diazonium. (a) Spectre de photoluminescence des QDs adsorbés sur la pointe de fibre optique avec une excitation laser de 405 nm depuis l'autre extrémité de la fibre. Le DCOOH a été utilisé pour la fonctionnalisation. (b) Spectre de photoluminescence d'une pointe de fibre optique fonctionnalisée au DNO_2. Les mêmes méthodes et paramètres de fabrication que pour a) ont été utilisés. L'intensité PL résultante a chuté d'un facteur 11.

3.2 Capteur à fibres de la concentration de nanoparticules de ZnO en solution

La figure 3-4a montre les courbes de photoluminescence résolue en temps (TRPL) de la pointe de QDs dans une solution de NPs de ZnO avec différentes concentrations allant de 0 mg/ml à 35 mg/ml. La durée de vie de la lumière d'émission était de 18,9 ns lorsque la pointe de QDs était placée dans une solution d'éthanol ainsi que dans une solution de NPs de ZnO à 0 mg/ml. Avec l'augmentation de la concentration en NP de ZnO, les durées de vie sont devenues 12,5 ns, 10,2 ns, 7,3 ns, 5,9 ns et 5,8 ns lorsque la concentration était de 7 mg/ml, 14 mg/ml, 21 mg/ml, 28 mg/ml et 35 mg/ml, respectivement. La tendance de la modification de la durée de vie est illustrée à la figure 3-17b. La durée de vie a diminué au fur et à mesure que la concentration de NP de ZnO augmentait. La sensibilité du capteur, définie comme la pente locale dans la figure 3-4, diminue de 0,91 ns/(mg/ml), 0,33 ns/(mg/ml), 0,41 ns/(mg/ml), 0,2 ns/(mg/ml), 0,01 ns/(mg/ml) lorsque la concentration augmente de 0 à 7 mg/ml, 7 à 14 mg/ml, 14 à 21 mg/ml, 21 à 28 mg/ml et 28 à 35 mg/ml respectivement. La sensibilité est presque constante lorsque la concentration est comprise entre 7 et 21 mg/ml. Toutefois, lorsque la concentration en NP de ZnO est supérieure à 28 mg/ml, les durées de vie varient faiblement entre les concentrations de 28 mg/ml et 35 mg/ml et la sensibilité est de 0,01 ns/(mg/ml). Ces conclusions suggèrent que cette approche serait plus adaptée à la détection de faibles concentrations. Cette pointe de QDs présente une limite lorsqu'elle est utilisée pour la détection d'une solution de NPs de ZnO de haute densité. Ce seuil de limitation est un paramètre important dans la détection des concentrations. La détection étant basée sur le transfert de charge entre les QD et les NP de ZnO , lorsque la concentration de ZnO augmente, l'interaction entre les deux types de NP est saturée. Nous pensons que c'est la raison pour laquelle la sensibilité diminue lorsque la concentration de ZnO augmente.

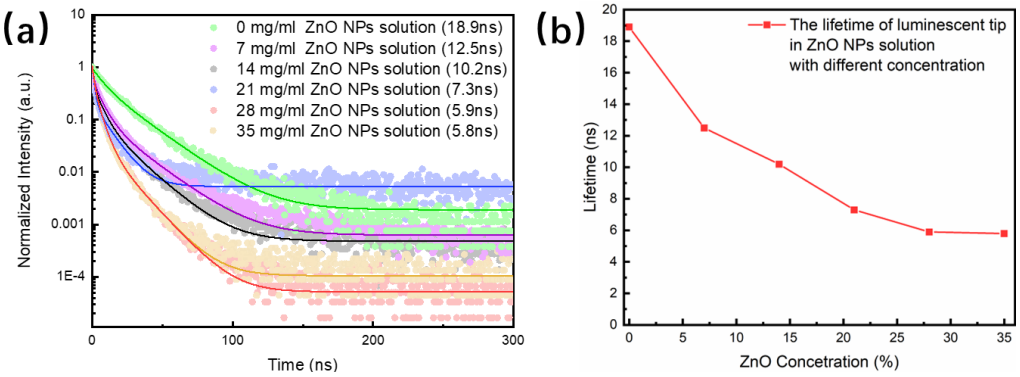

Figure 3-4. (a) Mesure de la durée de vie PL de la pointe du QD dans une solution de NP de ZnO à différentes concentrations. Dans différentes conditions, le temps de vie a diminué de 18,9 ns à 5,8 ns. (b) Tendance des changements de durée de vie de la pointe luminescente dans une solution de nanoparticules de ZnO à différentes concentrations. La diminution de l'intensité lumineuse et de la durée de vie indique l'existence d'une extinction des QDs dans la solution de NP de ZnO.

4 Nanoémetteur hybride basé sur l'adsorption de QDs sur des nanofils plasmoniques par un sel de diazonium

Dans ce chapitre, l'adsorption électrostatique des QDs ainsi que la fonctionnalisation de la surface du sel de diazonium seront réalisées à l'échelle nanométrique. La fonctionnalisation locale du sel de diazonium induite par plasmon a été réalisée sur une nanobande d'Au ou un nanofil d'argent (Ag NW), suivie par l'adsorption sélective de points quantiques (QDs) près du NW d'Ag par le biais d'interactions électrostatiques. Les nano-émetteurs hybrides QDs-Nanostrip d'Au et QDs-NW d'Ag qui en résultent présentent une émission photoluminescente (PL) plasmonique améliorée, avec un comportement de durée de vie contrôlable en corrélation positive avec les paramètres de fabrication. La morphologie sera analysée à l'aide de SEM et AFM, tandis que les spectres PL et les courbes TRPL seront mesurés pour évaluer leurs caractéristiques d'émission. Des émissions plasmoniques ont été observées pour les deux types de nano-émetteurs par l'analyse TRPL. En ce qui concerne les nano-émetteurs QDs-Ag NW. La propagation des polaritons plasmoniques de surface (SPP) a permis l'excitation à distance des QDs, qui peut être désactivée à la demande en changeant la direction de la polarisation d'excitation utilisée pour l'excitation SPP. La distance, qui est de 2,5 μm entre la position d'excitation et les emplacements du nano-émetteur sur Ag NW, devrait éviter la photo-oxydation et le photoblanchiment des QDs à partir de l'illumination laser et améliorer la durabilité du nano-émetteur hybride. L'excitation conditionnelle souligne l'application potentielle pour les systèmes photoniques à intégration avancée.

4.1 Nano-émetteurs QDs-Au en bandes : morphologie et émission PL plasmonique

Le MEB a été utilisé pour caractériser la morphologie des nano-émetteurs QDs-Au. La figure 4-1 présente les images SEM des nano-émetteurs fabriqués après le dépôt de QDs. Au cours du processus de fonctionnalisation de la surface, la couche greffée se forme le long des deux côtés de la nanobande d'Au, en suivant la distribution du champ électromagnétique amélioré plasmonique. La structure obtenue est illustrée à la figure 4-1a, pour laquelle le temps d'exposition au greffage est de 20 secondes. Bien que l'extension spatiale de la fonctionnalisation corresponde à la taille du laser incident, elle est confinée à l'échelle nanométrique perpendiculaire au fil métallique en raison du champ plasmonique évanescent local associé au mode de plasmon dipolaire transversal. Au fur et à mesure que la réaction de greffage se poursuit, les couches greffées près de la nanobande d'Au deviennent plus épaisses. Finalement, ces deux couches se connectent au-dessus de la nanobande Au, formant une couche unifiée, comme le montre la figure 4-1b, où le temps d'exposition était de 50 secondes.

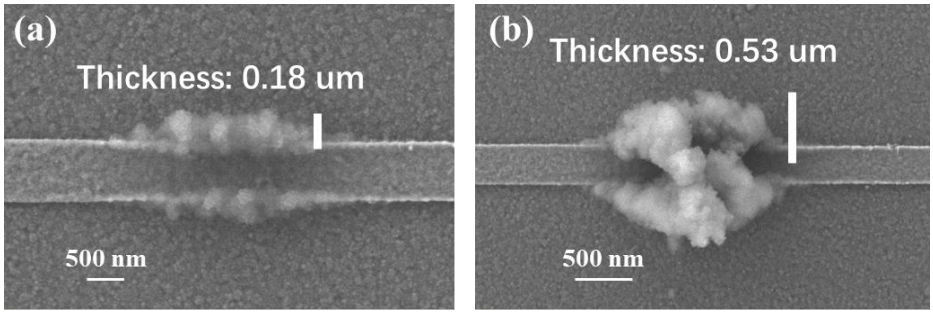

Figure 4-1. Image SEM du nano-émetteur QDs-Au fabriqué. (a) Le temps d'exposition dans le processus de greffage était de 20s, et l'épaisseur est de 0,18 μm. (b) Le temps d'exposition dans le processus de greffage était de 50s, et la demi-épaisseur est de 0,53 μm.

Le spectre PL du nano-émetteur QDs-Au est illustré à la figure 4-2a, avec une position de pic à 616,5 nm et une FWHM de 20 nm. En comparaison, le spectre PL des QDs étalés sur du verre ITO est présenté à la figure 4-2b, avec une position de pic à 614,5 nm et une FWHM de 21 nm. La cohérence du spectre PL tout au long du processus de fabrication indique que les QD peuvent être considérés comme faisant partie du nano-émetteur QDs-Au

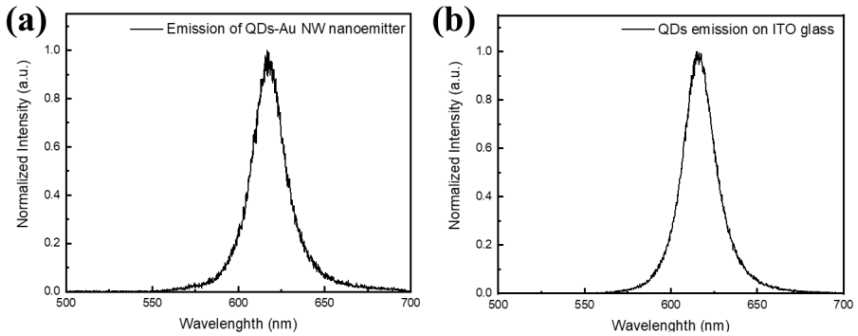

Figure 4-2. Spectre PL (a) du nano-émetteur QDs-Au (position du pic : 616,5 nm, FWHM : 20 nm) et (b) des QDs étalés sur du verre ITO (position du pic : 614,5 nm, FWHM : 21 nm).

Alors que le spectre PL est resté constant, la durée de vie de l'émission PL a varié en raison du couplage entre les QDs et les nanorubans d'Au. Dans notre cas, la quantité de QDs déposés n'est pas contrôlée. La durée de vie est le point clé pour évaluer l'amélioration du plasmon. La figure 4-3a présente le spectre TRPL du nano-émetteur QDs-Au, qui montre une durée de vie de 2,51 ns. En revanche, le spectre TRPL des QDs étalés sur le verre ITO, illustré à la figure 4-3b, indique une durée de vie de 17,4 ns. L'effet plasmonique et le transfert de porteurs indiqué entre les QD et la nanoruban Au sont attribués à la diminution de la durée de vie observée après que les QD ont été adsorbés sur la couche de sel de diazonium greffé. Le résultat prouve qu'il y a un effet Purcell dû à la bande nanométrique d'Au.

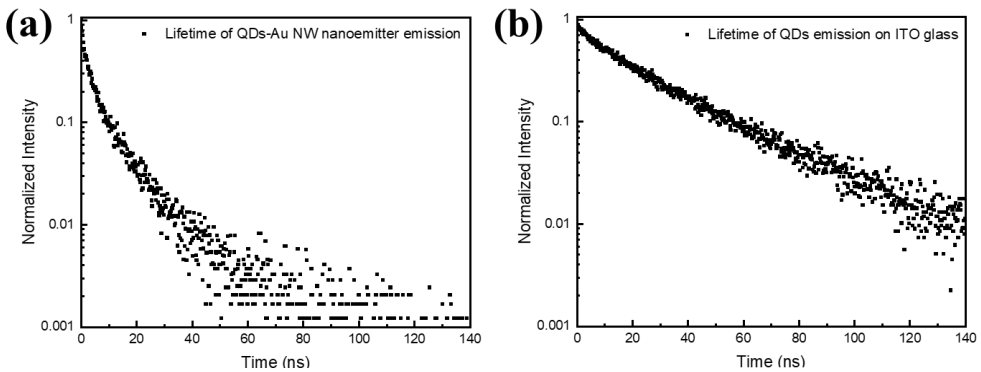

Figure 4-3. Courbes TRPL de (a) QDs-Au nano-émetteur en bande (τ = 2,51 ns) et (b) Spread QDs sur verre ITO (τ = 17,4 ns).

En comparant les durées de vie avant et après l'adsorption, nous avons exploré la relation entre la durée de vie et l'épaisseur de la couche de sel de diazonium greffée, qui peut également être considérée comme l'espace entre les QD adsorbés et la nanoruban Au. Cet espace représente la distance entre les QDs et la nanobande Au. Il peut influencer le couplage QDs-NW.

La figure 4-4 présente un diagramme de dispersion mettant en corrélation l'épaisseur et la durée de vie correspondante pour 17 nano-émetteurs QDs-Au. Les données indiquent une corrélation claire entre les épaisseurs et les durées de vie, avec une valeur P de 0,0002. En statistique, la valeur p est une mesure qui permet de déterminer la cohérence entre deux groupes de données. Si $p < 0,05$, la cohérence est considérée comme existante. Dans ce cas, il doit y avoir une corrélation positive entre l'épaisseur du nano-émetteur et la durée de vie de l'émission.

Lorsque la couche greffée devient plus épaisse, la durée de vie du nano-émetteur QDs-Au augmente également, en raison de la plus grande distance entre les QDs et le nanobrin Au. Cette corrélation positive confirme la présence de l'effet plasmonique dans le comportement d'émission du nano-émetteur QDs-Au fabriqué. En outre, comme l'épaisseur peut être contrôlée pendant la fabrication, la durée de vie de ce type de nanodispositif peut être ajustée d'environ 2,5 ns à 3,4 ns.

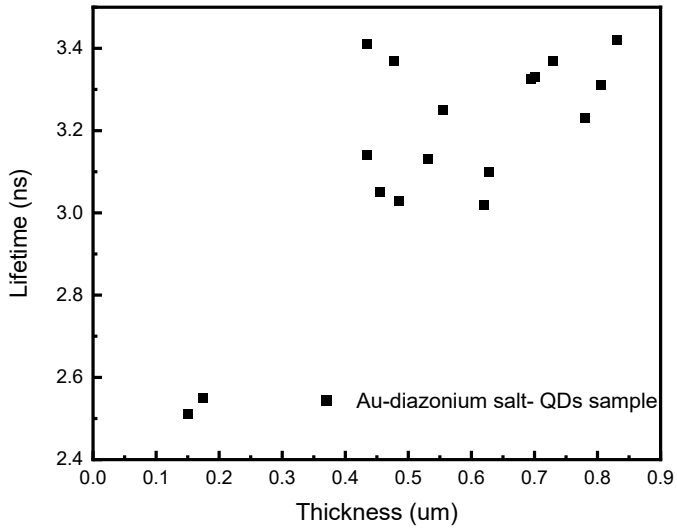

Figure 4-4. Diagramme de dispersion de l'épaisseur et de la durée de vie pour chaque nano-émetteur QDs-Au. L'épaisseur et la durée de vie sont en corrélation positive avec une valeur P de 0,0002.

4.2 Morphologie et propriétés optiques du nano-émetteur QDs-Ag NW

Les fils d'argent ont d'abord été dispersés sur un substrat de verre ITO de 15 mm * 15 mm avec une couche d'ITO de 135 nm d'épaisseur et la solution de sel de diazonium a été déposée sur l'échantillon. Un laser de 532 nm a illuminé le substrat par le bas, avec sa polarisation alignée sur l'axe court du fil d'argent. Les images SEM de la fonctionnalisation de surface réalisées avec différents temps d'illumination T sont présentées dans la figure 4-5. Le temps

d'exposition utilisé pour la fonctionnalisation de surface assistée par plasmon avec des sels de diazonium était de (a) 10 s, (b) 20 s, (c) 40 s, (d) 60 s, (e) 120 s et (f) 180 s, avec une densité de puissance lumineuse fixe de 0,0468 mW/μm^2. L'épaisseur de la couche de polyaryle obtenue variait de 0,118 μm (T=10 s) à 2,504 μm (T=180 s). Au temps d'exposition de 10 s, la couche fonctionnalisée s'est principalement greffée le long du NW d'Ag principalement sur les bords du NW. Au fur et à mesure que le temps d'exposition augmentait, la couche greffée devenait plus épaisse dans les dimensions horizontales et verticales. La forme générale de la couche ressemblait à de multiples sphères dont les diamètres variaient de 20 nm à 200 nm. L'origine de ces matériaux polymérisés en forme de sphère n'est pas encore claire. La taille de ces sphères augmente avec le temps d'exposition. En outre, lorsque le temps d'exposition dépassait 60 s, comme l'illustrent les figures 4-5e-f, la fonctionnalisation de la surface a également commencé à se produire sur la surface ITO adjacente au fil d'argent, avec une structure d'interférence s'étendant au fur et à mesure que le temps d'exposition augmentait. En outre, à proximité des fils d'argent, la couche de fonctionnalisation de surface s'est développée dans le sens vertical sur la surface horizontale au fur et à mesure que l'exposition se poursuivait.

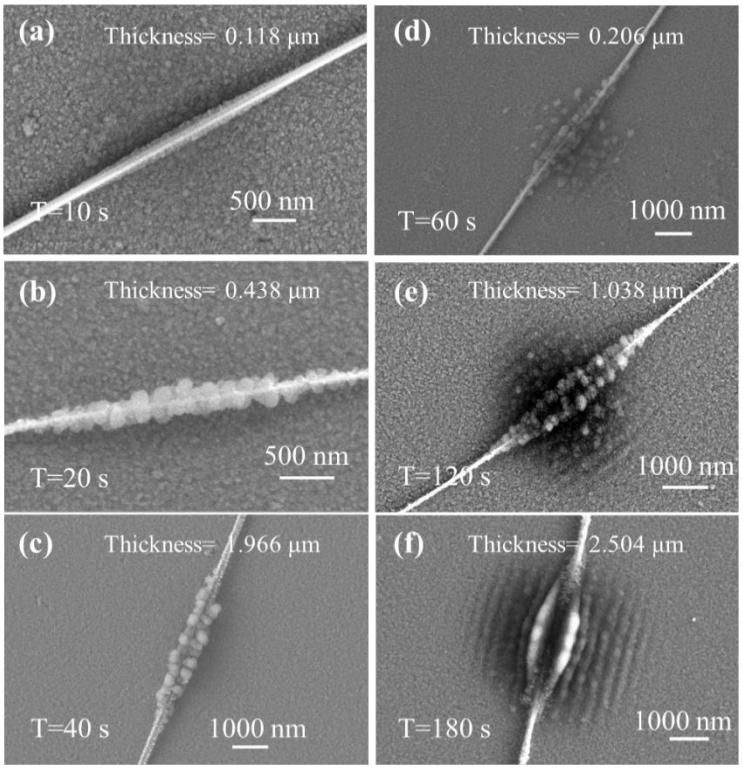

Figure 4-5. Images SEM de la fonctionnalisation de la surface des sels de diazonium sur les nanoparticules d'Ag. Les temps d'exposition ont été ajustés comme suit : (a) 10 s, (b) 20 s, (c) 40 s, (d) 60 s, (e) 120 s et (f) 180 s. Les épaisseurs varient de 0,118 μm à 2,504 μm.

En plus des résultats précédents, nous avons ajusté la densité d'énergie laser de 0,0468 mW/μm² à 0,468 mW/μm² et fait varier le temps d'exposition de 10 s à 180 s. Au total, 32 structures hybrides ont été fabriquées en utilisant des procédures similaires. Les épaisseurs greffées en fonction des densités d'énergie lumineuse d'exposition ont été analysées statistiquement, les résultats étant présentés dans la figure 4-6. L'analyse a révélé une corrélation positive entre la densité d'énergie lumineuse d'exposition et l'épaisseur, avec une valeur p de corrélation de 1,37865*10^{-12}et un facteur de corrélation de Pearson de 0,8866. Cela indique que l'épaisseur obtenue peut être contrôlée en ajustant la densité d'énergie

lumineuse d'exposition.

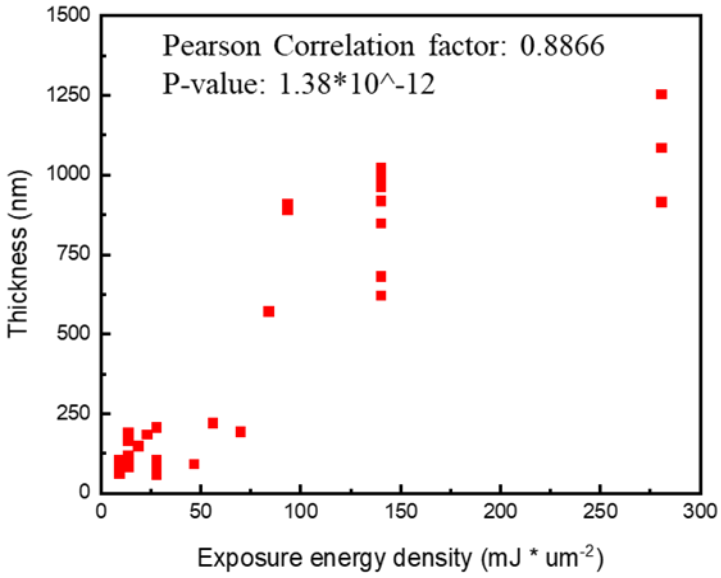

Figure 4-6. Relation entre la taille de la structure hybride et la densité d'énergie d'exposition au laser. Le facteur de corrélation de Pearson est de 0,88658.

La figure 4-7 présente les spectres PL de la nanostructure avant et après l'étape de dépôt des QDs. Les images AFM et le profil de la section transversale sont présentés dans les figures 4-7a et 4-7b respectivement, révélant une hauteur de 257 nm. La section transversale présente deux pics de hauteur. L'image SEM est représentée à la figure 4-7c, indiquant que l'épaisseur de cette nanostructure est de 91 nm.

Dans la figure 4-7d, l'intensité PL avant le dépôt de QDs est observée comme étant d'environ 40-70, sans pics significatifs, ressemblant au spectre PL de fond de la couche greffée à large bande discuté dans le chapitre 2. Cependant, après le dépôt de QDs, le spectre PL illustré à la figure 4-7e révèle un pic proéminent d'une intensité d'environ 15 000. La différence substantielle dans les spectres PL confirme que la source d'émission PL dans ce nano-émetteur est les QDs, plutôt que d'autres composants.

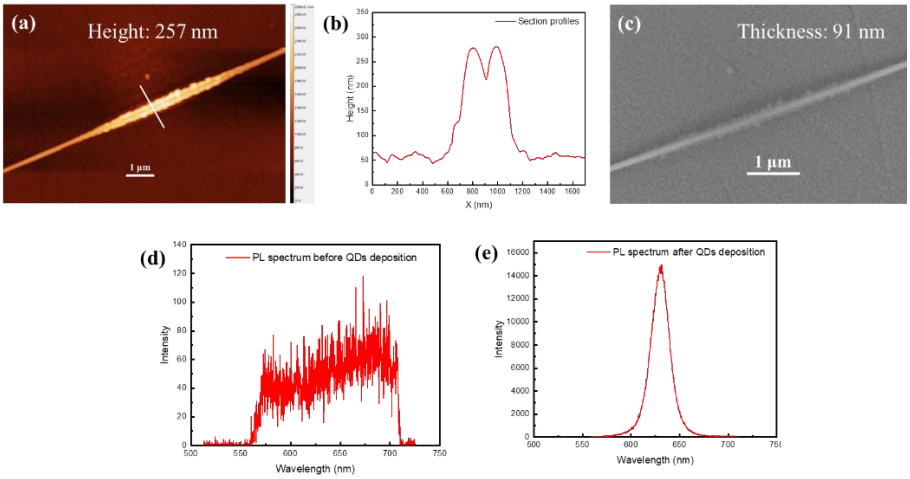

Figure 4-7. (a) et (b) profil AFM et profil de section, hauteur : 231 nm. (c) l'image SEM, épaisseur : 91 nm. (d) Spectre PL avant le dépôt de QDs : pas de pic. (e) Spectre PL après le dépôt de QDs : intensité du pic ~15000.

La morphologie des nano-émetteurs QDs-DCOOH-Ag NW et QDs-DNO_2-Ag NW

fabriqués a été analysée à l'aide du MEB et de l'AFM, comme le montre la figure 4-8. L'image AFM et le profil de section du nano-émetteur QDs-DCOOH-Ag NW sont présentés dans les Figures 4-8a, indiquant une hauteur de 231 nm. L'épaisseur du polyaryle dans le plan, mesurée à partir de l'image SEM de la figure 4-8b, est de 136 nm. En revanche, le nano-émetteur QDs-DNO_2-Ag NW présente une hauteur de 307 nm, comme le montrent l'image AFM et le profil de section des figures 4-8d. L'épaisseur du polyaryle dans le plan de cet échantillon, mesurée à partir de l'image SEM de la figure 4-8e, est de 126 nm. Avec une hauteur et une épaisseur similaires, les deux types de nano-émetteurs ont des surfaces comparables pour l'adsorption des QDs.

Le spectre PL du nano-émetteur QDs-DCOOH-Ag NW est présenté dans la figure 4-8c, montrant une intensité maximale de 13235. Pour le nano-émetteur QDs-DNO_2-Ag NW, l'intensité PL maximale est d'environ 255, comme le montre la figure 4-8f, ce qui est 51,9 fois inférieur à celle du nano-émetteur à base de DCOOH. La diminution du PL dans le cas du DNO_2peut être associée à un nombre plus faible de QD adsorbés sur le fil d'Ag. Ce résultat est en accord avec la présence d'une adsorption électrostatique dans le nano-émetteur QDs-DCOOH-Ag NW, par rapport à la faible interaction de van der Waals possible dans le système QDs-DNO_2-Ag NW.

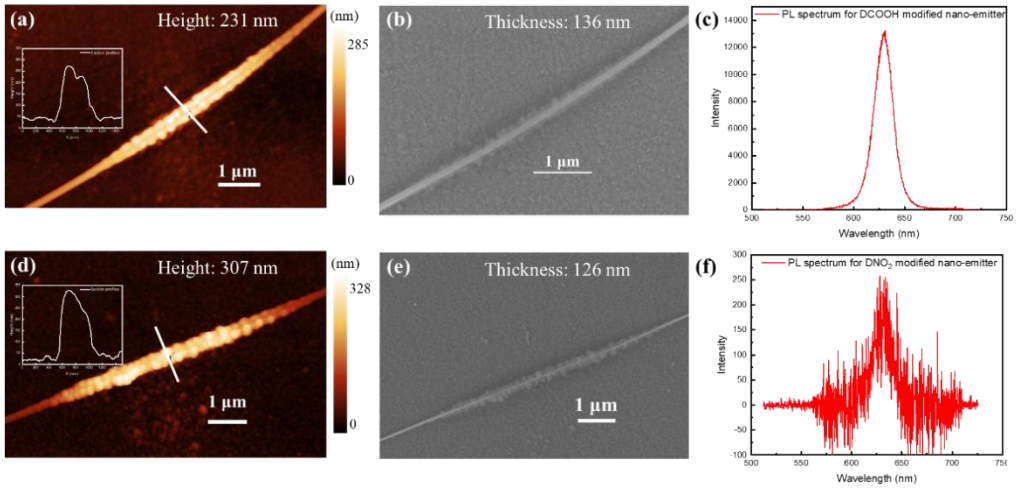

Figure 4-8. Comparaison entre deux types de nano-émetteurs. (a-c). Nanoémetteur QDs-DCOOH -Ag NW. (a) AFM et coupe transversale, hauteur : 231 nm. (b) Image SEM, épaisseur : 136 nm. (c) Spectre PL. Intensité PL ~ 13235. (d-f) Nanoémetteur QDs-DNO_2-Ag NW. (d) Profil AFM et section, hauteur : 307 nm. (e) L'image SEM, épaisseur : 126 nm. (f) Spectre PL. Intensité PL ~ 255 (diminution de 51,9 fois).

Après le second dépôt de la solution de QDs pour fabriquer la nanostructure QDs-DCOOH, les spectres PL et TRPL de la nanostructure QDs-DCOOH ont été mesurés et comparés aux spectres des nano-émetteurs QDs-DCOOH-Ag NW. Les figures 4-9a et 4-9c comparent les spectres PL. Les deux intensités PL maximales sont situées à 631 nm, ce qui correspond à la solution colloïdale originale de QDs. L'intensité PL maximale des nano-émetteurs QDs-DCOOH-Ag NW est de 21277, tandis qu'elle est de 4864 pour la nanostructure QDs-DCOOH. Les temps d'intégration pour les deux spectres ont été maintenus à 5s. On observe une diminution de 4,37 fois de l'intensité PL après l'élimination des fils d'Ag. Les spectres TRPL ont été comparés dans les figures 4-9b et 4-9d. La durée de vie des nano-émetteurs QDs-DCOOH-Ag NW est de 0,545 ns, et de 4,32 ns pour la nanostructure QDs-DCOOH. La durée de vie augmente de 7,93 fois après l'élimination du fil d'argent.

La comparaison de l'intensité et de la durée de vie de la PL confirme la présence d'un effet plasmonique provenant du fil d'Ag dans le nano-émetteur fabriqué. Avec le retrait in situ du fil d'argent, les autres composants, y compris les QD, la couche greffée et le substrat ITO, ont conservé leur forme et leur position dans les deux nanostructures. Sur la base de la comparaison, le facteur de Purcell de cette nanostructure est évalué à 7,93 tandis que le facteur d'amélioration PL est de 4,37.

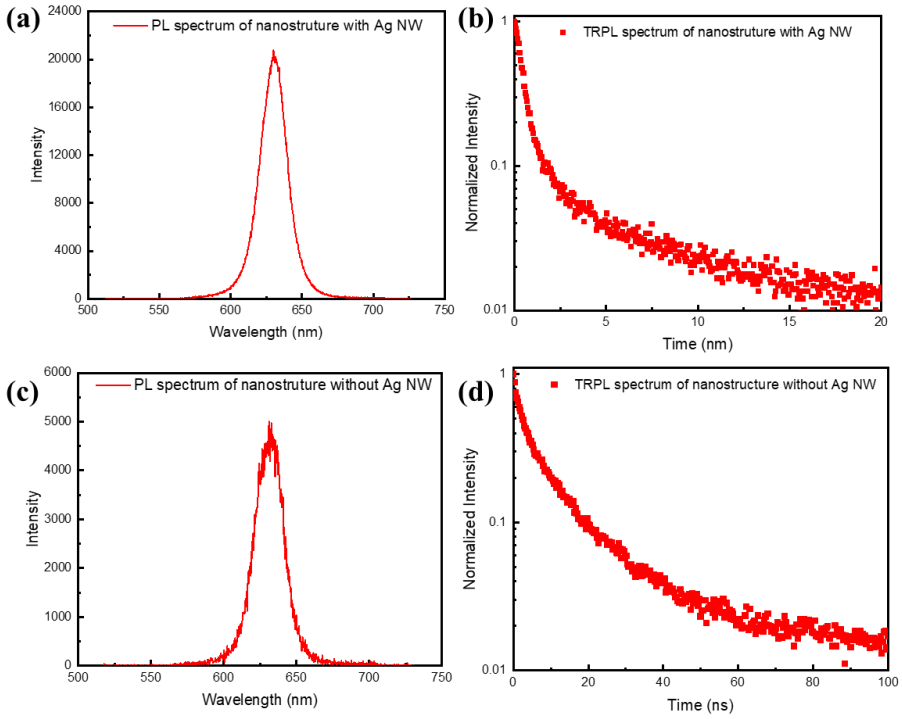

Figure 4-9. (a) PL et (b) TRPL du nano-émetteur QDs-DCOOH Ag NW. L'intensité PL est de 21277, et la durée de vie est de 0,545 ns. (c) PL et (d) TRPL du nano-émetteur QDs-DCOOH. L'intensité PL est de 4864, et la durée de vie est de 4,32 ns. Après avoir retiré le fil d'Ag du nano-émetteur, l'intensité PL a diminué d'un facteur de 4,37 et la durée de vie a augmenté d'un facteur de 7,93.

Pour étudier plus avant la relation entre les épaisseurs des nano-émetteurs et les durées de vie correspondantes, une analyse statistique a été réalisée, comme le montre la figure 4-10. Une corrélation positive a été observée avec une valeur p de $2{,}00595*10^{-11}$et un facteur de corrélation de Pearson de 0,9603. Ce résultat implique que, pour les nano-émetteurs fabriqués, une épaisseur plus importante se traduit par une durée de vie plus longue. Cette constatation corrobore l'effet plasmonique, où un écart plus important entre la source plasmonique et l'émetteur conduit à un facteur de Purcell plus faible. De plus, l'épaisseur peut être contrôlée en ajustant les paramètres de fabrication. Par conséquent, l'émission PL du nano-émetteur QDs-DCOOH-Au peut être ajustée à partir du processus de fabrication.

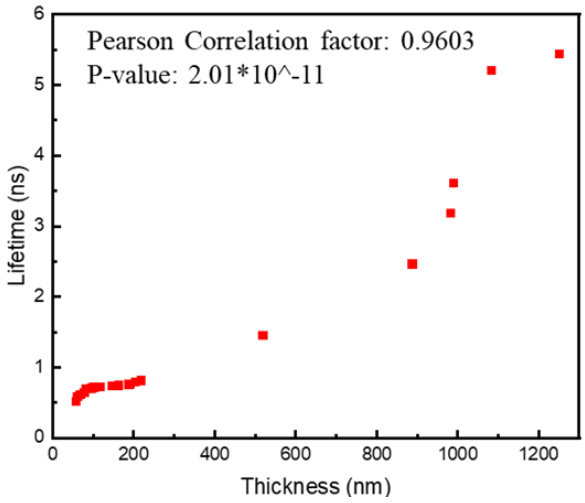

Figure 4-10. Relation entre l'épaisseur des nano-émetteurs hybrides et les durées de vie correspondantes. Le facteur de corrélation de Pearson est de 0,96032

La figure 4-11a présente l'image SEM modifiée illustrant la méthode de mesure par excitation à distance. La position d'excitation A est située à l'extrémité du fil d'Ag, où une lumière laser de 6,32 mW est utilisée pour l'excitation avec la même longueur d'onde et la même taille de spot que dans les figures 4-34a et 4-34b. Deux types de direction de polarisation laser avec les modes α et β ont été utilisés pour l'excitation à la position A. La zone de détection avec une taille de 1 μm*1 μm est positionnée à l'endroit fonctionnalisé où les QDs sont attachés, qui est à 2,5 μm loin de l'extrémité du NW Ag. À titre de référence, pour exclure toute diffusion à partir de la position d'excitation A, qui pourrait également exciter le nano-émetteur à distance, une comparaison a été effectuée avec la position d'excitation B, qui est contrôlée pour maintenir la même distance et la même polarisation d'excitation par rapport au nano-émetteur.

La figure 4-11b montre les spectres PL obtenus dans différentes conditions d'excitation, ainsi que le spectre de fond de la zone de détection, qui est mesuré sans aucune illumination de l'échantillon. Lorsque l'excitation laser est concentrée sur la position A, l'intensité de l'émission PL dépend fortement de la direction de polarisation. Un pic d'émission PL est observé à 633 nm lorsque la polarisation est alignée avec l'axe long (mode α). Dans le cas du mode β, dans lequel la polarisation est alignée avec l'axe court, le spectre PL est similaire au spectre de fond. Cependant, même si la direction de polarisation a été définie comme le mode α, il n'y a pas de pic d'émission sur le spectre PL sous excitation en position B. Ce résultat prouve que la lumière de la position B ne se propage pas à travers la distance par le substrat ou l'air pour atteindre la zone du nano-émetteur. En outre, les spectres de la position A (mode β) et de la position B correspondent au spectre PL obtenu pour l'arrière-plan. Compte tenu des quatre spectres, deux conditions sont nécessaires pour réaliser l'excitation à distance : i) utiliser des fils d'Ag comme support pour la propagation de l'onde de surface à 532 nm pour l'excitation à distance des QDs, ii) et aligner la polarisation d'excitation avec son axe long pour lancer l'onde de surface.

En soustrayant le bruit de fond du spectre PL à la position A (mode α), le spectre PL résultant est illustré à la figure 4-11c, avec un pic à 630 nm, cohérent avec l'émission PL excitée localement du nano-émetteur QDs-DCOOH-Ag NW.

Ces observations confirment que, grâce à la propagation SPP, le laser excite le nano-

émetteur plasmonique à distance. En commutant la polarisation d'excitation, l'excitation à distance peut être activée ou désactivée. Ce résultat illustre l'application potentielle des structures hybrides fabriquées dans la photonique intégrée avancée.

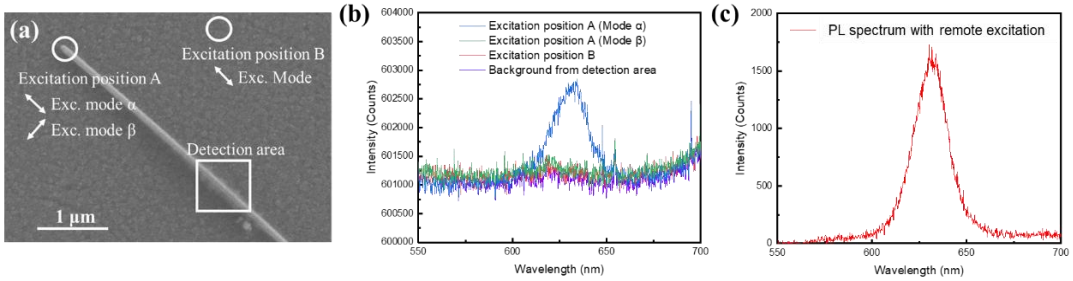

Figure 4-11. (a) Schéma des méthodes de mesure de l'excitation à distance. (b) Les spectres PL obtenus avec différentes conditions d'excitation ainsi que l'arrière-plan de la zone de détection. (c) Le spectre PL calculé.

5 Résumé et conclusions

Cette thèse présente une nouvelle méthode de fabrication de nano-émetteurs hybrides en tirant parti de la fonctionnalisation des surfaces à l'aide de sels de diazonium et de l'adsorption électrostatique de points quantiques (QDs), dans le but de faire progresser les applications photoniques intégrées. La stratégie de base repose sur l'interaction électrostatique entre les surfaces fonctionnalisées par DCOOH, chargées négativement, et les QDs encapsulés par cystéamine, chargés positivement, ce qui permet un contrôle spatial précis et un couplage plasmonique puissant. La méthodologie a été validée sur différentes plateformes, du verre ITO et des pointes de fibres optiques aux nanofils d'Au et d'Ag, démontrant une adsorption cohérente des QDs, une photoluminescence (PL) renforcée par les plasmons, et une émission accordable via les paramètres structurels. En particulier, dans les émetteurs à nanofils QDs-Ag, la modulation de la durée de vie et l'excitation à distance via la propagation des plasmons de surface mettent en évidence le potentiel des sources de lumière à l'échelle nanométrique. Les résultats suggèrent de nouvelles possibilités d'intégration efficace et évolutive des QDs dans les dispositifs photoniques, tout en identifiant les orientations futures de la recherche, telles que la minimisation de l'émission de fond des couches fonctionnelles et l'exploration des mécanismes de transfert d'énergie pour améliorer les performances de l'émetteur.

Les références

1. Uppu, R., Midolo, L., Zhou, X., Carolan, J. & Lodahl, P. Quantum-dot-based deterministic photon–emitter interfaces for scalable photonic quantum technology. *Nat. Nanotechnol.* **16**, 1308–1317 (2021).
2. Liu, Z. *et al.* Micro-light-emitting diodes with quantum dots in display technology. *LIGHT-Sci. Appl.* **9**, 83 (2020).
3. García de Arquer, F. P. *et al.* Semiconductor quantum dots: Technological progress and future challenges. *Science* **373**, eaaz8541 (2021).
4. Heindel, T., Kim, J.-H., Gregersen, N., Rastelli, A. & Reitzenstein, S. Quantum dots for photonic quantum information technology. *Adv. Opt. Photonics* **15**, 613–738 (2023).
5. Han, Y., Chang, X., Cheng, X., Lin, Y. & Cui, B.-B. Recent Progress of Organic–Inorganic Hybrid

Perovskite Quantum Dots: Preparation, Optical Regulation, and Application in Light-Emitting Diodes. *Laser Photonics Rev.* **17**, 2300383 (2023).
6. Hildebrandt, N., Lim, M., Kim, N., Yeon Choi, D. & Nam, J.-M. Plasmonic quenching and enhancement: metal–quantum dot nanohybrids for fluorescence biosensing. *Chem. Commun.* **59**, 2352–2380 (2023).
7. Pfeiffer, M. *et al.* Enhancing the optical excitation efficiency of a single self-assembled quantum dot with a plasmonic nanoantenna. *Nano Lett.* **10**, 4555–4558 (2010).
8. Yin, Z. *et al.* Local Field Modulation Induced Three-Order Upconversion Enhancement: Combining Surface Plasmon Effect and Photonic Crystal Effect. *Adv. Mater.* **28**, 2518–2525 (2016).
9. Chung, T., Lee, S.-Y., Song, E. Y., Chun, H. & Lee, B. Plasmonic Nanostructures for Nano-Scale Bio-Sensing. *Sensors* **11**, 10907–10929 (2011).
10. Seo, J. *et al.* Hybrid optical materials of plasmon-coupled CdSe/ZnS coreshells for photonic applications. *Opt. Mater. Express* **2**, 1026–1039 (2012).
11. Ge, D. *et al.* Hybrid plasmonic nano-emitters with controlled single quantum emitter positioning on the local excitation field. *Nat. Commun.* **11**, 3414 (2020).
12. Nicoli, F. *et al.* DNA-mediated self-assembly of plasmonic antennas with a single quantum dot in the hot spot. *Small* **15**, 1804418 (2019).
13. Groß, H., Hamm, J. M., Tufarelli, T., Hess, O. & Hecht, B. Near-field strong coupling of single quantum dots. *Sci. Adv.* **4**, eaar4906 (2018).
14. Park, Y.-S., Bae, W. K., Pietryga, J. M. & Klimov, V. I. Auger Recombination of Biexcitons and Negative and Positive Trions in Individual Quantum Dots. *ACS Nano* **8**, 7288–7296 (2014).
15. Jha, P. P. & Guyot-Sionnest, P. Trion Decay in Colloidal Quantum Dots. *ACS Nano* **3**, 1011–1015 (2009).
16. Liras, M., González-Béjar, M. & Scaiano, J. C. On-off QD switch that memorizes past recovery from quenching by diazonium salts. *Phys. Chem. Chem. Phys.* **12**, 9757–9762 (2010).

Scientific productions

Articles:

1. ***Li S.,*** Chen H., Hu M., Shi L., Gu M., Trotsiuk L., Issa A., Jradi S., Jia S., Ma J., *et al.* Fibered Optical Sensor Based on the Integration of Quantum Dots on a Polymer Tip. *J. Phys. Chem. C* (2024) 128, 20624−20634.
2. ***Li S.,*** Gu M., Chen H., Trotsiuk L., Chen M., Issa A., Jradi S., Jia S., Luo Y., Adam P., *et al.* A diazonium salt functionalization strategy for photoluminescent hybrid plasmonic nanosystems. (Under review) (The Journal of Physical Chemistry C)
3. ***Li, S.,*** Gu, M., Garzandat, S., Sun, X.W. and Bachelot, R. (2024), 8-2: The micro-scale adsorption of QDs on select surface by click chemistry. SID Symposium Digest of Technical Papers, 55: 80-82.
4. Liang S., Tang Z., ***Li S.,*** Guo X., Jia S., Sun X. W., Efficient ZnSeTe-Based Blue Quantum-Dot Light-Emitting Diodes via Phosphine Oxide Dual Passivation of Quantum Dots and ZnMgO Interfaces. (online) (Advanced Optical Materials)
5. Yang Y., Gu M., Lin W., Zhang X., ***Li S.,*** Zhao Q., Sun X. W., Li Y., Enhanced Fluorescence at Low Excitation Power with GaP Hybrid Nanoantennas. (Under review) (Advanced Optical Materials)
6. Cheng P., Lau-Truong S., Derouich S., Bonnet R., Chevillot-Biraud A., Braïk M., Mezeghrane A., Belkhir A., ***Li S.,*** Dewynter M., *et al.* Aluminum Surface Lattice Resonances for Enhanced Near-Infrared Performance in Asymmetric Environments. (Under review) (Advanced Optical Materials)

Conferences:

1. 2024 International Conference on Display Technology (ICDT 2024), ***Oral Topic:*** The micro-scale adsorption of QDs on select surface by click chemistry. (March 31, 2024)
2. The Postgraduate Workshop on Display Research (PGWS), ***Oral Topic:*** Click Chemistry-Assisted Fabrication of Quantum Dot-Adsorbed Optical Fiber Tip. (August 21, 2023)
3. CNRS GDR Conference on Active Plasmonics, ***Oral Topic:*** Attachement of QDs on selected area for hybrid plasmonics. (July 1, 2021)

Acknowledgement

First of all, I would like to thank to my supervisors, Prof. Renaud Bachelot and Prof. Xiao Wei Sun, for their delighting guidance, encouragements and friendship throughout my PhD. Without their patient instruction, insightful criticism and expert guidance, I could not finish this thesis.

Apart from my supervisors, I want to thank Prof. Nordin Felidj and Prof. Claire Mangeney. They helped me a lot on the work about diazonium salt, which is an important part of my thesis. I also want to thank Prof. Pierre-Michel Adam, he guided me to start my research on plasmonic. Dr. Liudmila Tratsiuk helped to review my publications and thesis. Thanks for her efforts during the time we work together.

I also want to thank all the working partners for the help during my experiments and the knowledge sharing. They are Dr. Tiziana Ritacco, Dr. Dandan Ge, Dr. Hongshi Chen, Dr. Ali Issa, Dr. Minyu Chen, Dr. Théo Geronimi Jourdain, Mi Gu, Menglei Hu, Sara Garzandat. Also thanks to all the members from labs of UTT and SUSTech for their great help. Thanks to the happy and wonderful times spent with my friends: Fankai Zheng, Jingrui Ma, Siqi Jia, Guohong Xiang, Zhengbiao Liu, Tianqi Zhang, Sambhav Kumar, Sarabjeet Kaur, Baptiste Prunot and others.

My special thanks would go to my family for all your love. To my parents for their endless understanding and support. To my fiancée, Ying Pei, for the consistent support and encouragement during this period.

Finally, I would like to thank the experience and study in UTT and SUSTech. I love these universities!

Shang LI

Doctorat : Matériaux, Mécanique, Optique et Nanotechnologie

Année 2025

Emetteurs hybrides de lumière basés sur la fonctionnalisation de surface photoinduite d'un sel de diazonium

Cette thèse présente une nouvelle méthode fabrication de nanoémetteurs de lumière à base de boites quantiques (QD) basée sur l'interaction électrostatique entre des QDs CdSe/ZnS modifiés en surface et une couche greffée de tétrafluoroborate de 4-carboxybenzènediazonium (DCOOH) qui peut être optiquement structurée. Cette approche permet un contrôle précis de la localisation de boites quantiques sur des surfaces fonctionnalisées au diazonium aux échelles nanométriques et micrométriques, applicable à divers substrats, notamment le verre ITO, les fibres optiques et les nanofils d'or/d'argent. Les boites quantiques modifiés en surface par des ligands cystéamine présentent des charges positives ($-NH3^{+}$) en solution aqueuse, permettant un couplage électrostatique avec les groupes $-COO^{-}$ chargés négativement provenant de DCOOH. Des expériences de référence utilisant le tétrafluoroborate de 4-ntrbenzèn-ediazonium (DNO2) ont confirmé la spécificité desinteractions électrostatiques. L'intégration sur verre ITO a permis d'étudier les conditions d'intégration des QDs et de définir les protocoles. L'intégration sur fibre optique a permis de réaliser un prototype de capteur fibré de concentration de nanoparticules en milieu liquide. La couche fonctionnalisée DCOOH greffée en surface a été également intégrée via des champs plasmoniques de nanofils métalliques : sa forme suit la distribution du champ électrmagnétique confiné amplifié par plasmons. En contrôlant l'épaisseur de la couche fonctionnalisée, cette stratégie permet d'obtenir des écarts ajustables entre les boites quantiques et lessources plasmoniques, et conduit à des émissions de lumière contrôlables.

Mots clés : points quantiques - photoluminescence - fonctionnalisation des surfaces (chimie) - sels de diazonium - nanoplasmonique.

Development of Hybrid Light Emitters based on Photoinduced Surface Functionalization of a Diazonium Salt

This thesis presents a new method for fabricating quantum dot (QD)-based nano-light emitters based on the electrostatic interaction between surface-modified CdSe/ZnS QDs and a grafted layer of 4-carboxybenzenediazonium tetrafluoroborate (DCOOH) that can be optically structured. This approach allows precise control of the localization of quantum dots on diazonium-functionalized surfaces at nanometric and micrometric scales, applicable to a variety of substrates including ITO glass, optical fibers and gold/silver nanowires. Quantum dots surface-modified with cysteamine ligands exhibit positive charges ($-NH3^{+}$) in aqueous solution, allowing electrostatic coupling with negatively charged -COO- groups from DCOOH. Reference experiments using 4-nitrobenzenediazonium tetrafluoroborate (DNO2) confirmed the specificity of the electrostatic interactions. Integration on ITO glass was first used to study QD integration conditions and define protocols. Integration on optical fibers enabled the production of a prototype fibered sensor for the concentration of nanoparticles in a liquid medium. The functionalized DCOOH layer grafted onto the surface was also integrated via plasmonic fields of metal nanowires: its shape follows the distribution of the confined electromagnetic field amplified by plasmons. By controlling the thickness of the functionalized layer, this strategy makes it possible to obtain adjustable gaps between the quantum dots and the plasmonic sources, and leads to controllable light emissions.

Keywords: quantum dots - photoluminescence - surface functionalization - diazonium salts - nanoplasmonics.

Thèse réalisée en partenariat entre :

南方科技大学 SOUTHERN UNIVERSITY OF SCIENCE AND TECHNOLOGY

utt UNIVERSITÉ DE TECHNOLOGIE TROYES

Ecole Doctorale "Sciences pour l'Ingénieur"